DISSERTATION

Search for cosmological gravitational-wave background at high frequencies

Graduate School of Human and Environmental Studies,
Kyoto University

NISHIZAWA, Atsushi

28 November, 2008: ver.1.0
(22 July, 2009: updated ver.1.1)

Abstract

We describe the general framework for a cosmological gravitational-wave background (GWB) search with a laser-interferometric gravitational-wave (GW) detector. What we studied in this thesis can be divided into two topics: (i) the search for non-tensorial polarization modes (scalar- and vector-like polarizations) of a GWB with a large-scale laser-interferometric detector pair on the ground, (ii) the GWB search at ultra-high frequencies ($\sim 100\,\mathrm{MHz}$) with a pair of meter-sized laser-interferometric detectors.

The first topic is involved in the theories with extra dimensions and the modified gravity theories. In the general relativity, there are two polarization modes of a GW. However, in the general theories of gravity, six polarization modes are allowed. If the extra polarization modes of GWB are detected, we can obtain some information about new physics. The search has not been performed at all so far with an interferometer. So, we extended the conventional formalism of a cross-correlation analysis to non-tensorial polarization modes and calculated the sensitivity to the GWB. We also discussed the detectability with real detector pairs.

The second topic is the search for a GWB at ultra high frequencies. It is also important because some models in cosmology and particle physics predict relatively large GWB at ultra-high frequency $\sim 100\,\mathrm{MHz}$. Upper limits on GWB in wide-frequency ranges have been obtained from various observations. However, they are all indirectly derived from the observations. As far as we know, little direct experiment has been done above $100\,\mathrm{kHz}$ except for a few experiments, though the direct constraint is much weaker than the constraints at other frequencies. Thus, a much tighter bound above $100\,\mathrm{kHz}$ is needed to test various theoretical models.

First, we investigated the laser-interferometric detector designs that can effectively respond to GW at high frequencies, and found that the configuration, a so-called synchronous-recycling interferometer (SRI) is the best at these sensitivities. Then, we investigated the location and orientation dependence of two SRIs in detail, and derived the optimal location of the two detectors and the cross-correlation sensitivity to a GWB. We also describe the experiment done by our group and the results. These studies are not limited at the search at $\sim 100\,\mathrm{MHz}$, but can also be applied to the detectors in which the wavelength of a GW is comparable with the detector size.

As a developed version of the SRI, we proposed a new detector design, a so-called resonant speed meter (RSM). The remarkable feature of this interferometer is that, at certain frequencies, gravitational-wave signals are amplified, while displacement noises are not. We also studied the quantum noise in a RSM, and its ultimate sensitivity.

Contents

Chapter 1

Introduction

1.1 Gravitational waves

A gravitational wave (GW) is a ripple of spacetime, which propagates as a wave with the speed of light. The GW is predicted according to the theory of general relativity, published in 1916 by Einstein [1]. Nowadays, the many predictions of the General relativity have been confirmed in many observations and experiments [2]: gravitational lensing, Shapiro delay in the solar system, the perihelion advance of the planet Mercury, dragging of an inertial frame, etc.. In addition, the binary pulsars supply us with the splendid opportunities to test the general relativity, owing to the considerable stability and the strong gravity. From the observation of the change in the revolution period of B1931+16 (Hulse-Taylar binary pulsar), general relativity has been tested at a level of 1%, and the indirect evidence of the existence of GWs has been obtained [3, 4]. Recently, Valtonen *et al.* have claimed that a new indirect evidence is found by the observation of a binary system of two candidate black holes in the quasar OJ 287 [5].

These evidences lead us to strongly believe the existence of GWs. Nevertheless, GWs have not directly detected yet. Aiming for the first direct detection of GWs, many research groups have constructed large detectors and done observations with the sensitivity improved by degrees.

1.2 Gravitational-wave sources

GWs are radiated by objects whose motion involves acceleration, provided that the motion is not spherically symmetric nor axisymmetric [6]. A number of GW sources have been theoretically predicted, as shown in Fig. 1.1 together with the sensitivities of GW detectors.

Gravitational waves from astrophysical sources

The promising GW sources with astronomical origins are violent events involving compact objects, such as supernovae, gamma-ray bursts, the binaries of neutron stars, black holes, and white dwarfs and their mergers, and spinning-down pulsars. Recent

study and observational data suggested a part of supernovae and gamma-ray bursts are related to the mergers of neutron stars, black holes, and white dwarfs. The GWs from these systems are important in that not only do they provide the test in the strong regime of gravity, but also they will bring new information that one cannot obtain by the observations with electromagnetic waves. This is owing to the strong transparency of GWs. Electromagnetic waves are scattered at the outer layer of the stars and the plasma around it, and prevent us from directly seeing the core of the stars. In contrast, GWs can escape from the dense regions of the stars and directly propagate to the Earth. Thus, we can investigate the equation of state in extremely high-density region such as an inner core of a neutron star, the strong regime of gravity and its environment around a black hole, the explosion mechanism of a supernova, the central engine of a gamma-ray burst, the inner region veiled by dust such as the accretion disk around a compact object, etc..

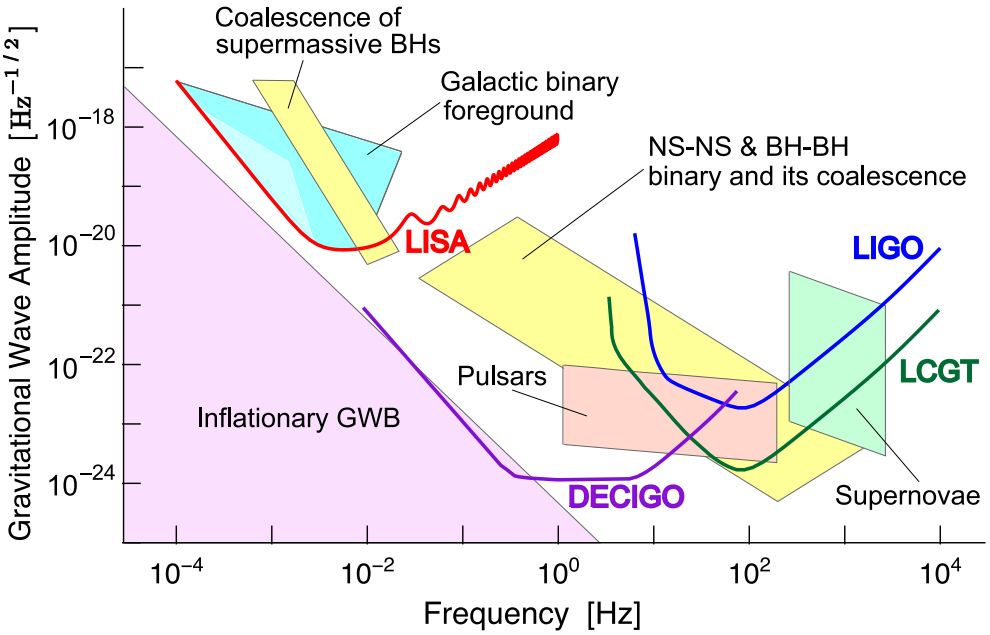

Figure 1.1: Schematic view of GW sources and detector sensitivities. In the figure, the noise curves of LIGO, LCGT, LISA, and DECIGO are representationally shown. As for the magnitude of the noise curve, VIRGO is almost the same as LIGO, BBO is almost the same as DECIGO, and the second-generation interferometers (advanced LIGO, advanced VIRGO, and AIGO) are almost the same as LCGT, though TAMA and GEO are slightly worse than LIGO and VIRGO.

Cosmological gravitational-wave background

There is another type of GWs, called gravitational wave background (GWB), which is the superposition of a huge number of GWs with random phases (for the review, [7]). This is an analogy of cosmic microwave background (CMB). The CMB was discovered

by Penzias and Wilson in the mid 1960s as an isotropic radiation over the sky [8], and the COsmic Background Explorer (COBE) was first detected the anisotropy of the CMB in 1992 [9]. Then, the Wilkinson Microwave Anisotropy Probe (WMAP) satellite was launched in 2001, precisely measured the CMB anisotropic temperature fluctuations, and determined cosmological parameters with astonishing accuracy in 2003 [10, 11, 12, 13, 14] (The WMAP has been yielded the observational data, and the updated cosmological parameters with fifth-year data have been published [15].). The difference between CMB and GWB is the epoch of the decoupling. CMB photons decouple when the energy scale of the universe is $\sim 0.3\,\mathrm{eV}$, corresponding to the redshift $z \sim 1100$. On the other hand, gravitons decouple at the Planck energy scale of $\sim 10^{19}\,\mathrm{GeV}$, because of the small coupling rate of the gravitational interaction. Therefore, the GWB created in the early universe survives without loss of the information of the universe when it created, and would be a powerful tool for a probe of the early universe beyond the last scattering surface for the CMB. Such a GWB and the detection are the main topic of this thesis.

The most popular mechanism generating cosmological GWB is inflation. The inflation is the most successful theoretical paradigm in the early universe. In the scenario, the universe undergoes a rapid accelerating expansion, and provides the seeds of inhomogeneity for large-scale structure today [16, 17, 18, 19]. During the inflation, quantum fluctuations in spacetime curvature are also extended beyond the horizon, and may transit to classical fluctuations. In particle-physics point of view, this process is described as gravitational particle production. The relic gravitons would exist today as a stochastic GWB. The basic predictions in the inflationary scenario have confirmed by the analysis combining the data of the WMAP, the galaxy redshift surveys, the supernova observations [15, 20, 21, 22]. However, there are still many inflationary models that are compatible with current observational constraints. Hence, complementary observations are necessarily required in order to shrink the parameter space. The GWB is adequate for this purpose, since it is an only way to directly probe the inflation and the involved high-energy physics.

Other processes in the early universe, such as preheating and phase transitions, and cosmic strings also produces GWB, whose spectrum strongly depends on the production mechanism. Therefore, the detection or non-detection of the GWB bring us crucial imformation of the early universe and high-energy physics, and can be used for the tests of theoretical models.

Astrophysical gravitational-wave background

GWBs also generated by astrophysical objects such as neutron stars, black holes, white dwarfs, and massive stars, though this is not the topic of this thesis. If the event rate is small, the superposition of GWs does not become a stochastic GWB, but a popcorn-like GWB that individual sources can be resolved. However, if the event rate is large, such GWBs cannot be distinguished from the inflationary GWB. So, the astrophysical GWB would often be obstacle to detect the inflationary GWB. However, the astrophysical GWB brings us crucial information in the early universe with the redshift from a few to tens: the formation rate of the first stars, the event rate of supernovae, branching

ratio between black hole and neutron star formation, mass and angular-momentum distribution of black holes at the births, black-hole growth mechanisms. Hence, such information plays very important role in the study of large-scale structures and their evolutions.

Therefore, the GW is promising tool for cosmology and astronomy, since they brings new information that one cannot obtain by the observations with electromagnetic waves.

1.3 Gravitational-wave detectors

A gravitational-wave detector can be classified into two types: a laser-interferometric-type and a resonant-mass type. For the more detailed review of the up-to-date status of the ground-based detectors, see [23].

Resonant-mass-type detectors

Surprisingly, the history of GW detector is long. In the 1960s, the research of the resonant mass was started by Weber [24]. The principle is simple, that the vibration of an elastic (large metal cylinder) induced by GWs is electrically amplified and detected by transducers. In 1969, Weber reported the coincident detection of the GW with resonant bars apart by 1000 km [25]. However, no GW was detected in subsequent experiments by various people. Thus, in these days, it is not believed that the Weber's event was due to true GWs.

In the initial period of the history of GW search by the mid-1990s, the bar detectors had been a popular detector design, and a number of the bar detector in various countries were evolved. However, the large community today has shrunk to four operating detectors [26, 27, 28]: EXPLORER (CERN, Geneva, Switzerland), NAUTILUS (INFN Frascati Laboratory, near Rome, Italy), AURIGA (INFN Legnaro Laboratory, near Padua, Italy), ALLEGRO [1] (Louisiana State University, Louisiana, USA). These bar detectors is a $\sim 3\,\mathrm{m}$-long aluminum cylinder with the mass of $(2.2 - 2.3) \times 10^3\,\mathrm{kg}$, and are operating at cryogenic temperatures to reduce thermal noise. The defect of the bar detector is its narrow bandwidth in the sensitivity, which is $\sim \pm 20\,\mathrm{Hz}$ around the resonant frequency of $\sim 900\,\mathrm{Hz}$. Even at the resonant frequency, the sensitivity is not significantly high. Therefore, in these days, the resonant bars are superseded by interferometers in the sensitivity. The bar detectors will continue to operate, but they are gradually loosing scientific interests (Burst GWs of supernovae etc. in a kHz band still keep the interests of people.).

Ground-based interferometric detectors

The study of a laser-interferometric detector has been started in the 1970s, which was $\sim$ 10 years later from a resonant-bar detector. In the 1990s, interferometers with the arm length of tens of meter were constructed and had been developed toward a

[1] It was announced in April 2007 that the ALLEGRO would soon cease operation.

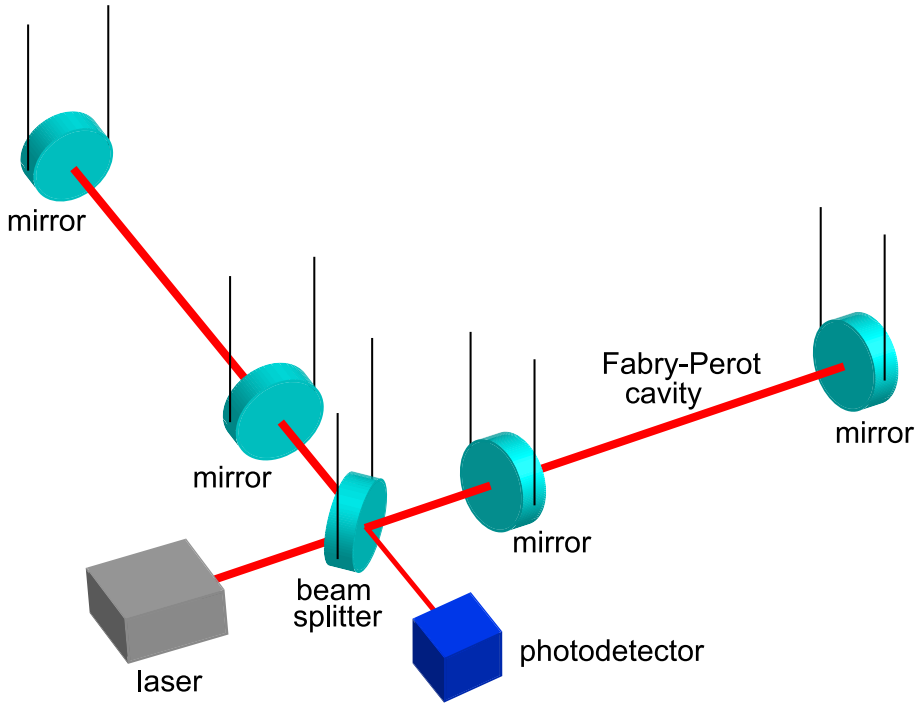

Figure 1.2: Schematic view of laser-interferometric GW detector (Fabry-Perot Michelson interferometer). All optics are suspended with thin wires.

kilometer-sided laser-interferometric detector, which mainly aims for the detection of GW sources from astrophysical compact objects with a few or several solar masses, as mentioned in the previous section. The sensitivity of the detector and the expected GW targets are shown in Fig. 1.2. The first large-scale interferometer in the world for GWs is TAMA300 [29], which located at Mitaka, Tokyo, Japan, and has two arms with the length of 300 m extended in perpendicular directions. Nowadays, other three large-scale interferometer, LIGO [30], VIRGO [31], GEO600 [32] are also constructed and operating. In Table 1.1, the characters of each detector are tabulated. The sensitive frequency range is from $10-10^4$ Hz. The goal sensitivity of the first-generation detectors is limited by seismic noise at lower frequencies, seismic noise at lower frequencies, thermal noise at middle frequencies, shot noise at high frequencies.

There are two reasons why the interferometric GW detector is more popular than resonant one today. For one reason, the advantage of the interferometers, compared with the resonant bars, is that the interferometers have broad-frequency-band sensitivity and can observe the waveform of GWs, though the resonant bars have narrow-frequency-band sensitivity. For another reason, the interferometric-type is easy to improve the sensitivity by extending the baseline, since the longer baseline produces the larger GW signal without amplifyng the displacement noise of mirrors. In fact, the best sensitivity of the interferometric detector (LIGO and VIRGO) is higher than that of resonant detectors at all frequencies in the observation band.

Among the first-generation detectors (upper four interferometers in the Table 1.1),

generation	interferometer	country	arm length	starting date
1st	LIGO	USA	4 km	operating
	VIRGO	Italy and France	3 km	operating
	GEO600	Germany and UK	600 m	operating
	TAMA300	Japan	300 m	operating
2nd	Adv. LIGO	USA, UK, and Germany	4 km	2014 -
	Adv. VIRGO	Italy and France	3 km	2014 -
	AIGO	Australia	5 km	2017 -
	LCGT	Japan	3 km	201x -
3rd	ET	Europe	10 km	202x -

Table 1.1: Current and planned large-scale interferometric detectors on the ground. The design parameters and the starting date of the second- and third-generation interferometers are not necessarily fixed and could be changed in the future.

LIGO and VIRGO have almost accomplished the goal sensitivity at the time in 2008. However, the event rate [2] is much smaller than unity per a year. Therefore, the second generation of the interferometric detectors, whose sensitivity is roughly ten times better than the first generation, is needed to firmly detect GWs and to pioneer the GW astronomy. Such detectors, which is currently planned and developed, are advanced LIGO [33], advanced VIRGO [34], AIGO [35], and LCGT [36]. The characters of each detector are listed at the lower half of Table 1.1, and the sensitivity is drawn in Fig. 1.1, together with that of the first-generation interferometer. The advanced LIGO and VIRGO are an upgraded version of current LIGO and VIRGO, respectively, while AIGO and LCGT will be constructed at new places. The GW event rate is expected to be a few or several in a year. In these detectors, the sensitivity is limited by quantum noise in almost all frequencies, and the applied technique of quantum optics will be essential. Thus, quantum optical techniques for the interferometric GW detectors have been vigorously investigated and developed experimentally.

The project for the third-generation interferometer, Einstein Telescope (ET) [37], has been formally started in Europe since 2008, after the budget for the design study was approved. The investigation of the detector configuration is under way, aiming for roughly 10 times better sensitivity than that of the second-generation interferometers.

Space-based interferometric detectors

In the frequency band of a ground-based detector, the rich GW sources are expected. More massive object, such as intermediate ($\sim 10^3 - 10^5\,M_\odot$) and supermassive ($\sim 10^5 - M_\odot$) black holes, and the early stage of the evolution of the solar-mass compact objects will be observed in a lower frequency band below 10 Hz. However, seismic disturbances prevent the ground-based detectors from searching such objects. Therefore, three space-based detectors are planned, aiming for low-frequency GW astronomy.

[2] The event rate depends on the GW sources and theoretical models that we consider. So, there is still uncertainty of a factor or even of an order of the magnitude in the event rate.

interferometer	country or institution	frequency band	arm length	starting date
LISA	ESA and NASA	$10^{-4} - 10^{-2}\,\mathrm{Hz}$	$5 \times 10^6\,\mathrm{km}$ (transponder-type)	2018 -
BBO	NASA	$10^{-2} - 10\,\mathrm{Hz}$	$5 \times 10^4\,\mathrm{km}$ (transponder-type)	202x -
DECIGO	Japan	$10^{-2} - 10\,\mathrm{Hz}$	$1 \times 10^3\,\mathrm{km}$ (FP-type)	2024 -

Table 1.2: Planned interferometric detectors in space. DECIGO will use Fabry-Perot cavity, not a transponder type of LISA and BBO. The finesse is 10 so that the effective arm length is $10^4\,\mathrm{km}$. The design parameters and the starting date are not fixed and could be changed in the future.

The space-based interferometer, Laser Interferometer Space Antenna (LISA) [38], was proposed by ESA in 1993 and is a joint program of ESA and NASA, which targets GWs at $10^{-4} - 10^{-2}\,\mathrm{Hz}$. LISA is located at the place 20° behind the Earth in the Heliocentric orbit, and consists of three spacecrafts apart by the distance of $5 \times 10^6\,\mathrm{km}$ each other, forming an equilateral triangle [3]. The relative distance between spacecrafts is measured by a laser interferometry with drag-free test masses in the spacerafts. The target GW source for LISA is the binary and merger of super massive black holes at cosmic distance up to the redshift $z \sim 20$, extreme mass ratio inspirals, GWBs from cosmic strings and electroweak phase transition. In the frequency range, there are many resolved and unresolved galactic binaries composed of white dwarfs. To subtract them, much effort is devoted. However, it would be an obstacle limiting the sensitivity.

The frequency range between LISA and the ground-based detectors, $10^{-2} - 10\,\mathrm{Hz}$, is also important range for science, because there are intermediate black holes and compact binaries before moving into the observational band of the ground detectors. In addition, no significant astrophysical foreground would exist there so that $10^{-2} - 10\,\mathrm{Hz}$ is a good window for the inflationary GWB. At the frequencies, two space detectors are proposed: DECi-hertz Interferometer Gravitational-wave Observatory (DECIGO) [39] and Big-Bang Observer (BBO) [40]. In Table 1.2, the parameters are tabulated.

GW detectors at ultra-high frequencies

Important other frequency range especially for cosmology is an ultra-high frequency band. The frequency range is defined and called in various ways in the literatures, depending on the authors. We call the frequency range $10\,\mathrm{kHz} - 10\,\mathrm{MHz}$ very high frequency (VHF), $10\,\mathrm{MHz} - 10\,\mathrm{GHz}$ ultra-high frequency (UHF), $10\,\mathrm{GHz}-$ super high frequency (SHF). The generic term, high frequency (HF), describes the frequency range above $\sim 10\,\mathrm{Hz}$ [4].

[3] Exactly speaking, one percent of the arm length changes during the annual orbiting.

[4] These definitions are not popular one and has not obtained the consensus, because it depends on the frequencies, in which one is interested. Say, low frequencies is below $\sim 1-100\,\mathrm{Hz}$ and high frequen-

There is no astronomical GW source at VHF, UHF and SHF, since the object mass has to be much less than $\sim 1M_{\odot}$ to produce GWs at the frequencies. The reason why GWs at UHF is important is because GWs at $\sim 100\,\mathrm{MHz}$ corresponds to the energy scale $\sim 10^{15}\,\mathrm{GeV}$ in the early universe, during which inflation may occur, and because, in some theoretical scenarios, the GW energy produced in the early universe is much larger than that in the standard scenario. Furthermore, compact object with cosmological motivation, such as primordial black holes produced by inhomogeneous fluctuation in the early stage of universe and black strings in the braneworld scenario, would emit UHF GWs. If the objects exist around the Earth, they can be detected through GWs. Therefore, from GW detection at UHF, one can directly see traces of a scenario in the early universe and obtain the implication in new physics.

Nevertheless, much effort has not been devoted into GW search at this frequencies. Consequently, the direct constraint due to GW detector is so loose, though the indirect constraint due to the big-bang nucleosynthesis has been obtained. This is because the GW amplitude is much smaller at high frequencies than that at low frequencies, and it makes the detection difficult. However, pioneering works are vital for future GW astronomy and cosmology. At present, as far as I know, GW detectors are developed with different methods by four groups: at INFN, Genova, Italy [41, 42], Birmingham University, UK [43, 44, 45], Chongqing University, China [46, 47], NAO, Tokyo, Japan [48, 49, 50].

1.4 Outline and notation of the thesis

This thesis is organized as follows:

Chapter 2

We briefly introduce the property of GWs and the principle of GW detection with laser interferometer. Then, as for stochastic GWB, various assumption and fundamental quantities are provided.

Chapter 3

We overview the creation of GWB in inflation and several other models in the early universe. Such backgrounds motivate us to search physics in the early universe.

Chapter 4

This chapter is devoted to the current upper limit on GWB with indirect observations. The limits are complementary to the direct search with interferometers.

---

cies is above $\sim 100\,\mathrm{Hz} - 10\,\mathrm{kHz}$ for people working on the ground-based large-scale interferometers. We call the terms for convenience.

Chapter 5

In the former part of this chapter, we review cross-correlation analysis for GWB and current tightest constraint from direct observation by LIGO. In the latter part, our original work that searches for non-tensorial polarization mode of GW is described. This work will be published as

A. Nishizawa, A. Taruya, S. Kawamura, and M. Sakagami, "Searching for non-tensorial polarizations of a gravitational-wave background with laser interferometers", in preparation.

Chapter 6

We turn our attention to GW search at ultra-high frequencies. The experiment with interferometers has not been studied well in the past. Thus, first, we investigate the optimal interferometer design and derive the cross-correlation sensitivity to GWB, as described in

A. Nishizawa *et al.*, "Laser-interferometric detectors for gravitational wave backgrounds at 100 MHz: Detector design and sensitivity", *Phys. Rev.* D **77**, 022002 (2008),

A. Nishizawa *et al.*, "Optimal location of two laser-interferometric detectors for gravitational wave backgrounds at 100 MHz", *Class. Quantum Grav.* **25**, 225011 (2008).

Then, we give experimental results obtained by our group, based on

T. Akutsu *et al.*, "Search for a Stochastic Background of 100-MHz Gravitational Waves with Laser Interferometers", *Phys. Rev. Lett.* **101**, 101101 (2008).

Chapter 7: Resonant speed meter

As the solution of displacement-amplified problem in a synchronous-recycling interferometer, we introduce a so-called *resonant speed meter*, which is a displacement noise-canceled configuration based on a ring-shaped synchronous recycling interferometer, proposed in

A. Nishizawa, S. Kawamura, and M. Sakagami, "Resonant Speed Meter for Gravitational-Wave Detection", *Phys. Rev. Lett.* **101**, 081101 (2008).

The remarkable feature of this interferometer is that, at certain frequencies, gravitational-wave signals are amplified, while displacement noises are not. We also show that the resonant speed meter works well for quantum noise. This work is pre-

pared for a paper as

A. Nishizawa, S. Kawamura, and M. Sakagami, "Quantum noise in a resonant speed meter", in preparation.

Chapter 8: Conclusions

This chapter is devoted to summarize this thesis and discuss the future work.

Notations

- Natural units
  In this thesis, we use $c = \hbar = k_B = 1$. However, they are written explicitly in some sections where is likely to be confused or at the place where it is easy to understand.

- Planck mass
  In this thesis, the reduced Planck mass

  $$M_{\rm Pl} = (8\pi G)^{-1/2} \approx 2.436 \times 10^{18}\,{\rm GeV}$$

  is used, instead of $m_{\rm Pl} = G^{-1/2} \approx 1.221 \times 10^{19}\,{\rm GeV}$.

- Tensors indices
  We follow the rules of super- and subscrpts for the relativistic theory in a D-dimensional spacetime:
  greek alphabets for spacetime, μ, ν, $\alpha = 0, 1, 2, \cdots, D$,
  roman alphabets for space, i, j, $k = 1, 2, \cdots, D$.

- Convention of metrics
  We follow the convention of the metric sign for a Minkowski spacetime:

  $$\eta_{\mu\nu} = {\rm diag}(-1, +1, +1, \cdots, +1)\ .$$

Chapter 2

Stochastic gravitational-wave background

2.1 Gravitational waves

2.1.1 Linearized Einstein equation

Einstein equation is given by

$$G_{\mu\nu} \equiv R_{\mu\nu} - \frac{1}{2} g_{\mu\nu} R = 8\pi G\, T_{\mu\nu} \ . \tag{2.1}$$

$G_{\mu\nu}$ is the Einstein tensor, and $T_{\mu\nu}$ is the stress-energy tensor. Christoffel symbol, Riemann curvature tensor, Ricci tensor, and scalar curvature are defined as

$$\begin{aligned}
\Gamma^{\mu}_{\ \nu\lambda} &\equiv \frac{1}{2} g^{\mu\alpha} (g_{\alpha\nu,\lambda} + g_{\alpha\lambda,\nu} - g_{\nu\lambda,\alpha}) \ , \\
R^{\mu}_{\ \ \nu\alpha\beta} &\equiv \Gamma^{\mu}_{\nu\beta,\alpha} - \Gamma^{\mu}_{\nu\alpha,\beta} + \Gamma^{\mu}_{\gamma\alpha}\Gamma^{\gamma}_{\nu\beta} - \Gamma^{\mu}_{\gamma\beta}\Gamma^{\gamma}_{\nu\alpha} \ , \\
R_{\mu\nu} &\equiv R^{\alpha}_{\ \ \mu\alpha\nu} \ , \qquad (2.2) \\
R &\equiv R^{\alpha}_{\ \ \alpha} \ . \qquad (2.3)
\end{aligned}$$

Let us consider gravitational waves propagating in a vacuum. The Einstein equation can be written as

$$G_{\mu\nu} = 0 \ . \tag{2.4}$$

Suppose that a metric tensor is slightly deviated from the background spacetime,

$$g_{\mu\nu} = g^{(0)}_{\mu\nu} + h_{\mu\nu}, \qquad |h_{\mu\nu}| \ll 1 \ .$$

We use the superscript (0) for the zeroth order quantity and (1) for the first order quantity with respect to $h_{\mu\nu}$. Taking the first order of $h_{\mu\nu}$, one can write Eqs. (2.1),

(2.2) and (2.3) as

$$G^{(1)}_{\mu\nu} = R^{(1)}_{\mu\nu} - \frac{1}{2}g^{(0)}_{\mu\nu}R^{(1)} - \frac{1}{2}h_{\mu\nu}R^{(0)} \ , \tag{2.5}$$

$$R^{(1)}_{\mu\nu} = \frac{1}{2}\Big[h_{\nu\ ;\alpha\mu}^{\ \alpha} + h_{\mu\ ;\alpha\nu}^{\ \alpha} - h_{\mu\nu}^{\ \ ;\alpha}{}_{;\alpha} - h_{;\mu\nu} + R^{(0)}_{\nu\beta}h^{\beta}_{\mu} + R^{(0)}_{\mu\beta}h^{\beta}_{\nu} + \left(R^{(0)}_{\mu\beta\alpha\nu} + R^{(0)}_{\nu\beta\alpha\mu}\right)h^{\beta\alpha}\Big] \ , \tag{2.6}$$

$$R^{(1)} = h^{\mu\ ;\alpha}_{\ \alpha\ ;\mu} - h^{;\alpha}_{\ ;\alpha} - h^{\mu\nu}R^{(0)}_{\mu\nu} \ , \tag{2.7}$$

where the symbol ; denotes a covariant derivative, and $h \equiv h^{\mu}_{\ \mu}$. Substituting Eqs. (2.6) and (2.7) into Eq. (2.5), and using (2.4) and the fact $R^{(0)}_{\mu\nu} = 0$ and $R^{(0)} = 0$ in the vacuum, one can obtain

$$h_{\nu\ ;\alpha\mu}^{\ \alpha} + h_{\mu\ ;\alpha\nu}^{\ \alpha} - h_{\mu\nu}^{\ \ ;\alpha}{}_{;\alpha} - h_{;\mu;\nu} - g^{(0)}_{\mu\nu}(h_{\beta\ ;\alpha}^{\ \alpha\ ;\beta} - h^{;\alpha}_{\ ;\alpha}) + \left(R^{(0)}_{\mu\beta\alpha\nu} + R^{(0)}_{\nu\beta\alpha\mu}\right)h^{\beta\alpha} = 0 \ . \tag{2.8}$$

Now we define the traceless part of $h_{\mu\nu}$,

$$\bar{h}_{\mu\nu} \equiv h_{\mu\nu} - \frac{1}{2}g^{(0)}_{\mu\nu}h \ . \tag{2.9}$$

Using the new definition, we can rewrite Eq. (2.8) as

$$\bar{h}_{\mu\nu}^{\ \ ;\alpha}{}_{;\alpha} - \bar{h}_{\nu\ ;\alpha\mu}^{\ \alpha} - \bar{h}_{\mu\ ;\alpha\nu}^{\ \alpha} + g^{(0)}_{\mu\nu}\bar{h}_{\beta\ ;\alpha}^{\ \alpha\ ;\beta} + 2R^{(0)}_{\mu\alpha\nu\beta}\bar{h}^{\alpha\beta} = 0 \ . \tag{2.10}$$

In addition, to fix the degrees of gauge freedom, we impose the following conditions (harmonic gauge conditions),

$$\bar{h}^{\nu}_{\ \mu;\nu} = 0 \ . \tag{2.11}$$

Then, Eq. (2.10) gives

$$\bar{h}_{\mu\nu}^{\ \ ;\alpha}{}_{;\alpha} + 2R^{(0)}_{\mu\alpha\nu\beta}\bar{h}^{\alpha\beta} = 0 \ . \tag{2.12}$$

The contribution of each term in the left-hand side of the equation can be estimated. For the GW wavelength λ and the background curvature scale L, the first term is $\mathcal{O}(\lambda^{-2})$ and the second term is $\mathcal{O}(L^{-2})$. Therefore, if $\lambda \ll L$, the second term can be ignored and Eq. 2.12 results in the sourceless wave equation of GWs,

$$\Box\bar{h}_{\mu\nu} \equiv \bar{h}_{\mu\nu}^{\ \ ;\alpha}{}_{;\alpha} = 0 \ . \tag{2.13}$$

2.1.2 Gravitational waves

To investigate the components of $\bar{h}_{\mu\nu}$, we consider a plane GW propagating on the background of a 4-dimensional spacetime with flar curvature,

$$\bar{h}_{\mu\nu} = A_{\mu\nu}e^{ik_{\alpha}x^{\alpha}} \ . \tag{2.14}$$

Substituting this into the harmonic gauge conditions, Eq. (2.11), and the wave equation, Eq. (2.13), we can obtain two conditions,

$$k^\nu A_{\mu\nu} = 0 \ , \qquad A_{\mu\nu} k_\rho k^\rho = 0 \ , \tag{2.15}$$

in order to be a solution of the wave equation. Here we used the fact that $\bar{h}_{\mu\nu}$ is traceless. The second condition is satisfied if $k_\rho k^\rho = 0$. So, the GW has to propagate along a null geodesic.

At Eq. (2.11), we have already imposed the gauge conditions, however, the gauge freedom is not completely fixed yet. To see it, let us consider an infinitesimal gauge transformation,

$$x'^\mu = x^\mu + \xi^\mu \ . \tag{2.16}$$

Then, the metric tensor is transformed as

$$\begin{aligned} g'_{\mu\nu}(x^\gamma + \xi^\gamma) &= g_{\alpha\beta} \frac{\partial x^\alpha}{\partial x'^\mu} \frac{\partial x^\beta}{\partial x'^\nu} \\ &= (\eta_{\alpha\beta} + h_{\alpha\beta}) \frac{\partial x^\alpha}{\partial x'^\mu} \frac{\partial x^\beta}{\partial x'^\nu} \ , \end{aligned}$$

and, to the first order in $h_{\mu\nu}$ and ξ_μ, it can be written as

$$g'_{\mu\nu}(x^\gamma) = g^{(0)}_{\mu\nu} + (h_{\mu\nu} - \xi_{\mu,\nu} - \xi_{\nu,\mu}) \ .$$

So, $h_{\mu\nu}$ is transformed as

$$h'_{\mu\nu} = h_{\mu\nu} - \xi_{\mu,\nu} - \xi_{\nu,\mu} \ . \tag{2.17}$$

Tracing Eq. (2.17) and using Eq. (2.9) give

$$\bar{h}'_{\mu}{}^{\rho}{}_{,\rho} = \bar{h}_{\mu}{}^{\rho}{}_{,\rho} - \xi_{\mu}{}^{,\rho}{}_{,\rho} \ . \tag{2.18}$$

Therefore, there remain the degrees of gauge freedom concerning ξ_μ. If the additional conditions,

$$\Box \xi_\mu = 0 \ ,$$

is satisfied, Eq. (2.18) is consistent with the harmonic gauge conditions, and the gauge is completely fixed.

In conclusions, $\bar{h}_{\mu\nu}$ or $A_{\mu\nu}$ is traceless by definition of Eq. (2.9), and transverse by the first condition of Eq. (2.15). This gauge is a so-called transverse-traceless (TT) gauge. For GW propagating in the z direction, the complex amplitude of the GW can be written as

$$A_{\mu\nu} = \begin{pmatrix} 0 & 0 & 0 & 0 \\ 0 & A_+ & A_\times & 0 \\ 0 & A_\times & -A_+ & 0 \\ 0 & 0 & 0 & 0 \end{pmatrix} \ , \tag{2.19}$$

where the degrees of freedom A_+ and $A_\times$, which does not vanish by the gauge transformation, are gravitational waves, and each polarization mode is called *plus* and *cross* modes, respectively.

2.1.3 Quadrupole nature of gravitational waves

To see the effect of GWs on test masses, let us consider the simple case that GW with + polarization is propagating on the background $\eta_{\mu\nu} = \mathrm{diag}(-1, 1, 1, 1)$ in z direction,

$$ds^2 = -dt^2 + \big[1 + h_+(t-z)\big]dx^2 + \big[1 - h_+(t-z)\big]dy^2 + dz^2 \ , \tag{2.20}$$

$$h_+(t-z) = h_+ \cos[\Omega(t-z)] \ , \qquad |h_+| \ll 1 \ ,$$

where Ω is the angular frequency of a GW.

Suppose that light pulse is emitted at the origin A and is received at the point B on the surface of a sphere with the radius R_0. Taking a polar coordinate, ($x = r\sin\theta\cos\phi,\ y = r\sin\theta\sin\phi,\ z = r\cos\theta$), and setting $ds^2 = 0$ for light, one can write the metric, Eq. (2.20), as

$$dr = dt\left[1 - \frac{1}{2}h_+ \cos[\Omega(t - r\ \cos\theta)]\sin^2\theta\ \cos 2\phi\right] . \tag{2.21}$$

The time delay due to GWs vanishes when $\theta = 0$ and is maximum when $\theta = \pi/2$. This is because GWs are transverse. Fixing $\theta = \pi/2$ and integrating Eq. (2.21) from $r = 0$ to $r = R_0$ give

$$\begin{aligned} R_0 &= \int_{t_0}^{t_0+\Delta t(\phi)} \left(1 - \frac{h_+}{2}\cos\Omega t\ \cos 2\phi\right) dt \\ &= \Delta t(\phi) - \frac{h_+}{2\Omega}\Big[\sin[\Omega\{t_0 + \Delta t(\phi)\}] - \sin\Omega t_0\Big]\ \cos 2\phi \ . \end{aligned} \tag{2.22}$$

In the case when the wavelength of GWs is much larger than test mass separation (the distance between the points A and B), $\Omega R_0 \ll 1$, Eq. (2.22) can be written as

$$R(\phi) \equiv c\,\Delta t(\phi) = R_0\left[1 + \frac{h_+}{2}\cos\Omega t_0 \cos 2\phi\right] .$$

Thus, the strain induced by GWs with + polarization is proportional to $\cos 2\phi$. As for $\times$ polarization, the strain is proportional to $\sin 2\phi$. In Fig. 2.1, the effects on test masses are shown for GWs propagating vertical to the plane of a paper. Both polarization modes are related by 45 degrees rotation. While, each polarization mode is symmetric with respect to 180 degrees rotation. This indicates that gravitons have spin 2.

2.2 Stochastic gravitational-wave backgrounds

In this section, assumptions and physical quantities to describe stochastic GWB are defined, and common features involving GWB are discussed.

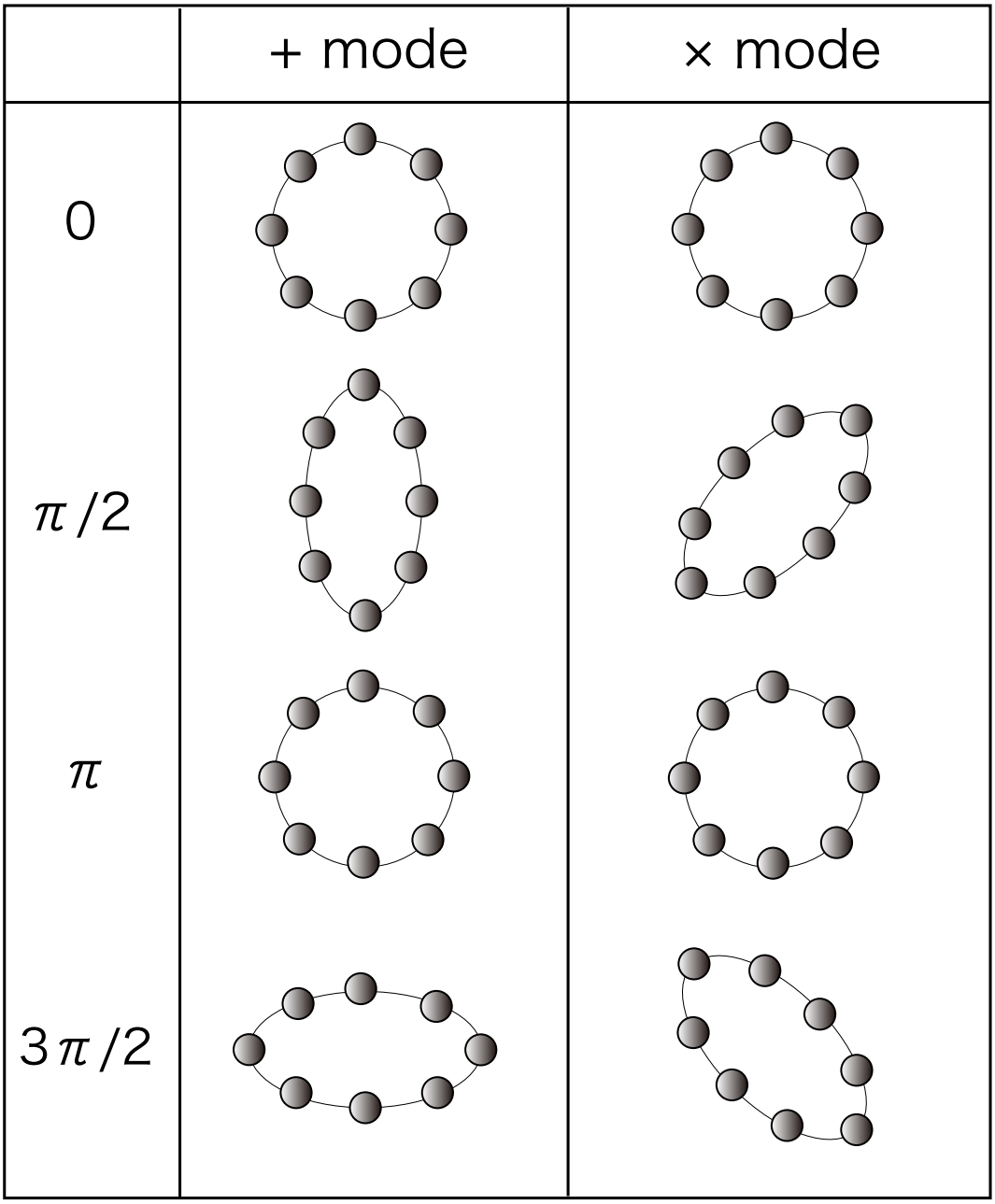

Figure 2.1: Influences of gravitational waves on test masses for each GW polarization mode: + mode (left) and × mode (right).

2.2.1 Assumptions

A GWB is the superposition of a number of gravitational waves with random phases, which exists as a background in the universe. At generic point $\vec{\mathbf{X}}$, the gravitational metric perturbations in the TT gauge are given by

$$\mathbf{h}(t,\vec{\mathbf{X}}) = \sum_A \int_{S^2} d\hat{\mathbf{\Omega}} \int_{-\infty}^{\infty} df\, \tilde{h}_A(f,\hat{\mathbf{\Omega}})\, e^{2\pi i f(t-\hat{\mathbf{\Omega}}\cdot\vec{\mathbf{X}})}\, \mathbf{e}_A(\hat{\mathbf{\Omega}})\,, \tag{2.23}$$

where $\hat{\mathbf{\Omega}}$ is a unit vector directed at GW propagation and $\tilde{h}_A(f,\hat{\mathbf{\Omega}})$ is the Fourier transform of GW amplitude with polarizations $A = +,\times$. Note that $\tilde{h}_A(-f,\hat{\Omega}) = \tilde{h}^*_A(f,\hat{\Omega})$. Polarizarion tensors $\mathbf{e}_A(\hat{\mathbf{\Omega}})$, are defined as

$$\begin{aligned} \mathbf{e}_+(\hat{\mathbf{\Omega}}) &\equiv \hat{\mathbf{m}}\otimes\hat{\mathbf{m}} - \hat{\mathbf{n}}\otimes\hat{\mathbf{n}}, \\ \mathbf{e}_\times(\hat{\mathbf{\Omega}}) &\equiv \hat{\mathbf{m}}\otimes\hat{\mathbf{n}} + \hat{\mathbf{n}}\otimes\hat{\mathbf{m}}\,, \end{aligned} \tag{2.24}$$

where the unit vectors $\hat{\mathbf{m}}$, $\hat{\mathbf{n}}$ are orthogonal to $\hat{\mathbf{\Omega}}$ and to each other. See Fig. 5.8. The polarizarion tensors satisfy $\mathbf{e}_A(\hat{\Omega})\mathbf{e}_{A'}(\hat{\Omega}) = 2\delta_{AA'},\ A, A' = +,\times$.

The followings are usually assumed about stochastic GWB, (i) isotropic, (ii) unpolarized, (iii) stationary, and (iv) Gaussian [51]. (i) It is observationally known that CMB is highly isotropic [52, 53]. However, this might not be true because a large number of unresolved GW sources, for example, white dwarf binaries and neutron star binaries, would exist as foreground in the direction of the galactic plane, or one can consider non-standard cosmological scenarios in which GWB is not necessarily isotropic as well as CMB. So, anisotropic GWB search in data analysis is important, but here we assume GWB is isotropic for the simplest case. (ii) The assumption "unpolarized" GWB is natural since there is no strong evidence to believe that GWB has preferred polarization, plus or cross (right- or left-handed), though it is possible that inflationary background can be polarized with the gravitational Chern-Simons term that might be derived from string theory [54, 55]. (iii) The statistical property of GWB does not change during the observation. This seems to be valid since the age of the universe is far much longer than the observation time. (iv) The assumption that the amplitude of GWB has Gaussian distribution is justified by the central limit theorem, because GWB was created by a large number of independent gravitational wave sources. These assumptions (i) - (iv) are expressed by

$$\langle \tilde{h}^*_A(f,\hat{\Omega})\tilde{h}_{A'}(f',\hat{\Omega}')\rangle = \delta(f-f')\frac{1}{4\pi}\delta^2(\hat{\Omega},\hat{\Omega}')\delta_{AA'}\frac{1}{2}S_h(f)\,, \tag{2.25}$$

where $\delta^2(\hat{\Omega},\hat{\Omega}') \equiv \delta(\phi-\phi')\delta(\cos\theta - \cos\theta')$ and $\langle\cdots\rangle$ denotes ensemble average. $S_h(f)$ is the one-sided power spectral density defined by Eq. (2.25), and satisfies $S_h(-f) = S_h(f)$.

2.2.2 Energy density

The amount of GWB is defined by the energy density per logarithmic frequency bin normalized by the critical energy density of the universe, that is,

$$\Omega_{\rm gw}(f) \equiv \frac{1}{\rho_c}\frac{d\rho_{\rm gw}}{d\ln f}\,, \tag{2.26}$$

where $\rho_c = 3M_{\rm Pl}^2 H_0^2$ and H_0 is the Hubble constant. It is useful to represent the energy density with the form $h_0^2\,\Omega_{\rm gw}(f)$ and $H_0 = 100\,h_0\,{\rm km\,s^{-1}\,Mpc^{-1}}$ because H_0 still has observational uncertainty. $\Omega_{\rm gw}(f)$ is related to $S_h(f)$ as follows. The energy density of GW is given by [56, 57, 6]

$$T_{00}^{\rm gw} = \rho_{\rm gw} = \frac{M_{\rm Pl}^2}{4}\langle \dot{h}_{ab}\dot{h}^{ab}\rangle_\lambda \ ,$$

where $\langle\cdots\rangle_\lambda$ denotes the average over several GW wavelengths, in which the subscript λ is fixed so as not to be confused with the ensemble average. Substituting Eq. (2.23) and using Eq. (2.25), we obtain

$$\begin{aligned} \rho_{\rm gw} &= M_{\rm Pl}^2 \int_{f=0}^{f=\infty} d(\ln f) f (2\pi f)^2 S_h(f) \ , \\ \frac{d\rho_{\rm gw}}{d\ln f} &= 4\pi^2 M_{\rm Pl}^2 f^3 S_h(f) \ . \end{aligned}$$

Therefore, from Eq. (2.26), $\Omega_{\rm gw}$ is related to the power spectral density $S_h(f)$ as

$$\Omega_{\rm gw}(f) = \left(\frac{4\pi^2}{3H_0^2}\right) f^3 S_h(f) \ . \tag{2.27}$$

2.2.3 Characteristic amplitude

A dimensionless characteristic GW amplitude can be defined, using Eqs. (2.23) and (2.25), by

$$\begin{aligned} \langle h_{ab}(t)h^{ab}(t)\rangle &= 2\int_{-\infty}^{\infty} df S_h(f) \qquad (2.28) \\ &= 4\int_{f=0}^{f=\infty} d(\ln f) f S_h(f) = 2\int_{f=0}^{f=\infty} d(\ln f) h_c^2(f) \ , \end{aligned}$$

that is,

$$h_c^2(f) = 2 f S_h(f) \ . \tag{2.29}$$

Combining with Eq. (2.27), one can obtain the relation

$$\Omega_{\rm gw}(f) = \left(\frac{2\pi^2}{3H_0^2}\right) f^2 h_c^2(f) \ . \tag{2.30}$$

Dimensionless quantity, the tensor power spectrum

$$P_T(k) \equiv 2h_c^2(k) \ , \tag{2.31}$$

is often used in cosmology, where the factor 2 results from two polarization modes. In terms of $P_T(k)$, the energy density of GWB is given by

$$\Omega_{\rm gw}(k) = \frac{k^2}{12H_0^2} P_T(k) \ . \tag{2.32}$$

2.2.4 Number density of gravitons

The energy density $\Omega_{\rm gw}(f)$ can also be expressed in terms of gravitons. Suppose the number of gravitons per polarization mode per unit volume in phase space, $n(\vec{x},\vec{k})$. For a isotropic stochastic GWB, the number density only depends on frequency f and can be written as $n(\vec{x},\vec{k}) = n_f$. So,

$$\begin{aligned}\rho_{\rm gw} &= 2\int \frac{d^3k}{(2\pi)^3}\, k\, n_f = 16\pi^2 \int_0^\infty d(\ln f) f^4 n_f \\ \frac{d\rho_{\rm gw}}{d(\ln f)} &= 16\pi^2 n_f f^4\end{aligned}$$

By definition of Eq. (2.26), one can obtain

$$h_0^2 \Omega_{\rm gw}(f) \approx 2.3\times 10^{-6}\left(\frac{n_f}{10^{42}}\right)\left(\frac{f}{1\,{\rm Hz}}\right)^4 . \tag{2.33}$$

2.2.5 Decoupling of gravitons

CMB photons are decoupled from other components of universe at the redshift $z\sim 1100$ and carry information of the universe at the epoch to us. Similarly, gravitons are decoupled far early in the history of the universe, because the gravitational interaction is much weaker than the electromagnetic interaction. Let us estimate the time of the decoupling of gravitons. In general, the rate of interaction is given by $\Gamma = n\sigma|v|$, where n is the number density of particles, σ is cross section, and $|v|$ is mean velocity of the particles. For gravitons, $|v|$=1 and $\sigma \sim M_{\rm Pl}^{-4}T^2$ by dimensional analysis, then, $\Gamma \sim M_{\rm Pl}^{-4}T^5$. On the other hand, the rate of expansion of the universe is given by the Friedmann equation, and is $H^2 \sim M_{\rm Pl}^{-2}T^4$ for relativistic particles. Therefore, the decoupling time of gravitons is at $\Gamma \sim H$, that is, $T\sim M_{\rm Pl}\sim 10^{19}\,{\rm GeV}$. This means that gravitons are in thermal equilibrium only at the epoch of Planck scale and decoupled below Planck scale. This is the reason why GWB is a powerful tool to directly prove the very early universe and a particle theory beyond the standard model.

Is there thermal relic GWB on the analogy of CMB? One can infer the temperature of GWB using entropy conservation. Entropy per unit volume is given by

$$s = \frac{4}{3}\sigma_{\rm SB}T^3 , \tag{2.34}$$

where $\sigma_{\rm SB}$ is Stefan-Boltzmann constant. Since the entropy is conserved in comoving volume, it follows

$$\begin{aligned} g_s(T)T^3a^3 &= \text{constant} , \\ g_s(T) &\equiv \sum_{i={\rm boson}} g_i\left(\frac{T_i}{T}\right)^3 + \frac{7}{8}\sum_{i={\rm fermion}} g_i\left(\frac{T_i}{T}\right)^3 , \end{aligned}$$

where a is a scale factor, and $g_s(T)$ is the number of entropy degrees of freedom, which is $g_s(T_0)=3.91$ at present and $g_s(T_*)=106.75$ at energy scales above 300 GeV if we

assume that the particle standard model holds. Thus, the temperature of thermal relic GWB at present is

$$T_g = \left(\frac{3.91}{106.75}\right)^{1/3} T_\gamma \approx 0.9\,\mathrm{K}\ . \tag{2.35}$$

Here the temperature of CMB photon at present $T_\gamma = 2.725\,\mathrm{K}$ is used. However, such a thermal spectrum is unlikely to survive because (i) it is diluted if inflation occurs at relatively low energy scales, (ii) it is unclear whether one can apply low energy physics to Planck era or not, (iii) non-thermal gravitons are produced by various mechanisms though the history of the universe and might hide the thermal spectrum.

2.2.6 Characteristic frequency

GWB observed today is produced at certain epoch of the universe and is red-shifted by cosmic expansion. Thus, the frequency of the GWB and the energy scale of the universe can be related.

Suppose that GWB with the frequency f_* is generated when the temperature of the universe is T_* by some mechanisms. Using entropy conservation, Eq. (2.34), one can calculate the frequency today,

$$f = f_*\left(\frac{a_*}{a_0}\right) \approx 8.00\times 10^{-14}\left(\frac{f_*}{1\,\mathrm{Hz}}\right)\left(\frac{106.75}{g_{s*}}\right)^{1/3}\left(\frac{1\,\mathrm{GeV}}{T_*}\right)\ \ \mathrm{Hz}\ . \tag{2.36}$$

a_* and a_0 are the scale factors at $T = T_*$ and at present. The frequency f_* depends on the generation mechanism of GWB, however, at least, it should be generated within the horizon of the universe. So, we will write the characteristic scale as $\lambda_* = \epsilon H_*^{-1}$, $(0 < \epsilon < 1)$. The Hubble parameter is given by the Friedmann equation for relativistic particles,

$$\begin{aligned} H_*^2 &= \frac{\pi^2 g_* T_*^4}{90 M_{\mathrm{Pl}}^2}\ , \\ g_* &\equiv \sum_{i=\mathrm{boson}} g_i\left(\frac{T_i}{T}\right)^4 + \frac{7}{8}\sum_{i=\mathrm{fermion}} g_i\left(\frac{T_i}{T}\right)^4\ . \end{aligned}$$

Substituting f_* into Eq. (2.36), one can obtain

$$f = 1.71\times 10^{-7}\epsilon^{-1}\left(\frac{T_*}{1\mathrm{GeV}}\right)\left(\frac{g_*}{106.75}\right)^{1/6}\ \ \mathrm{Hz}\ , \tag{2.37}$$

or,

$$T_* = 5.85\times 10^{6}\,\epsilon\left(\frac{f}{1\mathrm{Hz}}\right)\left(\frac{g_*}{106.75}\right)^{-1/6}\ \ \mathrm{GeV}\ .$$

Therefore, if the GWB is generated at the horizon scale ($\epsilon = 1$), one can prove physics in the early universe at $T_* > 1\,\mathrm{TeV}$ by investigating GWB with the frequencies $f > 0.1\,\mathrm{mHz}$. This is the reason why GWB at high frequencies is so important for cosmology.

Chapter 3

Creation of cosmological GWB

.

3.1 Inflation

Hot big-bang cosmology has several problems [58]: the horizon problem (Why is our universe so homogeneous and isotropic over causally disconnected regions in the early age of the universe?), the flatness problem (Why is our universe considerably flat?), and the seed for cosmological structures (Small inhomogeneity must be needed to create galaxies, stars, and clusters.). To overcome these problems, the theory of inflation, the idea that the universe underwent a brief period of rapid accelerating expansion, was originally proposed by [16, 17, 18, 19].

Einstein equation with a perfect fluid gives the Friedmann equation,

$$H^2 = \left(\frac{\dot{a}}{a}\right)^2 = \frac{1}{3M_{\rm Pl}^2}\rho \ , \tag{3.1}$$

and the acceleration equaiton,

$$\frac{\ddot{a}}{a} = -\frac{1}{6M_{\rm Pl}^2}(\rho + 3p) \ , \tag{3.2}$$

where "dot" denotes derivatives with respect to time t and $M_{\rm Pl} \equiv (8\pi G)^{-1/2}$. From Eq. (3.2), the expansion of the universe is accelerated if the condition $\rho + 3p < 0$ holds. One of Such fluids is a scalar field. The stress-energy tensor of a scalar field ϕ is given by

$$\begin{aligned} T_{\mu\nu} &= \phi_{,\mu}\phi_{,\nu} - \eta_{\mu\nu}\mathcal{L} \ , \\ \mathcal{L} &= -\frac{1}{2}\phi_{,\alpha}\phi^{,\alpha} - V(\phi) \ . \end{aligned} \tag{3.3}$$

$\mathcal{L}$ is Lagrangian density of the scalar field, and V is the potential. Here flat spacetime, $\eta_{\mu\nu} = {\rm diag}(-1, +1, +1, +1)$, is assumed. In the homogeneous and isotropic universe,

from Eq. (3.3), energy density ρ and pressure p can be simply written as

$$\begin{aligned} \rho &= \frac{1}{2}\dot{\phi}^2 + V(\phi) \,, \\ p &= \frac{1}{2}\dot{\phi}^2 - V(\phi) \,. \end{aligned}$$

The evolution of the field ϕ can be derived using $T_\nu{}^\mu{}_{;\mu} = 0$ and the equation of motion is given by

$$\ddot{\phi} + 3H\dot{\phi} + V' = 0 \,, \tag{3.4}$$

where the prime denotes the derivative with respect to ϕ.

If the scalar field potential changes slowly, namely,

$$\epsilon_V(\phi) \equiv \frac{M_{\rm Pl}^2}{2}\left(\frac{V'}{V}\right)^2 \ll 1 \,, \qquad \left|\eta_V(\phi)\right| \equiv M_{\rm Pl}^2\left|\frac{V''}{V}\right| \ll 1 \,, \tag{3.5}$$

or, consistently,

$$\left|\frac{\dot{\phi}^2}{V}\right| \ll 1 \,, \qquad \left|\frac{\ddot{\phi}}{H\dot{\phi}}\right| \ll 1 \,,$$

the equation of state $p \approx -\rho$ is satisfied and hence the universe is accelerated. The latter condition states that the scalar field slowly rolls down the hill of a potential. Therefore, the above condition and parameters ϵ_V and η_V are called slow-roll condition and slow-roll parameters [1], respectively [59]. In the slow-roll approximation, Eq. (3.4) can be approximated to $3H\dot{\phi} \approx -V'$. The Eq. (3.1) can also be approximated to

$$\frac{\dot{a}}{a} \approx \sqrt{\frac{1}{3M_{\rm Pl}^2}V} \approx \text{constant} \,. \tag{3.6}$$

Then, the solution is

$$a(t) \propto \exp\left[\sqrt{\frac{V}{3M_{\rm Pl}^2}}\ t\right] \,, \tag{3.7}$$

and the acceleration expansion can be obtained. Such a scalar field is called inflaton.

3.2 GWB creation in de-Sitter inflation

Gravitational waves are an inevitable consequence of all inflationary models, being created in the same manner as the density perturbation [60, 61, 62, 63]. In the context of quantum field theory in a curved spacetime, which is more strict description,

[1] Slow-roll parameters in Hamilton-Jacobi formulation are defined as

$$\epsilon \equiv 2M_{\rm Pl}\left(\frac{H'(\phi)}{H(\phi)}\right)^2 \,, \qquad \eta \equiv 2M_{\rm Pl}\frac{H''(\phi)}{H(\phi)} \,.$$

To distinguish from them, the subscripts V are fixed to the slow-roll parameters defined by the inflaton potential.

gravitational-wave production can be interpreted as the amplification of vacuum fluctuations by cosmic expansion (gravitational particle creation) [64, 65, 66].

We assume a spatially flat universe, and that the background is homogeneous and isotropic, as well as the previous section. If there are gravitational waves, the spacetime metric can be described by the Friedmann-Robertson-Walker (FRW) metric with tensor perturbations,

$$ds^2 = a(\tau)^2[-d\tau^2 + (\delta_{ij} + h_{ij})dx^i dx^j] \ .$$

Here the conformal time τ is defined by $d\tau = dt/a(t)$. The tensor perturbation can be written in a form with a time-dependent function $\phi^A_{\mathbf{k}}(\tau)$ and a spatial plane-wave part,

$$\mathbf{h}(\tau, \mathbf{x}) = M_{\rm Pl}^{-1} \sum_{A=+,\times} \sum_{\mathbf{k}} \phi^A_{\mathbf{k}}(\tau) e^{i\mathbf{k}\cdot\mathbf{x}} \mathbf{e}^A(\hat{\Omega}) \ ,$$

where it is summed with respect to a GW polarization A and a comoving wave-number vector $\mathbf{k}$, and a unit vector $\hat{\mathbf{\Omega}} \equiv \mathbf{k}/|\mathbf{k}|$ is defined. From the linearized Einstein equation (2.13), the time evolution of the tensor perturbation can be given by

$$\frac{d^2\phi_{\mathbf{k}}}{d\tau^2} + 2\mathcal{H}\frac{d\phi_{\mathbf{k}}}{d\tau} + k^2\phi_{\mathbf{k}} = 0 \ , \tag{3.8}$$

where

$$\mathcal{H} \equiv \frac{1}{a}\frac{da}{d\tau} \ .$$

This equation is the same equation as for a massless scalar field, and can be solved if $a(\tau)$ is given explicitly as a function of τ. Here we consider de-Sitter phase in the early universe, followed by the radiation-dominated (RD) and matter-dominated (MD) phases. We do not consider the dark energy-dominated phase, since it would dominate the universe only after the redshift $z \lesssim 1$ and hardly affects a broad spectrum of GWB [2].

First we start with a qualitative look at the shape of a GWB spectrum. From Eq. (3.8) by writing $\phi_{\mathbf{k}}(\tau)$ as $h(\tau)$,

$$\frac{d^2h}{d\tau^2} + 2\mathcal{H}\frac{dh}{d\tau} + k^2h = 0 \ , \tag{3.9}$$

is obtained. When $k \ll \mathcal{H}$, the solution is

$$h = \text{constant} \ . \qquad \text{for } \ k \ll \mathcal{H}$$

On the other hand, when $k \gg \mathcal{H}$, substituting $h(\tau) = A(\tau)\exp[iB(\tau)]$ into Eq. (3.9) and keeping the leading terms, we can obtain a WKB solution,

$$h \propto \frac{1}{a} \exp[\pm ik\tau] \qquad \text{for } \ k \gg \mathcal{H} \ .$$

[2]However, the dark-energy domination indeed affects the frequencies $f_{\rm eq}$ etc. through the cosmological parameters determined in the universe with the dark-energy dominated phase. Thus, in this section, we take the dark-energy domination into account indirectly through the cosmological parameters.

Therefore, GW amplitude is frozen out after the horizon exit during inflation, and is damped after the re-entry inside of the horizon during the RD or MD phases. GW amplitude after the horizon re-entry can be written using the amplitude $h_{\rm ini}$ and the scale factor $a(t_*)$ at the time of the horizon exit,

$$|h_{\rm obs}| \approx |h_{\rm ini}| \, \frac{a(t_*)}{a(t_0)} \, , \tag{3.10}$$

where t_* and t_0 are the time at the horizon exit and at present, respectively.

The frequency of GWs seen today is

$$2\pi f = \frac{k}{a(t_0)} = \frac{a(t_*)}{a(t_0)} H(t_*) \, . \tag{3.11}$$

For the modes re-entering inside the horizon during the RD phase, using Eqs. (3.10) and (3.11), and $H^2(t_*) \propto a^{-4}(t_*)$, we obtain $|h_{\rm obs}| \propto f^{-1}$, and for the modes re-entering inside the horizon during the MD phase, using $H^2(t_*) \propto a^{-3}(t_*)$, we obtain $|h_{\rm obs}| \propto f^{-2}$. Substituting the these relations into Eq. (2.30) gives the frequency dependence of $\Omega_{\rm gw}(f)$,

$$\Omega_{\rm gw}(f) = \frac{2\pi^2}{3H_0^2} f^2 |h_{\rm obs}|^2 \propto \left\{ \begin{array}{ll} \text{constant} & (f_{\rm eq} < f) \\ f^{-2} & (f < f_{\rm eq}) \end{array} \right. ,$$

where $f_{\rm eq}$ is the frequency corresponding to the matter-radiation equality.

Next, we treat GWB creation in a quantitative way, using a quantum field theory. In a particle point of view (graviton), gravitational waves can be written as

$$\mathbf{h}(\tau, \mathbf{x}) = M_{\rm Pl}^{-1} \sum_{A=+,\times} \int \frac{d^3k}{(2\pi)^3 \sqrt{2k}} \left[a_A(\mathbf{k}) \phi_{\mathbf{k}}(\tau) e^{i\mathbf{k}\cdot\mathbf{x}} + a_A^\dagger(\mathbf{k}) \phi_{\mathbf{k}}^*(\tau) e^{-i\mathbf{k}\cdot\mathbf{x}} \right] \mathbf{e}^A(\hat{\Omega}) \, ,$$

where $a_A(\mathbf{k})$ and $a_A^\dagger(\mathbf{k})$ are the creation and annihilation operators. Vacuum states in each phase of the universe are defined using the annihilation operators by

$$\begin{aligned} a_A^{\rm I} |0\rangle_{\rm I} &= 0 \, , \\ a_A^{\rm R} |0\rangle_{\rm R} &= 0 \, , \\ a_A^{\rm M} |0\rangle_{\rm M} &= 0 \, . \end{aligned}$$

The subscripts $\rm I, R, M$ represent the inflation, RD, MD, respectively. Transforming $\phi_{\mathbf{k}}$ to $\psi_{\mathbf{k}} = a\phi_{\mathbf{k}}$ in Eq. (3.8), the following equation can be obtained [3] ,

$$\frac{d^2\psi_{\mathbf{k}}}{d\tau^2} + \left[k^2 - \frac{1}{a} \frac{d^2 a}{d\tau^2} \right] \psi_{\mathbf{k}} = 0 \, . \tag{3.12}$$

Hereafter we assume that the universe is isotropic and replace the wave number vector $\mathbf{k}$ with k. Cosmic expansions in the de-Sitter phase, followed by the RD and MD

[3] The variable a is used for both the scale factors and the annihilation operator. Be careful so as not to be confused.

phases as a function of τ, are given by

$$a_{\rm I}(\tau) = -\frac{1}{H\tau}\,, \qquad (\text{Inflation} : -\infty < \tau < \tau_1)\,, \tag{3.13}$$

$$a_{\rm R}(\tau) = \frac{1}{H\tau_1^2}(\tau - 2\tau_1)\,, \qquad (\text{RD} : \tau_1 < \tau < \tau_{\rm eq})\,, \tag{3.14}$$

$$a_{\rm M}(\tau) = \frac{(\tau + \tau_{\rm eq} - 4\tau_1)^2}{4H\tau_1^2(\tau_{\rm eq} - 2\tau_1)}\,, \qquad (\text{MD} : \tau_{\rm eq} < \tau < \tau_0)\,. \tag{3.15}$$

In the above expressions, the scale factor $a(\tau)$ and its first derivative are smoothly continued at a phase transition of cosmic expansion. H is the Hubble parameter at the de-Sitter inflationary epoch, and has a constant value. Note that the sign of the conformal time is $\tau_1 < 0$ and $\tau_{\rm eq} > 0$ so that $a(\tau)$ is positive and a monotonously growing function. The equation (3.12) can be analytically solved by substituting Eqs. (3.13) - (3.15) and gives solutions for positive frequency modes,

$$\psi_k^{\rm I}(k\tau) = -\left(\frac{\pi}{2}\right)^{1/2}(k\tau)^{1/2}H_{3/2}^{(2)}(k\tau)\,, \qquad (-\infty < \tau < \tau_1)\,, \tag{3.16}$$

$$\psi_k^{\rm R}(k\tau) = e^{-ik\tau}\,, \qquad (\tau_1 < \tau < \tau_{\rm eq})\,, \tag{3.17}$$

$$\psi_k^{\rm M}(k\tau) = -\left(\frac{\pi}{2}\right)^{1/2}\{k(\tau+s)\}^{1/2}H_{3/2}^{(2)}[k(\tau+s)]\,, \qquad (\tau_{\rm eq} < \tau < \tau_0) \tag{3.18}$$

where $s \equiv \tau_{\rm eq} - 4\tau_1$, and $H_{3/2}^{(2)}$ is the Hankel function of the second kind. Overall coefficients are chosen to give $\psi_k \to e^{-ik\tau}$ at the subhorizon limit, $k\tau \to \infty$. The above expressions Eqs. (3.16) - (3.18) can be reduced, by using an explicit form of the Hankel function $H_{3/2}^{(2)}$, to simpler forms,

$$\psi_k^{\rm I}(k\tau) = \left[1 - \frac{i}{k\tau}\right]e^{-ik\tau}\,, \tag{3.19}$$

$$\psi_k^{\rm R}(k\tau) = e^{-ik\tau}\,, \tag{3.20}$$

$$\psi_k^{\rm M}(k\tau) = \left[1 - \frac{i}{k(\tau+s)}\right]e^{-ik(\tau+s)}\,. \tag{3.21}$$

These functions are the exact solutions for Eq. (3.12). However, no continuity between each expanding epoch is imposed. The continuity condition is given by Bogolubov transformation (Detailed explanation is given in Appendix A.) [67],

$$\psi_k^{\rm I} = \alpha_k^{\rm IR}\psi_k^R + \beta_k^{\rm IR}(\psi_k^{\rm R})^*\,, \tag{3.22}$$

$$\psi_k^{\rm R} = \alpha_k^{\rm RM}\psi_k^M + \beta_k^{\rm RM}(\psi_k^{\rm M})^*\,. \tag{3.23}$$

Substituting Eqs. (3.19) - (3.21) into Eqs. (3.22) and (3.23), we obtain the Bogolubov

coefficients,

$$\alpha_k^{\rm IR} = 1 - \frac{i}{k\tau_1} - \frac{1}{2k^2\tau_1^2} \ , \tag{3.24}$$

$$\beta_k^{\rm IR} = \frac{1}{2k^2\tau_1^2} e^{-2ik\tau_1} \ , \tag{3.25}$$

$$\alpha_k^{\rm RM} = \left[1 + \frac{i}{2k(\tau_{\rm eq} - 2\tau_1)} - \frac{1}{8k^2(\tau_{\rm eq} - 2\tau_1)^2}\right] e^{iks} \ , \tag{3.26}$$

$$\beta_k^{\rm RM} = -\frac{1}{8k^2(\tau_{\rm eq} - 2\tau_1)^2} e^{-ik(2\tau_{\rm eq}+s)} \ . \tag{3.27}$$

What is needed to obtain a present GWB spectrum is the Bogolubov coefficients from the inflationary phase to the MD phase. It is determined by the relation,

$$\psi_k^{\rm I} = \alpha_k^{\rm total}\psi_k^{\rm M} + \beta_k^{\rm total}(\psi_k^{\rm M})^* \ . \tag{3.28}$$

Therefore, substituting Eqs. (3.22) and (3.23) into Eq. (3.28), we find the total Bogolubov coefficients,

$$\begin{pmatrix} \alpha_k^{\rm total} & \beta_k^{\rm total} \\ \beta_k^{\rm total\,*} & \alpha_k^{\rm total\,*} \end{pmatrix} = \begin{pmatrix} \alpha_k^{\rm IR} & \beta_k^{\rm IR} \\ \beta_k^{\rm IR\,*} & \alpha_k^{\rm IR\,*} \end{pmatrix} \begin{pmatrix} \alpha_k^{\rm RM} & \beta_k^{\rm RM} \\ \beta_k^{\rm RM\,*} & \alpha_k^{\rm RM\,*} \end{pmatrix} \ , \tag{3.29}$$

together with Eqs. (3.24) - (3.27).

We assume the universe is in a vacuum state during the inflation phase. From Eqs. (3.29), (A.4), and (A.6), the number of created gravitons is given by

$$\begin{aligned} n_k &= |\beta_k^{\rm total}|^2 \\ &= |\beta_k^{\rm IR}|^2 + 2|\beta_k^{\rm RM}|^2\left(|\beta_k^{\rm IR}|^2 + \frac{1}{2}\right) + 2\,{\rm Re}\left[\alpha_k^{\rm IR}\beta_k^{\rm IR\,*}\alpha_k^{\rm RM}\beta_k^{\rm RM}\right] . \end{aligned} \tag{3.30}$$

This equation clearly show that some gravitons are created from vacuum fluctuations at the inflation-RD transition, and that the created gravitons are subsequently amplified at the RD-MD transition.

To evaluate Eq. (3.30), let us consider four cases shown in Fig. 3.1, with respect to the epochs when the fluctuations come into the cosmic horizon. As mentioned in Appendix A, particle creation does not occur at the mode within the horizon. Hence, we do not consider the case 1. We do not consider case 4 either, as it is not observable today. Consequently, what is important is case 2 (horizon re-entry during RD) and case 3 (horizon re-entry during MD) [4]

[4]The number density of gravitons can be derived without the classification of horizon re-entry. In that case, a continuous solution is

$$n_k \approx \frac{1}{4}\left(\frac{f_1}{f}\right)^4\left[1 + \frac{1}{4}\left(\frac{f_{\rm eq}}{f}\right)^2\right] .$$

is obtained.

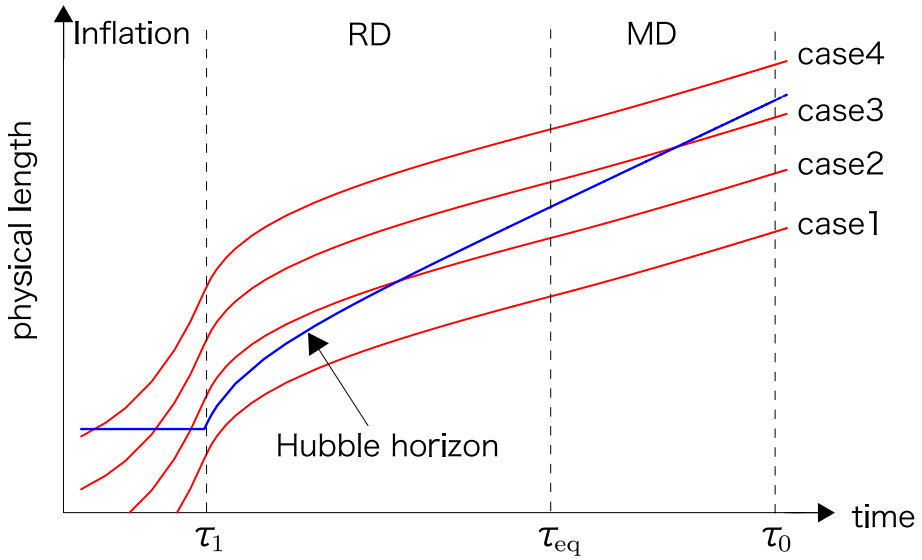

Figure 3.1: Schematic view of horizon exit and re-entry.

- Case 2: horizon re-entry during RD.
  The wavelength of a mode is larger than the Hubble horizon at the inflation-RD. The condition $k \ll \mathcal{H}(\tau_1)$ is $y_1 \equiv k|\tau_1| \ll 1$. Then, the wavelength of a mode is smaller than the Hubble horizon at the RD-MD transition. The condition $k \gg \mathcal{H}(\tau_{\rm eq})$ is $y_1 \equiv k\tau_{\rm eq} \gg 1$. The equation (3.30) being substituted Eqs. (3.24) - (3.27) and taken a leading-order term, gives

$$n_k \approx \frac{1}{4y_1^4} \, .$$

  y_1 can be related to a physical frequency at present f by

$$\begin{aligned} y_1 &= k|\tau_1| = \frac{2\pi f}{H}\frac{a_0}{a_1} = \frac{f}{f_1} \, , \\ f_1 &\equiv \frac{H}{2\pi}\frac{a_1}{a_0} = \frac{H}{2\pi(1+z_{\rm eq})}\left(\frac{t_1}{t_{\rm eq}}\right)^{1/2} \, , \end{aligned} \tag{3.31}$$

  where Eq. (3.13) is used at the second equal sign of the upper equation, $a_0 = 1$ is the scale factor at present, and $z_{\rm eq}$ is the redshift at the radiation-matter equality. Using $t_1 \approx 1/(2H)$ and the values [5],

$$1 + z_{\rm eq} \approx 2.41 \times 10^4 \, \Omega_m h_0^2, \qquad t_{\rm eq} \approx 3.23 \times 10^{10} \, (\Omega_m h_0^2)^{-2} \, {\rm sec} \, , \tag{3.32}$$

  where Ω_m is the energy-density parameter of matter in the universe today, we obtain

$$f_1 \approx 5.01 \times 10^8 \left(\frac{H}{10^{-4} M_{\rm Pl}}\right)^{1/2} \, {\rm Hz} \, . \tag{3.33}$$

[5] Dark-energy domination is not considered here, and neutrinos are assumed to be relativistic.

Note that f_1 does not depend on $\Omega_m h_0^2$. The frequency f_1 is a cutoff frequency above which no GWB is produced. Therefore, the number density of gravitons for the modes horizon re-entering during RD is

$$n_k \approx \frac{1}{4}\left(\frac{f_1}{f}\right)^4 .$$

- Case 3: horizon re-entry during MD.
  The conditions for the wavelength of a mode are $y_1 \ll 1$ and $y_{\rm eq} \ll 1$. The equation (3.30) with leading-order terms is

$$n_k \approx \frac{1}{4y_1^4}\left[\frac{1}{4(y_{\rm eq}+2y_1)^2}\right] .$$

  $(y_{\rm eq}+2y_1)$ can be written as

$$\begin{aligned} y_{\rm eq}+2y_1 &= k(\tau_{\rm eq}-2\tau_1) = ka_{\rm eq}H\tau_1^2 = -\frac{a_{\rm eq}}{a_1}k\tau_1 = \frac{a_{\rm eq}}{a_1}\frac{f}{f_1} = \frac{f}{f_{\rm eq}} , \\ f_{\rm eq} &\equiv \frac{H(t_{\rm eq})}{2\pi}\frac{a_{\rm eq}}{a_0} . \end{aligned}$$

  Here we used Eqs. (3.13), (3.14), and (3.31). Using $H(t_{\rm eq}) = 4(\sqrt{2}-1)/3t_{\rm eq}$ [58] and Eq. (3.32) gives

$$f_{\rm eq} \approx 1.13 \times 10^{-16}\Omega_m h_0^2 \ {\rm Hz} .$$

  Therefore, the number density of gravitons for the modes horizon re-entering during MD is

$$n_k \approx \frac{1}{16}\left(\frac{f_1}{f}\right)^4\left(\frac{f_{\rm eq}}{f}\right)^2 .$$

From (2.33), we finally obtain the GWB energy density

$$h_0^2\Omega_{\rm gw}(f) \approx \begin{cases} 3.6\times10^{-14}\left(\dfrac{H}{10^{-4}M_{\rm Pl}}\right)^2 , & (f_{\rm eq} < f < f_1) , \\ 3.6\times10^{-14}\left(\dfrac{H}{10^{-4}M_{\rm Pl}}\right)^2\left(\dfrac{f_{\rm eq}}{f}\right)^2 , & (f_0 < f < f_{\rm eq}) , \end{cases} \tag{3.34}$$

where $f_0 = H_0/h_0 = 3.24\times10^{-18}$ Hz. The GWB spectrum is shown in Fig. 3.2 with $H = 2.7\times10^{-5}M_{\rm Pl}$. The reason for this choice of the inflation energy scale is that a stringent limit on the GWB spectrum of de-Sitter inflation comes from CMB observations, as described in the next section.

3.3 GWB creation in slow-roll inflation

The Hubble parameter H is constant during de-Sitter inflation, however, is not constant but slowly changes in slow-roll inflation, depending on the shape of the potential.

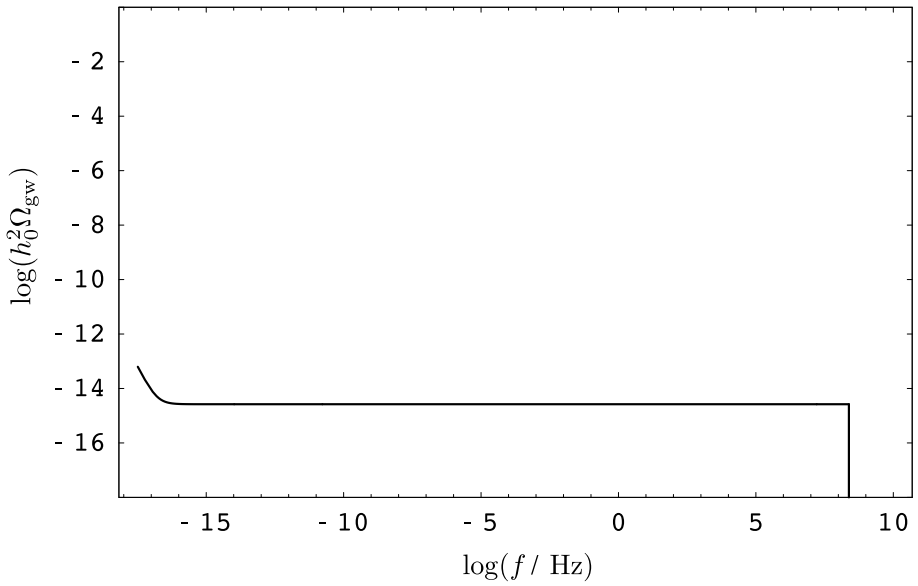

Figure 3.2: GWB spectrum produced by de-Sitter inflation. The enegy scale of inflation is selected as $H = 2.7 \times 10^{-5} M_{\rm Pl}$.

Consequently, the spectrum of the produced gravitons is also modified. The evolution of the Hubble parameter is governed by the equation of motion [68, 69],

$$\begin{aligned} \dot{\phi} &= -2M_{\rm Pl}^2 H'(\phi) \,, \\ \left[H'(\phi)\right]^2 &= \frac{3}{2M_{\rm Pl}^2} H^2(\phi) - \frac{1}{2M_{\rm Pl}^4} V(\phi) \,, \end{aligned} \tag{3.35}$$

which can be derived from Eqs. (3.1) and (3.4) by regarding the Hubble parameter as a function of ϕ and assuming that ϕ varies monotonically with time. The Eq. (3.35) is called the Hamilton-Jacobi equation. The dynamics of the Hubble parameter is quantified by the generalized Hubble slow-roll parameters [70],

$$\begin{aligned} \epsilon(\phi) &\equiv 2M_{\rm Pl}^2 \left[\frac{H'(\phi)}{H(\phi)}\right]^2 \,, \\ {}^{\ell}\lambda_H &\equiv (2M_{\rm Pl}^2)^{\ell} \frac{(H')^{\ell-1}}{H^{\ell}} \frac{d^{(\ell+1)}H}{d\phi^{(\ell+1)}} \,, \qquad (\ell \geq 1) \,. \end{aligned}$$

We can identify the first and second slow-roll parameters ${}^1\lambda_H$ and ${}^2\lambda_H$ with η and ξ^2 in the literature [71] [6].

The primordial power spectra of scalar and tensor fluctuations at the end of inflation

[6] Note that, in some papers, the squared index 2 is often omitted in the definition, though it is of the second order.

are written by

$$\begin{aligned}\mathcal{P}_S(k) &= \mathcal{P}_S(k_0)\left(\frac{k}{k_0}\right)^{n_S-1+(\alpha_S/2)\ln(k/k_0)}, \\ \mathcal{P}_T(k) &= \mathcal{P}_T(k_0)\left(\frac{k}{k_0}\right)^{n_T+(\alpha_T/2)\ln(k/k_0)}, \end{aligned} \tag{3.36}$$

where k_0 is a fiducial pivot scale observed at present in CMB, and is given by $k_0 = 0.002\ \mathrm{Mpc}^{-1}$, which corresponds to f_0, is conventionally used. The spectral indices n_S and n_T up to the second order in the slow-roll parameters [7] are given by [72],

$$\begin{aligned} n_S - 1 &\equiv \left.\frac{d\ln\mathcal{P}_S(k)}{d\ln k}\right|_{\alpha_S\to 0} \\ &\approx 2\eta - 4\epsilon - 2(1+C)\epsilon^2 - \frac{1}{2}(3-5C)\epsilon\eta + \frac{1}{2}(3-C)\xi^2 , \\ n_T &\equiv \left.\frac{d\ln\mathcal{P}_T(k)}{d\ln k}\right|_{\alpha_T\to 0} \\ &\approx -2\epsilon - (3+C)\epsilon^2 + (1+C)\epsilon\eta , \end{aligned} \tag{3.37}$$

and the derivatives [73, 74] are

$$\begin{aligned}\alpha_S &\equiv \frac{d^2\ln\mathcal{P}_S(k)}{d\ln k^{\,2}} \approx 16\epsilon\eta - 24\epsilon^2 - 2\xi^2 , \\ \alpha_T &\equiv \frac{d^2\ln\mathcal{P}_T(k)}{d\ln k^{\,2}} \approx 4\epsilon\eta - 4\epsilon^2 , \end{aligned}$$

where $C \equiv 4(\ln 2+\gamma)-5 \approx 0.08145$ and $\gamma \approx 0.57722$ is the Euler-Mascheroni constant.

The tensor-to-scalar ratio is defined by

$$r \equiv \left.\frac{\mathcal{P}_T}{\mathcal{P}_S}\right|_{k=k_0} \approx 16\epsilon\big[1+2C(\epsilon-\eta)\big] .$$

Note that n_S, n_T, and r are evaluated at the scale $k_0 = 0.002\ \mathrm{Mpc}^{-1}$. From Eq. (3.37), the tensor spectral index n_T is negative, since ϵ is positively defined in Eq. (3.5). This means that the slow-roll inflation predicts smaller GWB spectrum than that of the de-Sitter inflation at high frequencies.

In Eq. (2.32), the energy density of the GWB is related to the tensor power spectrum at the present day $P_T(k)$ as

$$\Omega_{\mathrm{gw}}(k) = \frac{k^2}{12H_0^2}P_T(k) . \tag{3.38}$$

[7] The slow-roll parameters here are related to those in Hamilton-Jacobi formulation like $\epsilon = \epsilon_V$ and $\eta = \eta_V - \epsilon_V$, to the lowest order.

The $P_T(k)$ can be related to the primordial tensor power spectrum $\mathcal{P}_T(k)$ by a transfer function $\mathcal{T}(k)$,

$$P_T(k) = \mathcal{T}^2(k)\mathcal{P}_T(k) \ . \tag{3.39}$$

By numerically integrating Eq. (3.8), the transfer function is found to be well approximated by the form [75]

$$\mathcal{T}(k) = \frac{3j_1(k\tau_0)}{k\tau_0}\sqrt{1.0 + 1.34\left(\frac{k}{k_{\rm eq}}\right) + 2.50\left(\frac{k}{k_{\rm eq}}\right)^2} \ . \tag{3.40}$$

where $k_{\rm eq} = 0.073\,\Omega_m h_0^2$ Mpc^{-1} is the wave number corresponding to the Hubble radius at the time of the matter-radiation equality. Combining Eqs. (3.36), (3.38), (3.39), and (3.40) gives

$$\Omega_{\rm gw}(k) = \frac{3[j_1(k\tau_0)]^2}{4H_0^2\tau_0^2}\mathcal{P}_T(k_0)\left(\frac{k}{k_0}\right)^{n_T}\left[1.0 + 1.34\left(\frac{k}{k_{\rm eq}}\right) + 2.50\left(\frac{k}{k_{\rm eq}}\right)^2\right] ,$$

and, particularly for $k \gg k_{\rm eq}$,

$$\Omega_{\rm gw}(k) \approx \frac{15}{16H_0^2k_{\rm eq}^2\tau_0^4}\mathcal{P}_T(k_0)\left(\frac{k}{k_0}\right)^{n_T} \ . \tag{3.41}$$

Comparing Eq. (3.41) with Eq. (3.34), one can obtain the GW energy spectrum

$$h_0^2\Omega_{\rm gw}(f) \approx \begin{cases} 3.6\times10^{-14}\left(\dfrac{H_*}{10^{-4}M_{\rm Pl}}\right)^2\left(\dfrac{f}{f_0}\right)^{n_T} , & (f_{\rm eq} < f < f_1) \ , \\ 3.6\times10^{-14}\left(\dfrac{H_*}{10^{-4}M_{\rm Pl}}\right)^2\left(\dfrac{f}{f_0}\right)^{n_T}\left(\dfrac{f_{\rm eq}}{f}\right)^2 , & (f_0 < f < f_{\rm eq}) \ , \end{cases} \tag{3.42}$$

where H_* is the Hubble parameter when the scale k_0 crosses the horizon during the inflation. In Eq. (3.42), the extra factor $(f/f_0)^{n_T}$ shows that the slow-roll inflation does not produce larger GW spectrum than that of the de-Sitter inflation. Examples of the spectrum are shown in Fig. 3.3.

The GW spectrum is often written using the tensor-to-scalar ratio r [76]. The amplitude of $\mathcal{P}_T(k_0)$ in Eq. (3.41) has not yet been observed in CMB, but the amplitude of $\mathcal{P}_S(k_0)$ has been determined well [15],

$$\mathcal{P}_S(k_0) \approx 2.457\times10^{-9} \ .$$

Using the cosmological parameters determined by 5th year WMAP data, type Ia supernovae and baryon acoustic oscillations [15], one finds $k_{\rm eq} = 0.010$ Mpc^{-1} and $\tau_0 = 1.44\times10^4$ Mpc. Therefore, Eq. (3.41) can be rewritten as

$$h_0^2\Omega_{\rm gw}(f) = 4.81\times10^{-15}\,r\left(\frac{f}{f_0}\right)^{n_T} ,$$

for $f \gg f_{\rm eq}$. A constraint on r has been obtained by the observations of 5th year WMAP, type Ia supernovae and baryon acoustic oscillations, and the result is $r < 0.54$

(95% C.L.) [15]. This is a conservative limit, in that the nonzero running n_S is allowed in the analysis, where a prior on n_S that has no running can impose a tighter limit on r, but in general inflation models, the running of n_S would be nonzero. Consequently, the upper limit of the GW energy spectrum due to slow-roll inflation is

$$h_0^2\Omega_{\rm gw}(f) \leq 2.60 \times 10^{-15} \quad \text{for} \quad f > f_{\rm eq} \ .$$

In terms of H_*, this limit can be translated into $H_* \leq 2.7 \times 10^{-5} M_{\rm Pl}$.

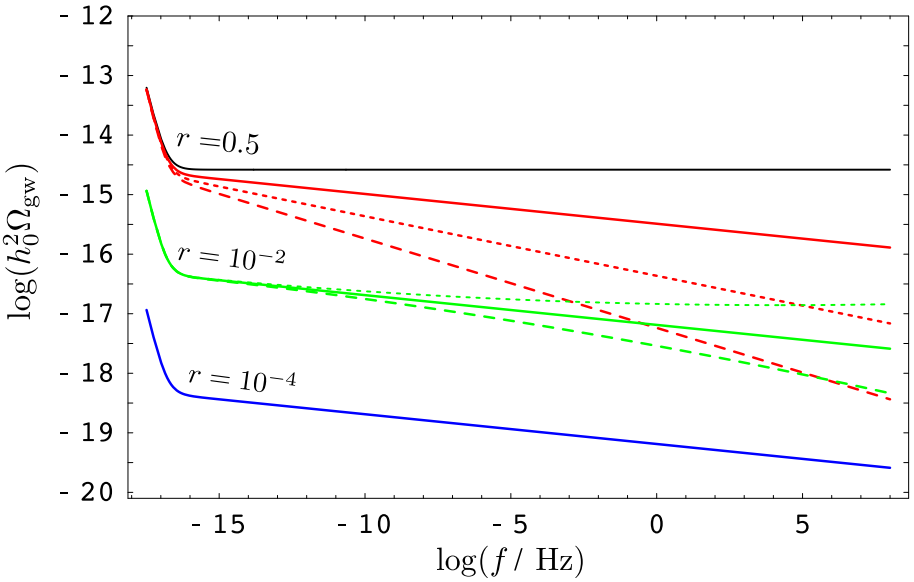

Figure 3.3: GWB spectrum produced by slow-roll inflations. From the top on the left side, the curves are plotted for the tensor-to-scalar ratios $r = 0.5$ (red), 10^{-2} (green), 10^{-4} (blue). For $r = 0.5$ (red), the tensor spectral index is selected as $n_T = -0.05$ (solid), -0.10 (dotted), -0.15 (dashed) with $\alpha_T = 0$. For $r = 10^{-2}$ (green), the running spectral index is selected as $\alpha_T = 0$ (solid), -10^{-3} (dotted), $+10^{-3}$ (dashed). The spectra of slow-roll inflations never exceed that of the de-Sitter inflation (black).

3.4 GWB creation in quintessential inflation

3.4.1 Quintessential inflation

Peebles and Vilenkin presented a model where the idea of a post-inflationary phase stiffer than radiation is dynamically realized [77]. One of motivations of this model is to explain *two* accelerations of the universe during the inflation and the current epoch, with a single scalar field like the quintessence field [78, 79]. The potential of the scalar field (inflaton) ϕ is given by

$$V(\phi) = \begin{cases} \lambda(\phi^4 + M^4) \ , & (\phi < 0) \ , \\ \dfrac{\lambda M^8}{\phi^4 + M^4} \ , & (0 < \phi) \end{cases}$$

The λ is a normalization factor and can be determined by COBE normalization as $\lambda \approx 1 \times 10^{-14}$. M is a characteristic energy parameter. If we want the energy density in ϕ to be compatible with the present total energy ($\Omega_\phi \sim 0.7$) and moderately accelerate the universe, it is required to take $M \sim 10^6\,\mathrm{GeV}$. The potential is similar to that of a chaotic inflation in the range $\phi < M$, and is a slowly decaying function in $\phi > M$. Note that this scenario can be implemented with any other inflationary potential for $\phi < 0$, and the chaotic potential is one of illustrative examples.

The inflaton starts at $\phi < -M_{\rm Pl}$ and rolls toward zero. The inflaton ends slow-rolling at $\phi \sim M_{\rm Pl}$, then the inflaton evolves toward a phase where the kinetic energy of the inflaton dominates. We will call the phase a kinetic energy-dominated (KD) phase [8]. In the phase, from Eqs. (3.1) and (3.4), the energy density of the inflaton ρ_ϕ and the scale factor evolve as

$$\rho_\phi(\tau) = 3H_1^2 M_{\rm Pl}^2 \left(\frac{a_1}{a}\right)^6 ,$$

where the Hubble parameter H_1 at the end of the inflation is

$$H_1 = \frac{1}{a_1 \tau_1} \sim \sqrt{\lambda} M_{\rm Pl} .$$

Since $\rho \propto a^{-3(1+w)}$ for a barotropic fluid with the equation of state $p = w\rho$, the kinetic energy-dominated scalar field behaves like the fluid with $w = 1$, which is stiffer than radiation.

At the end of the inflation, not only gravitons but also massless scalar fields are amplified [67, 80]. Indeed there are various scalar, vector, and tensor degrees of freedom during the inflationary phase. However, free massless spinor and gauge fields are conformally invariant, so their contributions to the total energy density are suppressed. Suppose that during the inflationary phase the number of massless scalar fields is N_s. As well as gravitons, the amplified energy density has been calculated in the case of nearly conformal coupling scalar fields [80], arbitrary coupling scalar fields [81], and arbitrary power-law expansion after inflation [82]. In all cases, the result is

$$\rho_r(\tau) = R\, H_1^4 \left(\frac{a_1}{a}\right)^4 , \qquad R = \sum_{i=1}^{N_s} R_i \sim 10^{-2} N_s . \tag{3.43}$$

R_i is the contribution of each massless scalar degrees of freedom to the energy density of the amplified fluctuations and it is of the order of 10^{-2}. As indicated in [77], the thermalization of the massless scalar fields occurs immediately after the particle creation, when $a_{\rm th}/a_1 \sim (10^2 - 10^3)\, N_s^{-1/2}$.

Since ρ_r decays more slowly than ρ_ϕ, a radiation-dominated phase follows the kinetic energy-dominated phase. The onset of the radiation-dominated phase is computed from $\rho_r(\tau_r) \sim \rho_\phi(\tau_r)$,

$$\frac{a_1}{a_r} \sim \sqrt{\frac{R}{3}} \frac{H_1}{M_{\rm Pl}} \sim \sqrt{\lambda R} .$$

[8] It is also called *deflation* or *kinetion* in other references.

By red-shifting the horizon sclale at τ_r up to now, we obtain

$$\begin{aligned} f_r &= \frac{H_r}{2\pi}\left(\frac{a_r}{a_0}\right) = \frac{H_1}{2\pi}\left(\frac{a_1}{a_r}\right)^3\left(\frac{a_r}{a_0}\right) \\ &\approx 3.65\times 10^{-3} R^{3/4}\left(\frac{\lambda}{10^{-14}}\right)\left(\frac{g_s(\tau_0)}{g_s(\tau_{\rm th})}\right)^{1/3} \text{Hz} , \end{aligned}$$

where $g_s(\tau_{\rm th})$ is the number of degrees of freedom after the thermalization of the massless scalar fields. It is also important to compute the frequency f_1 corresponds to the horizon scale at the end of inflation, which is given by

$$\begin{aligned} f_1 &= \frac{H_1}{2\pi}\left(\frac{a_1}{a_0}\right) = \frac{H_1}{2\pi}\left(\frac{a_1}{a_r}\right)\left(\frac{a_r}{a_0}\right) \\ &\approx 3.65\times 10^{11} R^{-1/4}\left(\frac{g_s(\tau_0)}{g_s(\tau_{\rm th})}\right)^{1/3} \text{Hz} . \end{aligned}$$

The frequency corresponding to the matter-radiation equality is the same as that in de-Sitter inflation, and is given by $f_{\rm eq} \approx 1.13\times 10^{-16}\,\Omega_{\rm m} h_0^2\,\text{Hz}$.

3.4.2 GWB spectrum

A GWB energy spectrum in the quintessential inflation has been calculated by the method of particle creation in a curved spacetime, as described in Sec. 3.2 [82, 83]. In quintessential inflation scenario, the smoothly continued solutions of cosmic expansion are

$$\begin{aligned} a_{\rm I}(\tau) &= -\frac{1}{H\tau} , && (\text{Inflation} : -\infty < \tau < \tau_1) , \\ a_{\rm K}(\tau) &= \frac{1}{H\tau_1}\sqrt{\frac{3\tau_1 - 2\tau}{\tau_1}} , && (\text{KD} : \tau_1 < \tau < \tau_r) , \\ a_{\rm R}(\tau) &= -\frac{\tau + \tau_r - 3\tau_1}{H\tau_1\sqrt{\tau_1(3\tau_1 - 2\tau_r)}} , && (\text{RD} : \tau_r < \tau < \tau_{\rm eq}) , \\ a_{\rm M}(\tau) &= \frac{(\tau + \tau_{\rm eq} + 2\tau_r - 6\tau_1)^2}{4H\tau_1(3\tau_1 - \tau_r - \tau_{\rm eq})\sqrt{\tau_1(3\tau_1 - 2\tau_r)}} , && (\text{MD} : \tau_{\rm eq} < \tau < \tau_0) . \end{aligned}$$

Here we assume that the inflation is de-Sitter inflation. Given the cosmic expansions, one can solve Eq. (3.12) and obtain solutions for positive frequency modes in each phase,

$$\begin{aligned} \psi_k^{\rm I}(k\tau) &= \left(\frac{\pi}{2}\right)^{1/2}(k\tau)^{1/2} H^{(2)}_{3/2}(k\tau) , && (-\infty < \tau < \tau_1) , \\ \psi_k^{\rm K}(k\tau) &= \left(\frac{\pi}{2}\right)^{1/2}\{k(\tau+p)\}^{1/2} H^{(2)}_{0}[k(\tau+p)] , && (\tau_1 < \tau < \tau_r) , \\ \psi_k^{\rm R}(k\tau) &= e^{-ik\tau} , && (\tau_r < \tau < \tau_{\rm eq}) , \\ \psi_k^{\rm M}(k\tau) &= \left(\frac{\pi}{2}\right)^{1/2}\{k(\tau+q)\}^{1/2} H^{(2)}_{3/2}[k(\tau+q)] , && (\tau_{\rm eq} < \tau < \tau_0) , \end{aligned}$$

where $p \equiv -3\tau_1/2$ and $q \equiv \tau_{\rm eq} + 2\tau_r - 6\tau_1$. The normalizaiton of the mode functions is chosen to be $\psi_k \to e^{-ik\tau}$ when $k\tau \to \infty$.

Following procedures are the same as those in Sec. 3.2. The amount of created gravitons is given by the Bogolubov coefficients connecting from the inflationary phase to the matter-dominated phase today. The Bogolubov transformations are defined by

$$\begin{aligned}
\psi_k^{\rm I} &= \alpha_k^{\rm IK}\psi_k^K + \beta_k^{\rm IK}\psi_k^{\rm K\,*}\,, \\
\psi_k^{\rm K} &= \alpha_k^{\rm KR}\psi_k^R + \beta_k^{\rm KR}\psi_k^{\rm R\,*}\,, \\
\psi_k^{\rm R} &= \alpha_k^{\rm RM}\psi_k^M + \beta_k^{\rm RM}\psi_k^{\rm M\,*}\,,
\end{aligned}$$

and the total Bogolubov coefficients are given by

$$\begin{aligned}
&\begin{pmatrix} \alpha_k^{\rm total} & \beta_k^{\rm total} \\ \beta_k^{\rm total\,*} & \alpha_k^{\rm total\,*} \end{pmatrix} \\
&= \begin{pmatrix} \alpha_k^{\rm IK} & \beta_k^{\rm IK} \\ \beta_k^{\rm IK\,*} & \alpha_k^{\rm IK\,*} \end{pmatrix}
\begin{pmatrix} \alpha_k^{\rm KR} & \beta_k^{\rm KR} \\ \beta_k^{\rm KR\,*} & \alpha_k^{\rm KR\,*} \end{pmatrix}
\begin{pmatrix} \alpha_k^{\rm RM} & \beta_k^{\rm RM} \\ \beta_k^{\rm RM\,*} & \alpha_k^{\rm RM\,*} \end{pmatrix}\,.
\end{aligned}$$

We assume the universe is in a vacuum state during the inflation phase. The number of created gravitons is given by $n_k = |\beta_k^{\rm total}|^2$, and the approximated GWB-energy spectrum obtained in [83] is

$$\Omega_{\rm gw}(f) = \begin{cases}
K\left(\dfrac{f}{f_{\rm r}}\right)\left[\ln\left(\dfrac{f}{f_1}\right)\right]^2\,, & (f_{\rm r} < f < f_1)\,, \\[2ex]
\dfrac{\pi}{4}K\left[\ln\left(\dfrac{f_{\rm r}}{f_1}\right)\right]^2\,, & (f_{\rm eq} < f < f_{\rm r})\,, \\[2ex]
\dfrac{\pi}{4}K\left(\dfrac{f_{\rm eq}}{f}\right)^2\left[\ln\left(\dfrac{f_{\rm r}}{f_1}\right)\right]^2\,, & (f_0 < f < f_{\rm eq})\,,
\end{cases}$$

where

$$K \equiv \frac{81}{16\pi^3}\left(\frac{g_s(\tau_0)}{g_s(\tau_{\rm th})}\right)^{1/3}\lambda\,\Omega_\gamma \approx 1.34\times 10^{-20}\,h_0^{-2}\left(\frac{\lambda}{10^{-14}}\right)\,.$$

Here we used $g_s(\tau_0) = 3.91$ and $g_s(\tau_{th}) = 106.75$ in the standard model of particle physics. In supersymmetric extension of the standard model, the number of degrees of freedom is doubled because of supersymmetric partners. However, the correction to the GWB spectrum is small, and only a factor $2^{1/3} \approx 1.26$ appears.

In quintessential inflationary models, the energy density of GWB has a peak at high frequencies and becomes much larger than in the case of ordinary inflationary models. The location of the peak, $f_{\rm peak} = e^{-2}f_1 \propto R^{-1/4}$, weakly depends on R, but does not depend on λ. The height of the peak is given by

$$h_0^2\Omega_{\rm gw}(f_{\rm peak}) \approx 0.725\times 10^{-6}R^{-1}\,, \tag{3.44}$$

and does not depend on λ either. Therefore, the peak cannot move one order of magnitude and is firmly localized around 100 GHz.

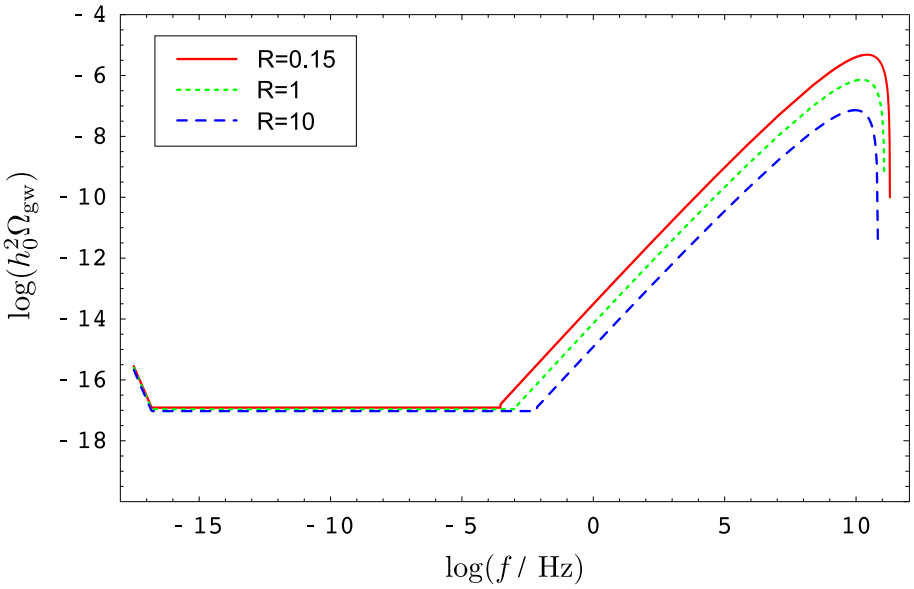

Figure 3.4: GWB spectrum produced by quintessential inflation for a fixed value of $\lambda = 10^{-14}$. Other parameters are selected as $g_s(\tau_0) = 3.91$, $g_s(\tau_{th}) = 106.75$, and $h_0^2\Omega_{\rm m} = 0.1369$ [15]. Three curves corresponds to $R = 0.15$ (red, solid curve), $R = 1$ (green, dotted curve), and $R = 10$ (blue, dashed curve).

The constraint on the spectrum comes from not CMB limit but big-bang nucleosynthesis limit. Using Eqs. (4.7) and (3.44), one can obtain $0.13 \lesssim R$. From Eq. (3.43), this means that the number of massless scalar degrees of freedom N_s has to exceed 13. The GWB spectra with three values of R are plotted in Fig. 3.4.

Note that such a GWB spectrum with large peak at high frequencies is not a specific feature appearing only in a quintessential inflation model, but is a common feature in scenarios with KD epoch of scalar fields. The gravitational reheating process we considered above is an inefficient reheating process and is likely to result in a long KD phase. Another reheating process, a so-called instant preheating has been proposed [84, 85, 86]. Instant reheating is much more efficient than gravitational reheating, and completes the reheating process earlier. Consequently, the duration of the KD phase is shorter, and the peak on the GWB spectrum become smaller. The dependences of the spectrum on the reheating mechanisms have been investigated by Tashiro *et al.* [87]. Therefore, the GWB at high frequencies is important because it brings us information regarding the reheating mechanism and thermal history of the universe after inflation.

3.5 Pre-big-bang model

Pre-big-bang model is a cosmological model motivated by the string theory and was originally proposed by Gasperini and Veneziano [88, 89]. In this model, the initial state of the universe is assumed to be the string perturbative vacuum with the weak coupling and low curvature. Then, the perturbative approach is well justified. The low-energy

string effective action at the lowest order in the derivatives and in e^{ϕ} is given by [88, 89]

$$S \sim \int d^4x\sqrt{-g}\left[e^{-\phi}(R + \partial_\mu\phi\,\partial^\mu\phi) - V(\phi)\right] , \tag{3.45}$$

where ϕ is the dilaton field. The dilaton potential $V(\phi)$ is due to nonperturbative effects and, thus, can be neglected in the low-energy perturbative regime. There is a phase, called a dilaton-dominated (DD) phase, that the kinetic energy of the dilaton field drives the universe through an superinflationary evolution (which is an accelerated expansion in the string frame, or accelerated contraction in the Einstein frame). The spacetime curvature increases in the DD phase , eventually reaching the string scale. In this string phase, the low-energy string effective action is not valid, and the perturbative treatment breaks down. Although the transition between the pre-big-bang (DD) phase and the post-big-bang phase is not well understood, some models, which can partially described it, have been proposed. The de-Sitter phase with linearly growing dilaton is considered to be the representative of a typical solution in the large curvature regime, where non-perturbative corrections are expected to avoid the big-bang singularity and to stop the dilaton field to grow. Then, it is assumed, at the end of the stringy phase, that the standard RD phase with the constant dilaton field is restored. As we will see later, MD phase does not much contribute to the GWB spectrum and is not important for the computation. So, we do not consider MD phase here.

An exact GWB spectrum in the pre-big-bang model has derived in [90]. In a homogeneous, isotropic, and spatially flat background, for simplicity, the equation of motion derived from the action in Eq. (3.45), gives the solutions of the evolving universe in the string frame,

$$a(\tau) = -\frac{1}{H_s\tau_s}\left(\frac{\tau - (1-\alpha)\tau_s}{\alpha\tau_s}\right)^{-\alpha} , \qquad \phi(\tau) = \phi_s - \gamma\,\ln\left[\frac{\tau - (1-\alpha)\tau_s}{\alpha\tau_s}\right] ,$$

for the DD phase ($-\infty < \tau < \tau_s$),

$$a(\tau) = -\frac{1}{H_s\tau} , \qquad \phi(\tau) = \phi_s - 2\beta\,\ln\left(\frac{\tau}{\tau_s}\right) ,$$

for the stringy phase ($\tau_s < \tau < \tau_1$),

$$a(\tau) = \frac{1}{H_s\tau_1^2}(\tau - 2\tau_1) , \qquad \phi = \phi_0 ,$$

for the RD phase ($\tau_1 < \tau < \tau_r$). The conformal time $\tau_s < 0$, $\tau_1 < 0$, and $\tau_r > 0$ are defined at the time of the DD-string, string-RD, RD-MD phase transition, respectively. The solutions are connected so that the evolution is continuous across each phase transition. The value α and γ are constants and given by $\alpha = 1/(1+\sqrt{3})$ and $\gamma = \sqrt{3}$, in the absence of external matter [91]. In stringy phase, the Hubble parameter H and the derivative of the dilaton field $\dot{\phi}$ is set to be constants so that it produces the de-Sitter expansion.

The model has several parameters: α, β, γ, H_s, τ_s, and τ_1. Among these parameters, α and γ concerns the solution in DD phase, but, they are fixed, as mentioned above, if

we assume the absence of external matter. β and H_s are parameters that determines the growth of the dilaton and the energy scale during the stringy phase, respectively. However, the natural value of H_s is considered to be $H_s \approx 1/\lambda_s \approx 0.03\, M_{\rm Pl}$ due to the string length λ_s in the string theory [90]. The parameters τ_s and τ_1 concerns the duration of the string era, and determines the phase when the fluctuation with a certain wave number crosses outside the horizon (the horizon crossing occurs at $k\tau \sim 1$). The corresponding frequency today is given by redshifting the horizon scale at the time. From Eq. (3.33), it follows

$$f_1 = 6.13 \times 10^{10} \left(\frac{H_s}{0.03\, M_{\rm Pl}}\right) \left(\frac{t_1}{\lambda_s}\right)^{1/2} \ {\rm Hz} \ .$$

On the other hand, τ_s or f_s are totally unknown, even as an order of magnitude. Since $|\tau_1| < |\tau_s|$, f_s is in the range $0 < f_s < f_1$. Therefore, we fix the model parameters α and γ at the values above, and H_s and τ_1 at the typical values $H_s \approx 0.03\, M_{\rm Pl}$ and $f_1 = 6.13 \times 10^{10}\,{\rm Hz}$. The unknown parameters are β and f_s.

The equation for the Fourier modes of metric tensor perturbations is [92]

$$\frac{d^2\psi_k}{d\tau^2} + \left[k^2 - V(\tau)\right]\psi_k = 0 \ ,$$

$$V(\tau) = \frac{1}{a} e^{\phi/2} \frac{d^2}{d\tau^2}\left(a\, e^{-\phi/2}\right) \ .$$

The procedures to compute the created gravitons is the same as those for the de-Sitter and quintessential inflations in the previous sections. The exact GWB spectrum in the pre-big-bang model is obtained in [90] as

$$\begin{aligned} \Omega_{\rm gw}(f) &= b(\mu) \frac{2\pi^3 f_s^4}{H_0^2 M_{\rm Pl}^2} \left(\frac{f_1}{f_s}\right)^{2\mu+1} \left(\frac{f}{f_s}\right)^{5-2\mu} \\ &\times \left| H_0^{(2)}\left(\frac{\alpha f}{f_s}\right) J'_\mu\left(\frac{f}{f_s}\right) + H_1^{(2)}\left(\frac{\alpha f}{f_s}\right) J_\mu\left(\frac{f}{f_s}\right) \right. \\ &\quad \left. - \frac{(1-\alpha)}{2\alpha} \frac{f_s}{f} H_0^{(2)}\left(\frac{\alpha f}{f_s}\right) J_\mu\left(\frac{f}{f_s}\right) \right|^2 \ , \end{aligned} \tag{3.46}$$

with

$$b(\mu) \equiv \frac{\alpha}{48} 2^{2\mu} (2\mu - 1)^2 \Gamma^2(\mu) \ , \qquad \mu \equiv \frac{1}{2}|2\beta - 3| \ .$$

In the spectrum, the new parameter μ explicitly appears instead of β. Thus, the shape of the spectrum is completely determined by two parameters μ and f_s.

For $f \ll f_s \ll f_1$, the expression (3.46) can be expanded as

$$\begin{aligned} \Omega_{\rm gw}(f) &\approx \frac{(2\mu-1)^2}{192\mu^2\alpha} \frac{2\pi^3 f_s^4}{H_0^2 M_{\rm Pl}^2} \left(\frac{f_1}{f_s}\right)^{2\mu+1} \left(\frac{f}{f_s}\right)^3 \\ &\times \left[(2\mu\alpha - 1 + \alpha)^2 + \frac{4}{\pi^2} \left\{ (2\mu\alpha - 1 + \alpha) \left(\ln \frac{\alpha f}{2 f_s} + \gamma_E \right) - 2 \right\}^2 \right] \end{aligned} \tag{3.47}$$

where $\gamma_E \approx 0.5772$ is the Euler constant. On the other hand, for $f_s \ll f \ll f_1$, Eq. (3.46) can be approximated to

$$\Omega_{\rm gw}(f) \approx \frac{4b(\mu)}{\pi^2\alpha}\frac{2\pi^3 f_s^4}{H_0^2 M_{\rm Pl}^2}\left(\frac{f}{f_1}\right)^{3-2\mu} . \tag{3.48}$$

It is important to stress that in the high frequency limit the unknown parameter f_s cancels. The approximated expressions (3.47) and (3.48) give the frequency dependence of the GWB spectrum, f^3 at low frequencies (the factor $(\ln f)^2$ is a small correction.), and $f^{3-2\mu}$ at high frequencies, which reproduce the frequency dependence of the approximated spectrum first found in [93, 94, 95]. At the frequency $f = f_1$, there is a sharp cutoff in the spectrum because the fluctuation never cross the horizon above the frequencies, and its amplification is suppressed.

In Fig. 7.8, the GWB spectra are plotted for three parameter sets $(\mu,\ f_s) = (1.5,\ 100\,\mathrm{Hz})$, $(1.3,\ 100\,\mathrm{Hz})$, $(1.4,\ 10^5\,\mathrm{Hz})$. We select μ in the range $0 < \mu < 3/2$, because the case with $\mu > 3/2$ has large energy at lower frequency than f_1 and easily violates the observational bounds due to big-bang nucleosynthesis or GW detectors (LIGO) (see, Fig. 4.2 in Chap. 4). On the other hand, f_s is allowed to have much lower values than our choices of f_s in Fig. 3.5, because the spectrum rapidly decreases as f^3 at the frequencies $f < f_s$, and the observational limits due to pulsar timing and CMB can be easily avoided. So, the GWB spectrum can be extended toward much lower frequencies, unless it violates the pulsar-timing limit. While, for this reason, MD phase is unimportant for GWB spectrum in the pre-big-bang model.

The most stringent limit comes from those at high frequencies. Therefore, the pre-big-bang model is significantly interesting for GW experiments at high frequencies. Advanced detectors will be able to search a part of a parameter space of the pre-big-bang model, and would be a test of the string theory. The observational data of 4th science run of LIGO have already begun to bound the model parameters, though the limit is still very weak [96].

3.6 Other production mechanisms

Preheating after inflation

At the end of inflation, the process by which the energy density driving inflation was converted into the matter and radiation we observe today, is called reheating. The first stage of the conversion, preheating, is known to be violent and accompanies rapid growth of inhomogeneities by parametric resonance. Subsequently, the large concentrations of energy density in bubble structures collide, and generate a significant fraction of energy in the form of gravitational waves. Then, the bubbles are dissipated through turbulences, and are finally thermalized. The process also produces gravitational waves. The computation of a GWB in the process is quite complicated, nonlinear problem, and needs a numerical simulation. Such a GWB in chaotic inflation has first been examined by Khlebnikov and Tkachev [97], and recently has been reanalyzed more accurately by Easther *et al.* [98, 99]. The GWB in hybrid inflation has been computed by

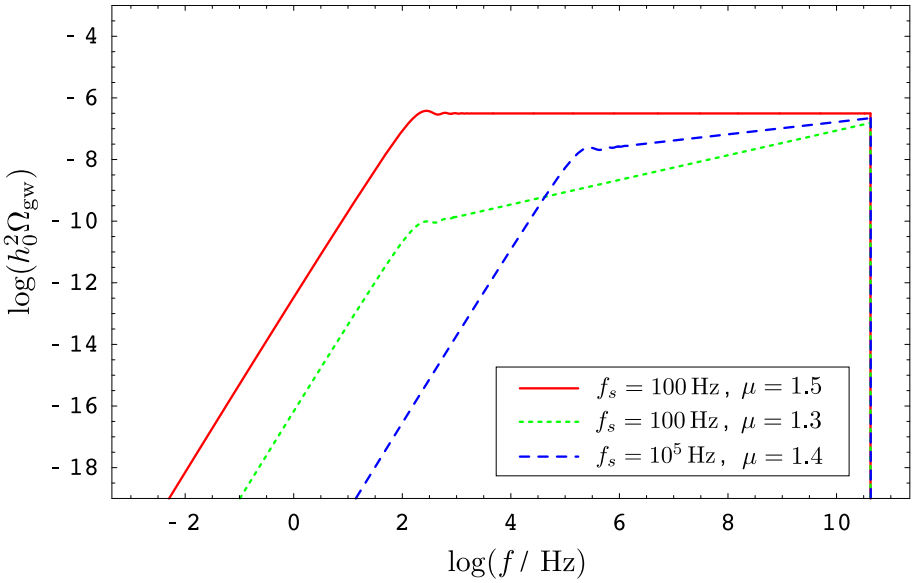

Figure 3.5: GWB spectrum produced in the minimal pre-bing-bang model with the fixed values of $H_s \approx 0.03\,M_{\rm Pl}$ and $f_1 = 6.13 \times 10^{10}\,{\rm Hz}$.

Garcia-Bellido *et al.* [100, 101]. In both cases of inflations, the predicted GWB energy density is $h_0^2\Omega_{\rm gw} \sim 10^{-10}$, localized at the frequencies $10^7 - 10^9\,{\rm Hz}$ on the spectrum [9], depending on the energy scale the preheating occurs. Thus, the GWB from the preheating open a new window for searching for unknown physics in the early universe.

Phase transition

In the early universe, the restored symmetry is broken at a certain temperature. For example, one of first-order phase transitions from false vacuum to true vacuum might be electroweak symmetry breaking, though it is not known yet whether the electroweak phase transition is the first-order or not. If the first-order phase transitions occurred, explosive thermal bubbles by the release of potential energy are generated, then collide, and form turbulent plasma. In the case, a GWB spectrum with characteristic peaks is produced via the bubble collisions [102, 103] and the turbulence [104, 105], which is similar to the preheating, and could produce larger spectrum than that due to inflation. The detectability of the GWB has been discussed in the LISA band by Nicolis [106], and in the higher frequency band up to $\sim 100\,{\rm Hz}$ by Grojean and Servant [107]. The energy density is, at most, $\Omega_{\rm gw} \sim 10^{-10}$ at the peak of the spectrum, being independent of the frequency band. If the first-order phase transitions occurred at the temperature $T \sim 100\,{\rm GeV}$, the peak frequency of the GWB corresponds to the frequency range of LISA, according to Eq. (2.37). If the transitions occurred at the higher temperature, say, $T \sim 10^7\,{\rm GeV}$, advanced LIGO might detect the GWB.

[9] The generation of the GWB at the frequencies, say, $\sim 1 - 100\,{\rm Hz}$, is also possible, though the amount of the produced energy is relatively small.

Cosmic strings

Cosmic strings were topological defects which may be formed during phase transitions in the early universe [108]. Cosmic superstrings are produced in certain string theory. A cosmological network of oscillating string loops generates a stochastic GWB [109, 110, 111]. The spectrum is characterized by three parameters: the string tension (mass per unit length) $G\mu$, the string reconnection probability p, and the parameter ϵ related to the string loop size, where G is the gravitational constant. In the most cases, broad GWB spectra are predicted in the frequency range from 10^{-12} Hz to 10^{6} Hz, though the bump of the GWB spectrum depends on ϵ. For relatively small ϵ, the maximal amplitude could reach the big-bang nucleosynthesis bound, which is described in the next chapter. The most-recent theoretical estimate of the upper limit on the parameters has been discussed by Siemens *et al.* [112]. The large volume of the parameter space can be complementarily explored by the ground- and space-based GW detectors and the pulsar timing.

Chapter 4

Observational constraints on GWB

As reviewed in Chap. 3, inflation creates a GWB spectrum broadly ranging in frequencies $\sim 10^{-18}$ - 10^{9} Hz. The shape of the spectrum reflects inflation potentials and phase transitions, predicted in extended theories of high-energy physics. Therefore, it is very important to obtain constraints on the GWB spectrum not at a particular frequency but several frequencies much different one another. In this chapter, we will see how various observations impose the limits on the amount of GWB. At the end of this chapter, we summarize observational constraints on GWB and the predicted spectra of stochastic GWBs in Fig. 4.2.

4.1 Big-bang nucleosynthesis limit

Big-bang nucleosynthesis (BBN) admirably predicts the abundance of light-elements (H, D, ^{3}He, ^{4}He, ^{7}Li) in the universe currently observed. The abundance depends on two parameters: a baryon-to-photon ratio τ and effective degrees of freedom of particles at the temperature $\sim 1\,\mathrm{MeV}$, $g_* = g(T \sim 1\,\mathrm{MeV})$. These parameters are strongly constrained by observations. Therefore, the energy density of GWs can not be much larger not so as to impair the predictions of the light-element abundances. Tightest limit can be obtained by the abundance of ^{4}He, which is determined by the ratio of the number density of neutrons to protons available at the beginning of the nucleosynthesis,

$$\left(\frac{n_\mathrm{n}}{n_\mathrm{p}}\right) \approx \exp\left(-\frac{Q}{T_\mathrm{f}}\right) , \qquad Q \equiv m_\mathrm{n} - m_\mathrm{p} \approx 1.3\,\mathrm{MeV} .$$

The ratio significantly depends on the freezing temperature T_f that neutrons decouple from an weak interaction with protons.

The freezing temperature can be estimated from a balance between the rate of cosmic expansion and of the weak interaction, which is the same argument as that in Sec. 2.2.5. The rate of expansion of the universe is given by

$$H^2 = \frac{1}{3M_\mathrm{Pl}^2}\rho = \frac{\pi^2}{90M_\mathrm{Pl}^2} g_* T^4 ,$$

for relativistic particles, where g_* is defined as

$$g_* \equiv \sum_{i=\text{boson}} g_i \left(\frac{T_i}{T}\right)^4 + \frac{7}{8} \sum_{i=\text{fermion}} g_i \left(\frac{T_i}{T}\right)^4 . \tag{4.1}$$

In the standard model of a particle theory, relativistic particles at $T_* \approx 1\,\text{MeV}$ are a photon, an electron and positron, and three species of neutrinos ($N_\nu = 3$): γ, $e^\pm$, ν, $\bar{\nu}$. Then, $g_* = 43/3$. If there would exist extra particles, g_* increases. So, conventionally, extra degrees of freedom are included into the species of neutrinos and are defined by the quantity N_ν^{eff}, which is generally not an integer. Therefore, the degrees of freedom (4.1) is

$$g_*(N_\nu^{\text{eff}}) = 2 + \frac{7}{8}(4 + 2N_\nu^{\text{eff}}) = \frac{43}{4} + \frac{7}{8}(N_\nu^{\text{eff}} - 3) . \tag{4.2}$$

On the other hand, the weak interaction can be approximated by the Fermi interaction if the energy scale considered is low enough compared to the mass of weak bosons, $80 - 90\,\text{GeV}$. Since the nucleosynthesis occurs at the energy scale around $1\,\text{MeV}$, the cross section is given by $\sigma \sim G_\text{F}^2 T^2$, where the Fermi constant is $G_\text{F} = 1.166 \times 10^{-5}\,\text{GeV}^{-2}$ (This is really appropriate in the limit $T \gg Q$. But we will use it for simplicity.). Using particle velocities $|v| \sim 1$ and the number density $n \sim T^3$, one can obtain the rate of weak interaction $\Gamma \sim G_\text{F}^2 T^5$.

Consequently, the condition $\Gamma \sim H$ gives

$$G_\text{F}^2 T_\text{f}^5 \approx \left(\frac{g_*}{90}\right)^{1/2} \frac{\pi\, T_\text{f}^2}{M_\text{Pl}} ,$$

that is,

$$T_\text{f} \propto g_*^{1/6} .$$

If g_* increases, the cosmic expansion at that time become rapid, and T_f rises. This follows the increase of neutron abundance available at the time of freeze-out. Then, more ^{4}He is produced. However, another parameter of the BBN, τ also affects the amount of ^{4}He: lower τ leads to small amount of ^{4}He. Thus, we need to know both the upper limit of the ^{4}He abundance and the lower limit of τ in order to constrain g_* or N_ν^{eff}. According to [113], although there are some astronomical uncertainty after the primordial production of light elements due to the BBN, a conservative limit $N_\nu^{\text{eff}} \leq 4$ is obtained.

From Eqs. (4.1) and (4.2), the energy density of gravitons has to be

$$\left(\frac{\rho_\text{gw}}{\rho_\gamma}\right)_\text{BBN} = \left(\frac{T_\text{gw}}{T}\right)^4_\text{BBN} \leq \frac{7}{8}(N_\nu^{\text{eff}} - 3) . \tag{4.3}$$

This quantity should be translated to the energy density today. Entropy conservation in a comoving volume, as well as the discussion in Sec. 2.2.5, gives the relation

$$\left(\frac{\rho_\text{gw}}{\rho_\gamma}\right)_0 = \left(\frac{\rho_\text{gw}}{\rho_\gamma}\right)_\text{BBN} \left(\frac{g_s(T_0)}{g_s(1\,\text{MeV})}\right)^{4/3} , \tag{4.4}$$

where $g_s(T_0) = 3.91$ and $g_s(1\,\mathrm{MeV}) = 10.75$ [1]. Combining Eqs. (4.3) and (4.4), we obtain

$$\left(\frac{\rho_{\rm gw}}{\rho_\gamma}\right)_0 \leq 0.227\,(N_\nu^{\rm eff} - 3)\ . \tag{4.5}$$

In the above equation, $\rho_{\rm gw}$ is an integrated energy density over frequencies. Using

$$\rho_{\rm gw} = \int d(\ln f)\,\frac{d\rho_{\rm gw}(f)}{d\ln f}\ ,$$

the observed value of $\rho_{\gamma 0}$, and Eq. (2.26) gives

$$\int_{f_{\rm min}}^{f_{\rm max}} d(\ln f)\,h_0^2\Omega_{\rm gw}(f) \leq 5.6\times 10^{-6}\,(N_\nu^{\rm eff} - 3)\ . \tag{4.6}$$

The choice of the upper and lower cutoff frequencies is discussed in [114]. The frequency $f_{\rm min}$ corresponds to the horizon scale at the time of the BBN, and $f_{\rm min} = f_{\rm BBN} \sim 10^{-10}\,\mathrm{Hz}$, because GWs whose wavelength is larger than the horizon scale do not contribute as radiation. As for $f_{\rm max}$, it would be taken to be $f_{\rm max} = f_1 \sim 10^9\,\mathrm{Hz}$ for an inflationary GWB and $f_{\rm max} = f_{\rm Pl} \sim 10^{43}\,\mathrm{Hz}$ for a general situation.

Adopting $N_\nu^{\rm eff} \leq 4$ and assuming that the spectrum can be regarded as flat in a frequency range $\Delta\ln f \sim 1$, we obtain

$$h_0^2\Omega_{\rm gw}(f) \leq 5.6\times 10^{-6}\ , \qquad \text{at}\ \ 10^{-10}\,\mathrm{Hz} \lesssim \mathrm{f} \lesssim \mathrm{f_{max}}\ . \tag{4.7}$$

Note that this limit is only valid for the GWB present at the time of the BBN and cannot be applied to GWB produced after that by astrophysical sources or some other processes.

4.2 CMB limit

Gravitational waves contribute to temperature fluctuations of CMB today. The amplitude of the fluctuations cannot exceed that of current observations. Consequently, the amplitude of GWB has to be limited. As described in Sec. 3.3, 5th year WMAP data combined with type Ia supernovae and baryon acoustic oscillation data tightly limits the inflationary GWB energy spectrum in broad frequency ranges. However, this limit can be derived, assuming that the tensor spectral index has a negative index of the tensor mode, $n_T < 0$. In general, n_T could be positive. Therefore, the CMB limit derived in Sec. 3.3 is only valid at the pivot scale $k_0 = 0.002\,\mathrm{Mpc}^{-1}$ and gives

$$h_0^2\Omega_{\rm gw}(k_0) \leq 5.93\times 10^{-14} \qquad \text{at}\ \ k_0 = 0.002\,\mathrm{Mpc}^{-1}\ . \tag{4.8}$$

On the other hand, Seljak *et al.* [22] has analyzed cosmological parameters with WMAP, SDSS galaxy clustering and SDSS Lyα forest data, taking the pivot scale at $k_{\rm pivot} = 0.05\,\mathrm{Mpc}^{-1}$. They have obtained a constraint $r < 0.45$ (95% C.L.), allowing

[1] We assumed that relativistic particles are γ, $e^\pm$, ν, $\bar\nu$ at $T = 1\,\mathrm{MeV}$, and are γ, ν, $\bar\nu$ at $T = T_0$.

a running spectral index of a scalar mode. Then, the constraint on GWB energy spectrum is

$$h_0^2\Omega_{\rm gw}(k_{\rm pivot}) \leq 3.41 \times 10^{-15} \qquad \text{at} \;\; k_{\rm pivot} = 0.05\,{\rm Mpc}^{-1}\,. \tag{4.9}$$

Assuming that no steep peak exists on GWB energy spectrum between k_0 and $k_{\rm pivot}$, we can interpolate the CMB limits, Eqs. (4.8) and (4.9), and obtain the limit between $f_0 = 3.24 \times 10^{-18}\,{\rm Hz}$ and $f_{\rm pivot} = 8.10 \times 10^{-17}\,{\rm Hz}$.

Another limit to GWB has been obtained by CMB and galaxy observations [115]. GWB with frequencies $\gtrsim 10^{15}\,{\rm Hz}$ contributes to the radiation density of the universe at the time of decoupling of CMB, and affects on the expansion rate. It also affects on the growth of perturbations at later times. As a result, CMB power spectrum and matter spectrum today would be changed. This concept is similar to the constraint to GWB due to BBN. However, the advantage is that the limit can be extended to the lower frequencies than that of BBN. The frequency corresponds to wavelengths comparable to the comoving horizon at CMB decoupling.

The excess energy of radiation at the time of CMB decoupling is constrained by current observations in terms of effective neutrino degrees of freedom at the time of decoupling of CMB $N_\nu^{\rm eff}(t_{\rm dec})$. Then, $N_\nu^{\rm eff}(t_{\rm dec})$ is translated into the limit to $\Omega_{\rm gw}$. In [115], the authors carried out likelihood analyses, using the constraints from CMB, galaxy surveys, and the Lyα forest, and assuming that the number of neutrino degrees of freedom (not including extra degrees of freedom) is $N_\nu = 3.04$ and that the neutrino masses are free to vary. For GWB produced with homogeneous initial conditions (in inflation, pre-big-bang or ekpyrotic scenario) [2], they have obtained

$$h_0^2\Omega_{\rm gw}(f) \leq 8.4 \times 10^{-6} \qquad \text{at} \;\; f \gtrsim 10^{-15}\,{\rm Hz} \qquad (95\%\,{\rm C.L.})\,,$$

in a frequency range $\Delta \ln f \sim 1$. The lower end of frequencies that the limit can be applied is taken as $10^{-15}\,{\rm Hz}$. This is a conservative choice, because the gravitational-wave wavelength must be within the horizon at the time of slightly before recombination. The CMB limit is comparable to the big-bang nucleosynthesis limit.

4.3 Pulsar-timing limit

Pulsars are rapidly rotating compact objects, which are considered to be formed by the supernovae of massive stars. The pulsars emit pulses with periods considerably stable in time. Particularly, the periods of millisecond pulsars are extremely stable, and has the time derivatives of the periods $\dot{\Omega} \sim 10^{-19}\,{\rm sec\,sec}^{-1}$ [116]. For instance, the observations of the first millisecond pulsar discovered, B1937+21, after 9 year of data, give a period of $1.557\,806\,468\,819\,794\,5 \pm 0.000\,000\,000\,000\,000\,4\,{\rm msec}$, which is comparable to the accuracy of atomic clocks.

One can take advantage of the stability of pulsars to test general relativity. From the observation of the change in the revolution period of B1931+16 (Hulse-Taylar binary pulsar), general relativity has been tested at a level of 1%, and the indirect evidence

[2] For adiabatic initial conditions, a limit at 95 % C.L. of $h_0^2\Omega_{\rm gw}(f) \leq 4.0 \times 10^{-5}$ is obtained.

of the existence of GWs has been obtained [3, 4]. Such highly accurate clocks can also be used for the direct detection of GWs.

4.3.1 Limit from spinning pulsars

Since the period of pulsars is extremely stable, one can detect the influence of gravitational waves on the pulses by monitoring the change of pulse arrival times. In other words, pulsar timing can be regarded as a gravitational-wave detector with a very long arm.

Suppose that pulses are emitted at a pulsar at the time t_0 and received at the Earth at the time t_1, and that a GW is propagating in the direction of z axis with the polarization along x axis. The coordinates is shown in Fig. 4.1, where L is the distance between the Earth and the pulsar, and θ is the angle between the direction of the pulsar from the Earth and the direction the GW propagates. The change of arrival times observed by the observer on the Earth can be written as [117, 118],

$$\frac{\Delta\nu(t_1)}{\nu(t_0)} = -\frac{1}{2}(1-\cos\theta)[h(t_1) - h(t_0 - L\,\cos\theta)]\ ,$$

in frequency shifts, or, equivalently,

$$\Delta t(t_1) = -\frac{1}{2}(1-\cos\theta)\int_0^{L(1+\cos\theta)} h(t_0-\xi)d\xi\ ,$$

in time residuals.

The residual times in pulse arrival times are obtained by differentiating between observed arrival times and the arrival times predicted with timing models (for the review, see [116]). The timing model is written in a Taylor-expanded form,

$$\phi(\tau) = \phi_0 + (\tau-\tau_0)\,\Omega_0 + \frac{1}{2}(\tau-\tau_0)^2\,\dot{\Omega}_0 + \dots\ , \tag{4.10}$$

where τ is the proper time of the pulsar, τ_0 is the fiducial time, ϕ_0 is the phase at τ_0, Ω_0 and $\dot{\Omega}_0$ are the pulse period and the derivative at τ_0. The proper time τ in Eq. (4.10) is related to the time on the Earth by including various corrections on the light path from the pulsar to the Earth: relativistic effects in the solar system and around the pulsar, revolution and peculiar motions of the Earth, dispersion measures, etc.. In addition, the timing model has plural parameters intrinsic to an individual pulsar, such as pulsar's pulse frequency, its first derivative, astrometric, and binary parameters. These parameters are fitted so that the residual times have a zero-mean Gaussian distribution after subtracting the predicted arrival times from the observed one. If a systematic error is found in the residual, it will be the contributions from GWs.

Denoting errors in the pulse arrival time ϵ and observation time T, one can estimate the sensitivity to GWs as

$$h_c(f_*) \sim \frac{\epsilon}{T} \sim \epsilon f_*\ ,$$

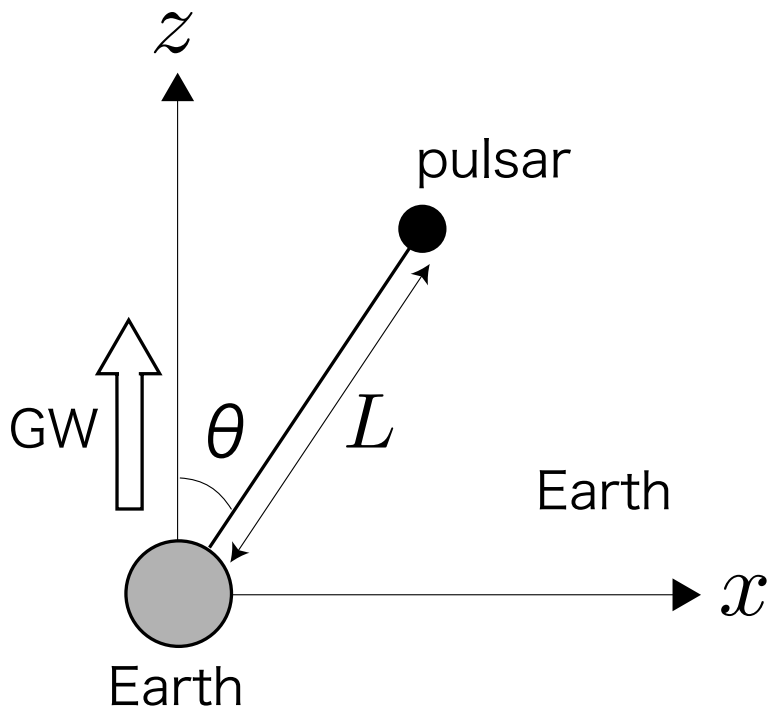

Figure 4.1: Doppler tracking.

where f_* is the frequency given by the observation time. If no GW signal would find in the residual data, the limit on h_c is translated to the limit on $\Omega_{\rm gw}$ according to Eq. (2.30). More detailed analysis of 7 years data of PSR B1855+09 by Kaspi et al. [119] gives

$$h_0^2\Omega_{\rm gw}(f_*) < 6 \times 10^{-8}, \qquad (95\%\,\text{C.L.})\ ,$$

where $f_* = 1/7\text{yr} \approx 4.5 \times 10^{-9}\,\text{Hz}$. Since $h_c \propto T^{-1} \propto f$ and $h_0^2\Omega_{\rm gw} \propto f^2 h_c^2$, the limit on $h_0^2\Omega_{\rm gw}$ for $f > f_*$ is

$$h_0^2\Omega_{\rm gw}(f) < 6 \times 10^{-8} \left(\frac{f}{f_*}\right)^4, \qquad (95\%\,\text{C.L.})\ .$$

No constraint can be obtained for $f < f_*$, because the systematic residuals are removed by the parameter fitting.

Although the above limit results from the time residual of a single millisecond pulsar, combining multiple pulsars provides us a powerful method that can remove systematic errors, because the time residuals of the pulsars include identical noise sources due to proper motion of the Earth, systematic errors of clocks, etc., and they are correlated. Recent discovery of multiple millisecond pulsars allows such an analysis. Consequently, the sensitivity to a GWB can also be improved.

More stringent limit will be placed soon by Parkes Pulsar Timing Array (PPTA) project [120], which started in February 2004 as a collaborative effort between the ATNF, Swinburne University of Technology, the University of Brownsville, Texas. The project aims to observe 20 millisecond pulsars with an RMS timing residual of 100 nsec

over 5 years. According to Hobbs [120], the limit on a GWB of $h_0^2\Omega_{\rm gw} < 5 \times 10^{-10}$ can be achieved after the 5 year observation. In the future, the Square-Kilometre-Array (SKA) [121] is planned by an international collaboration. SKA will be a radio telescope with a collecting area that will exceed that of existing telescopes by a factor of a hundred or so. Due to its outstanding sensitivity, sky and frequency coverage, SKA will discover about 20,000 pulsars in our galaxy, including more than 1,000 millisecond pulsars. Therefore, the sensitivity to a GWB of $h_0^2\Omega_{\rm gw} \lesssim 3 \times 10^{-13}$ would be reached [121].

Recently, a technique to detect GWB by looking for correlations between pulsar observations was developed by Jenet et al. [122], and they found a slightly different limit on a GWB with almost the same data set as the previous studies. Using the data set with data spans $\sim 20\,\mathrm{yr}$ for PSR B1855+09 and $\sim 2-4\,\mathrm{yr}$ for seven other pulsars, they obtained the limits on $h_0^2\Omega_{\rm gw}$ with flat spectrum [123],

$$h_0^2\Omega_{\rm gw}(f) < 2.0 \times 10^{-8} \ ,$$

at the frequencies $1/1\,\mathrm{yr}$, $1/8\,\mathrm{yr}$, and $1/20\,\mathrm{yr}$. The threshold of the detection is defined so that detection rate is 95% and false alarm rate is 0.1%. If the full observation data of PPTA (20 millisecond pulsars with an RMS timing residual of 100 nsec over 5 years) will be available, the limit will be $h_0^2\Omega_{\rm gw}(f) < 9.1 \times 10^{-11}$ at the frequencies $1/1\,\mathrm{yr}$, $1/8\,\mathrm{yr}$, and $1/20\,\mathrm{yr}$.

4.3.2 Limit from binary pulsars

Another important limit comes from pulsars in binary systems. The orbit of binary pulsars is predicted by the general relativity and is well agreed with observations [3, 4]. So, it can be used as another clock. In most cases, the first derivative of the period $\dot{P}$ is negligibly small and no fitting to unknown parameters is needed. This fact allows us to constrain GWB at lower frequencies than $1/T$ by monitoring the gradual change of the orbital period. Lower end of frequencies the limit can be obtained is $f = 1/D$, where D is distance to the pulsar. The detailed analysis of PSR B1855+09 [124] gives the limit

$$h_0^2\Omega_{\rm gw} < 2.7 \times 10^{-4} \qquad \text{at } \ 1.1 \times 10^{-11}\,\mathrm{Hz} < f < 4.5 \times 10^{-9}\,\mathrm{Hz} \ .$$

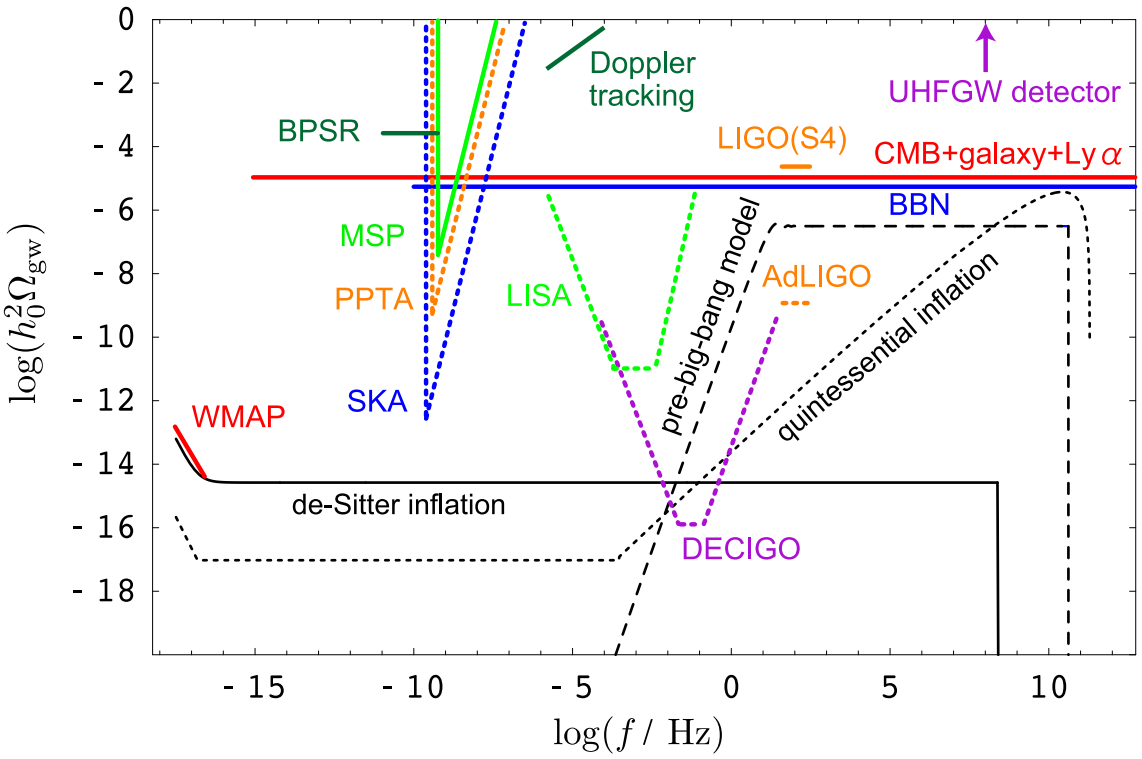

Figure 4.2: Observational constraints on a GWB and the predicted spectra of stochastic GWBs. The observational constraints denote already obtained limits with solid lines and future limits with dotted lines. The GWB spectra are due to the de-Sitter inflation ($H = 2.7 \times 10^{-5}\,M_{\rm Pl}$), the quintessential inflation ($g_s(\tau_0) = 3.91$, $g_s(\tau_{th}) = 106.75$, $\lambda = 10^{-14}$, $R = 0.15$), and the pre-big-bang model ($\mu = 1.5$, $f_s = 10\,{\rm Hz}$). The limits come from the big-bang nucleosynthesis (BBN), WMAP, CMB+galaxy+Lyα, the binary pulsar (BPSR), the millisecond pulsar (MSP), the pulsar timing array (PPTA), and the square kilometre array (SKA), which are all explained in this chapter. There is also shown the limit by a spacecraft Doppler tracking (Cassini) [125], the ground-based GW detector (LIGO and advanced LIGO), the space-based GW detector (LISA and DECIGO) [126], and the ultra-high frequency GW detectors [50]. The LIGO bound and the sensitivity of advanced LIGO is described in Sec. 5.3.

Chapter 5

Direct search for GWB

5.1 Correlation analysis

Let us consider the outputs of a detector, $s(t) = h(t) + n(t)$, where $h(t)$ and $n(t)$ are the GW signal and the noise of a detector. From Eq. (2.23), at generic point $\vec{\mathbf{X}}$, the gravitational metric perturbations in the transverse traceless gauge are given by

$$\mathbf{h}(t, \vec{\mathbf{X}}) = \sum_A \int_{S^2} d\hat{\mathbf{\Omega}} \int_{-\infty}^{\infty} df\, \tilde{h}_A(f, \hat{\mathbf{\Omega}})\, e^{2\pi i f(t - \hat{\mathbf{\Omega}}\cdot\vec{\mathbf{X}}/c)}\, \mathbf{e}_A(\hat{\mathbf{\Omega}})\,, \tag{5.1}$$

where $\hat{\mathbf{\Omega}}$ is a unit vector directed at GW propagation and $\tilde{h}_A(f, \hat{\mathbf{\Omega}})$ is the Fourier transform of GW amplitude with polarizations $A = +, \times$. Polarizarion tensors $\mathbf{e}_A(\hat{\mathbf{\Omega}})$ are defined in Eq. (2.24).

GW signal $h(t)$ from a detector is given by $\mathbf{D}(f, \hat{\mathbf{\Omega}}) : \mathbf{h}(f, \hat{\mathbf{\Omega}})$, where the symbol : denotes contraction between tensors, and $\mathbf{D}(f, \hat{\mathbf{\Omega}})$ is a so-called detector tensor, which describes the total response of a detector and maps the gravitational metric perturbation to the GW signal from a detector. We define it including detector response functions as

$$\mathbf{D}(f, \hat{\mathbf{\Omega}}) \equiv \frac{1}{2}\left[(\hat{\mathbf{u}} \otimes \hat{\mathbf{u}})\mathcal{T}(f, \hat{\mathbf{\Omega}}\cdot\hat{\mathbf{u}}) - (\hat{\mathbf{v}} \otimes \hat{\mathbf{v}})\mathcal{T}(f, \hat{\mathbf{\Omega}}\cdot\hat{\mathbf{v}})\right]\,. \tag{5.2}$$

Here $\hat{\mathbf{u}}$ and $\hat{\mathbf{v}}$ are unit vectors. We assume that they are orthogonal to each other and are directed to each detector arm. The function $\mathcal{T}$ is a detector response function that describes the effect of finite arm length on propagating light. In the detector whose arm length is much smaller than the wavelength of GW, that is, in low frequency limit, this function is approximated to unity, while in a detector whose size is comparable to GW wavelength, the function significantly affects the response of the detector. This is true for a synchronous recycling interferometer at ultra-high frequencies, which we will investigate in Chap. 6.

Using Eqs. (5.1) and (5.2), GW signal $h(t)$ can be written as

$$h(t, \vec{\mathbf{X}}) = \sum_A \int_{S^2} d\hat{\mathbf{\Omega}} \int_{-\infty}^{\infty} df\, \tilde{h}_A(f, \hat{\mathbf{\Omega}})\, e^{2\pi i f(t - \hat{\mathbf{\Omega}}\cdot\vec{\mathbf{X}}/c)} F_A(f, \hat{\mathbf{\Omega}})\,, \tag{5.3}$$

where an angular pattern function of a detector $F_p(f, \hat{\mathbf{\Omega}})$ is defined by

$$F_A(f, \hat{\mathbf{\Omega}}) \equiv \mathbf{D}(f, \hat{\mathbf{\Omega}}) : \mathbf{e}_A(\hat{\mathbf{\Omega}}) \,. \tag{5.4}$$

Cross-correlation signal Y between two detectors is defined as

$$Y \equiv \int_{-T/2}^{T/2} dt \int_{-T/2}^{T/2} dt' \, s_1(t) s_2(t') Q(t - t') \,, \tag{5.5}$$

where s_1 and s_2 are an output from each detector, T is observation time. $Q(t-t')$ is an arbitrary real function, which is called an optimal filter. Its form is determined below so that signal-to-noise ratio (SNR) is maximized. Fourier transforming $s_1(t)$ and $s_2(t)$, one can obtain

$$Y = \int_{-\infty}^{\infty} df \int_{-\infty}^{\infty} df' \delta_T(f - f') \tilde{s}_1^*(f) \tilde{s}_2(f') \tilde{Q}(f'), \tag{5.6}$$

where $\tilde{s}_1(f)$, $\tilde{s}_2(f)$ and $\tilde{Q}(f)$ are the Fourier transforms of $s_1(t)$, $s_2(t)$ and $Q(t - t')$, respectively. $\delta_T(f)$ is the finite-time approximation to the Dirac delta function defined by

$$\delta_T(f) \equiv \int_{-T/2}^{T/2} dt \, e^{-2\pi i f t} = \frac{\sin(\pi f T)}{\pi f} \,.$$

In the above derivation, we took the limit of large T for one of the integrals. This is justified by the fact that, in general, $Q(t - t')$ rapidly decreases for large $|t - t'|$. The correlation signal obtained above ideally has a contribution from only the GW signal since we assume that noise has no correlation between two detectors. Thus, we take ensemble average of Eq. (5.6) and obtain the signal from GWB,

$$\mu \equiv \langle Y \rangle = \int_{-\infty}^{\infty} df \int_{-\infty}^{\infty} df' \delta_T(f - f') \langle \tilde{h}_1^*(f) \tilde{h}_2(f') \rangle \tilde{Q}(f') \,. \tag{5.7}$$

Substituting the Fourier transform of Eq. (5.3),

$$\tilde{h}(f) = \sum_A \int_{S^2} d\hat{\mathbf{\Omega}} \, \tilde{h}_A(f, \hat{\mathbf{\Omega}}) e^{-2\pi i f \hat{\mathbf{\Omega}} \cdot \vec{\mathbf{X}}/c} F^A(f, \hat{\mathbf{\Omega}}) \,, \tag{5.8}$$

into Eq. (5.7), and using Eqs. (2.25) and (2.27), one can obtain

$$\mu = \frac{3H_0^2}{20\pi^2} T \int_{-\infty}^{\infty} df |f|^{-3} \Omega_{\rm gw}(|f|) \, \gamma(|f|) \, \tilde{Q}(f). \tag{5.9}$$

Here we defined the overlap reduction function,

$$\gamma(f) \equiv \frac{1}{(2/5)} \sum_A \int_{S^2} \frac{d\hat{\mathbf{\Omega}}}{4\pi} \, e^{2\pi i f \hat{\mathbf{\Omega}} \cdot \Delta \vec{\mathbf{X}}/c} F_1^{A\,*}(f, \hat{\mathbf{\Omega}}) F_2^A(f, \hat{\mathbf{\Omega}}) \,, \tag{5.10}$$

where the separation of two detectors is $\Delta \vec{\mathbf{X}} \equiv \vec{\mathbf{X}}_1 - \vec{\mathbf{X}}_2$. The factor in a right-hand side of Eq. (5.10) is a normalization factor so that the overlap reduction function gives unity in low frequency limit.

This definition is slightly different from that in other papers [51, 7], because the detector response function $\mathcal{T}$ is included in Eq. (5.2). In low frequency limit, $\mathcal{T}$ gives unity, and the definition of Eq. (5.10) coincides with the equation in [51, 7]. The overlap reduction function is defined as meaning how GW signals in two detectors are correlated, and equals unity for colocated and coaligned detectors. However, the difference is conspicuous at high frequencies. The overlap reduction function does not give unity even for colocated and coaligned detector. Namely, the loss of GW signals of detectors can be regarded as the reduction of overlap between two detectors. We will return to this issue in Chap. 6 and investigate in detail. In this chapter, we will treat detectors that GW wavelength is much larger than the size of the detectors and can set the detector response function $\mathcal{T} = 1$.

Next, we will calculate the variance of a correlation signal. Here we assume that noises in two detectors do not correlate at all and that the magnitude of GW signal is much smaller than that of noise. Consequently, the variance of correlation signal is

$$\sigma^2 \equiv \langle Y^2 \rangle - \langle Y \rangle^2 \approx \langle Y^2 \rangle \,. \tag{5.11}$$

Then, using Eq. (5.6), it follows

$$\begin{aligned} \sigma^2 &\approx \int_{-\infty}^{\infty} df \int_{-\infty}^{\infty} df' \, \tilde{Q}(f)\tilde{Q}^*(f') \, \langle \tilde{s}_1^*(f)\tilde{s}_1(f') \rangle \, \langle \tilde{s}_2(f)\tilde{s}_2^*(f') \rangle \\ &\approx \frac{T}{4} \int_{-\infty}^{\infty} df \, P_1(|f|)P_2(|f|) \, |\tilde{Q}(f)|^2 \,, \end{aligned} \tag{5.12}$$

where the one-sided power spectrum density of noise is defined by

$$\langle \tilde{n}_i^*(f)\tilde{n}_i(f') \rangle \equiv \frac{1}{2}\delta(f - f')P_i(f), \qquad i = 1, 2 \,.$$

Now we can determine the form of the optimal filter $\tilde{Q}(f)$. Equations (5.9) and (5.12) are expressed more simply, using an inner product

$$(A, B) \equiv \int_{-\infty}^{\infty} df A^*(f)B(f)P_1(|f|)P_2(|f|) \,,$$

as

$$\mu = \frac{3H_0^2}{20\pi^2} T \left(\tilde{Q}, \frac{\gamma(|f|)\Omega_{\rm gw}(|f|)}{|f|^3 P_1(|f|)P_2(|f|)} \right) \,, \tag{5.13}$$

$$\sigma^2 \approx \frac{T}{4} \left(\tilde{Q}, \tilde{Q} \right) \,. \tag{5.14}$$

From Eqs. (5.13) and (5.14), SNR for GWB is defined as $\mathrm{SNR} \equiv \mu/\sigma$. Therefore, the optimal filter function turns out to be

$$\tilde{Q}(f) = K \, \frac{\gamma(f)\Omega_{\rm gw}(|f|)}{|f|^3 P_1(|f|)P_2(|f|)}, \tag{5.15}$$

with an arbitrary normalization factor K. Applying this optimal filter to the above equations, we obtain maximal SNR

$$\mathrm{SNR} = \frac{3H_0^2}{10\pi^2} \sqrt{T} \left[\int_{-\infty}^{\infty} df \frac{\gamma^2(|f|)\Omega_{\rm gw}^2(|f|)}{f^6 P_1(|f|)P_2(|f|)} \right]^{1/2} \,. \tag{5.16}$$

5.2 Overlap reduction functions

5.2.1 Tensorial expansion

The overlap reduction functions can be analytically investigated by expanding them in tensorial bases and carrying out the angular integral with respect to the propagating direction of GWs [127, 51].

For real detectors on the Earth such as LIGO etc., the wavelength of GWs is much larger than the size of detector. In this case, the angular pattern function defined in Eq. (5.4) does not depend on frequencies, and is simply given by

$$F_A(\hat{\mathbf{\Omega}}) = \mathbf{D}(\hat{\mathbf{\Omega}}) : \mathbf{e}_A(\hat{\mathbf{\Omega}}) \,, \tag{5.17}$$

$$\mathbf{D}(\hat{\mathbf{\Omega}}) = \frac{1}{2}\left[\hat{\mathbf{u}} \otimes \hat{\mathbf{u}} - \hat{\mathbf{v}} \otimes \hat{\mathbf{v}}\right] \,. \tag{5.18}$$

Then, a non-normalized overlap reduction function $\bar{\gamma}$ for a colocated and coaligned detector pair (ideal case) is given by

$$\bar{\gamma}_{\rm ideal} \equiv \sum_A \int_{S^2} \frac{d\hat{\mathbf{\Omega}}}{4\pi} F_{A\,*}(\hat{\mathbf{\Omega}}) F_A(\hat{\mathbf{\Omega}}) = \frac{2}{5} \,, \tag{5.19}$$

which is exactly the same as the normalization factor appearing in Eq. (5.10). Defining

$$\Delta\vec{X} = \vec{X}_1 - \vec{X}_2 \equiv |\Delta\vec{X}|\hat{d} \,,$$
$$\alpha(f) \equiv \frac{2\pi f|\Delta\vec{X}|}{c} \,,$$

and

$$\Gamma_{ijk\ell}(\alpha, \hat{d}\,) \equiv \frac{1}{\bar{\gamma}_{\rm ideal}} \sum_A \int_{S^2} \frac{d\hat{\Omega}}{4\pi}\, e^{i\alpha\hat{\Omega}\cdot\hat{d}}\, \tilde{e}^A_{ij}(\hat{\Omega}) \tilde{e}^A_{k\ell}(\hat{\Omega}) \,, \tag{5.20}$$

one can write the overlap reduction function as

$$\gamma(f) = D^{ij} D^{k\ell} \Gamma_{ijk\ell}(\alpha, \hat{d}\,) \,. \tag{5.21}$$

Note that $\Gamma_{ijk\ell}$ satisfies the symmetric properties,

$$\Gamma_{ijk\ell} = \Gamma_{jik\ell} \,, \qquad \Gamma_{ijk\ell} = \Gamma_{ij\ell k} \,, \qquad \Gamma_{ijk\ell} = \Gamma_{k\ell ij} \,.$$

Consequently, thank to the symmetries, $\Gamma_{ijk\ell}$ can be expanded in tensorial bases like

$$\begin{aligned}\Gamma_{ijk\ell}(\alpha, \hat{d}\,) &= C_1(\alpha)\delta_{ij}\delta_{k\ell} + C_2(\alpha)(\delta_{ik}\delta_{j\ell} + \delta_{jk}\delta_{i\ell}) + C_3(\alpha)(\delta_{ij}\hat{d}_k\hat{d}_\ell + \delta_{k\ell}\hat{d}_i\hat{d}_j) \\ &= C_4(\alpha)(\delta_{ik}\hat{d}_j\hat{d}_\ell + \delta_{i\ell}\hat{d}_j\hat{d}_k + \delta_{jk}\hat{d}_i\hat{d}_\ell + \delta_{j\ell}\hat{d}_i\hat{d}_k) + C_5(\alpha)\hat{d}_i\hat{d}_j\hat{d}_k\hat{d}_\ell \,.\end{aligned} \tag{5.22}$$

Here we define the contracted quantities of $\Gamma_{ijk\ell}$ with the tensorial bases.

$$\begin{aligned} q_1 &\equiv \Gamma_{ijk\ell}\delta^{ij}\delta^{k\ell}, \quad q_2 \equiv \Gamma_{ijk\ell}(\delta^{ik}\delta^{j\ell} + \delta^{jk}\delta^{i\ell}) \,, \quad q_3 \equiv \Gamma_{ijk\ell}(\delta^{ij}\hat{d}^k\hat{d}^\ell + \delta^{k\ell}\hat{d}^i\hat{d}^j) \,, \\ q_4 &\equiv \Gamma_{ijk\ell}(\delta^{ik}\hat{d}^j\hat{d}^\ell + \delta^{i\ell}\hat{d}^j\hat{d}^k + \delta^{jk}\hat{d}^i\hat{d}^\ell + \delta^{j\ell}\hat{d}^i\hat{d}^k) \,, \quad q_5 \equiv \Gamma_{ijk\ell}\hat{d}^i\hat{d}^j\hat{d}^k\hat{d}^\ell \,, \end{aligned} \tag{5.23}$$

Then, from Eqs. (5.22) and (5.23), the contractions $q_1, \cdots, q_5$ can be related to the coefficients $C_1, \cdots, C_5$ by

$$\begin{pmatrix} q_1 \\ q_2 \\ q_3 \\ q_4 \\ q_5 \end{pmatrix} = \begin{pmatrix} 9 & 6 & 6 & 4 & 1 \\ 6 & 24 & 4 & 16 & 2 \\ 6 & 4 & 8 & 8 & 2 \\ 4 & 16 & 8 & 24 & 4 \\ 1 & 2 & 2 & 4 & 1 \end{pmatrix} \begin{pmatrix} C_1 \\ C_2 \\ C_3 \\ C_4 \\ C_5 \end{pmatrix} ,$$

or, conversely,

$$\begin{pmatrix} C_1 \\ C_2 \\ C_3 \\ C_4 \\ C_5 \end{pmatrix} = \frac{1}{8} \begin{pmatrix} 3 & -1 & -3 & 1 & 1 \\ -1 & 1 & 1 & -1 & 1 \\ -3 & 1 & 5 & -1 & -5 \\ 1 & -1 & -1 & 2 & -5 \\ 1 & 1 & -5 & -5 & 35 \end{pmatrix} \begin{pmatrix} q_1 \\ q_2 \\ q_3 \\ q_4 \\ q_5 \end{pmatrix} . \tag{5.24}$$

On the other hand, $q_1, \cdots, q_5$ can be calculated explicitly from Eq. (5.20), by integrating with respect to the propagation direction of GWs over the celestial sphere. Formulae of spherical Bessel functions $j_n(x)$ needed for the calculation are provided in the Appendix B. The results are

$$q_1 = 0 , \qquad q_2 = 20 j_0(\alpha) , \qquad q_3 = 0 , \qquad q_4 = 40 \frac{j_1(\alpha)}{\alpha} , \qquad q_5 = 20 \frac{j_2(\alpha)}{\alpha^2} ,$$

and Eq. (5.24) can be reduced to

$$\begin{pmatrix} C_1 \\ C_2 \\ C_3 \\ C_4 \\ C_5 \end{pmatrix} = \frac{1}{42} \begin{pmatrix} -28 & 80 & 3 \\ 42 & -60 & 3 \\ 0 & -120 & -15 \\ 0 & 90 & -15 \\ 0 & 0 & 105 \end{pmatrix} \begin{pmatrix} j_0 \\ j_2 \\ j_4 \end{pmatrix} .$$

From Eqs. (5.21) and (5.22) together with the traceless property of D_{ij}, the overlap reduction function can be written as

$$\gamma(f) = \rho_1(\alpha) D^{ij} D_{ij} + \rho_2(\alpha) D^i{}_k D^{kj} d_i d_j + \rho_3(\alpha) D^{ij} D^{k\ell} d_i d_j d_k d_\ell , \tag{5.25}$$

with redefinitions of the coefficients, $\rho_1(\alpha) = 2C_2(\alpha)$, $\rho_2(\alpha) = 4C_4(\alpha)$, and $\rho_3(\alpha) = C_5(\alpha)$. The new coefficients are given by

$$\begin{pmatrix} \rho_1 \\ \rho_2 \\ \rho_3 \end{pmatrix} = \frac{1}{14} \begin{pmatrix} 28 & -40 & 2 \\ 0 & 120 & -20 \\ 0 & 0 & 35 \end{pmatrix} \begin{pmatrix} j_0 \\ j_2 \\ j_4 \end{pmatrix} .$$

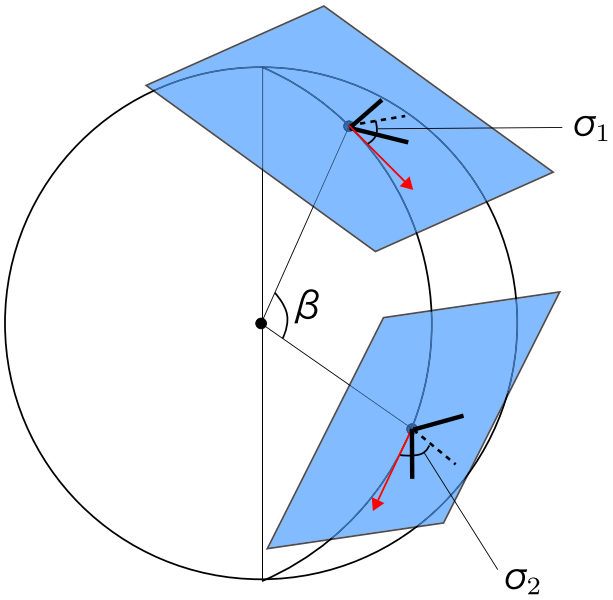

Figure 5.1: Coordinate on the Earth for a detector pair.

5.2.2 Optimal configuration

To further investigate the dependence of the overlap reduction function on the detector configurations, we introduce a coordinate, which simplifies the expression in Eq. (5.25), as shown in Fig. 5.1. The relative location and orientation of two detectors are characterized by the three parameters, $(\beta,\ \sigma_1,\ \sigma_2)$. The β is the separation angle between two detectors measured from the center of the Earth. The angles σ_1 and σ_2, are the orientations of the bisector of two arms of each detector, measured in counterclockwise manner relative to the great circle connecting the two detectors. The distance between two detectors is given by

$$|\Delta\mathbf{X}| = 2R_E \sin\frac{\beta}{2} ,$$

where the radius of the Earth is $R_E = 6371\,\mathrm{km}$. Defining new parameters,

$$\sigma_+ \equiv \frac{\sigma_1 + \sigma_2}{2} , \qquad \sigma_- \equiv \frac{\sigma_1 - \sigma_2}{2} ,$$

one can characterize the overlap reduction function by the three parameters $(\beta,\ \sigma_+,\ \sigma_-)$, which determine a detector configuration. The overlap reduction function is given by

$$\gamma^T(\alpha,\ \beta,\ \sigma_+,\ \sigma_-) = \Theta_{T+}(\alpha,\ \beta)\ \cos(4\sigma_+) + \Theta_{T-}(\alpha,\ \beta)\ \cos(4\sigma_-) , \tag{5.26}$$

together with

$$\begin{aligned}\Theta_{T+}(\alpha,\,\beta) \;\equiv\; & -\left(\frac{3}{8}j_0-\frac{45}{56}j_2+\frac{169}{896}j_4\right)\\ & +\left(\frac{1}{2}j_0-\frac{5}{7}j_2-\frac{27}{224}j_4\right)\cos\beta\\ & -\left(\frac{1}{8}j_0+\frac{5}{56}j_2+\frac{3}{896}j_4\right)\cos 2\beta\,, \qquad (5.27)\\ \Theta_{T-}(\alpha,\,\beta) \;\equiv\; & \left(j_0+\frac{5}{7}j_2+\frac{3}{112}j_4\right)\cos\left(\frac{\beta}{2}\right)^4\,, \qquad (5.28)\end{aligned}$$

Here the super- and sub-script "T" are fixed on the functions in order to distinguish the tensor mode (+ and × modes) from scalar and vector mode, introduced in the later section.

From Eq. (5.26), the candidates for the optimal configuration of the detectors can be classified into two types:

$$\begin{aligned}&\text{Type (i)}: \qquad \cos(4\sigma_+)=\cos(4\sigma_-)=\pm 1\,,\\ &\text{Type (ii)}: \qquad \cos(4\sigma_+)=-\cos(4\sigma_-)=\pm 1\,. \qquad (5.29)\end{aligned}$$

In the type (i), the solutions are $\sigma_1 = 0 \mod \pi$, $\sigma_2 = 0 \mod \pi$ for the plus sign, and $\sigma_1 = \pi/2 \mod \pi$, $\sigma_2 = 0 \mod \pi$ for the minus sign. This means that the great circle connecting two detectors is parallel to the bisector of the two arms of the detector, including the orientations when one of the detectors is rotated by multiples of a right angle. In the type (ii), the solutions are $\sigma_1 = \pi/4 \mod \pi$, $\sigma_2 = -\pi/4 \mod \pi$ for the plus sign, and $\sigma_1 = \pi/4 \mod \pi$, $\sigma_2 = \pi/4 \mod \pi$ for the minus sign. This is the case when the great circle connecting two detectors is parallel to one of the arms of the detectors, including the orientations when one of the detectors is rotated by multiples of a right angle. Therefore, the optimal configurations is implemented when one of the arms of two detectors is parallel or rotated by multiples of 45 degrees, relative to the great circle connecting two detectors. Note that all of the configurations are not simultaneously optimal one, since whether the configuration is optimal or not depends on the signs of the functions Θ_{T+} and Θ_{T-}.

In Fig. 5.2 and Fig. 5.3, the functions Θ_{T+} and Θ_{T-} are plotted as a function of β for a fixed frequency and as a function of frequency for a fixed β (Tensor mode is shown with red, solid curve.). When two detectors are close each other ($\beta \to 0$), or at low frequencies ($f \to 0$), the magnitude of overlap reduction function is maximized.

5.2.3 Overlap reduction functions of realistic detector pairs

The positions and orientations of the ongoing and planed kilometer-size interferometers are listed in Table 5.1. We use a spherical coordinate system ($\theta,\ \phi$) with which the north pole is at $\theta = 0°$, and ϕ represents longitude. The orientation angle ψ is the angle between the local east direction and the bisecting line of two arms of each detector measured counterclockwise. Hereafter we will consider only advanced (the second-generation) detectors: AIGO [35], LCGT [36], advanced LIGO (H1) and LIGO (L1)

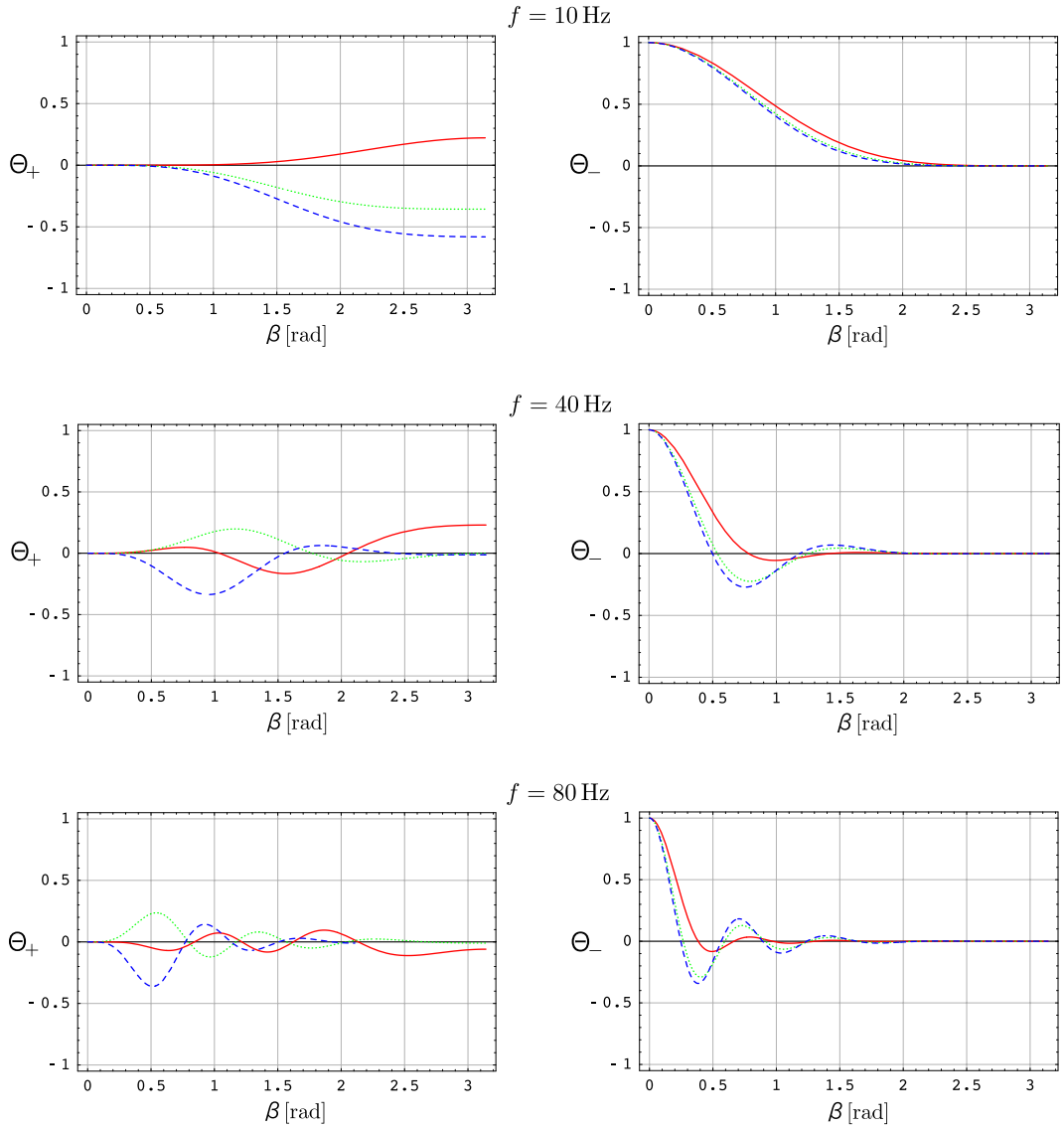

Figure 5.2: Plots of Θ_{M+} and Θ_{M-}, $M = T, V, S$, as a function of β for fixed frequencies: $f = 10\,\mathrm{Hz},\ 40\,\mathrm{Hz},\ 80\,\mathrm{Hz}$. Each curve shows tensor mode (red, solid), vector mode (green, dotted), scalar mode (blue, dashed).

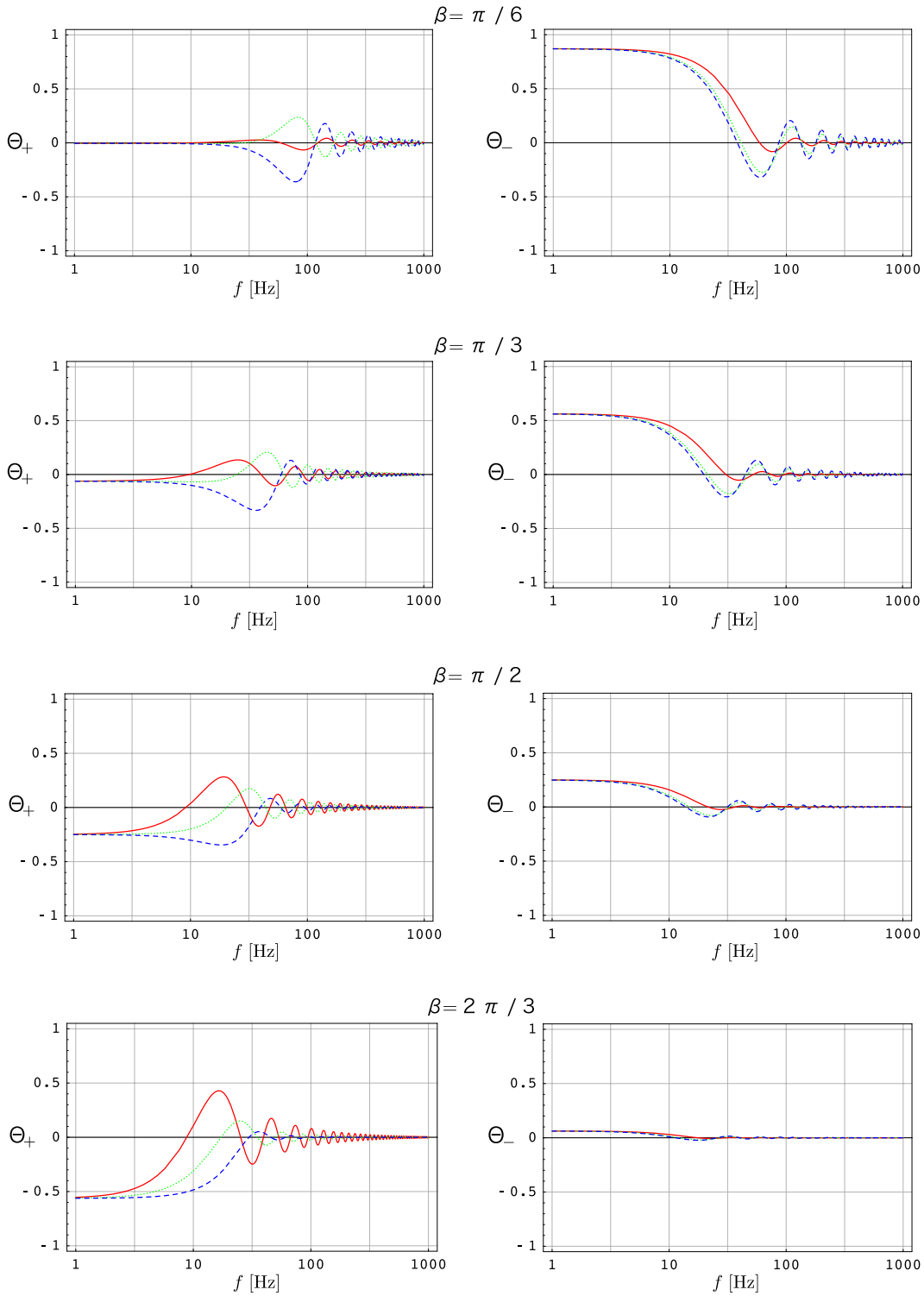

Figure 5.3: Plots of Θ_{M+} and Θ_{M-}, $M = T, V, S$, as a function of frequency for a fixed β: $\beta = \pi/6,\ \pi/3,\ \pi/2,\ 2\pi/3$. Each curve shows tensor mode (red, solid), vector mode (green, dotted), scalar mode (blue, dashed).

[33], advanced VIRGO [34]. The reasons are because the number of pairs including TAMA300 and GEO600 is too much to be presented here, and because the pair with initial-generation interferometer is less sensitive to a GWB and has little opportunity to detect a GWB. From the positions and orientations in Table 5.1, the relative positions and orientations ($\beta,\ \sigma_+,\ \sigma_-$) for each detector pair turn out to be those listed in Table 5.2. The combinations are also illustrated in Fig. 5.4.

Given a parameter set ($\beta,\ \sigma_+,\ \sigma_-$), the overlap reduction function for the detector pair can be calculated. The overlap reduction functions are shown in Fig. 5.5 and Fig. 5.6.

The functions start to oscillate and decay rapidly above the frequency whose wavelength corresponds to the separation between the detectors. The cutoff frequency f_c is given by $f_c \equiv c/(2|\Delta\mathbf{X}|)$, and is listed in Table 5.3. Hence, largely separated detectors are less sensitive to GWB at high frequencies. In addition, the functions approach constant values at low frequencies. This value is completely determined by the relative orientation of the detector pair.

5.3 Observational constraints on GWB by LIGO

LIGO has three power-recycled Michelson interferometers, with a Fabry-Perot cavity in each orthogonal arm. They are located at two sites: Hanford, Washinton, and Livingston, Louisiana. There are two colocated interferometers at Hanford: H1 with 4 km-long arm, and H2 with 2 km-long arm. At Livingston site, there is one interferometer: L1 with 4 km-long arm.

So far, five science runs (S1 - S5) have been done since 2002. S5 has been finished in September, 2007. However, the cross-correlation analysis is proceeding now, and the result has not been published yet. Thus, here we will refer the result of S4, which took place between 2005 February 22 and March 23 [129].

Cross-correlation analysis of S4 data was performed, but no signal of GWB found. Then, the upper limit on the energy density of GWB was obtained. During the S4 run, three interferometers, H1, H2, and L1, were operated, but H1-H2 pair was contaminated by instrumentally correlated noise. On the other hand, the instrumental noises of H1-L1 and H2-L1 pairs will, in general, be uncorrelated, though, in practice, negligible amount of correlated noise within statistically uncertainty exists. Therefore, the constraint on the energy density of GWB comes from the cross-correlated data of H1-L1 and H2-L1 pairs. For a frequency independent spectrum, the upper limit is

$$h_0^2\Omega_{\rm gw} < 3.4 \times 10^{-5}\ , \qquad (90\%\ \text{C.L.})\ ,$$

in the frequency range 51-150 Hz.

In the future, 1-year data of H1 and L1 with goal sensitivity will reach the sensitivity to GWB, $h_0^2\Omega_{\rm gw} \leq 1 \times 10^{-6}$ in the 40-314-Hz band [130], which exceeds the current BBN bound. Moreover, advanced LIGO, which is the updated version of H1 and L1 and whose sensitivity [131] is roughly 10 times better than that of initial LIGO in a broad frequency range, will reach the sensitivity, $h_0^2\Omega_{\rm gw} \leq 2 \times 10^{-9}$.

interferometer	θ	ϕ	ψ
AIGO (A)	121.4	115.7	-45.0
LCGT (C)	53.6	137.3	70.0
LIGO-H1 (H)	43.5	-119.4	171.8
LIGO-L1 (L)	59.4	-90.8	243.0
VIRGO (V)	46.4	10.5	116.5
TAMA300 (T)	54.3	139.5	225.0
GEO600 (G)	47.7	9.8	68.8

Table 5.1: Positions and orientations of kilometer-sized interferometers on the Earth [128]. The figures are in an unit of degree.

detector pair	β	σ_+	σ_-
A - C	70.8	31.4	31.9
A - H	135.6	45.1	53.7
A - L	157.3	2.1	38.0
A - V	121.4	60.8	20.2
C - H	72.4	25.6	89.1
C - L	99.2	68.1	42.4
C - V	86.6	5.6	28.9
H - L	27.2	62.2	45.3
H - V	79.6	55.1	61.1
L - V	76.8	83.1	26.7

Table 5.2: Relative positions and orientations of a detector pair on the Earth. The figures are in an unit of degree. Each detector is represented by initial letters indicated in Table 5.1.

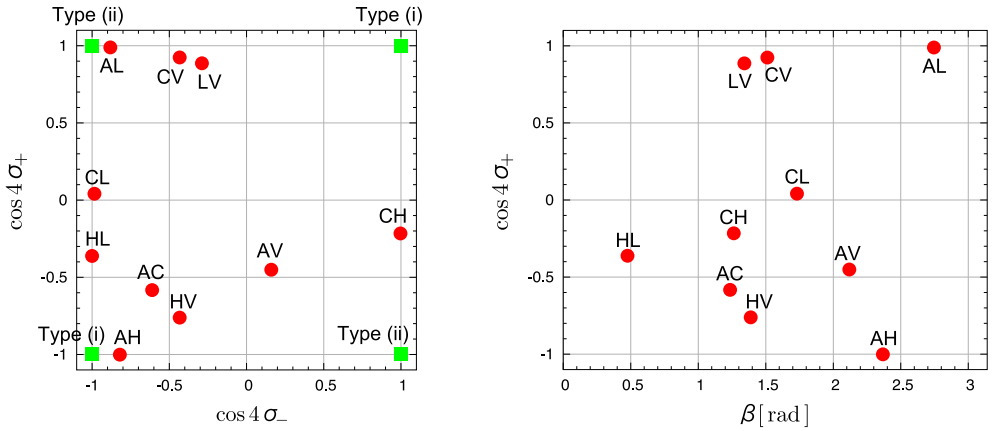

Figure 5.4: Relative positions and orientations of a realistic-detector pair. Left panel shows the combinations $(\cos 4\sigma_-, \cos 4\sigma_+)$. Right panel shows the combinations $(\beta, \cos 4\sigma_+)$. The condidates for the optimal configuration, type (i) and (ii), are also shown in the left panel.

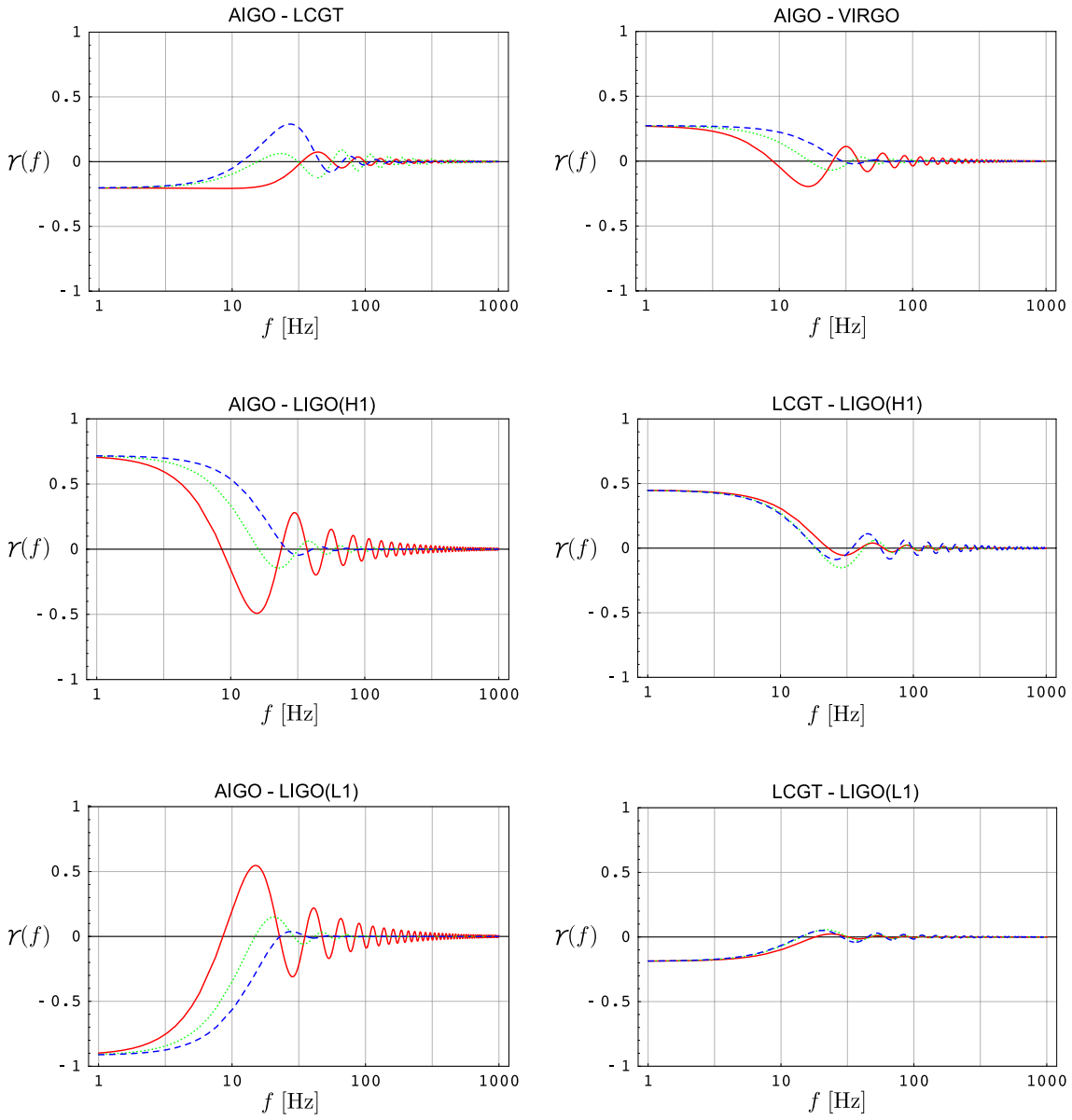

Figure 5.5: Overlap reduction functions for real-detector pairs on the Earth. Each curve shows tensor mode (red, solid), vector mode (green, dotted), scalar mode (blue, dashed).

detector pair	separation [km]	f_c [Hz]
A - C	7377	20
A - H	11796	13
A - L	12493	12
A - V	11113	13
C - H	7522	20
C - L	9707	15
C - V	8735	17
H - L	2996	51
H - V	8156	18
L - V	7912	19

Table 5.3: Separation between two detectors and the cutoff frequency of the overlap reduction function.

5.4 Searching for non-tensorial polarizations of gravitational waves

Recent cosmological observations surprisingly indicate that the expansion of the universe is accelerating [132, 133]. To explain the acceleration, various models are suggested. The models are divided into two classes: modified gravity theories beyond the general relativity, and extra-dimensional models such as brane-world type and Kaluza-Klein type. In these models, extra degrees of freedom of spacetime allows non-tensorial polarization modes of a GW to exist. Since the extra dimensions must be compactified so as not to contradict observations, we cannot directly see them. However, if the GW propagates in the extra dimensions, the GWs projected onto our three-dimensional space can be seen for us as non-tensorial polarization modes, other than plus and cross modes. This is also true for a modified gravity theory. If the modified gravity theory itself contains another degree of freedom such as a coupling with spacetime curvature, there exist non-tensorial polarization modes. Such a GW can be used as a probe for new physics concerning the extra dimensions and the modified gravity theory. In a pulsar timing array, the detectability of the non-tensorial mode is discussed in [134]. However, in a laser-interferometric GW detector, little work can be found.

5.4.1 Non-tensorial polarization mode

In general, it is known that a metric gravity theory in the four dimensional spacetime allows, at most, six polarization modes of a GW [135, 2]. For the GW propagating in z direction, the bases of the six polarizations are defined by (the tensor components

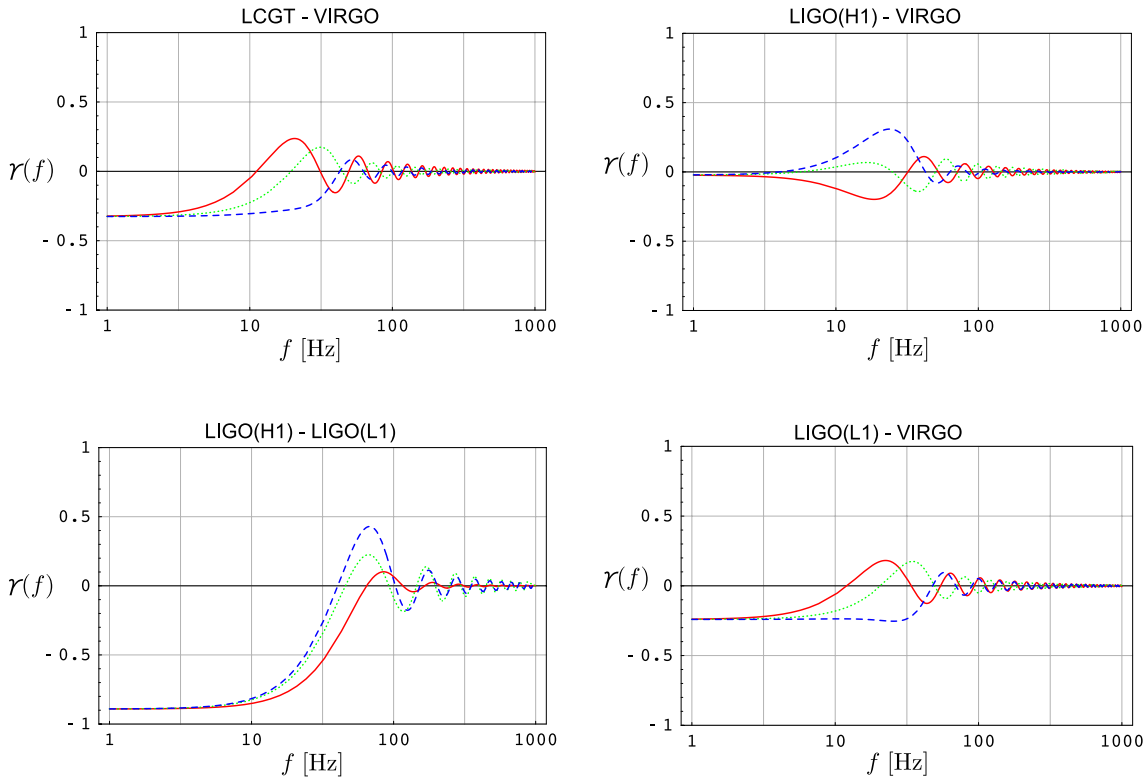

Figure 5.6: Overlap reduction functions for real-detector pairs on the Earth. Each curve shows tensor mode (red, solid), vector mode (green, dotted), scalar mode (blue, dashed).

are x, y, z from the left or the top.),

$$\begin{aligned}
\tilde{e}^{+}_{ij} &= \begin{pmatrix} 1 & 0 & 0 \\ 0 & -1 & 0 \\ 0 & 0 & 0 \end{pmatrix}, \quad \tilde{e}^{\times}_{ij} = \begin{pmatrix} 0 & 1 & 0 \\ 1 & 0 & 0 \\ 0 & 0 & 0 \end{pmatrix}, \quad \tilde{e}^{b}_{ij} = \begin{pmatrix} 1 & 0 & 0 \\ 0 & 1 & 0 \\ 0 & 0 & 0 \end{pmatrix}, \\
\tilde{e}^{x}_{ij} &= \begin{pmatrix} 0 & 0 & 1 \\ 0 & 0 & 0 \\ 1 & 0 & 0 \end{pmatrix}, \quad \tilde{e}^{y}_{ij} = \begin{pmatrix} 0 & 0 & 0 \\ 0 & 0 & 1 \\ 0 & 1 & 0 \end{pmatrix}, \quad \tilde{e}^{\ell}_{ij} = \sqrt{2} \begin{pmatrix} 0 & 0 & 0 \\ 0 & 0 & 0 \\ 0 & 0 & 1 \end{pmatrix},
\end{aligned} \tag{5.30}$$

where, in the first line, $+$, $\times$, and b denote plus, cross, breathing mode, in the second line, x, y, and ℓ denote vector-x, vector-y, longitudinal mode, respectively. The tilde is fixed at each polarization bases like $\tilde{e}$ in order to represent that they are projected polarizations onto our three-dimensional spacetime in a general spacetime with extra dimensions, and are defined in a three-dimensional space. Each polarization mode is orthogonal one another, and is normalized so that $\tilde{e}^{A}_{ij}\tilde{e}^{ij}_{A'} = 2\delta_{AA'}$, $A, A' = +, \times, b, \ell, x, y$. Note that the breathing and longitudinal modes are not traceless. As we will see later, the b and ℓ modes have a scalar-like property, and x and y have a vector-like property. In Fig. 5.7, it is shown how each GW polarization affects the test masses on a circle.

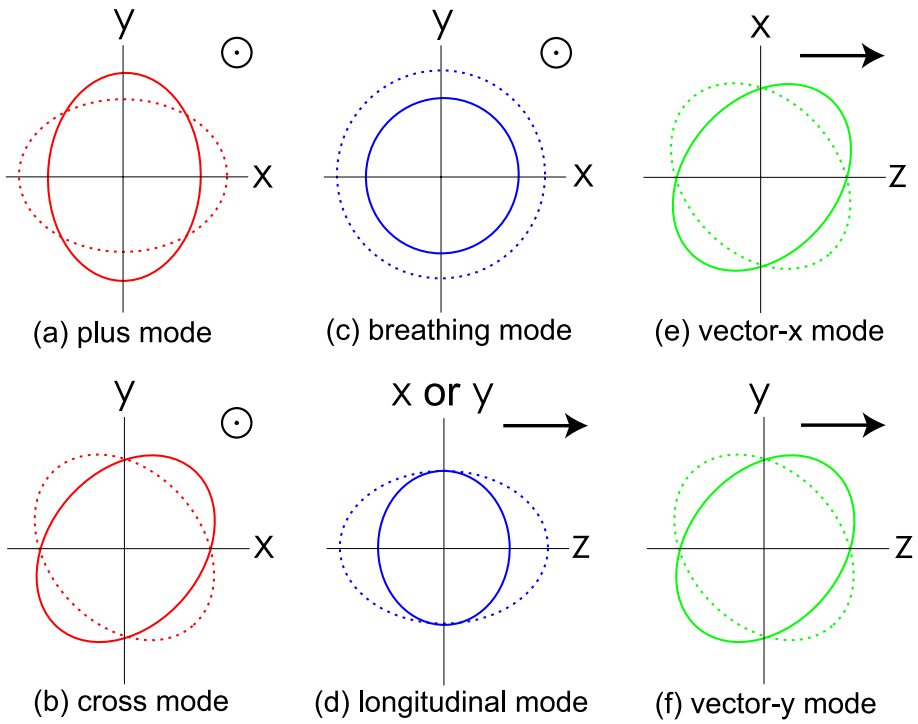

Figure 5.7: Six GW polarizations. Two ellipses show the effect of the GW polarization on the test masses on a circle. The symbol $\odot$ and the arrow represent the propagating direction of a GW.

Which modes appear in several alternative theories is arranged in Table 5.4. As one can see in the Table, the extra scalar polarizations appear more easily than the vector polarizations.

5.4.2 Angular response of a single detector

The metric tensor with perturbations due to GWs is written as

$$\begin{aligned} ds^2 &= -dt^2 + \left[\delta_{ij} + h_{ij}(\omega t - \vec{k}\cdot\vec{x})\right] dx^i dx^j + (\text{extra dim. terms}) \,, \\ h_{ij}(\omega t - \vec{k}\cdot\vec{x}) &= h_+(\omega t - \vec{k}\cdot\vec{x})\tilde{e}^+_{ij} + h_\times(\omega t - \vec{k}\cdot\vec{x})\tilde{e}^\times_{ij} + h_b(\omega t - \vec{k}\cdot\vec{x})\tilde{e}^b_{ij} \\ &\quad + h_\ell(\omega t - \vec{k}\cdot\vec{x})\tilde{e}^\ell_{ij} + h_x(\omega t - \vec{k}\cdot\vec{x})\tilde{e}^x_{ij} + h_y(\omega t - \vec{k}\cdot\vec{x})\tilde{e}^y_{ij} \,, \end{aligned} \tag{5.31}$$

where $h_A, A = +, \times, b, \ell, x, y$ are complex amplitudes of GWs for each mode. In Eq. (5.31), "(Extra dim. terms)" are added only in the theories with extra dimensions. The angular response function of a detector to GWs can be calculated from Eqs. (5.17) and (5.18),

$$F_A(\hat{\mathbf{\Omega}}) = \mathbf{D}(\hat{\mathbf{\Omega}}) : \tilde{\mathbf{e}}_A(\hat{\mathbf{\Omega}}) \,, \qquad \mathbf{D}(\hat{\mathbf{\Omega}}) = \frac{1}{2}\left[\hat{\mathbf{u}}\otimes\hat{\mathbf{u}} - \hat{\mathbf{v}}\otimes\hat{\mathbf{v}}\right] \,, \tag{5.32}$$

theoretical model	$\tilde{e}^{+}_{ij}$	$\tilde{e}^{\times}_{ij}$	$\tilde{e}^{b}_{ij}$	$\tilde{e}^{\ell}_{ij}$	$\tilde{e}^{x}_{ij}$	$\tilde{e}^{y}_{ij}$
GR in pure 5D Minkowski spacetime	◯	◯	◯[1]	◯[1]	◯	◯
GR in pure 6D Minkowski spacetime	◯	◯	◯	◯	◯	◯
5D Kaluza-Klein compactification	◯[2]	◯	◯[2]	—	△[3]	△[3]
RS braneworld	◯	◯	—	—	—	—
DGP braneworld (normal branch)	◯	◯	◯	◯	◯	◯
DGP braneworld (self-accelerating branch)	◯	◯	◯	◯	◯	◯
scalar-tensor theory	◯	◯	◯	◯	—	—
Brans-Dicke theory	◯	◯	◯	◯	—	—
$f(R)$ gravity	◯	◯	◯	◯	—	—
bimetric theory	◯	◯	◯[4]	◯[4]	◯[4]	◯[4]

Table 5.4: GW polarization modes in various theories. The polarization modes in pure Minkowski spacetimes are provided in Appendix D. Reference papers are [136] for the 5D Kaluza-Klein compactification, [137] for the RS braneworld, [138] for the DGP braneworld, [139, 140] for the scalar-tensor theory, [141, 139] for the Brans-Dicke theory, [142, 143] for the $f(R)$ gravity, and [144] for the bimetric theory. [1]In a general five-dimensional spacetime, five degrees of freedom for polarizations are allowed. In general relativity (GR) in pure 5D Minkowski spacetime without the compactification, two scalar modes are correlated and behave as one degree of freedom. [2]The plus and breathing modes are correlated. [3]No vector mode appears in the absence of anisotropy (a vector field) at cosmological scales. [4]Extra polarizations can exist, but, would be much small at high frequencies.

in which it is implicitly assumed that the wavelength of GWs is much larger than the detector size. The absolute response of the detector, of course, depends on h_A. However, given the polarization tensors, the angular response function F_A can be discussed independently on the GW amplitude. We would not like to adhere to a model-dependent search here, though it is important to investigate the prediction and parameter constraint on a theoretical model [1]. So, in this section, we describe only the detectability of the non-tensorial polarization of GWs with a laser-interferometric detector.

Suppose that an orthonormal coordinate in the three-dimensional space for a detector is

$$\begin{cases} \hat{\mathbf{u}} = (1,0,0) \\ \hat{\mathbf{v}} = (0,1,0) \\ \hat{\mathbf{w}} = (0,0,1) \end{cases},$$

and the coordinate rotated by angles (θ, ϕ) for a GW is

$$\begin{cases} \hat{\mathbf{u}}' = (\cos\theta\cos\phi, \cos\theta\sin\phi, -\sin\theta) \\ \hat{\mathbf{v}}' = (-\sin\phi, \cos\phi, 0) \\ \hat{\mathbf{w}}' = (\sin\theta\cos\phi, \sin\theta\sin\phi, \cos\theta) \end{cases}.$$

The most general choice is obtained with the rotation with respect to the angle ψ

[1]We will leave them as future works.

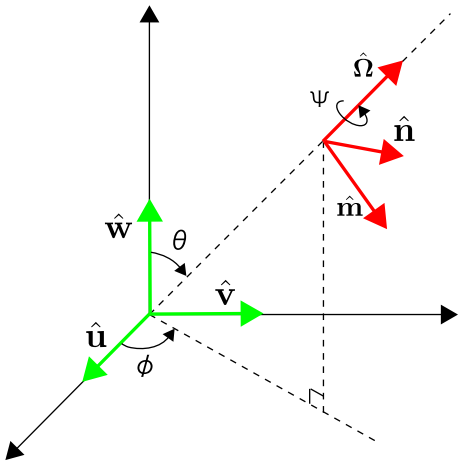

Figure 5.8: Coordinate systems are related by the rotation angles (ϕ, θ, ψ).

around the propagating axis of the GW,

$$\begin{cases} \hat{\mathbf{m}} = \hat{\mathbf{u}}' \cos\psi + \hat{\mathbf{v}}' \sin\psi \\ \hat{\mathbf{n}} = -\hat{\mathbf{v}}' \sin\psi + \hat{\mathbf{u}}' \cos\psi \\ \hat{\mathbf{\Omega}} = \hat{\mathbf{w}}' \end{cases} .$$

The coordinate systems are drawn in Fig. 5.8.

With the coordinate $(\hat{\mathbf{m}}, \hat{\mathbf{n}}, \hat{\mathbf{\Omega}})$, the polarization tensor is

$$\begin{aligned} \tilde{\mathbf{e}}_+ &= \hat{\mathbf{m}} \otimes \hat{\mathbf{m}} - \hat{\mathbf{n}} \otimes \hat{\mathbf{n}} , \\ \tilde{\mathbf{e}}_\times &= \hat{\mathbf{m}} \otimes \hat{\mathbf{n}} + \hat{\mathbf{n}} \otimes \hat{\mathbf{m}} , \\ \tilde{\mathbf{e}}_b &= \hat{\mathbf{m}} \otimes \hat{\mathbf{m}} + \hat{\mathbf{n}} \otimes \hat{\mathbf{n}} , \\ \tilde{\mathbf{e}}_\ell &= \sqrt{2}\, \hat{\mathbf{\Omega}} \otimes \hat{\mathbf{\Omega}} , \\ \tilde{\mathbf{e}}_x &= \hat{\mathbf{m}} \otimes \hat{\mathbf{\Omega}} + \hat{\mathbf{\Omega}} \otimes \hat{\mathbf{m}} , \\ \tilde{\mathbf{e}}_y &= \hat{\mathbf{n}} \otimes \hat{\mathbf{\Omega}} + \hat{\mathbf{\Omega}} \otimes \hat{\mathbf{n}} . \end{aligned}$$

From Eq. (5.32), the angular pattern functions for each polarization result in

$$\begin{aligned} F_+(\theta,\phi,\psi) &= \frac{1}{2}(1+\cos^2\theta)\cos 2\phi \cos 2\psi - \cos\theta \sin 2\phi \sin 2\psi , \\ F_\times(\theta,\phi,\psi) &= -\frac{1}{2}(1+\cos^2\theta)\cos 2\phi \sin 2\psi - \cos\theta \sin 2\phi \cos 2\psi , \\ F_x(\theta,\phi,\psi) &= \sin\theta\,(\cos\theta \cos 2\phi \cos\psi - \sin 2\phi \sin\psi) , \qquad (5.33) \\ F_y(\theta,\phi,\psi) &= -\sin\theta\,(\cos\theta \cos 2\phi \sin\psi + \sin 2\phi \cos\psi) , \qquad (5.34) \end{aligned}$$

$$\begin{aligned} F_b(\theta,\phi) &= -\frac{1}{2}\sin^2\theta \cos 2\phi , \qquad (5.35) \\ F_\ell(\theta,\phi) &= \frac{1}{\sqrt{2}}\sin^2\theta \cos 2\phi . \qquad (5.36) \end{aligned}$$

The ψ dependence indicates that the + and $\times$ modes have a tensor property (spin-2), the x and y modes have a vector property (spin-1), the b and ℓ modes have a scalar property (spin-0). Unfortunately, the angular pattern functions of the breathing and longitudinal modes are completely degenerated, which prohibits to decompose them with a laser-interferometric GW detector (It is also true for a laser-interferometric GW detector with non-orthogonal arms.). In Fig. 5.9, the angular pattern functions for the non-tensorial polarizations are shown. In Fig. 5.10, we also show the angular pattern functions for the tensor, vector, scalar modes. These results are consistent with those obtained by Tobar, Suzuki, Kuroda [145].

5.4.3 Overlap reduction function

Next, we consider not GWs from a point-source but GWB. The reason is that, the GWB has less parameters because of its stochastic nature. The non-Einstein mode in a GW from a point source is a interesting subject that should be studied. However, to decompose the polarizations, one has to identify the source location on the sky, in addition to the six polarizations. Thus, more than eight detectors (for two sky coordinate parameters and six polarizations) are needed for the complete decomposition. On the other hand, in the case of the GWB, there is no preferred direction. In addition, in most of the cosmological scenarios, it is natural to assume that the + and $\times$ modes, or x and y modes are not polarized. Since the number of parameters are less, three detector is enough to decompose the polarization modes (tensor, vector and scalar).

Definitions

Let us define generalized overlap reduction functions for the non-tensorial polarizations. From Eqs. (5.9), (5.10) and (5.19), the cross-correlation signal for the tensor mode can be written as

$$\mu = \frac{3H_0^2}{20\pi^2} T \int_{-\infty}^{\infty} df |f|^{-3} \frac{1}{\bar{\gamma}^T_{\rm ideal}} \sum_{A=+,\times} 2\Omega^A_{\rm gw}(|f|) \bar{\gamma}_A(|f|) \tilde{Q}(f) \ , \tag{5.37}$$

$$\bar{\gamma}_A \equiv \int_{S^2} \frac{d\hat{\mathbf{\Omega}}}{4\pi} e^{2\pi i f \hat{\mathbf{\Omega}}\cdot\Delta\vec{\mathbf{X}}/c} F_1^A F_2^A \ ,$$

where we assume that + and $\times$ modes are not polarized ($\Omega^A_{\rm gw} = \Omega_{\rm gw}/2$), and $\bar{\gamma}_A$ is a non-normalized overlap reduction function for each polarization. We also assume that x and y modes are not polarized. Then, the GWB energy density of tensor, vector, scalar modes can be written as

$$\Omega^T_{\rm gw} \equiv \Omega^+_{\rm gw} + \Omega^\times_{\rm gw} \qquad (\Omega^+_{\rm gw} = \Omega^\times_{\rm gw}) \ , \tag{5.38}$$

$$\Omega^V_{\rm gw} \equiv \Omega^x_{\rm gw} + \Omega^y_{\rm gw} \qquad (\Omega^x_{\rm gw} = \Omega^y_{\rm gw}) \ , \tag{5.39}$$

$$\Omega^S_{\rm gw} \equiv \Omega^b_{\rm gw} + \Omega^\ell_{\rm gw} = \Omega^b_{\rm gw}(1+\kappa) \ . \tag{5.40}$$

where the ratio of the energy density in the longitudinal mode to that in the breathing mode is $\kappa \equiv \Omega^\ell_{\rm gw}/\Omega^b_{\rm gw}$. Using Eqs. (5.33) - (5.36), one can calculate the ideal values

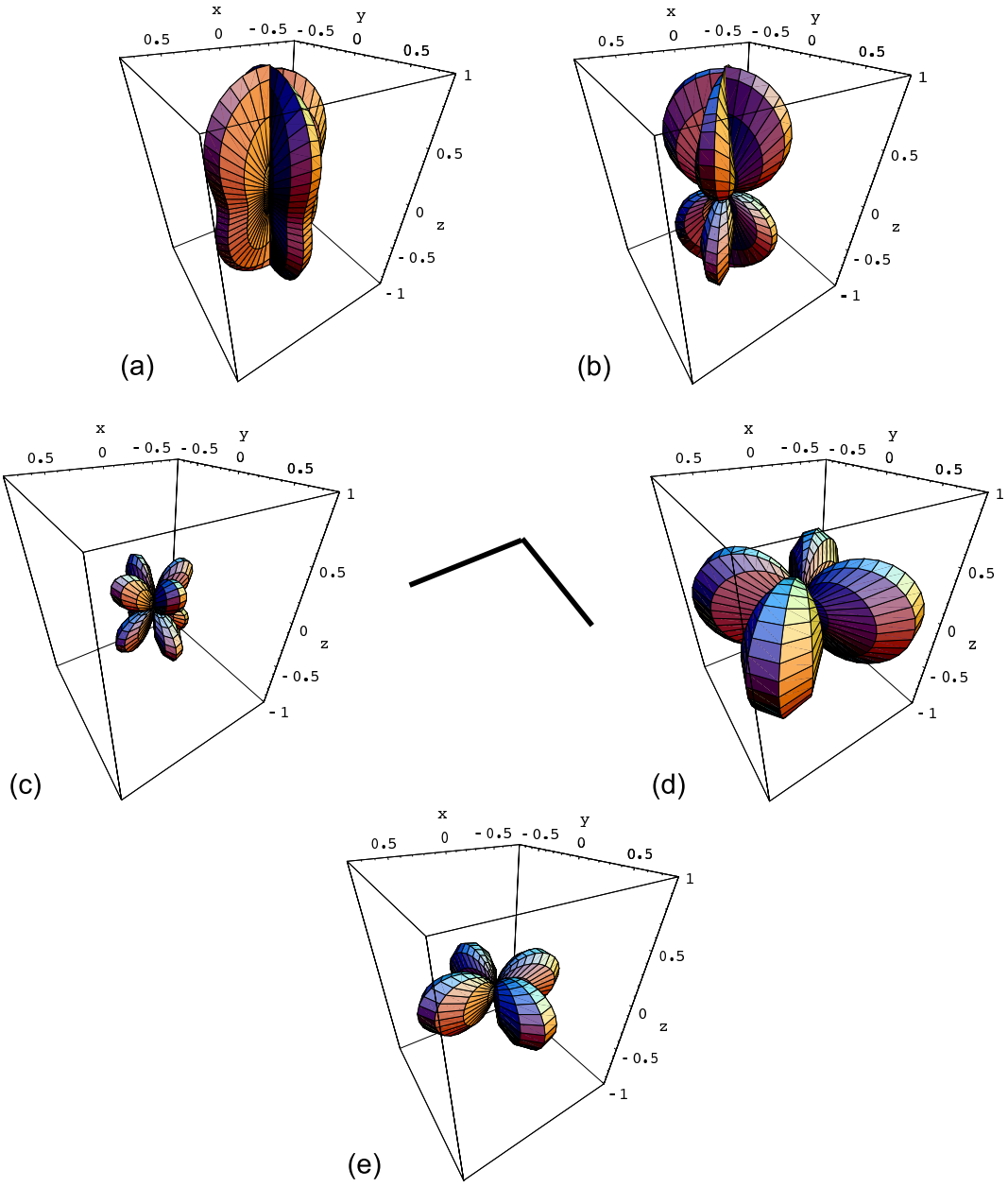

Figure 5.9: Angular pattern functions of a detector for the non-tensorial polarizations. (a) plus mode F_+, (b) cross mode $F_\times$, (c) x mode F_x, (d) y mode F_y, (e) longitudinal mode F_ℓ. The angular pattern function of the breathing mode is the same as that of the longitudinal mode except for an overall factor $1/\sqrt{2}$. At the center of the figure, the arms of an interferometer is shown.

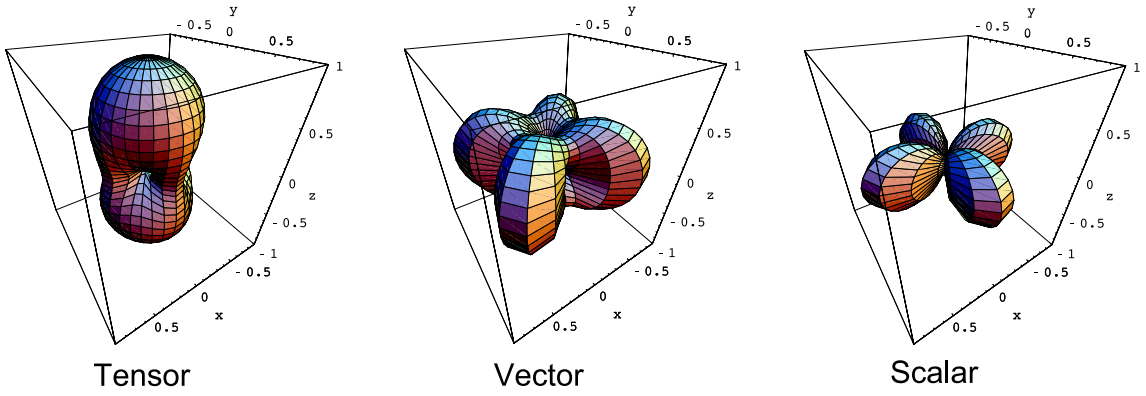

Figure 5.10: Angular pattern functions of a detector for the tensor, vector, scalar modes. Each plot is $\sqrt{F_+^2 + F_\times^2}$, $\sqrt{F_x^2 + F_y^2}$, $\sqrt{F_b^2 + F_\ell^2}$, respectively.

of the non-normalized overlap reduction functions for the non-tensorial polarizations, which gives

$$\begin{aligned}
\bar{\gamma}^T_{\rm ideal} &= \int_{S^2} \frac{d\hat{\mathbf{\Omega}}}{4\pi} (F_+^2 + F_\times^2) = \frac{2}{5} \,, \\
\bar{\gamma}^V_{\rm ideal} &\equiv \int_{S^2} \frac{d\hat{\mathbf{\Omega}}}{4\pi} (F_x^2 + F_y^2) = \frac{2}{5} \,, \\
\bar{\gamma}^S_{\rm ideal} &\equiv \int_{S^2} \frac{d\hat{\mathbf{\Omega}}}{4\pi} (F_b^2 + \kappa F_\ell^2) = \frac{1+2\kappa}{15} \,.
\end{aligned}$$

The first equation for the tensor mode is the same as Eq. (5.19). Then, the generalized overlap reduction functions for the non-tensorial polarizations are defined by

$$\gamma^T_{IJ}(f) = \frac{1}{\bar{\gamma}^T_{\rm ideal}} \int_{S^2} \frac{d\hat{\Omega}}{4\pi} e^{2\pi i f \hat{\Omega}\cdot\Delta\vec{X}/c} (F_I^+ F_J^+ + F_I^\times F_J^\times) \,, \tag{5.41}$$

$$\gamma^V_{IJ}(f) \equiv \frac{1}{\bar{\gamma}^V_{\rm ideal}} \int_{S^2} \frac{d\hat{\Omega}}{4\pi} e^{2\pi i f \hat{\Omega}\cdot\Delta\vec{X}/c} (F_I^x F_J^x + F_I^y F_J^y) \,, \tag{5.42}$$

$$\gamma^S_{IJ}(f) \equiv \frac{1}{\bar{\gamma}^S_{\rm ideal}} \int_{S^2} \frac{d\hat{\Omega}}{4\pi} e^{2\pi i f \hat{\Omega}\cdot\Delta\vec{X}/c} (F_I^b F_J^b + \kappa F_I^\ell F_J^\ell) \,, \tag{5.43}$$

The subscripts I, J represent I-th and J-th detectors, which are fixed for a general case with more than three detectors. The first equation (5.41) for the tensor mode is the same as Eq. (5.10). Here we assumed that gravitons propagate with the speed of light [2].

[2]Strictly speaking, the propagation speed is less than the speed of light if the gravitons are massive. It is true in a spacetime with extra dimensions or in some modified gravity theories. However, the mass is constrained by several observations of the galaxy [146], the solar system [147], and binary pulsars [148]. The limits from the galaxy and the solar system is obtained from the observation in static gravitational fields, while the limit of binary pulsars comes from the change of the orbital period of

Therefore, for generalized case including the non-tensorial polarizations, Eq. (5.37) can be extended as

$$\begin{aligned}
\mu &= \frac{3H_0^2}{20\pi^2}T\int_{-\infty}^{\infty} df|f|^{-3}\frac{1}{\bar{\gamma}^T_{\rm ideal}}\sum_{A=+,\times,x,y,b,\ell} 2\,\Omega^A_{\rm gw}\bar{\gamma}_A\tilde{Q}(f) \\
&= \frac{3H_0^2}{20\pi^2}T\int_{-\infty}^{\infty} df|f|^{-3}\left[\Omega^T_{\rm gw}\gamma^T+\Omega^V_{\rm gw}\gamma^V+\xi\,\Omega^S_{\rm gw}\gamma^S\right]\tilde{Q}(f)\ , \\
\xi &\equiv \frac{1}{3}\left(\frac{1+2\kappa}{1+\kappa}\right)\ ,
\end{aligned}$$

where, in the second line of μ, we used Eqs. (5.38) - (5.40) and (5.41) - (5.43). The parameter ξ is in the range $1/3 \leq \xi \leq 2/3$ and characterizes the ratio of the energy in the longitudinal mode to the breathing mode.

Specific expressions for real detectors on the Earth

The overlap reduction functions for the vector and scalar modes can be analytically expanded by tensor bases, as well as the tensor mode in Sec. 5.2.1. The calculation is parallel with those for the tensor mode. So, here we give only the final results (In Appendix C, the results in the course of the calculation is provided.),

$$\gamma^M_{IJ}(f) = \rho^M_1(\alpha)D^{ij}_I D^J_{ij} + \rho^M_2(\alpha)D^i_{I,\,k}D^{kj}_J d_i d_j + \rho^M_3(\alpha)D^{ij}_I D^{k\ell}_J d_i d_j d_k d_\ell\ , \tag{5.44}$$

with, for the vector mode,

$$\begin{pmatrix}\rho^V_1\\ \rho^V_2\\ \rho^V_3\end{pmatrix} = \frac{2}{7}\begin{pmatrix}7 & 5 & -2\\ 0 & -15 & 20\\ 0 & 0 & -35\end{pmatrix}\begin{pmatrix}j_0\\ j_2\\ j_4\end{pmatrix}\ .$$

and, for the scalar mode,

$$\begin{pmatrix}\rho^S_1\\ \rho^S_2\\ \rho^S_3\end{pmatrix} = \frac{1}{7}\begin{pmatrix}14 & 20 & 6\\ 0 & -60 & -60\\ 0 & 0 & 105\end{pmatrix}\begin{pmatrix}j_0\\ j_2\\ j_4\end{pmatrix}\ . \tag{5.45}$$

The superscript M in Eq. (5.44) denotes the modes $M = V$ (vector), S (scalar). Note that the parameter κ vanishes in the overlap reduction function because F_b and F_ℓ have the same response and γ is normalized. Equation (5.45) agrees with the previous result by Maggiore and Nicolis [149].

---

the binary pulsars (PSR B1913+16 and PSR B1534+12), in dynamical gravitational fields. Finn and Sutton considered energy loss from the binary system by emission of massive gravitons, and obtained the limit on the mass of gravitons, $(m_g/\omega_{\rm orbit})^2 < 0.003$, where $\omega_{\rm orbit}$ is the orbital frequency of the binary. This limit implies

$$\frac{v_g}{c} = \sqrt{1-\left(\frac{m_g}{\omega_{\rm orbit}}\right)^2} \gtrsim 0.998\ ,$$

The gravitons cannot change its speed by more than 0.2% from the speed of light. Thus, setting $v_g = c$ does not affect to cross-correlation analysis qualitatively.

Next, we consider the overlap reduction functions of real detectors on the Earth. The overlap reduction function (5.44) can be simply expressed by introducing the coordinate system on the Earth defined in Sec. 5.2.2, and is given by

$$\begin{aligned}\gamma^V(\alpha,\,\beta,\,\sigma_+,\,\sigma_-) &= \Theta_{V+}(\alpha,\,\beta)\,\cos(4\sigma_+) + \Theta_{V-}(\alpha,\,\beta)\,\cos(4\sigma_-)\,,\\ \gamma^S(\alpha,\,\beta,\,\sigma_+,\,\sigma_-) &= \Theta_{S+}(\alpha,\,\beta)\,\cos(4\sigma_+) + \Theta_{S-}(\alpha,\,\beta)\,\cos(4\sigma_-)\,,\end{aligned}$$

with, for the vector mode,

$$\begin{aligned}\Theta_{V+}(\alpha,\,\beta) \equiv & -\left(\frac{3}{8}j_0 + \frac{45}{112}j_2 - \frac{169}{224}j_4\right)\\ & + \left(\frac{1}{2}j_0 + \frac{5}{14}j_2 + \frac{27}{56}j_4\right)\cos\beta\\ & - \left(\frac{1}{8}j_0 - \frac{5}{112}j_2 - \frac{3}{224}j_4\right)\cos 2\beta\,, \qquad (5.46)\end{aligned}$$

$$\Theta_{V-}(\alpha,\,\beta) \equiv \left(j_0 - \frac{5}{14}j_2 - \frac{3}{28}j_4\right)\cos\left(\frac{\beta}{2}\right)^4\,, \qquad (5.47)$$

and, for the scalar mode,

$$\begin{aligned}\Theta_{S+}(\alpha,\,\beta) \equiv & -\left(\frac{3}{8}j_0 + \frac{45}{56}j_2 + \frac{507}{448}j_4\right)\\ & + \left(\frac{1}{2}j_0 + \frac{5}{7}j_2 - \frac{81}{112}j_4\right)\cos\beta\\ & - \left(\frac{1}{8}j_0 - \frac{5}{56}j_2 + \frac{9}{448}j_4\right)\cos 2\beta\,, \qquad (5.48)\end{aligned}$$

$$\Theta_{S-}(\alpha,\,\beta) \equiv \left(j_0 - \frac{5}{7}j_2 + \frac{9}{56}j_4\right)\cos\left(\frac{\beta}{2}\right)^4\,, \qquad (5.49)$$

Θ_{M+} and Θ_{M-}, $M = V, S$, are plotted as a function of β for fixed frequencies in Fig. 5.2 and as a function of frequency for a fixed β in Fig. 5.3, together with the tensor mode ($M = T$). The difference from the tensor mode appears at about the cutoff frequency of the overlap reduction function. Mathematically, this is because the coefficients of j_0 in Eqs. (5.27) and (5.28) for the tensor mode, Eqs. (5.46) and (5.47) for the vector mode, and Eqs. (5.48) and (5.49) for the scalar mode, are exactly same, and the difference comes from the terms of j_2 and j_4. In other words, at low frequencies where $j_0 \to 1$, $j_2 \to 0$, and $j_4 \to 0$, three modes are degenerated, while, at relatively high frequencies, they behave differently. However, at much higher frequencies, the overlap reduction function decays. Therefore, the most interesting frequency range is around the cutoff frequency, e.g. $\sim 10 - 100\,\mathrm{Hz}$ for detectors on the Earth. The overlap reduction functions for a real ground-based detector pair is plotted in Fig. 5.5 and Fig. 5.6, together with the tensor mode.

5.4.4 Detectability

Considering the overlap reduction functions in the previous section, one can expect to detect the non-Einstein modes as well as the tensor mode. However, the most

important quantity in an observation is a SNR given by integrating with respect to a frequency. In this section, we calculate the SNR for each mode with two detectors, assuming that only one mode exists.

The SNR can be calculated by using the formula defined in Eq. (5.16),

$$\mathrm{SNR} = \frac{3H_0^2}{10\pi^2}\sqrt{T}\left[2\int_0^\infty df\,\frac{\gamma^2(f)\Omega_{\rm gw}^2(f)}{f^6 P_1(f)P_2(f)}\right]^{1/2} ,$$

and replacing $\gamma^2\Omega_{\rm gw}^2$ with $\gamma_T^2(\Omega_{\rm gw}^T)^2$ for the tensor mode, with $\gamma_V^2(\Omega_{\rm gw}^V)^2$ for the vector mode, and with $\xi^2\gamma_S^2(\Omega_{\rm gw}^S)^2$ for the scalar mode. As for the power spectra of the detector noise $P_i(f)$, we assume that, for simplicity, all advanced detectors (A, C, H, L, V) have the same noise as that of advanced LIGO. The analytical fit of the noise power spectrum of the advanced LIGO, based on [131], is given by [128],

$$P(f) = \begin{cases} 10^{-44}\left(\dfrac{f}{10\,\mathrm{Hz}}\right)^{-4} + 10^{-47.25}\left(\dfrac{f}{100\,\mathrm{Hz}}\right)^{-1.7}\mathrm{Hz}^{-1} & \\ \qquad\qquad\qquad\qquad\qquad\qquad \text{for } 10\,\mathrm{Hz} \le f \le 240\,\mathrm{Hz}\,, & \\ 10^{-46}\left(\dfrac{f}{1000\,\mathrm{Hz}}\right)^{3}\mathrm{Hz}^{-1} & \text{for } 240\,\mathrm{Hz} \le f \le 3000\,\mathrm{Hz}\,, \\ \infty & \text{otherwise}\,. \end{cases}$$

In the calculation, we assume that the $\Omega_{\rm gw}$ is independent of frequency and the observation time is $T = 3\,\mathrm{yr}$. In Fig. 5.11, the SNRs of the optimal detector pairs, type (i) and (ii), are shown as a function of β. As one can see, detector pairs have almost the same sensitivity to the three modes. In Fig. 5.12, the optimal SNR, $\max\left\{\mathrm{SNR}|_{\rm type(i)}, \mathrm{SNR}|_{\rm type(ii)}\right\}$, is shown as a function of β, together with SNRs of real-detector pairs for each mode. The SNRs of real-detector pairs, except for AIGO-LIGO (H1) and AIGO-LIGO (L1) pairs, are smaller than the optimal one due to the incomplete coincidence of the detector orientations. It is interesting to note that the scalar mode is enhanced in the SNR at the distance relatively close, and that the tensor mode is enhanced at the distance relatively far. This feature can be intuitively interpreted by the anglular responses of the detector shown in Fig. 5.10. At $\beta \sim \pi/2$, the anglular responses of the tensor mode between two detectors are less overlapped than those of the scalar and vector modes. On the other hand, at $\beta \sim \pi$, the anglular responses of the tensor mode between two detectors are more overlapped. SNRs with a realistic detector pair are tabulated in Table 5.5. Therefore, a laser-interferometric GW detector is sensitive to a GWB with the non-tensorial polarizations, having almost the same SNR as the tensor mode.

In this section, we explored the detectability in the presence of an individual mode (tensor, vector, or scalar). However, in a general situation, three GWB modes are mixed in the detector cross-correlation signal. So, the decomposition of the modes is significant problem, which should be addressed. It would be possible if more than three detectors at different sites are available, because of the different dependence of the overlap reduction functions of the three modes on β. We will remain the problem as future work.

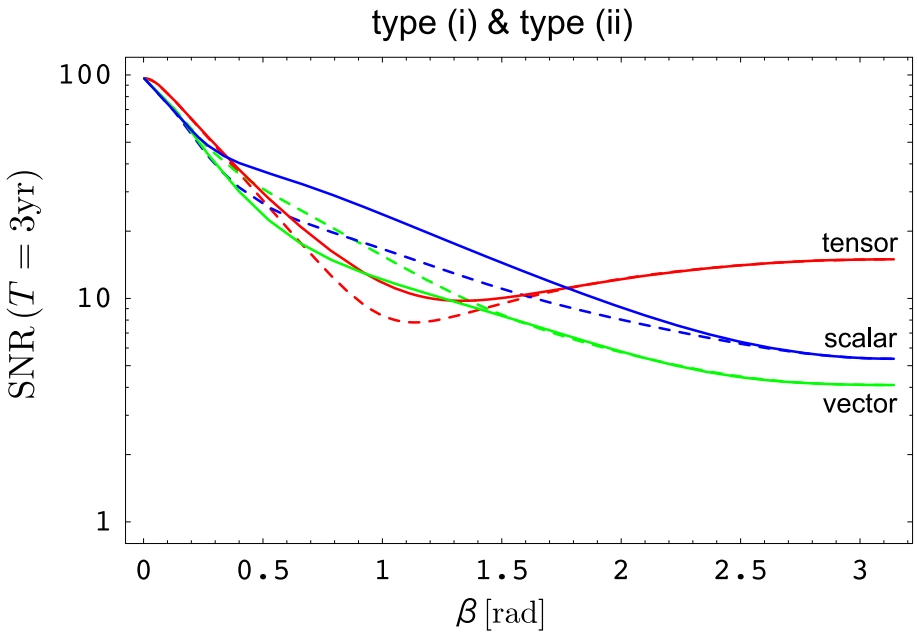

Figure 5.11: SNRs of the detector pair of type (i) (solid lines) and type (ii) (dashed lines) as a function of β. The tensor, vector, and scalar modes are represented by red, green, and blue curves, respectively. The energy density of a GWB is chosen as $h_0^2\Omega_{\rm gw}^M = 10^{-8}$, $M = T, V, S$.

detector pair	$h_0^2\Omega_{\rm gw}^T$	$h_0^2\Omega_{\rm gw}^V$	$\xi h_0^2\Omega_{\rm gw}^S$
A - C	8.6×10^{-9}	8.6×10^{-9}	4.5×10^{-9}
A - H	3.6×10^{-9}	1.1×10^{-8}	7.3×10^{-9}
A - L	3.4×10^{-9}	1.2×10^{-8}	8.8×10^{-9}
A - V	8.7×10^{-9}	2.1×10^{-8}	1.4×10^{-8}
C - H	1.2×10^{-8}	8.4×10^{-9}	8.4×10^{-9}
C - L	4.5×10^{-8}	2.8×10^{-8}	2.5×10^{-8}
C - V	5.7×10^{-9}	6.9×10^{-9}	4.7×10^{-9}
H - L	1.6×10^{-9}	2.0×10^{-9}	1.7×10^{-9}
H - V	7.1×10^{-9}	7.5×10^{-9}	4.5×10^{-9}
L - V	6.7×10^{-9}	6.4×10^{-9}	4.3×10^{-9}

Table 5.5: Detectable $\Omega_{\rm gw}$ for each mode with a real detector pair (SNR = 5). The observation time is selected as $T = 3\,$yr.

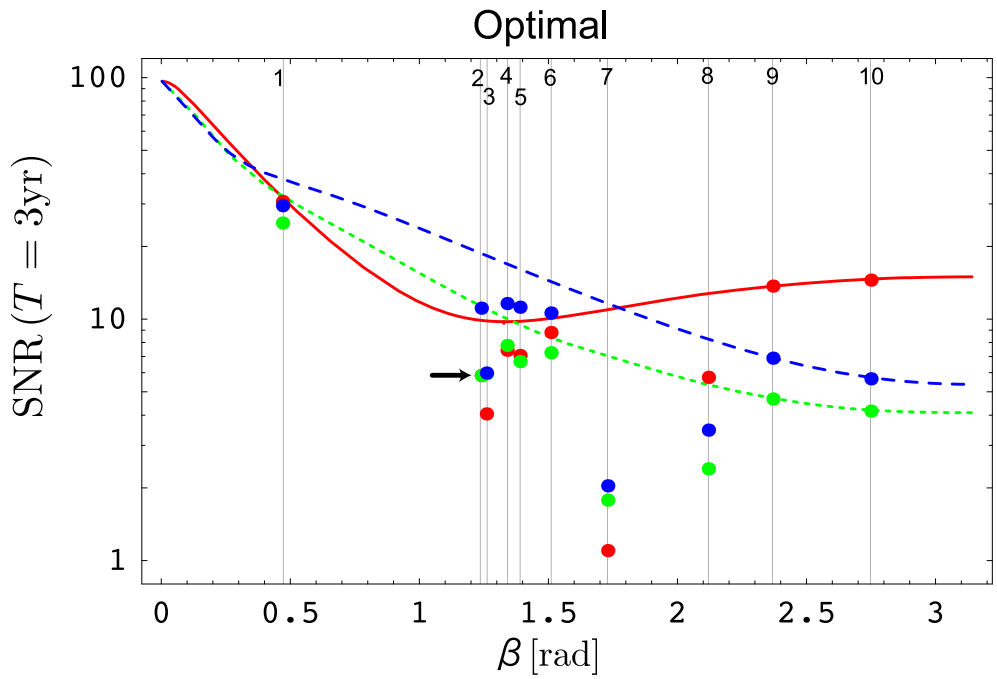

Figure 5.12: SNRs of the optimal and real detectors as a function of β. The energy density of a GWB is chosen as $h_0^2\Omega_{\rm gw}^M = 10^{-8}$, $M = T, V, S$. Each curve shows $\max\left\{\mathrm{SNR}|_{\rm type(i)}, \mathrm{SNR}|_{\rm type(ii)}\right\}$ for the tensor mode (red, solid), the vector mode (green, dotted), and the scalar mode (blue, dashed). The filled circles are the SNR of real detector pairs for the tensor mode (red), the vector mode (green), and the scalar mode (blue). At the arrow in the figure, four circles are overlapped: (detector pair, mode) = (2, tensor), (2, vector), (3, vector), and (3, scalar). The numbers in the figure represent the real detector pair: 1=HL, 2=AC, 3=CH, 4=LV, 5=HV, 6=CV, 7=CL, 8=AV, 9=AH, 10=AL.

Chapter 6

Direct GWB search at ultra-high frequencies

At ultra-high frequencies, much effort for the direct GW detection has not been devoted. Consequently, the direct constraint due to the GW detector is so loose, though the indirect constraint due to the big-bang nucleosynthesis has been obtained. This is because the GW amplitude is much smaller at high frequencies than that at low frequencies, and it makes the detection difficult. However, pioneering works are vital for future GW astronomy and cosmology.

At present, as far as I know, GW detectors have been constructed so far by the groups at INFN, Genova, Italy [41, 42], Birmingham University, UK [43, 44, 45], and is planned at Chongqing University, China [46, 47] [1]. The INFN detector is based on the principle of the parametric conversion of power between the resonant modes of two superconducting coupled microwave cavities. The Birmingham detector is based on detecting the rotation of the polarization vector of an electromagnetic wave induced by the interaction between a GW and the polarization vector of the electromagnetic wave. The Chongqing detector uses the electromagnetic interaction of a Gaussian beam propagating through a static magnetic field. These detectors are based on the different principles from the phase measurement with the laser interferometry developed well in the ground-based large-scale interferometers around 100 Hz.

We will first use a laser interferometer for the GW search at ultra-high frequencies. However, the application of the detection method to an ultra-high frequency band is not as simple as one expects, because, at ultra-high frequencies, GW wavelength is comparable to the size of a detector, which is, for example, the order of a few meters to detect GWs at 100 MHz. In such a case, a long-wave approximation that the GW wavelength is much larger than the detector size is not valid. The phase of GW changes during the one-way trip of light between mirrors. Therefore, we have to use a detector design that is able to integrate GW signals efficiently. Moreover, to detect GWB with smaller amplitude than detector noise, one has to correlate signals from two detectors in order to distinguish the GW signal. The analytical method has been well developed by several authors [51, 150, 127]. However, it is not applicable to our situation at

[1] The sensitive frequency ranges of the detectors is different each other: the INFN detector is at 1 MHz, the Birmingham detector is at 100 MHz, and the Chongqing detector would be 10 GHz.

ultra-high frequencies, because in these references, they assume that GW wavelength is much larger than the detector size. At ultra-high frequencies, the relative location of the two detectors significantly affects the correlation sensitivity to GWB.

In the following sections after briefly introducing GW sources at ultra-high frequencies, we investigate an optimal detector design at ultra-high frequencies by comparing the GW response functions of detectors [48]. Next, we will use the extended formalism of cross-correlation analysis, derived in Sec. 5.1. The formalism properly includes the effect of the response functions of the detectors. We investigate the dependence of the sensitivity on the relative location of two detectors [49]. For concreteness, we consider GWs at 100 MHz and select detector configuration to detect it. However, note that our investigation is general, and is always applicable to GWs other than 100 MHz.

6.1 Gravitational-wave sources at ultra-high frequencies

GW searches at ultra-high frequencies are strongly motivated by theoretical predictions. As described in Chap. 3, some theoretical models, such as quintessential inflation and pre-big-bang model etc., produces much larger GWB spectra than that in the standard slow-roll inflation, at ultra-high frequencies. There also exist GWs from a point source at ultra-high frequencies. The GWs from ordinary astronomical objects are radiated at the frequency range,

$$f_{\rm gw} \sim (G\rho)^{1/2} \sim \left(\frac{GM}{R^3}\right)^{1/2} \lesssim 10 \left(\frac{M_\odot}{M}\right) \text{ kHz} . \tag{6.1}$$

Here we used the Schwarzschild radius $R = 2GM$ for the most compact object. However, if there are compact objects with its mass smaller than $1\,M_\odot$, or, in the scenario with extra dimensions, ultra-high frequency GWs are emitted.

Primordial black holes

Primordial black holes (PBHs) may have formed in the early universe either from initial inhomogeneities or as a result of phase transition (for the recent review, see [151]). Consequently, the mass of a PBH formed in the early universe roughly corresponds to the total mass inside the Hubble horizon at that time, which is given by [152, 153]

$$M_H(t) \approx 10^{15} \left(\frac{t}{10^{-23}\,\text{sec}}\right) \text{ g} . \tag{6.2}$$

By contrast, black holes forming at the present epoch could never be smaller than about $1\,M_\odot$. The origin of such low mass black holes is necessarily of primordial. From Eq. (6.1), $100-$MHz GWs are radiated by the black holes of Jupiter mass, $\sim 10^{-4}\,M_\odot$.

If such PBHs are produced in the early universe, they survive until the present epoch, and emit GWs via binary evolution and coalescence [154, 155]. The quasi-normal ringing frequency of the PBH with the mass $\sim 10^{-4}\,M_\odot$ is ~ 100 MHz. On

the other hand, in many brane world models, PBHs with a lunar mass, $\sim 10^{-7}\,M_\odot$ might have been produced when the temperature of the universe was at $\sim 1\,\mathrm{TeV}$. If a significant fraction of the dark matter of our galaxy consists of these lunar mass PBHs, we have a chance to detect GWs from the PBHs at ultra-high frequencies, and could find some indications of extra dimensions in the phase evolution of the chirp waveform of GWs [156].

Black strings in a brane world

In braneworld scenario such as the Randall-Sundrum (RS) type [157, 158], one of black hole solutions in the presence of the second brane is a so-called *black string* solution, which is the Schwarzschild solution warped in the direction of an extra dimension. If the black string is perturbed, it radiates massive gravitational waves, namely, Kaluza-Klein (KK) modes, with a characteristic spectrum of an extra dimension [159, 160]. The waveform is quite different from that in a 4-dimensional case, and shows less damping than the massless mode and late-time monochromatic oscillations instead of a featureless power-law tail. The frequency is discrete, corresponding to the KK tower of the gravitons, and is determined by the bulk curvature scale and the brane separation, not depending on the black string and companion object masses. The typical frequency and amplitude predicted in [160] are relevant to the GW detector at ultra-high frequencies, $\sim 100\,\mathrm{MHz}$ or above. Therefore, it should be stressed the necessity to develop the detectors capable of measuring such a high-frequency signature of large extra dimensions.

6.2 Optimal detector design

6.2.1 Interferometric-detector designs

We will consider three detector designs, (i) synchronous recycling interferometer (SRI), (ii) Fabry-Perot Michelson interferometer (FPMI) and (iii) L-shaped cavity Michelson interferometer (LMI), and derive the response functions for GWs.

SRI (Fig.6.1) was first proposed by R. W. P. Drever in [161] and detailed calculations have been done in [162, 163]. Laser light is split at a beam splitter and sent into an synchronous recycling (SR) cavity through a recycling mirror, which is mirror A located at $\mathbf{X}_1$ in Fig.6.1. The beams circulating clockwise and counterclockwise in the cavity experience gravitational waves and mirror displacements, leave the cavity, and are recombined at the beam splitter. Then, the differential signal is detected at a photodetector. The advantage of SRI is that GW signals at certain frequencies are accumulated and amplified because the light beams experience GWs with the same phases during round trips in the folded cavity. Consider GW propagating normally to the detector plane with an optimal polarization. In this case, the GW signal is amplified at the frequencies $f = (2n-1) \times c/4L,\ n = 1, 2, \cdots$, where c is the speed of light and L is the arm length. More precisely, the arm length is the distance between $\mathbf{X}_1$ and $\mathbf{X}_2$ (or $\mathbf{X}_3$) in Fig.6.1. On the other hand, the disadvantage of SRI is less

sensitivity for GWs at low frequencies, $f < c/4L$, because the GW signal is integrated in the cavity and canceled out as the frequency is low.

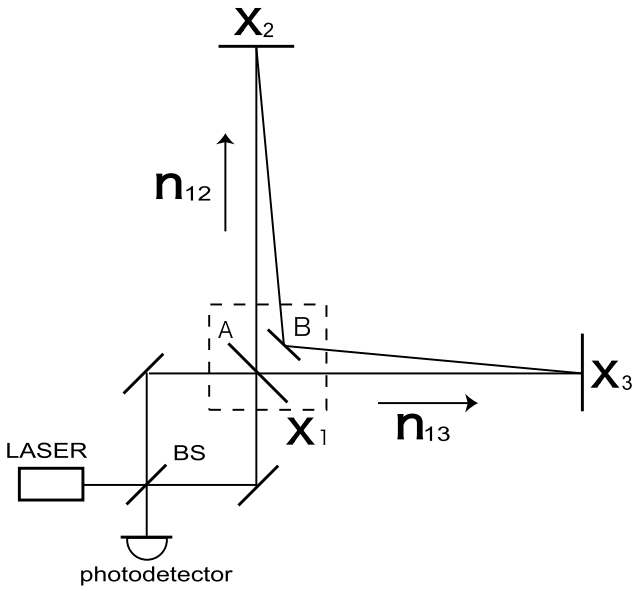

Figure 6.1: Synchronous recycling interferometer (SRI).

The competitive design of detectors with SRI is an ordinary FPMI (Fig.6.2). FPMI is the most popular design for current ground-based interferometers [30, 31, 32, 29] since it has good sensitivity at low frequencies due to the amplification of GW signals with Fabry-Perot cavities. However, to amplify the GW signals at high frequencies, one needs to use resonance due to the cavity. FPMI has the resonance of GW signals at the frequencies, $f = n \times c/2L,\ n = 1, 2, \cdots$ when the GW response is averaged over the entire sky. To take advantage of the resonant response to GW at 100 MHz, the arm length of FPMI should be 1.5 m. With this detector, one can achieve good sensitivity with narrow bandwidth as well as SRI.

Another possible design of detectors is LMI (Fig.6.3), whose optical configuration is the same as the L-shaped FPMI. However, the GW response resembles SRI rather than FPMI. Thus, this design can be regarded as being intermediate between SRI and FPMI.

To compare the detectors for GWB at 100 MHz, it is necessary to derive the GW response functions for GW propagating in arbitrary directions and to compare those averaged on the celestial sphere. For GW propagating normal to the detector plane with an optimal polarization, it is trivial that SRI and LMI with arm length 0.75 m have maximal sensitivity, while FPMI with 1.5 m is not sensitive at all, at 100 MHz. However, FPMI has nonzero sensitivity for GW not propagating orthogonally to the arms of the detector since the GW response of light *going* and *coming* differs. Furthermore, the geometries of detectors also affect the GW responses. Therefore, it is nontrivial which is the most sensitive detector.

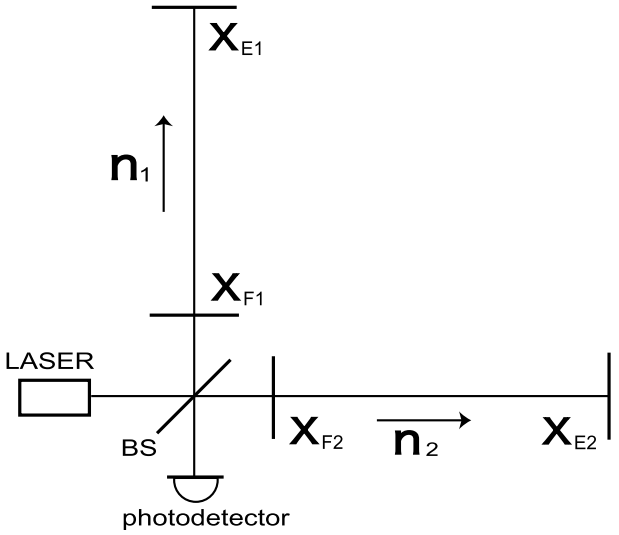

Figure 6.2: Fabry-Perot Michelson interferometer (FPMI).

6.2.2 GW response functions

The general expression of the phase shift of light induced by GW propagating in an arbitrary direction has been derived in many references, for example, [164, 117]. We will use the expression in [164]. When light travels between two test masses located at $\mathbf{X}_I$ and $\mathbf{X}_J$, the phase shift of light created by GW in TT (transverse-traceless) gauge is expressed as

$$\begin{aligned}\delta\phi_{IJ}(t) &= (\mathbf{n}_{IJ}\otimes\mathbf{n}_{IJ}) \\ &\quad : \frac{\omega}{2}\int_0^{L_{IJ}/c} dt' \sum_A \mathbf{e}^A h_A[t-(L_{IJ}+\mathbf{e}_z\cdot\mathbf{X}_I)/c+(1-\mathbf{e}_z\cdot\mathbf{n}_{IJ})t'] \ ,\end{aligned} \tag{6.3}$$

where t is the reception time of light at $\mathbf{X}_J$, ω is the angular frequency of light, h_A is the amplitude of GW with plus or cross polarization and $\mathbf{e}_z$ is a unit vector in the direction of GW propagation. The arm length and unit vector in the direction of the arm are defined as $L_{IJ} \equiv |\mathbf{X}_J - \mathbf{X}_I|$ and $\mathbf{n}_{IJ} \equiv (\mathbf{X}_J - \mathbf{X}_I)/L_{IJ}$, respectively. The symbol : means contraction between a tensor and vectors. The tensors $\mathbf{e}_A$, $A = +, \times$ are polarization tensors of GW and are defined as well as Eq. (2.24) by

$$\begin{aligned}\mathbf{e}_+ &= \mathbf{e}_x\otimes\mathbf{e}_x - \mathbf{e}_y\otimes\mathbf{e}_y \ , \\ \mathbf{e}_\times &= \mathbf{e}_x\otimes\mathbf{e}_y + \mathbf{e}_y\otimes\mathbf{e}_x \ ,\end{aligned} \tag{6.4}$$

where $\mathbf{e}_x$ and $\mathbf{e}_y$ are the unit vectors, which form the orthogonal coordinate with $\mathbf{e}_z$ [2]. For simplisity, we assume that there is no displacement noise, for example, thermal

[2]In this section, we use $\mathbf{e}_z$ instead of $\hat{\mathbf{\Omega}}$ used in other sections, so as not to be confused with the angular frequency of a GW Ω. Note that the coordinate systems $\{\mathbf{e}_x, \mathbf{e}_y, \mathbf{e}_z\}$ and $\{\hat{\mathbf{m}}, \hat{\mathbf{n}}, \hat{\mathbf{\Omega}}\}$ are identical.

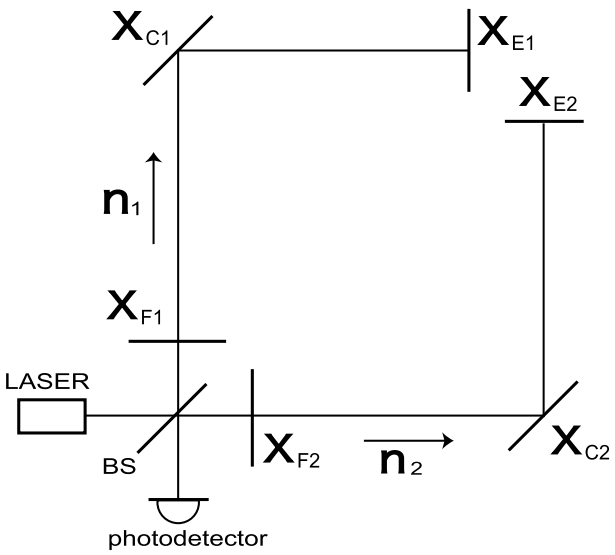

Figure 6.3: L-shaped cavity Michelson interferometer (LMI).

noise, seismic noise, radiation pressure noise, etc., at 100 MHz[3]. In practice, such undisirable noises deteriorate detector sensitivity in a real experiment. Treatments to avoid the noises are described later in the section of correlated noises. Under the assumption of no displacement, the positions of mirrors in the absence of GW are not perturbed and are just given by $\mathbf{X}_I$ and $\mathbf{X}_J$. The Fourier transform of Eq. (6.3) is given by

$$\tilde{\delta\phi}_{IJ}(\Omega) \;=\; \mathbf{n}_{IJ}\otimes\mathbf{n}_{IJ} \;:\; \frac{\omega}{2}\sum_A \mathbf{e}^A\tilde{h}_A\frac{e^{-i\Omega(\mathbf{e}_z\cdot\mathbf{X}_J)/c}-e^{-i\Omega(L_{IJ}+\mathbf{e}_z\cdot\mathbf{X}_I)/c}}{i\Omega(1-\mathbf{e}_z\cdot\mathbf{n}_{IJ})}\,, \qquad (6.5)$$

where $\tilde{h}_p$ is the Fourier component of the GW amplitude, and Ω is the angular frequency of GW and is related to the GW frequency with $\Omega = 2\pi f$.

In general, the response function of a detector is represented by the round-trip signal in cavities multiplied by an amplification factor in cavities. We denote the phase shift of the round-trip signal by $\tilde{\delta\phi}(\Omega)$ and the amplification factor by $\alpha(\Omega)$. Then, the total output from the detector $\tilde{\delta\Phi}(\Omega)$ is written as $\tilde{\delta\Phi}(\Omega) = \alpha(\Omega)\tilde{\delta\phi}(\Omega)$. Detailed calculations are described in the Appendix E. We show here only the results. Note that we change the notation of the unit vectors directed in arms and the reflectivity of mirrors in order to simplify the expression and make it easy to compare. The response functions of each detector are

$$\tilde{\delta\Phi}_{\rm all}(\Omega) = \alpha(\Omega, R_F, R_E)\tilde{\delta\phi}_{\rm all}(\Omega)\;, \qquad (6.6)$$

$$\alpha(\Omega, R_F, R_E) = -\frac{R_E T_F^2}{(R_F - R_E)(1 - R_F R_E\, e^{-4i\Omega\tau})}\;, \qquad (6.7)$$

[3]In fact, rough estimates show that this assumption is at least valid as long as the detector sensitivity is above $h \sim 10^{-20}\,\mathrm{Hz}^{-1/2}$. In the experiment that reaches better sensitivity, thermal noise of mirrors might limit the sensitivity, though other noises are far below.

and

- SRI
  Replacing $\mathbf{n}_{12} \to \mathbf{u}$, $\mathbf{n}_{13} \to \mathbf{v}$ and $(R_A, R_C) \to (R_F, R_E)$ in Eq. (E.7), the response function is

$$\begin{aligned}\tilde{\delta\phi}_{\rm all}(\Omega) &= (1-e^{-2i\Omega\tau})\frac{\omega}{\Omega}\, e^{-i\Omega(\tau+\mathbf{e}_z\cdot\mathbf{X}_1/c)}\sum_A \mathbf{e}^A\tilde{h}_A \\ &\quad : \left[(\mathbf{v}\otimes\mathbf{v})\, H_{\rm SRI}(\Omega, v_z) - (\mathbf{u}\otimes\mathbf{u})\, H_{\rm SRI}(\Omega, u_z)\right] ,\end{aligned} \tag{6.8}$$

  with

$$H_{\rm SRI}(\Omega, u_z) \equiv \frac{1}{1-u_z^2}\left[\sin\Omega\tau - iu_z(e^{-i\Omega\tau u_z} - \cos\Omega\tau)\right] ,$$

- FPMI
  Doubling the arm length, $\tau \to 2\tau$, so that the FPMI resonates at the same frequencies as the SRI, and replacing $\mathbf{n}_1 \to \mathbf{u}$, $\mathbf{n}_2 \to \mathbf{v}$ in Eq. (E.13), the response function is

$$\begin{aligned}\tilde{\delta\phi}_{\rm all}(\Omega) &= \frac{\omega}{i\Omega}\, e^{-i\Omega(2\tau+\mathbf{e}_z\cdot\mathbf{X}_F/c)}\sum_A \mathbf{e}^A\tilde{h}_A \\ &\quad : \left[(\mathbf{u}\otimes\mathbf{u})\, H_{\rm FPM}(2\Omega, u_z) - (\mathbf{v}\otimes\mathbf{v})\, H_{\rm FPM}(2\Omega, v_z)\right] ,\end{aligned} \tag{6.9}$$

  with

$$H_{\rm FPM}(\Omega, u_z) \equiv H_{\rm SRI}(\Omega, u_z) ,$$

- LMI
  Replacing $\mathbf{n}_1 \to \mathbf{u}$, $\mathbf{n}_2 \to \mathbf{v}$ in Eq. (E.18), the response function is

$$\begin{aligned}\tilde{\delta\phi}_{\rm all}(\Omega) &= \frac{\omega}{\Omega}\, e^{-i\Omega(2\tau+\mathbf{e}_z\cdot\mathbf{X}_F/c)}\sum_A \mathbf{e}^A\tilde{h}_A \\ &\quad : \left[(\mathbf{v}\otimes\mathbf{v})\, H_{\rm LMI}(\Omega, v_z) - (\mathbf{u}\otimes\mathbf{u})\, H_{\rm LMI}(\Omega, u_z)\right] .\end{aligned}$$

  with

$$\begin{aligned}H_{\rm LMI}(\Omega, u_z) \equiv \frac{1}{1-u_z^2}\Big[&\sin\Omega\tau\,(e^{-ip_1} + e^{-ip_2} - 2\cos\Omega\tau) \\ &-iu_z(e^{-i(p_1+p_2)} + \cos 2\Omega\tau - (e^{-ip_1}+e^{-ip_2})\cos\Omega\tau)\Big] .\end{aligned}$$

Here we defined $u_z \equiv \mathbf{e}_z\cdot\mathbf{u}$ and $v_z \equiv \mathbf{e}_z\cdot\mathbf{v}$. The phases p_1 and p_2 are defined by $p_1 \equiv \Omega\tau u_z$ and $p_2 \equiv \Omega\tau v_z$, τ is defined by $\tau \equiv L/c$ and R_F and R_E are the amplitude reflectivities of front and end mirrors of cavities, respectively. T_F is the amplitude transmissivity of a front mirror of cavities. Note that, in the case of SRI, the front and end mirrors correspond to a recycling mirror and three other mirrors. Here we doubled the arm length of FPMI so that the first resonant frequency of GW signal coincides with that of SRI and LMI. The formula for a FPMI is also calculated in [165, 166], and our result agrees with them.

6.2.3 Detector comparison

As mentioned in the previous section, in general, the GW response function has the form $\delta\tilde{\Phi}_{\rm all} = \alpha\ \delta\tilde{\phi}_{\rm all}$. We will consider α, which is the common factor for all detectors, and $\delta\tilde{\phi}$, which depends on the geometry of each detector, separately.

From Eq. (6.7), the magnitude of the optical amplification factor in the cavities is determined only by the (composite) reflectivities of the front and end mirrors. The frequencies of the peaks depend on the arm length of detectors. α is plotted in Fig. 6.4. In the figure, we selected $L = 0.75\,\mathrm{m}$ so that the first resonant peak is located at 100 MHz. At higher frequencies, there are many resonant peaks. At lower frequencies, optical amplification is stronger as the frequency is lower, since the wavelength of light is larger than the arm length of a detector. Here we selected the amplitude reflectivities $R_F = 0.99$ and $R_E = 1$ for an illustrative purpose. However, in a real experiment, one should select the reflectivities of the front mirrors much higher in order to achieve better sensitivity, though the bandwidth becomes narrower.

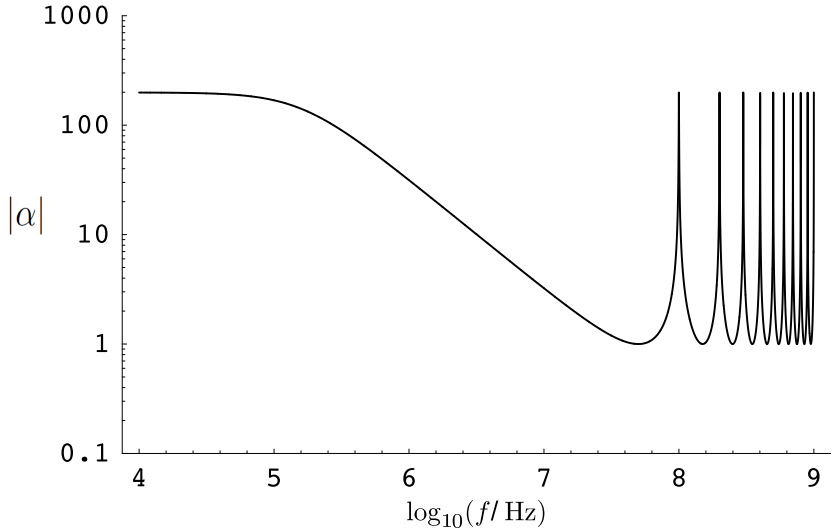

Figure 6.4: The optical amplification factor $\alpha(\Omega)$. Parameters are selected $L = 0.75$m, $R_F = 0.99$ and $R_E = 1$.

To evaluate the round-trip phase shift due to GWs $\delta\tilde{\phi}_{\rm all}$, we introduce coordinates here. The detectors are located on the X-Y plane. Two unit vectors $\mathbf{u}$ and $\mathbf{v}$ are written as $\mathbf{u} = (0, 1, 0)$ and $\mathbf{v} = (1, 0, 0)$, respectively. We denote the direction of GW propagation by the unit vector $\mathbf{e}_z$, and the two unit vectors normal to $\mathbf{e}_z$ and orthogonal to each other by $\mathbf{e}_x$ and $\mathbf{e}_y$. These are written as

$$\begin{aligned}
\mathbf{e}_x &= (\ \cos\theta\ \cos\phi,\ \cos\theta\ \sin\phi,\ -\sin\theta\ )\ , \\
\mathbf{e}_y &= (\ -\ \sin\phi,\ \cos\phi,\ 0\ )\ , \\
\mathbf{e}_z &= (\ \sin\theta\ \cos\phi,\ \sin\theta\ \sin\phi,\ \cos\theta\ )\ .
\end{aligned}$$

$\mathbf{e}_x$ and $\mathbf{e}_y$ define the GW polarization tensor in Eq. (6.4). Here we normalize and

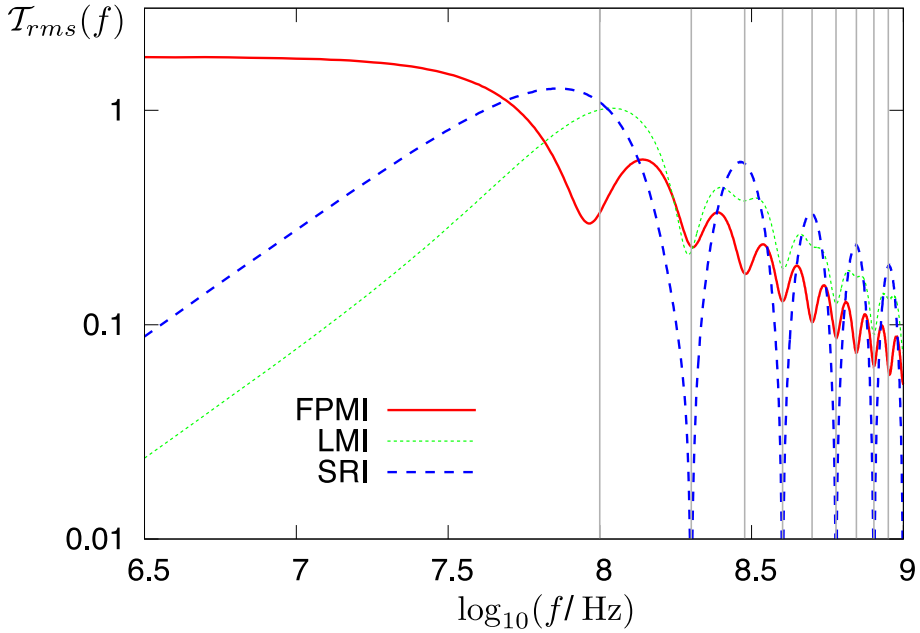

Figure 6.5: GW response function $\mathcal{T}_{\rm rms}(f)$. Vertical lines are plotted at multiples of 100 MHz.

redefine the GW response function as a dimensionless response function, namely,

$$\mathcal{T}(\Omega,\phi,\theta,\psi) \equiv \frac{\delta\tilde{\phi}_{\rm all}}{(\omega\tilde{h}\tau)}\ , \tag{6.10}$$

where we assumed that GW has the form $\sum \mathbf{e}_A\tilde{h}^A = \tilde{h}\,(\mathbf{e}_+\ \cos 2\psi + \mathbf{e}_\times\ \sin 2\psi)$. ψ is the polarization angle of GW. Integrating this function by ϕ, θ and ψ on the celestial sphere and averaging lead to

$$\mathcal{T}^2_{\rm rms}(\Omega) \equiv \frac{1}{4\pi}\int_0^{2\pi} d\phi \int_0^{\pi} d\theta\ \sin\theta \int_0^{2\pi} \frac{d\psi}{2\pi}\,|\mathcal{T}(\Omega,\phi,\theta,\psi)|^2.$$

The result of numerical calculation is shown in Fig. 6.5. All response functions decrease above 100 MHz. This is the common feature of interferometers because the GW signal is destructively integrated in the cavity and is canceled out. Below 100 MHz, the response functions of SRI and LMI also decrease because the GW signal is partially canceled out during round trips of light beams in the folded cavities. On the other hand, in the case of FPMI, the GW signal is more constructively integrated in the cavity and is more amplified, as the frequency is lower. At 100 MHz, SRI and LMI have almost the same sensitivity, while FPMI has sensitivity worse by a factor ≈ 3.3. This is because FPMI integrates GW signals less efficiently than other detectors. This difference becomes significant when one takes the correlation of two detectors into account, which results in a factor of $(3.3)^2 \sim 10$ in sensitivity to GWB energy density $\Omega_{\rm gw}$.

Let us consider the best sensitivity of SRI experimentally achievable with realistic parameters, which is almost the same as that of LMI. We assume that the sensitivity is

limited only by shot noise [4]. The magnitude of shot noise is determined by laser power, the arm length and the reflectivities of mirrors, and is calculated by the condition that the phase shift due to GWs is equal to that of quantum noise [162],

$$|\beta|\,\langle\delta\tilde{\Phi}_{\rm all}\rangle_{\rm rms} = \sqrt{\frac{2\hbar\omega}{\eta I_0}}\,, \tag{6.11}$$

where ω is the angular frequency of laser, η is the quantum efficiency of a photodetector, I_0 is original laser power, and

$$\beta \equiv \frac{R_F - R_E}{1 - R_F R_E}\,.$$

The reason why β is needed in the left-hand side of the Eq.(6.11) is that, in Eq.(E.4), the phase shift due to GWs must be converted into the amplitude of a sideband field. Substituting Eqs.(6.6) and (6.10) leads to

$$h(\Omega) = \frac{1}{\tau\alpha'(\Omega)\mathcal{T}_{\rm rms}(\Omega)}\sqrt{\frac{2\hbar}{\eta\omega I_0}}\,,$$

where we defined

$$\alpha'(\Omega) \equiv |\beta\,\alpha(\Omega)| = \left|\frac{R_E T_F^2}{(1 - R_F R_E)(1 - R_F R_E\, e^{-4i\Omega\tau})}\right|\,. \tag{6.12}$$

We select $L = 0.75\,\mathrm{m}$ so that GW signal resonates at 100 MHz, $\omega = 1.77\times10^{15}\,\mathrm{rad\,sec^{-1}}$ and $\eta = 1$. The sensitivity achievable at 100 MHz in an ideal situation is

$$h \approx 7.8\times10^{-21}\left(\frac{1\,\mathrm{W}}{I_0}\right)^{1/2}\left(\frac{1.6\times10^4}{\alpha'}\right)\mathrm{Hz}^{-1/2}$$

with bandwidth $\sim 10^8/\mathcal{F}\,\mathrm{Hz}$, where finesse is $\mathcal{F} \equiv \pi\sqrt{R_F R_E}/(1 - R_F R_E)$, which is related to α' by the relation $\mathcal{F} = \pi\sqrt{\alpha' R_F/T_F^2}$ at 100 MHz. Note that $\alpha' \approx 1.6\times10^4$ is realized with reflectivities, say, $R_F^2 = 0.99996$ and $R_E^2 = (0.99998)^3$. When we select the arm length $L = 0.75\,\mathrm{m}$, laser power $I_0 = 1\,\mathrm{W}$ and $|\alpha'| = 1.6\times10^4$, the best achievable sensitivity with SRI is $h \approx 7.8\times10^{-21}\,\mathrm{Hz}^{-1/2}$ at 100 MHz with bandwidth $\sim 2\,\mathrm{kHz}$. Note that our results can also be applied to detectors at other frequency bands by tuning the arm length and shifting the peak of sensitivity.

In this section, we investigated the GW responses of interferometers at 100 MHz. We considered three designs that took advantage of the first optical resonance due to cavities and derived the GW response functions. In conclusion, SRI and LMI have almost the same sensitivity at 100 MHz and FPMI has sensitivity worse by a factor of 3.3.

[4] Rough estimates of the displacement noise in the L-shaped SRI have been done. For typical parameters of the experiment, thermal and radiation-pressure noises have $h_n \approx 6.8\times10^{-21}\,\mathrm{Hz}^{-1/2}$ and $h_n \approx 1.6\times10^{-24}\,\mathrm{Hz}^{-1/2}$, respectively. These noises are marginally below the goal sensitivity of our experiment. Therefore, no improvement of the sensitivity beyond would be expected. A new detector design, which solves the issue of the displacement amplification, is discussed in Chap. 7.

Above conclusion in the detector sensitivity is theoretical one. That is, we determined the best detector configuration from the point of view of shot-noise limited sensitivity to GWs. However, in real experiments, there are many advantages and disadvantages of detectors that we have not considered here. One of the advantages of SRI is the simplicity of a control system. SRI has only one degree of freedom for locking the interferometer because clockwise and counterclockwise lights share light paths in the cavity and the Sagnac part, while FPMI and LMI have three degrees of freedom in operation, which are for cavities in both arms and the Michelson part. Another advantage of SRI is the symmetric optical configuration of the cavity. This means that clockwise and counterclockwise light in the cavity experience the same reflectivities of mirrors. Thus, SRI is expected to have high tolerance to the imbalance of the reflectivities and relatively smaller laser frequency noise than other detectors. Even if we take these facts into account, we can conclude that SRI is the best detector. These issues should be investigated in more detail when one constructs real detectors.

6.3 Correlation of two detectors

6.3.1 Identification of GW response and noise in a SRI

In the previous section, we derived the GW response of an SRI and found that it can be written in the form $\delta\tilde{\Phi}(f,\,\hat{\mathbf{\Omega}}) = \alpha(f)\,\delta\tilde{\phi}(f,\,\hat{\mathbf{\Omega}})$, using the Fourier component of phase shift due to GW during the round trip of light in a recycling cavity $\delta\tilde{\phi}(f,\,\hat{\mathbf{\Omega}})$ and an optical amplification factor of light in the cavity $\alpha(f)$. From Eqs. (6.7) and (6.8), the concrete expressions are written as

$$\alpha(f) = -\frac{R_E T_F^2}{(R_F - R_E)(1 - R_F R_E\, e^{-8\pi i f\tau})}\,,$$

$$\begin{aligned}\delta\tilde{\phi}(f,\hat{\mathbf{\Omega}}) &= (1 - e^{-4\pi i f\tau})\frac{\omega}{2\pi f}\, e^{-2\pi i f(\tau + \hat{\mathbf{\Omega}}\cdot\vec{\mathbf{X}}/c)} \sum_A \tilde{h}_A(f,\hat{\mathbf{\Omega}})\,\mathbf{e}_A(\hat{\mathbf{\Omega}}) \\ &\quad : \Big[\,(\hat{\mathbf{v}}\otimes\hat{\mathbf{v}})H_{\rm SRI}(f,\,\hat{\mathbf{\Omega}}\cdot\hat{\mathbf{v}}) - (\hat{\mathbf{u}}\otimes\hat{\mathbf{u}})H_{\rm SRI}(f,\,\hat{\mathbf{\Omega}}\cdot\hat{\mathbf{u}})\Big]\,, \qquad (6.13)\end{aligned}$$

where $\hat{\mathbf{\Omega}}$ can be identified with $\mathbf{e}_z$ in the previous section, and $\vec{\mathbf{X}}$ is a position vector of the mirror M_1 ($\mathbf{n}_{12}$, $\mathbf{n}_{13}$, $\mathbf{X}_1$ in Fig. 6.1 can be identified with $\mathbf{u}$, $\mathbf{v}$, and $\vec{\mathbf{X}}$ here, respectively.). We define an arm response function like

$$\mathcal{T}(f,\,\hat{\mathbf{\Omega}}\cdot\hat{\mathbf{u}}) \equiv \frac{-\,e^{-2\pi i f\tau}}{2\pi f\tau} H_{\rm SRI}(f,\,\hat{\mathbf{\Omega}}\cdot\hat{\mathbf{u}})\,, \qquad (6.14)$$

so that $\mathcal{T}$ gives unity in low frequency limit, as shown in Fig. 6.6. Using this response function, we can rewrite Eq. (6.13) in a simple form,

$$\begin{aligned}\delta\tilde{\phi}(f,\hat{\mathbf{\Omega}}) &= 2\,\omega\tau\, e^{-2\pi i f\hat{\mathbf{\Omega}}\cdot\vec{\mathbf{X}}/c}\,(1 - e^{-4\pi i f\tau}) \\ &\quad \times \sum_A \tilde{h}_A\,\mathbf{e}^A : \frac{1}{2}\Big[\,(\hat{\mathbf{u}}\otimes\hat{\mathbf{u}})\mathcal{T}(f,\,\hat{\mathbf{\Omega}}\cdot\hat{\mathbf{u}}) - (\hat{\mathbf{v}}\otimes\hat{\mathbf{v}})\mathcal{T}(f,\,\hat{\mathbf{\Omega}}\cdot\hat{\mathbf{v}})\Big] \\ &= 2\,\omega\tau\, e^{-2\pi i f\hat{\mathbf{\Omega}}\cdot\vec{\mathbf{X}}/c}\,(1 - e^{-4\pi i f\tau}) \sum_A \tilde{h}_A(f,\hat{\mathbf{\Omega}})\,F_A(f,\hat{\mathbf{\Omega}}) \qquad (6.15)\end{aligned}$$

Therefore, comparing Eq. (6.15) with Eq. (5.8), we obtain

$$\begin{aligned} \delta\tilde{\Phi}'(f) &\equiv \int d\hat{\mathbf{\Omega}}\, \delta\tilde{\Phi}(f,\hat{\mathbf{\Omega}}) \\ &= \kappa(f)\,\alpha(f)\,\tilde{h}(f)\,. \end{aligned} \tag{6.16}$$

where $\kappa(f) \equiv 2\,\omega\tau(1-e^{-4\pi i f\tau})$. To identify $\tilde{h}(f)$ and $\delta\tilde{\Phi}'(f)$, we incorporate the extra factor $\kappa(f)\,\alpha(f)$ into the noise spectrum[5], that is,

$$\begin{aligned} \sqrt{P_{\rm shot}(f)} &= |\kappa(f)\,\alpha'(f)|^{-1}\sqrt{P_{\rm qnoise}(f)} \\ &= |\kappa(f)\,\alpha'(f)|^{-1}\sqrt{\frac{2\hbar\omega}{\eta I_0}} \end{aligned} \tag{6.17}$$

where $P_{\rm qnoise}$ is the noise due to vacuum fluctuations. We assumed that shot noise is a dominant noise source around 100 MHz. In Eq. (6.17), $\alpha(f)$ is replaced with $\alpha'(f)$ defined in Eq. (6.12), since phase shift due to GW has to be converted into photocurrent at the photo detector by multiplying a constant factor.

We identified the specific forms of GW signal and noise in this subsection. The GW signal $\delta\tilde{\Phi}'(f)$ completely corresponds to $\tilde{h}(f)$ in Eq. (5.8), and can be calculated using $\mathcal{T}$ in Eq. (6.14). The power spectrum of shot noise can be calculated with Eq. (6.17), if experimental parameters are given.

6.3.2 Dependence of sensitivity on the relative locations between two detectors

The sensitivity to GWB is significantly influenced by the geometrical configuration of two SRIs through the overlap reduction function γ when the wavelength of GW is comparable to the size of a detector. In this section, we will perform detailed investigation of the dependence of the overlap reduction function on the relative location of two detectors in an experiment for the detection of GWB at 100 MHz.

The overlap reduction function can be calculated numerically from Eq. (5.10) using the arm response function $\mathcal{T}$ given in Eq. (6.14), where the phase factor $e^{2\pi i f\hat{\mathbf{\Omega}}\cdot\Delta\vec{\mathbf{X}}/c}$ plays an important role. To see this, we consider the four configurations of detectors and calculate $\gamma(f)$. The results are shown in Fig. 6.7 with the case of "exact" and "long wavelength limit". The former is calculated with the full arm response function $\mathcal{T}$. The latter is calculated with $\mathcal{T}=1$, which is just plotted for reference, though the approximation is not valid around 100 MHz. Each configuration of detectors is characterized by the relative position $\Delta\vec{\mathbf{X}} = \vec{\mathbf{X}}_1 - \vec{\mathbf{X}}_2$ and the relative angle β. Note that $\vec{\mathbf{X}}_I$ is the position vector of M_1 of I-th detector. In the case of (a) ideal, $\gamma(f)$ rapidly decreases even though the detectors are completely colocated and coaligned, because we defined the $\gamma(f)$ including arm response functions. Case (b) T-shaped has

[5]Note that the derivation of shot noise is slightly different from that in the previous section, where we have incorporated the angular response to GW into shot noise. However, here an angular averaging is contained in the GW signals.

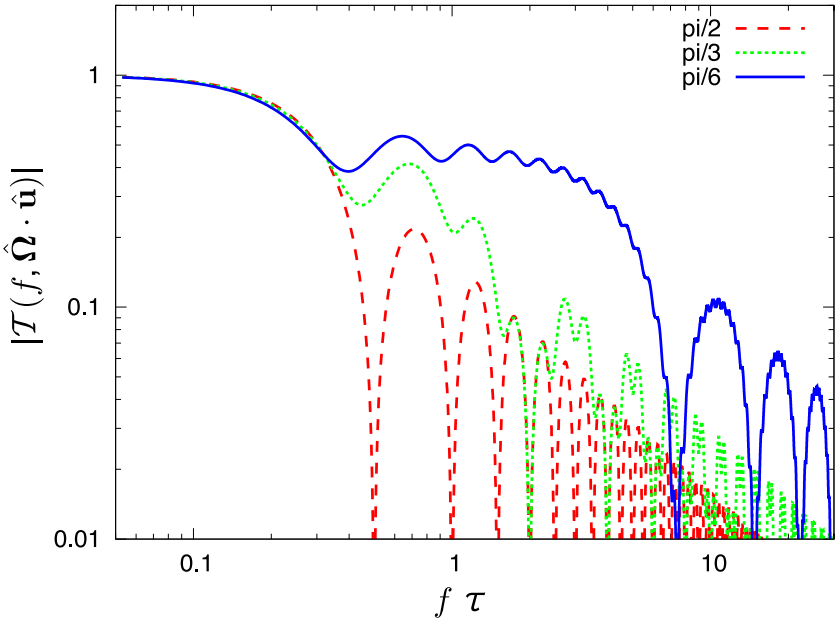

Figure 6.6: Arm response functions of SRI as a function of $f\tau$. Each plot is for $\arccos(\hat{\mathbf{\Omega}} \cdot \hat{\mathbf{u}}) = \pi/2$, $\pi/3$, $\pi/6$, respectively, as shown by plot labels in the figure.

a behavior similar to that of (a) for the same reason. The arm response function is needed to take the effect of the phase change of GW at high frequencies into account. Cases (a) and (b) are similar, but have a subtle difference since the arms of detectors are at different locations and experience different phases of GW. As a result, the overlap of case (b) is a little worse than case (a). In the cases of (c) crossed and (d) stacked, $\gamma(f)$ also decrease more rapidly than in the long wavelength limit. This is because the contribution of the GW phase change at high frequencies is added to that in the long wavelength limit. Therefore, we cannot obtain $\gamma(f) = 1$ at 100 MHz with the detectors where detector size and GW wavelength are comparable. It follows that SNR is worsened by a factor of $(0.377)^{-1} \approx 2.65$ at 100 MHz in contrast to the case where long wave approximation is valid, even if the two detectors' configuration is optimal. One may expect unit response to be obtained by constructing much smaller detectors. However, the total response of detectors $\delta\tilde{\Phi}$ is worsened since the resonant frequency of GW signal also depends on the detector size and is shifted upward. Thus, this loss of sensitivity due to the phase change of GW is inevitable.

Next, we will fix the frequency at 100 MHz and consider $\gamma(f)$. In fact, SRI has a narrow frequency band and what we are most interested in is γ at 100 MHz. In Fig. 6.8, the location of one detector is fixed, while the other detector is located at the same site ($\Delta\vec{X} = 0$) and the directions of arms are rotated. In this case, the magnitude of $\gamma(f)$ oscillates, however, it has the maximum peak at $\beta = 0$ and the minimum peak at $\beta = \pi$. It is intuitive that the GW signal is better correlated when the directions of arms are coaligned. In Figs. 6.9 and 6.10, the angle of detectors is fixed and the locations are translated. In an initially coaligned case ($\beta = 0$) in Fig. 6.9, as expected, $\gamma(f)$ has its maximum at $\Delta X = 0$ and keeps the moderate value in the range of $\Delta X = \pm 0.2$ m. In

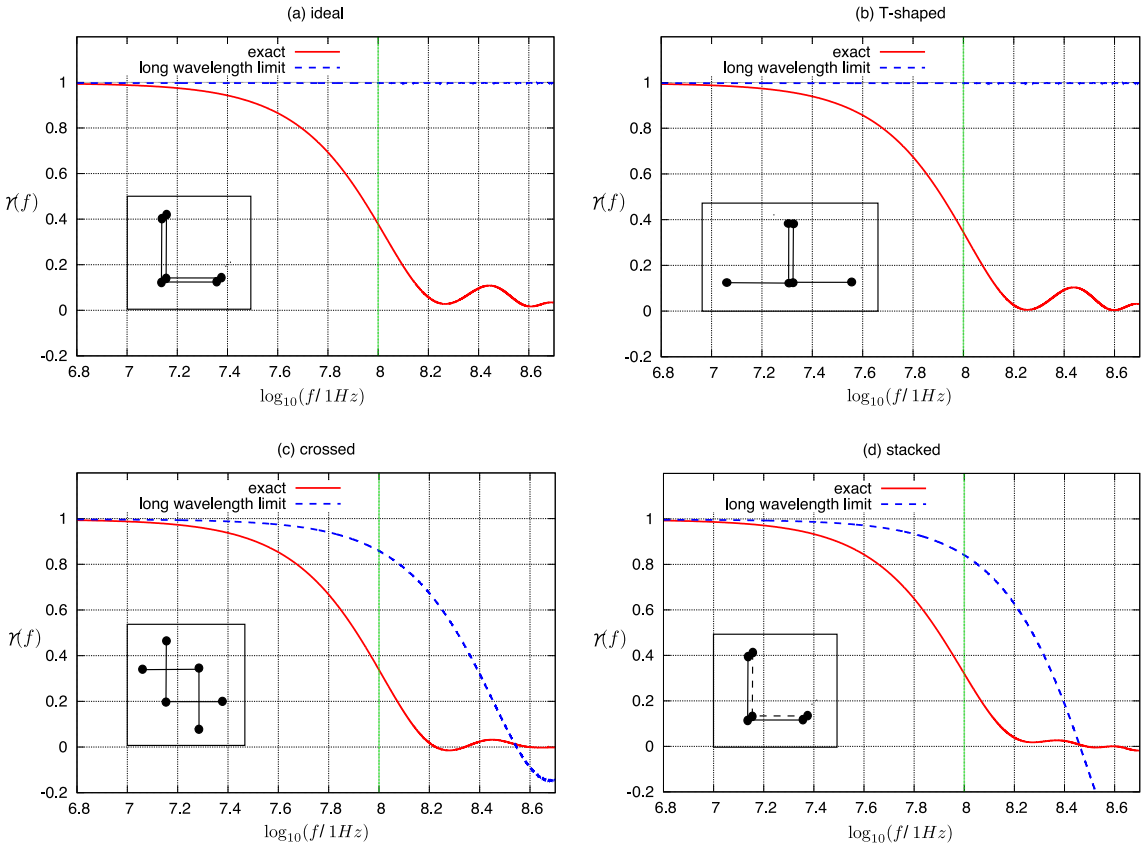

Figure 6.7: Overlap reduction function in the case of four detector configurations. Each setup is (a) ideal, $\Delta\vec{\mathbf{X}} = 0$, $\beta = 0$, (b) T-shaped, $\Delta\vec{\mathbf{X}} = 0$, $\beta = \pi/2$, (c) crossed, $\Delta\vec{\mathbf{X}} = (L/2, L/2, 0)$, $\beta = \pi$, (d) stacked, $\Delta\vec{\mathbf{X}} = (0, 0, L/2)$, $\beta = 0$, where the arm length is selected as $L = 0.75\,\mathrm{m}$. The "exact" means the calculation with arm response function $\mathcal{T}$ and the "long wavelength limit" $\mathcal{T} = 1$. The latter is not valid around 100 MHz, but merely plotted for comparison. Note that the sign of $\gamma(f)$ in (b) is inversed for convenience of comparison.

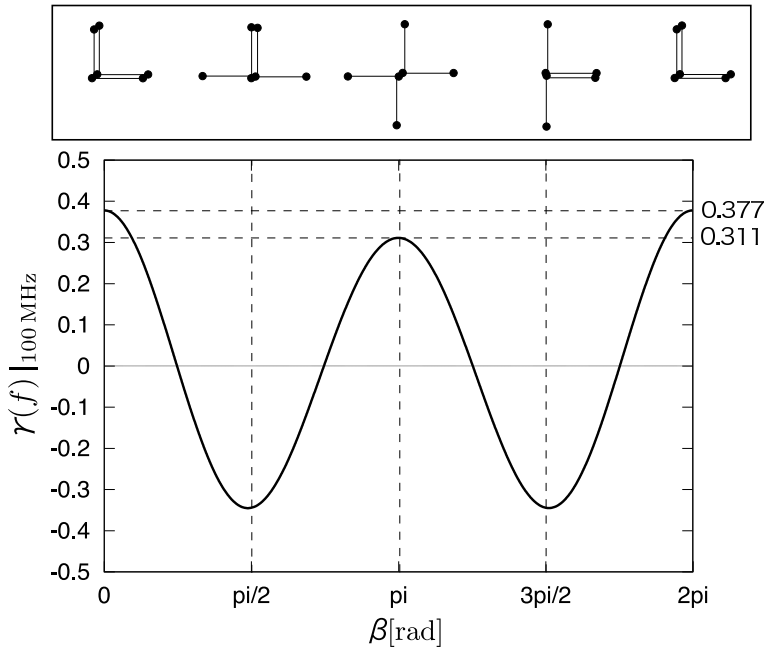

Figure 6.8: Overlap reduction function when the detector with $L = 0.75\,\mathrm{m}$ is initially colocated and coaligned and is rotated at the same location. β is the rotation angle.

an initially reversed case ($\beta = \pi$) in Fig. 6.10, an interesting feature can be seen. When the detector is translated to the direction $(\hat{\mathbf{u}} + \hat{\mathbf{v}})/\sqrt{2}$, the peak of $\gamma(f)$ is shifted. This is because the overlap of the two detectors is better when their arms are overlapped geometrically like (c) in Fig. 6.7.

Here we have considered a SRI as a detector configuration, and investigated the degradation and location dependence of the overlap reduction function. However, the property also hold for a Fabry-Perot Michelson interferometer because the transfer function is almost the same as that of a SRI, though the sensitivity is slightly worse, see Eqs. (6.8) and (6.9). Thus, the results we obtained in this subsection are general features in an interferometric GW detector at high frequencies.

6.3.3 Sensitivity to GWB

We will describe the best location of detectors with respect to the sensitivity, and calculate the sensitivity achievable with correlation analysis. From the results obtained above, the best location is obviously colocated and coaligned, and gives $\gamma(f)|_{100\,\mathrm{MHz}} \approx 0.377$. As shown in Fig. 6.9, this value is hardly changed in the range of $\Delta X = \pm 0.2\,\mathrm{m}$ for coaligned detectors. In an experiment, it is impossible to put the detectors in completely colocated and coaligned location because of the restricted experimental space of the optics. However, experimental detector configuration does not significantly affect $\gamma(f)$ if the detectors are nearly colocated and coaligned. Therefore, we fix it to $\gamma_{\mathrm{opt}} = 0.377$.

As for the power spectral density of noise in an SRI, one can calculate from

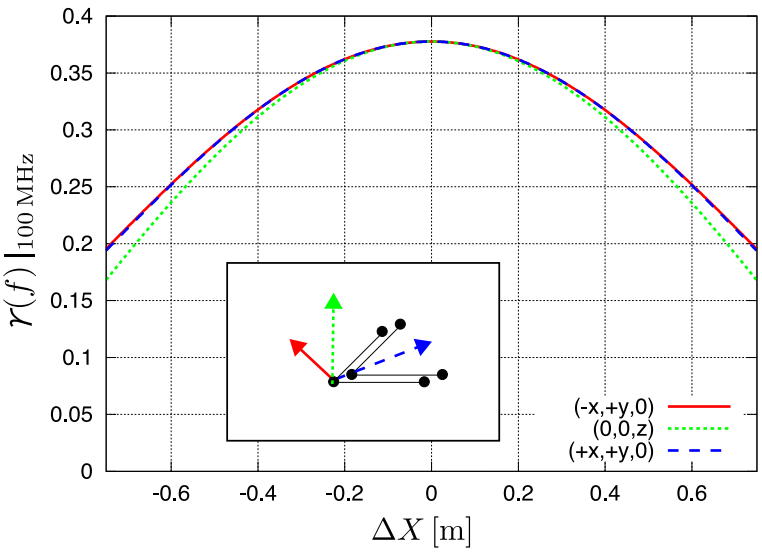

Figure 6.9: Overlap reduction function when the detector with $L = 0.75\,\mathrm{m}$ is initially colocated and coaligned ($\beta = 0$) and is translated in certain directions. Each curve means the direction of translation. $(+x, +y, 0)$ is the direction of $(\hat{\mathbf{u}} + \hat{\mathbf{v}})/\sqrt{2}$, $(-x, +y, 0)$ is the direction of $(\hat{\mathbf{u}} - \hat{\mathbf{v}})/\sqrt{2}$, and $(0, 0, z)$ is the direction perpendicular to the $\hat{\mathbf{u}}\,\hat{\mathbf{v}}$ plane.

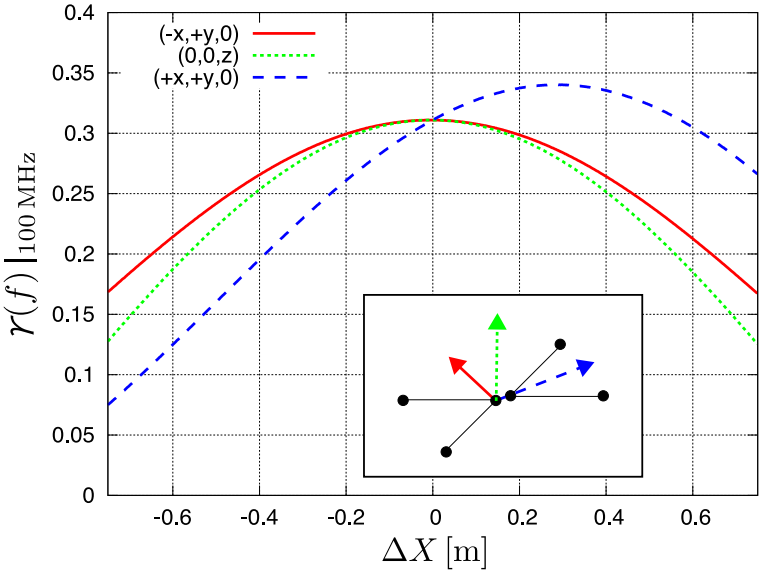

Figure 6.10: Overlap reduction function when the detector with $L = 0.75\,\mathrm{m}$ is initially colocated and reversed ($\beta = \pi$) and is translated in certain directions. Each curve means translation in the same direction as shown in Fig. 6.9.

Eq. (6.17). We select the arm length of a detector as $L = 0.75\,\mathrm{m}$ so that the GW signal resonates at 100 MHz. With experimental parameters, $\omega = 1.77 \times 10^{15}\,\mathrm{rad\,s^{-1}}$ and $\tau = 1$, the power spectral density of noise around 100 MHz is

$$P_i(f) \approx 4.65 \times 10^{-42} \left(\frac{1.60 \times 10^4}{\alpha'(f)} \right)^2 \left(\frac{1\mathrm{W}}{I_0} \right) \mathrm{Hz}^{-1}, \quad i = 1, 2. \tag{6.18}$$

The factor α' is called the optical amplification factor in a cavity and gives $\alpha' \approx 1.6 \times 10^4$ with the reflectivity of the recycling mirror, $R_F^2 = 0.99996$, and the reflectivity of the other three mirrors, $R_E^2 = (0.99998)^3$. The bandwidth is $\sim 2\,\mathrm{kHz}$ with these reflectivities. Note that the noise power spectrum in Eq. (6.18) is that for optimally incident GW and not angular-averaged, since the angular average is incorporated into the overlap reduction function in the correlation analysis. To convert Eq. (6.18) to angular-averaged one, the factor $(2\pi f\tau / \sin 2\pi f\tau)^2$ has to be multiplied.

Substituting $P_I(f)$ and γ_{opt} into Eq. (5.16), and assuming that observation time is $T = 1\,\mathrm{yr}$ and that $\Omega_{\mathrm{gw}}(f)$ has a flat spectrum around 100 MHz (which is sufficient for practical purposes [167]), one can calculate the sensitivity of two SRIs to GWB and obtain

$$h_0^2 \Omega_{\mathrm{gw}} \approx 1.4 \times 10^{14} \quad \text{at } 100\,\mathrm{MHz} \text{ with } L = 0.75\,\mathrm{m}. \tag{6.19}$$

This figure is obtained with practically feasible parameters in a laboratory and by assuming that the sensitivity is limited only by shot noise.

One might expect to improve the sensitivity with moderate technical development in the near future or with a longer armlength (lowering resonant frequency). However, it might be impossible to futher improved the sensitivity in this detector design, because other noises would contribute to the sensitivity. The SRI amplifies not only GW signal but also displacement noise of mirrors. Cosequently, a rough estimate shows that radiation-pressure or thermal noise prevent the SRI improving the sensitivity. This problem can be avoided by changing the detector design and usign ring-shaped cavity, a so-called resonant speed meter [168], which is described in a latter chapter.

6.3.4 Cross-correlated noise

In the real world, correlated environmental and instrumental noises would contribute to the cross-correlation signal of the detectors and mimic the presence of true GWB signals. For the two detectors far separated, a number of correlated noise sources can be ignored, while, for detectors close to each other like the case in this paper, there would be many correlated noise sources. So, it is important to investigate the noise sources in advance. In this subsection, we describe the possible noise sources and suggest some preventive treatments for them.

It is useful to derive the condition for the noise so as not to impair the cross-correlation search. Correlated noise in two detectors can be described by the cross-spectral function $P_c(f)$ defined by

$$\langle \tilde{n}_1^*(f) \tilde{n}_2(f') \rangle \equiv \frac{1}{2} \delta(f - f') P_c(f) \, .$$

If $\langle S^2\rangle \gg \langle S\rangle^2$ in (5.11), the correlated noise does not affect the GWB search. From Eqs. (5.7) and (5.12) by replacing $h_{1,2}(f) \to n_{1,2}(f)$, one can obtain the condition

$$\left[\frac{T}{2}\int_{-\infty}^{\infty} df P_c(|f|)\tilde{Q}(f)\right]^2 \ll \frac{T}{4}\int_{-\infty}^{\infty} df P_1(|f|)P_2(|f|)|\tilde{Q}(f)|^2 \,, \tag{6.20}$$

where P_1 and P_2 are uncorrelated noises of each detector. Narrow band approximation allows replacement of the integral in Eq. (6.20) with characteristic bandwidth $\Delta f \approx f_0/|\alpha'|$, f_0 is a central frequency. Then, Eq. (6.20) is

$$P_c(|f_0|) \ll \frac{P_1(|f_0|)}{\sqrt{T\Delta f}} \,, \tag{6.21}$$

where $P_1(|f|) = P_2(|f|)$ is used. For the parameters we used in the previous section, $T = 1\,\mathrm{yr}$ and $\alpha' = 1.6 \times 10^4$, the condition is

$$P_c(|f_0|) \ll 2.3 \times 10^{-5}\, P_1(|f_0|) \approx 1.0 \times 10^{-47}\ \mathrm{Hz}^{-1} \,. \tag{6.22}$$

Thus, the magnitude of noise with correlation should be much smaller than that of uncorrelated noise. Note that this condition is not valid for transient correlated noise. In the case, T in Eq. (6.21) is replaced with ΔT which is the duration of correlated transient disturbance, and the condition (6.22) is weakened.

In general, the properties (magnitude, angular pattern, time dependence, etc.) of correlated noise strongly depend on the details of the instruments. So, we devote our attention to qualitative aspects of correlated noise.

- Thermal and radiation pressure noises
  Thermal noise includes those of all optics such as mirrors, suspensions, etc., and radiation noise results from vacuum fluctuation. These noises would be the loudest noise if one goes beyond the sensitivity in Eq. (6.19). However, these have no correlation between two detectors in nature.

- Seismic noise
  Seismic noise is a dominant noise source at low frequencies below $\sim 10\,\mathrm{Hz}$ in large ground-based interferometers. However, the noise can be significantly suppressed by a seismic attenuation system at high frequencies. Furthermore, one can also place the detector on a stiff board to prevent the differential vibration mode from coming into effect. We can safely conclude that seismic noise at ultra-high frequencies is low enough to be ignored.

- Acoustic noise
  Sound waves (supersonic waves at $100\,\mathrm{MHz}$) around the two detectors would produce a correlative change in the light path length by directly disturbing the mirrors or perturbing the refraction index of gas. The noise can be reduced by putting the detector into a vacuum chamber. Another way to avoid the noise is

to insert an acoustic absorbent between the detectors. It is recommended that both noise reduction methods are used together in case there is residual gas in the vacuum chamber. In fact, the experiment in the air [50] shows no indication of the acoustic noise, though the sensitivity is still far above than Eq. (6.19).

- Scattered light
  Scattered light is also an awkward noise source when the detectors are closely situated. Preventive measures against scattered light should be taken. In addition, it is effective to use separate laser sources with frequencies significantly shifted in relation to one another, compared with the observation frequency, 100 MHz. A simpler solution is to stack the detectors with a partition. According to Fig. 6.9, the sensitivity is nearly optimized and hardly changed if the two detectors are located in a range ± 0.2 m.

- External electromagnetic fields
  There would be many radio-frequency electromagnetic fields around 100 MHz, such as those related to radio and television, which would depend on where one lives. In experiment [50], such frequency bands were investigated and were avoided before the experimental setup was constructed. Furthermore, an electromagnetic wave shield should be installed in case unanticipated electromagnetic fields exist.

- Electric noise
  One should be careful about electronic noises produced by measurement devices, electric wires, and power supply. The most awkward thing among them is the power supply because one usually uses an identical power supply. The problem can be avoided if one uses separate batteries.

Therefore, in principle, all anticipated noise sources correlated between the two detectors can be avoided. However, unexpected noise might exist in a real experiment. It is useful for noise hunting to shift and rotate one of the detectors and compare the behavior of the noise level, because most noises might strongly depend on the location and angle of the detectors. Rotating one of the detectors by $\pi/2, \pi, 3\pi/2$ rad is a good option for a detector configuration, since it hardly worsens the sensitivity as shown in Fig. 6.8. It is also useful for the confirmation of the existence of real GWB to check the location dependence of the sensitivity with the results in the section above.

6.4 Experimental search for GWB

6.4.1 Experimental setup

In the laboratory of National Astronomical Observatory of Japan (NAOJ), we have developed a GW detector that consists of two SRIs, which are constructed on a single

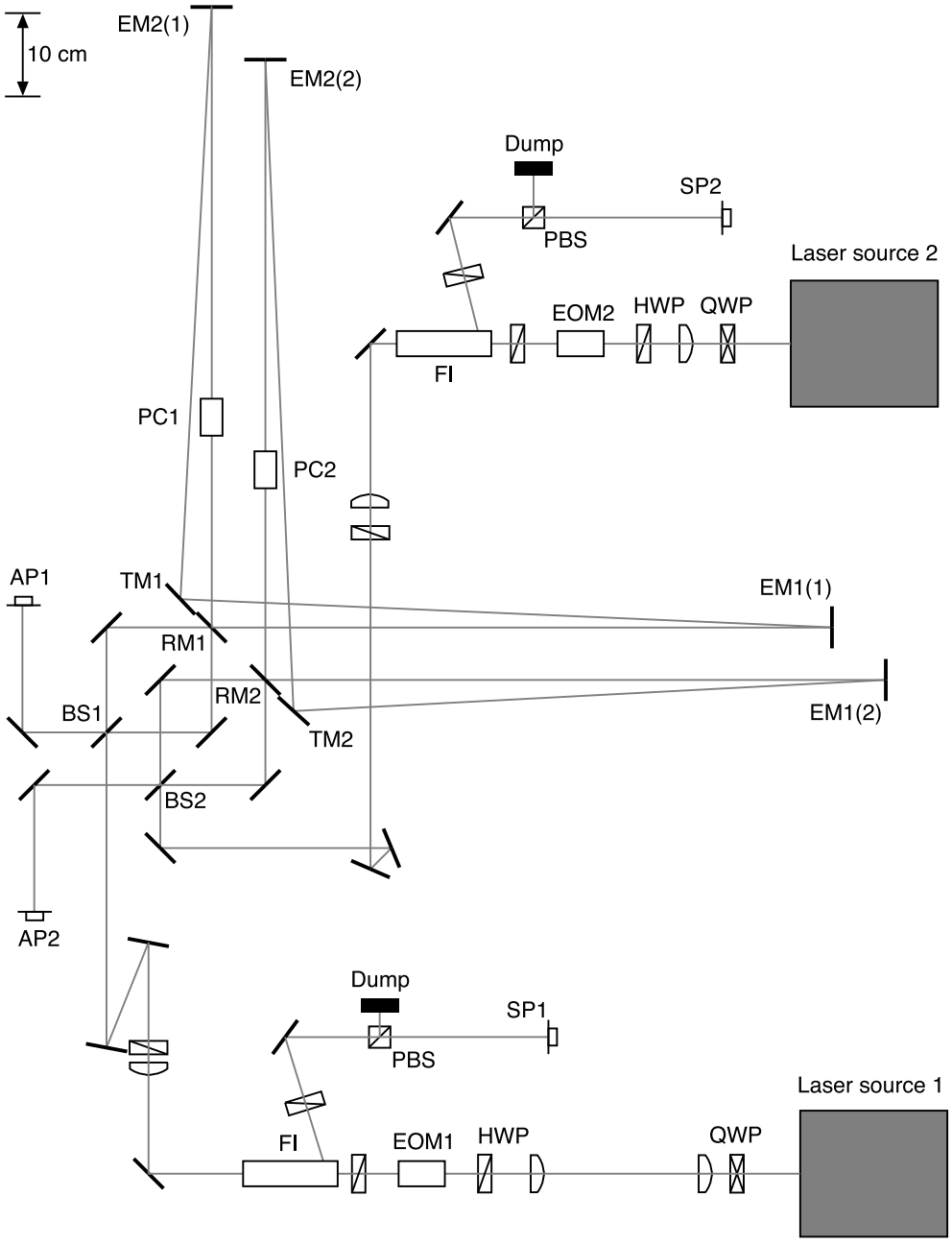

Figure 6.11: Optical design of the experiment with two SRIs, where optics are referred to beam splitter (BS), recycling mirror (RM), transfer mirror (TM), end mirror (EM), symmetric port (SP), antisymmetric port (AP), polarization beam splitter (PBS), Faraday isolator (FI), Pockels cell (PC), electro-optic phase modulator (EOM), half-wave plate (HWP), and quarter-wave plate (QWP). The suffixes "1" or "2" attached to each component indicate that the component belongs to IFO-1 or IFO-2, respectively. The figure is provided by T. Akutsu [169].

optical table [50]. In Fig. 6.11, the optical design of the experiment is shown. Hereafter we refer to the two interferometer as IFO-1 and IFO-2.

Each interferometer has a 75 cm-baseline cavity in order to be sensitive to GWs at 100 MHz. The size of Sagnac interferometer, which is the part in front of the recycling cavity, is relatively small (~ 12.5 cm) and its contribution to GW signal is insignificant compared to that of the cavity. Two SRIs are put within a range ~ 10 cm so that the overlap reduction function has nearly ideal value. The laser source is a Nd:YAG laser with the wavelength 1064 nm and the power 0.5 W. The laser frequency is stabilized to the recycling cavity by the Pound-Drever-Hall technique [170], using a radio-frequency (RF) sideband ($f_{RF} = 85.4$ MHz) modulated by EO1 in Fig. 6.12. The lasers of two interferometers are independent and have no correlation between them. Pockels cells are inserted in the recycling cavities and are used for calibration of GW signals. The reflectivity of the recycling mirror is $R_F^2 = 0.985 \pm 0.005$ and gives relatively low optical amplification, $\alpha(100\,\mathrm{MHz}) \sim 100$. This is because this experiment is the first step toward the direct detection of a GWB at 100 MHz.

GW signals are down-converted in frequency and are registered as output data, as depicted in Fig. 6.12. Since the BS is not exactly balanced, small fraction of the RF sideband leak into PD2. Hence, electrical signals at intermediate frequencies (IF), $f_{\mathrm{IF}} \equiv f_{\mathrm{GW}} - f_{\mathrm{RF}} \sim 15$ MHz, can be detected at PD2, where f_{GW} is the frequency of GWs. However, IF frequency is still too high to be sampled with an inexpensive data acquisition (DAQ) system. The IF signals are subsequently down-converted into audio-frequency (AF) signals at $f_{\mathrm{AF}} \equiv f_{\mathrm{IF}} - f_{\mathrm{LO}} \sim 3$ kHz with a local oscillator (LO), whose frequency is $f_{\mathrm{LO}} = 14.696840$ MHz.

The sensitivity to GW strain amplitude [6] is shown in Fig. 6.13. Red (solid) and green (dotted) curves are for IFO-1 and IFO-2, respectively. For IFO-1, the best sensitivity is $6.4\times10^{-17}\,\mathrm{Hz}^{-1/2}$ at 100.0 MHz, for IFO-2, $8.5\times10^{-17}\,\mathrm{Hz}^{-1/2}$ at 100.1 MHz

6.4.2 Data analysis

We define a cross-correlation statistic:

$$Z \equiv \frac{1}{T}\int_{-T/2}^{T/2} dt \int_{-T/2}^{T/2} dt'\, s_1(t) s_2(t') Q(t-t') \ ,$$

which is the normalized (divided by T) version of the cross-correlation signal, Eq. (5.5), and is approximated to

$$Z \approx \frac{1}{T}\int_{f_{\mathrm{min}}}^{f_{\mathrm{max}}} df\, \tilde{s}_1^*(f)\tilde{s}_2(f)\tilde{Q}(f) \ . \tag{6.23}$$

The mean and variance of Z are calculated, as well as Eqs. (5.9) and (5.12) except

[6] When the detector output is converted into detectable GW strain amplitude, it is assumed that a GW with optimal polarization are propagating vertical to the interferometer plane.

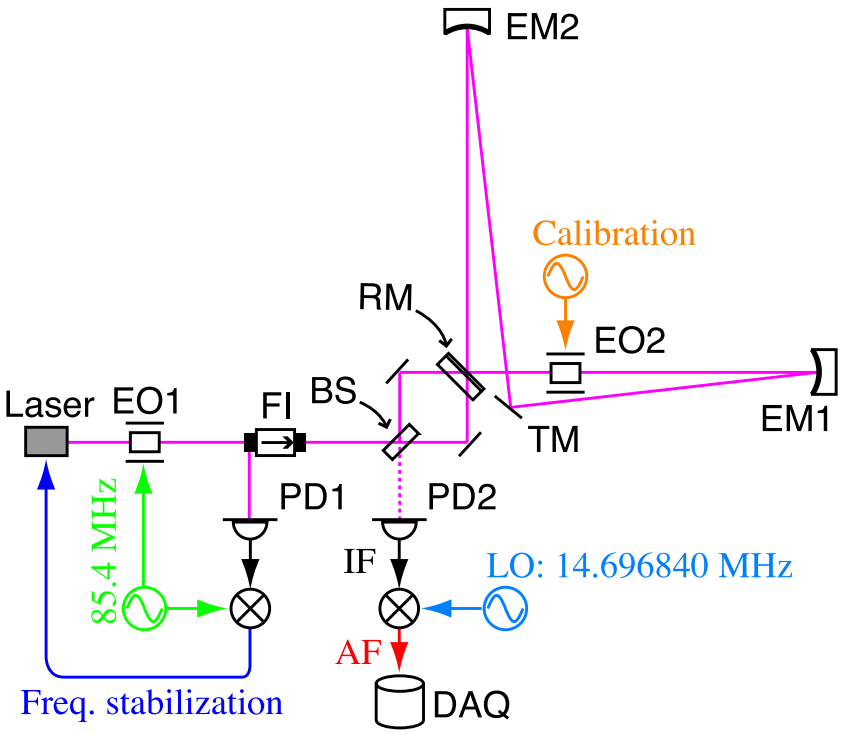

Figure 6.12: Schematic view of one of the interferometers [50]. DAQ: data aquisition system, EO: electro-optic phase modulator, PD: photodetector, LO: local oscillator, IF: intermediate frequency, and AF: audio frequency. Other acronyms are the same as those in Fig. 6.11.

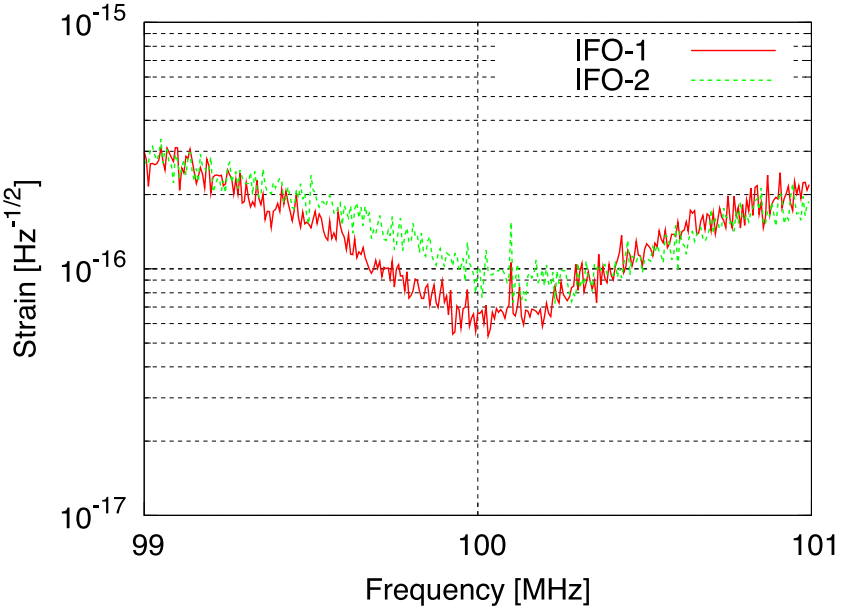

Figure 6.13: Noise curve of interferometers: IFO-1 (red, solid) and IFO-2 (green, dotted) [50]. The peaks at 100.1 MHz are generated for calibration.

for the division by T and the finite integration range, and are given by

$$\mu_Z = \langle Z \rangle = \frac{3H_0^2}{20\pi^2} 2 \int_{f_{\rm min}}^{f_{\rm max}} df |f|^{-3} \Omega_{\rm gw}(|f|) \gamma(|f|) \tilde{Q}(f) \,, \tag{6.24}$$

$$\sigma_Z^2 = \langle Z^2 \rangle - \langle Z \rangle^2 = \frac{1}{2T} \int_{f_{\rm min}}^{f_{\rm max}} df \, P_1(|f|) P_2(|f|) \, |\tilde{Q}(f)|^2 \,. \tag{6.25}$$

We will assume a frequency-independent spectrum of $\Omega_{\rm gw}$. This assumption is well motivated by the narrow band sensitivity of the detector. For the choice of the optimal filter in Eq. (5.15),

$$\tilde{Q}(f) = \mathcal{K} \frac{\gamma(f)}{|f|^3 P_1(|f|) P_2(|f|)} \,,$$

Eqs. (6.24) and (6.25) become

$$\mu_Z = \frac{3H_0^2}{20\pi^2} \Omega_{\rm gw} \mathcal{K} \left[2 \int_{f_{\rm min}}^{f_{\rm max}} df \frac{\gamma^2(f)}{f^6 P_1(f) P_2(f)} \right] \,,$$

$$\sigma_Z^2 = \frac{\mathcal{K}^2}{4T} \left[2 \int_{f_{\rm min}}^{f_{\rm max}} df \frac{\gamma^2(f)}{f^6 P_1(f) P_2(f)} \right] \,.$$

Choosing the normalization constant [7] as

$$\mathcal{K} = \left[2 \int_{f_{\rm min}}^{f_{\rm max}} df \frac{\gamma^2(f)}{f^6 P_1(f) P_2(f)} \right]^{-1} \,,$$

we obtain

$$\mu_Z = \frac{3H_0^2}{20\pi^2} \Omega_{\rm gw} \,, \qquad \sigma_Z^2 = \frac{\mathcal{K}}{4T} \,.$$

The SNR is defined as $|\mu_Z|/\sigma_Z$, which gives the same formula as Eq. (5.16). Note that the above choice of the normalization constant does not affect the SNR.

The observation has been done on 17 September 2007 (in Japanese standard time) at Mitaka, Tokyo, Japan. The measurement time is $T = 1070.5\,$sec. The data record is divided into $N = 439$ segments. The cross correlation and its uncertainty are calculated for each segment, yielding a set $\{Z_I, \sigma_{Z_I}\}$ with I labeling the intervals. The ensemble averages in Eqs. (6.24) and (6.25) are approximated by taking a weighted average over all intervals:

$$\mu_Z = \frac{1}{\sigma_Z^{-2}} \sum_{I=1}^{N} \frac{Z_I}{\sigma_{Z_I}^2} \,, \qquad \sigma_Z^{-2} = \sum_{I=1}^{N} \frac{1}{\sigma_{Z_I}^2} \,. \tag{6.26}$$

As for the integration range in Eq. (6.23), we choose the range from 2.08 to 4.19 kHz for AF signal, corresponding to a 2-kHz bandwidth around 100.1 MHz for GW signals.

The cross-correlation estimates, μ_Z and σ_Z, are shown in Fig. 6.14. Estimation of μ_Z is plotted as the red filled circles. The black curves enclose the two-sided 90% C.L. interval of μ_Z: $[\mu_Z - 1.65\,\sigma_Z,\ \mu_Z + 1.65\,\sigma_Z]$. We obtained $\mu_Z = 4.9 \times 10^{-12}\,{\rm sec}^{-2}$ with $\sigma_Z = 3.7 \times 10^{-12}\,{\rm sec}^{-2}$ after the integration of 1070.5 seconds, still including $\mu_Z = 0$

[7] The normalization constant has dimension of $\sec^{-3}$, then μ_Z and σ_Z have dimensions of $\sec^{-2}$.

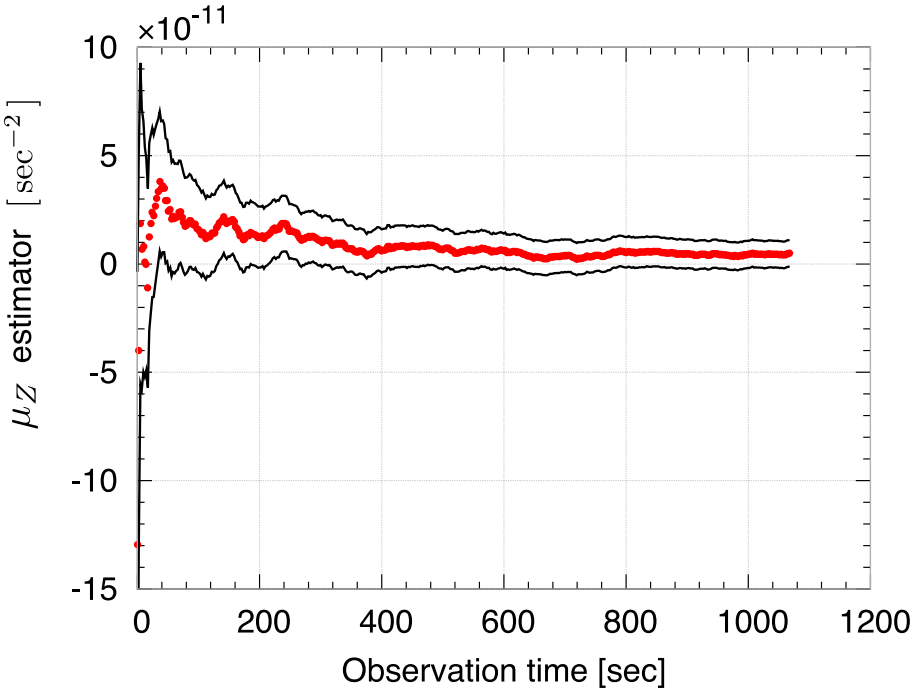

Figure 6.14: Estimated μ_Z (red filled circle) and its uncertain range $\mu_Z \pm 1.65\,\sigma_Z$ (black solid curve), which corresponds to 90% C.L. intervals [50].

within a 90% C.L. range, $\mu_Z \pm 1.65\,\sigma_Z$. Therefore, no signature of the existence of GWB was found. We can also conclude that a random noise dominates the cross-correlation signal, because the uncertainty σ_Z decreases proportional to $T^{-1/2}$.

No detection of GWB allows us to derive the upper limit on $\Omega_{\rm gw}$. From Eq. (6.26), we finds the upper limit [50], defined as a one-sided 90% confidence level corresponding to $\mu_Z + 1.28\,\sigma_Z$,

$$h_0^2 \Omega_{\rm gw}|_{100\,\rm MHz} \leq 6.0 \times 10^{+25} \ .$$

This limit is the first step of the experiment, and is not stringent at all. However, we improved the previous constraint on the GWB [45] by eight orders of magnitude.

Chapter 7

Resonant speed meter

In the previous chapter, it has been shown that a L-shaped SRI can amplify GW signal at resonant frequencies. However, mirror displacement noise is also amplified. When we increase the finesse of a cavity and improve the sensitivity beyond the goal sensitivity in the previous section, the amplified displacement noise would limit the sensitivity. Thus, it is a crucial defect of the L-shaped SRI.

In this chapter, we propose a resonant speed meter [168], as a displacement noise-canceled configuration [1], based on a ring-shaped synchronous recycling interferometer. In this method, the displacements of mirrors are sensed at different times with the interval Δt. At the frequency $(\Delta t)^{-1}$, the phase of the mirror motion rotates by 2π during one interval Δt. This means that the beams experience the mirror displacement with the same phase. Thus, the mirror displacements at different times can be canceled by subtracting the signals of these beams. Note that this cancellation occurs at the multiple frequencies of $(\Delta t)^{-1}$, and that residual displacement noise remains at other frequencies, as is well known in a Sagnac interferometer [175]. On the other hand, the cavity has to be designed to amplify the GW signals. Such a design is possible if one takes advantage of the quadrupole nature of GWs. At the noise cancellation frequency $(\Delta t)^{-1}$, if one beam propagates in one direction during the first half period and in the right-angled direction during the other half period, the GW signal can survive. For the beam propagating on the same path in the opposite direction, the GW signal with the opposite sign can also survive. Then, subtracting the two beams gives an amplified GW signal. The remarkable feature of this interferometer is that, at certain frequencies, gravitational-wave signals are amplified, while displacement noises are not.

[1] Displacement noise-free interferometry is originally proposed in Kawamura and Chen [171], and has been developed by [172, 173, 174]. However, since all design uses no cavity, the shot-noise level is the same as that of a Michelson interferometer. The resonant speed meter is the first design, which uses a cavity.

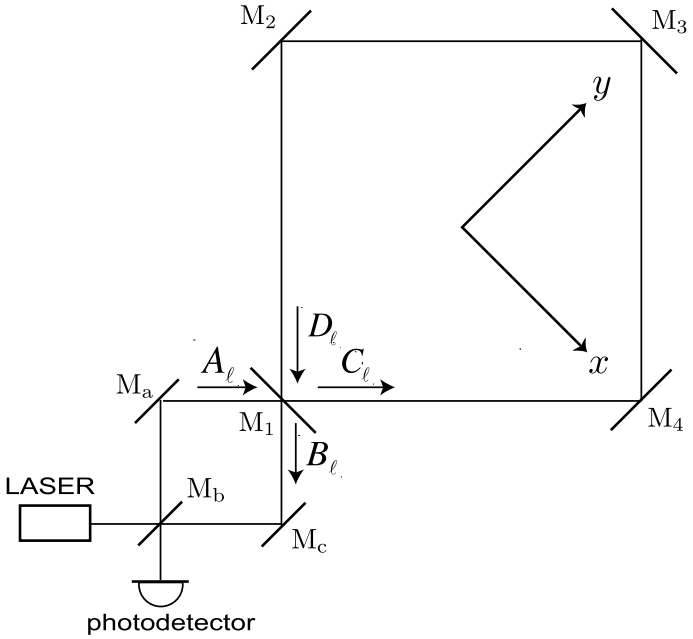

Figure 7.1: Design of a resonant speed meter. A synchronous recycling cavity is composed of the four mirrors $M_1 - M_4$. The electric fields of a CCW beam A_ℓ, B_ℓ, C_ℓ, and D_ℓ are shown. The fields of CW beam are obtained by reversing along the y axis.

7.1 Detector design and sensitivity

7.1.1 Detector response

The detector configuration of the resonant speed meter is shown in Fig. 7.1. Laser beams divided at the balanced beam splitter M_b are reflected by completely reflective mirrors M_a and M_c, and enter the (ring-shaped) synchronous recycling cavity, which is formed by an input mirror M_1 and three high-reflective mirrors $M_2 - M_4$. In the cavity, each beam circulates clockwise (CW) and counterclockwise (CCW), then leaves the cavity and is finally recombined at the beam splitter M_b [2]. First, we will derive the detector responses to mirror displacements and GWs in the resonant speed meter, and show that, at certain frequencies, the displacement noises can be suppressed, while GW signals are amplified. We also show that the detector sensitivity to GWs can be improved proportional to the circulating number of light in the cavity.

M_1 has an amplitude reflectivity and transmissivity (R_F, T_F). As for the three other mirrors M_2, M_3, M_4, one can deal with the reflectivities introducing the composite reflectivity R_E. For simplicity, none of the mirrors have loss. Let us denote the displacement of M_1, M_2, M_3, and M_4, in the absence of GWs, as $y_1(t)$, $x_2(t)$, $y_3(t)$, and $x_4(t)$, respectively, where the coordinates x and y are defined in Fig. 7.1. Electric fields

[2]This design is well known as a laser-ring gyroscope. It picks up the Earth rotation and shifts the frequency of the counterpropagating beams, which is called the Sagnac effect. The effect can be ignored when the size of the detector is relatively small. However, for a large detector, some treatment must be done to compensate the phase shift.

in the cavity are phase-shifted due to the GWs and the displacements of the mirrors. The field circulating CCW (denoted by fixing the subscript ℓ) can be written as

$$\begin{aligned} D_\ell(t) &= R_E C_\ell(t-4\tau) \\ &\quad \times \exp\left[i\phi_\ell^{(g)}(t) + \sqrt{2}\, i\omega/c\,\{-x_2(t-\tau) + y_3(t-2\tau) + x_4(t-3\tau)\}\right], \end{aligned} \tag{7.1}$$

where $\tau \equiv L/c$, L is the side length of the cavity, and ω is the angular frequency of laser light. $\phi_\ell^{(g)}(t)$ is the phase shift created by the GW and is expressed as the sum of each-side contribution during the propagation in the cavity,

$$\phi_\ell^{(g)}(t) \equiv \phi_{21}(t) + \phi_{32}(t-\tau) + \phi_{43}(t-2\tau) + \phi_{14}(t-3\tau)\,, \tag{7.2}$$

where, say, $\phi_{21}(t)$ is the phase shift due to the GW during the light trip from M_2 to M_1. The junction conditions at M_1 are

$$C_\ell(t) = R_F D_\ell(t)\, e^{-\sqrt{2}\, i\,\omega\, y_1(t)/c} + T_F A_\ell(t)\,, \tag{7.3}$$

$$B_\ell(t) = T_F D_\ell(t) - R_F A_\ell(t)\, e^{\sqrt{2}\, i\,\omega\, y_1(t)/c}\,. \tag{7.4}$$

Equations (7.1), (7.3), and (7.4) are solved separately from the CW fields, and give

$$\begin{aligned} B_\ell(t) &= -R_F A_\ell(t)\, e^{\sqrt{2}\, i\,\omega\, y_1(t)/c} + \sum_{k=1}^{\infty} T_F^2 R_E^k R_F^{k-1} A_\ell(t-4k\tau) \\ &\quad \times \exp\Bigg[\sqrt{2}\, i\,\omega\, y_1(t-4k\tau)/c \\ &\qquad + i\sum_{k'=1}^{k}\left\{\phi_\ell^{(g)}\big[t-4(k'-1)\tau\big] + \phi_\ell^{(d)}\big[t-4(k'-1)\tau\big]\right\}\Bigg], \end{aligned}$$

where $\phi_\ell^{(d)}(t)$ is the phase shift due to the displacement of the mirrors and is expressed by

$$\phi_\ell^{(d)}(t) \equiv \frac{\sqrt{2}\,\omega}{c}\left[-x_2(t-\tau) + y_3(t-2\tau) + x_4(t-3\tau) - y_1(t-4\tau)\right]. \tag{7.5}$$

We assume that the carrier field at M_1 is $A_\ell(t) = A_0 e^{i\omega t}$ and nonperturbed cavity length satisfies the resonant condition $4\omega\tau = 2\pi n$, $n = 1, 2, \cdots$. In addition, $|\phi_\ell^{(g)}| \ll 1$, $|\phi_\ell^{(d)}| \ll 1$, and $\omega\,|y_1|/c \ll 1$ are assumed. Using these assumptions and defining $\mathcal{T}_\ell(t) \equiv B_\ell(t)/A_\ell(t)$, we obtain

$$\begin{aligned} \mathcal{T}_\ell(t) &\approx -R_F\Bigg[1 + \sqrt{2} i\,\omega\, y_1(t)/c \\ &\qquad - T_F^2 \sum_{k=1}^{\infty} R_E^k R_F^{k-2}\Bigg\{1 + \sqrt{2} i\,\omega\, y_1(t-4k\tau)/c \\ &\qquad + i\sum_{k'=1}^{k}\Big(\phi_\ell^{(g)}\big[t-4(k'-1)\big] + \phi_\ell^{(d)}\big[t-4(k'-1)\big]\Big)\Bigg\}\Bigg]. \end{aligned} \tag{7.6}$$

Fourier transformation of Eq. (7.6), it can be written in the form,

$$\begin{aligned} \tilde{\mathcal{T}}_\ell(\Omega) &= \sqrt{2}\, i\,\omega\beta'(\Omega)\tilde{y_1}/c + i\alpha'(\Omega)(\tilde{\phi}_\ell^{(g)} + \tilde{\phi}_\ell^{(d)})\,, \\ \beta'(\Omega) &\equiv \frac{-R_F + R_E e^{-4i\Omega\tau}}{1 - R_F R_E e^{-4i\Omega\tau}}\,, \end{aligned} \tag{7.7}$$

and $\alpha'(\Omega)$ is defined in (6.12). Here $\beta'(\Omega)$ and $\alpha'(\Omega)$ are optical amplification factors due to the cavity. According to the axisymmetry of the system along the y axis, the transfer function for the CW beam is easily obtained,

$$\tilde{\mathcal{T}}_r(\Omega) = \sqrt{2}\, i\,\omega\beta'(\Omega)\tilde{y_1}/c + i\alpha'(\Omega)(\tilde{\phi}_r^{(g)} + \tilde{\phi}_r^{(d)}). \tag{7.8}$$

The differential of the two beams is detected at the photodetector, and gives

$$\begin{aligned} \tilde{\mathcal{T}}(\Omega) &\equiv \tilde{\mathcal{T}}_r(\Omega) - \tilde{\mathcal{T}}_\ell(\Omega) \\ &= -i\alpha'\big[(\tilde{\phi}_r^{(g)} - \tilde{\phi}_\ell^{(g)}) + (\tilde{\phi}_r^{(d)} - \tilde{\phi}_\ell^{(d)})\big]\,, \\ \tilde{\phi}_r^{(d)} - \tilde{\phi}_\ell^{(d)} &= \frac{2\sqrt{2}\, i\,\omega}{c}\, e^{-2i\Omega\tau} \sin\Omega\tau\,(\tilde{x}_2 + \tilde{x}_4)\,. \end{aligned} \tag{7.9}$$

At this stage, the displacements $\tilde{y}_1$ and $\tilde{y}_3$ in Eqs. (7.7) and (7.8) are automatically canceled out at any frequencies, because the CW and CCW beams simultaneously experience the displacement of M_1 and M_3 [3]. In addition, at the frequencies that satisfy $\Omega\tau = n\pi$, $n = 1, 2, \cdots$, Eq. (7.9) gives exactly zero, then all displacement noises vanish. This is because the CW and CCW beams in the cavity experience the displacement of M_2 and M_4 with the same phase, though the time of reflection is shifted by multiples of the period. Therefore, in our detector, displacement noises in the cavity are not amplified around the cancellation frequencies, though the cavity is on resonance.

Suppose that a GW propagates in the direction vertical to the detector plane with the polarization along the direction M_1-M_2 and M_1-M_4. In the transverse-traceless gauge, it can be written as $\mathbf{h}^{TT}(t,z) = h(t - z/c)[\mathbf{u}\otimes\mathbf{u} - \mathbf{v}\otimes\mathbf{v}]$, where $\mathbf{u}$ and $\mathbf{v}$ are unit vectors directed from M_1 toward M_2 and M_4, respectively. Let the detector be on the $x-y$ plane and set $z = 0$, for simplicity. The GW-induced phase shift of light during the trip from M_i to M_j is given by [176]

$$\tilde{\phi}_{ij}(\Omega) = \pm\tilde{h}\omega/\Omega \times e^{-i\Omega\tau/2}\, \sin(\Omega\tau/2). \tag{7.10}$$

The positive and negative signs correspond to the vertical and horizontal propagations in Fig. 7.1. $\tilde{h}$ is the Fourier component of GW amplitude. From Eq. (7.2) and the counterpart for the CW beam, the Fourier component of the total GW response is

$$\tilde{\phi}_r^{(g)} - \tilde{\phi}_\ell^{(g)} = \frac{8i\,\tilde{h}\omega}{\Omega}\, e^{-2i\Omega\tau} \cos(\Omega\tau)\, \sin^2(\Omega\tau/2)\,. \tag{7.11}$$

[3] The arrival times of light at M_1, or M_3 depend on the displacement of M_2 and M_4. However, it is the order of $\mathcal{O}(x^2/L^2)$ and can be ignored.

So far, we have ignored the contribution of displacements at the mirrors in the Sagnac part, M_a, M_b, and M_c, in Fig. 7.1. In fact, these displacements are not canceled, and will contribute as residual noise. The contribution is

$$\tilde{\phi}_r^{(s)} - \tilde{\phi}_\ell^{(s)} = -\sqrt{2}\omega/c\ (\tilde{x}_a - \tilde{x}_b + \tilde{x}_c),$$

where $\tilde{x}_a$, $\tilde{x}_b$, and $\tilde{x}_c$ are Fourier components of the displacements of the mirrors, M_a, M_b, and M_c.

Strictry speaking, in principle, the residual displacement noise can be canceled if the Sagnac lengths are made comparable to the cavity length. However, the created dip on a noise curve is too narrow to be practically useful, because beams sense the mirror displacement at the different moments with large time lag (before entering and after leaving the cavity). Therefore, we will not consider such a option here.

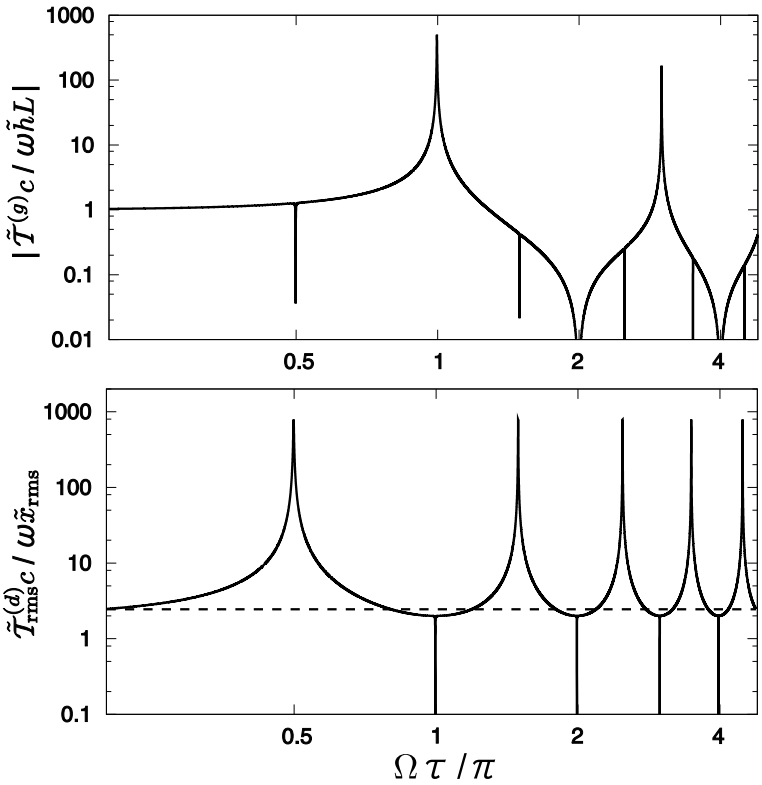

Figure 7.2: GW response $\tilde{\mathcal{T}}^{(g)}_{\rm rms}(\Omega)$ (upper figure), and displacement responses $\tilde{\mathcal{T}}^{(d)}_{\rm rms}(\Omega)$ and $\tilde{\mathcal{T}}^{(s)}_{\rm rms}(\Omega)$ (solid and dashed lines in the lower figure, respectively). Each quantity is normalized to be dimensionless. The reflectivities of mirrors are $R_F = 0.99$ and $R_E = 1$ for the illustration, which corresponds to $\alpha' \approx 200$.

Let us define each contribution of the total detector output as

$$\begin{aligned}
\tilde{\mathcal{T}}^{(g)}(\Omega) &\equiv i\alpha'(\tilde{\phi}_r^{(g)} - \tilde{\phi}_\ell^{(g)}), \\
\tilde{\mathcal{T}}^{(d)}(\Omega) &\equiv i\alpha'(\tilde{\phi}_r^{(d)} - \tilde{\phi}_\ell^{(d)}), \qquad (7.12) \\
\tilde{\mathcal{T}}^{(s)}(\Omega) &\equiv \tilde{\phi}_r^{(s)} - \tilde{\phi}_\ell^{(s)}. \qquad (7.13)
\end{aligned}$$

Assuming that the magnitude of disturbances at each mirror is the same (the phase is not), we define $\tilde{x}_{\rm rms} = \sqrt{\langle|\tilde{x}_i|^2\rangle}$, where $i = 1, 2, 3, 4, a, b, c$, and $\langle\cdots\rangle$ denotes the ensemble average. Then, root mean squares of Eqs. (7.12) and (7.13) are

$$\tilde{\mathcal{T}}^{(d)}_{\rm rms}(\Omega) = \frac{4\omega}{c}\,|\alpha'\,\sin\Omega\tau|\,\tilde{x}_{\rm rms}\,, \tag{7.14}$$

$$\tilde{\mathcal{T}}^{(s)}_{\rm rms}(\Omega) = \frac{\sqrt{6}\,\omega}{c}\,\tilde{x}_{\rm rms}\,. \tag{7.15}$$

The GW response $\tilde{\mathcal{T}}^{(g)}$, and the displacement responses $\tilde{\mathcal{T}}^{(d)}_{\rm rms}$ and $\tilde{\mathcal{T}}^{(s)}_{\rm rms}$, are shown in Fig. 7.2 as a function of normalized frequency $\Omega\tau/\pi$. The GW signal resonates at $\Omega_{\rm res} = 2\pi \times (2m-1)/2\tau$, while the cancellation of the displacement noise in the cavity occurs at $\Omega_{\rm cancel} = 2\pi \times n/2\tau$, where $m, n = 1, 2, \cdots$. For $m = n = 1$, the GW signal is amplified, while the cavity displacement noise is not, which can be explicitly seen from Eqs. (7.9) and (7.11) (In a L-shaped synchronous recycling interferometer in Chap. 6, $\Omega_{\rm res} = 2\pi \times (2m-1)/4\tau$ and $\Omega_{\rm cancel} = 2\pi \times 2n/4\tau$. Then, no solution exists.). Note that, in Fig. 7.2, the displacement response nulls at cancellation frequencies are so sharp because of the cavity enhancement of the residual noise around the frequencies. The essential is that the degeneracy between the amplification frequencies for GW signal and displacement noise is broken. Thus, there exist the frequencies where the GW signal is amplified and the displacement noise is canceled.

The noise cancellation mechanism is the same as that of a speed meter [177, 178, 179, 180, 181]. This can be understood explicitly in a time domain. From Eq. (7.5) and the CW counterpart, the round-trip displacement response in the cavity around the cancellation frequency $\Omega_{\rm res}$ can be written as

$$\begin{aligned}\phi^{(d)}_r(t) - \phi^{(d)}_\ell(t) &= \frac{\sqrt{2}\,\omega}{c}\,[x_2(t-\tau) - x_2(t-3\tau) + x_4(t-\tau) - x_4(t-3\tau)] \\ &\sim \frac{2\sqrt{2}\,\omega\tau}{c}\left(\frac{\delta\Omega}{\Omega_{\rm res}}\right)[v_2(t-\tau) + v_4(t-\tau)]\,,\end{aligned}$$

where $\delta\Omega$ is detuned frequency from the resonance, and we used

$$x_2(t-\tau) \approx x_2(t-3\tau) + 2\tau\left(\frac{\delta\Omega}{\Omega_{\rm res}}\right)v_2(t-\tau)\,.$$

Therefore, this detector senses not the mirror positions but the mirror velocities. Moreover, the GW signal is amplified by the resonant cavity. This is the reason why we call it a *resonant speed meter*.

7.1.2 Noise curves

The signal-to-noise ratio (SNR) can be calculated by SNR $= \tilde{\mathcal{T}}^{(g)} / (\tilde{\mathcal{T}}^{(d)}_{\rm rms} + \tilde{\mathcal{T}}^{(s)}_{\rm rms} + \tilde{\mathcal{T}}^{(q)})$. Here we added quantum noise $\tilde{\mathcal{T}}^{(q)}$, which has a frequency-independent spectrum. In Fig. 7.3, the noise curve of each component is shown. For the illustration of the noise cancellation, we choose the displacement noise significantly dominant, namely, $\tilde{x}_{\rm rms} = 10\,\tilde{x}_{\rm shot}$ at $\Omega\tau/\pi = 1$, where $\tilde{x}_{\rm shot} \equiv \tilde{\mathcal{T}}^{(q)}\,c/\omega$ (Note that whether the displacement

noise is dominant or not depends on the detection frequencies.). Around $\Omega\tau/\pi = 1$, cavity displacement noise is canceled. The cancellation does not exactly occur at other frequencies and the residual noise creates a dip on the displacement noise spectrum at the cancellation frequencies. The bandwidth of the dip is determined by the optical path length between M_2 and M_4, in other words, by the optical time lag that CW or CCW beams experience the displacements of M_2 and M_4. The time lag is 2τ and gives the factor $\sin\Omega\tau$ in Eq. (7.14). The total sensitivity at $\Omega\tau/\pi = 1$ is limited by residual displacement noise in the Sagnac part (or shot noise if the displacement noise is relatively small). However, both noises decrease proportional to α' because of the amplification of the GW signal. On the other hand, the displacement noise of the cavity mirrors is independent of α', but is already canceled around $\Omega\tau/\pi = 1$. Thus, within the narrow bandwidth, the total noise level diminishes as α increases.

In Fig. 7.4, the dependence of the relative total noise curve on α' is shown. The noise cancellation allows us to improve the sensitivity, being proportional to α' without being limited by displacement noises.

7.2 Quantum noise in a RSM

In the previous section, we derived the response of the RSM, and illustrated the sensitivity to GWs, where the displacement noise of a cavity is completely canceled at the resonant frequencies. The analysis is done only in classical regime, where forces on the mirrors have classical origins. In quantum mechanics, however, vacuum fluctuations unavoidably come into the system and contribute to noises (shot noise and radiation-pressure noise) [182, 183]. Particularly, radiation-pressure noise is caused by the coupling between electromagnetic fields of vacuum fluctuations and carriers, and have quantum origins. Consequently, it should be checked whether the RSM works well even for quantum noise or not. If the radiation-pressure noise is canceled, the RSM could be a quantum nondemolition (QND) interferometer [184, 185]. Hence, it is also interesting to investigate how is the standard quantum limit (SQL) [186] (see also, [184] for the review) of the RSM, and whether the sensitivity of the RSM could overcome the SQL or not.

Recent works on quantum noise in a laser interferometer are based on a quantum formalism by Kimble *et al.* [185]. According to the formalism, we will calculate quantum noise in the RSM. Brief review of the quantum noise in a Fabry-Perot Michelson interferometer (FPMI) is provided in Appendix F.

7.2.1 Input-output relation

An electromagnetic field at the time t is written as

$$\begin{aligned} E_d(t) &= [D + E_{d1}(t)]\ \cos\omega t + E_{d2}(t)\ \sin\omega t\ , \\ E_{d1,2}(t) &= \sqrt{\frac{4\pi\hbar\omega}{\mathcal{A}c}} \int_0^\infty (d_{1,2}\ e^{-i\Omega t} + d_{1,2}^\dagger\ e^{i\Omega t}) \frac{d\Omega}{2\pi}\ . \end{aligned} \tag{7.16}$$

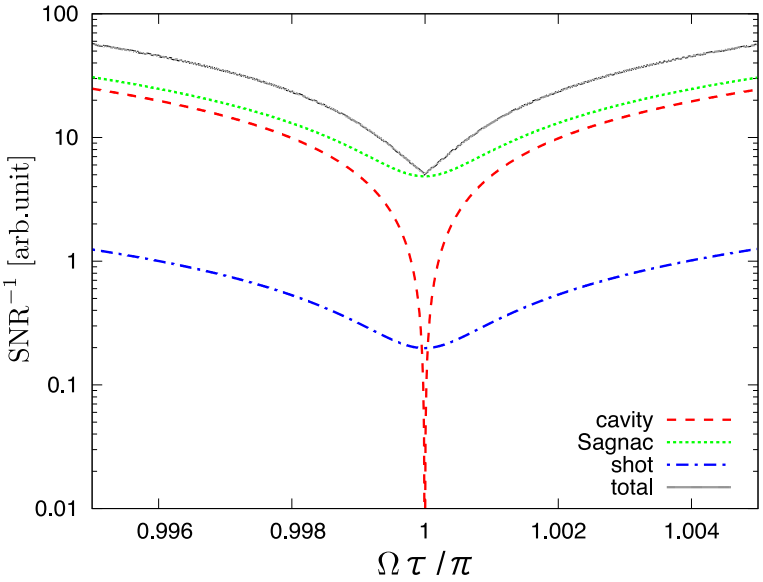

Figure 7.3: Relative noise curves of a resonant speed meter. The curves, "cavity", "Sagnac", and "shot" are the displacement noise in the cavity, the displacement noise in the Sagnac part, and quantum (shot) noise, respectively. The curve "total" is the sum of these three noises. The reflectivities are $R_F = 0.99$ and $R_E = 1$ ($\alpha' \approx 200$ at $\Omega\tau/\pi = 1$).

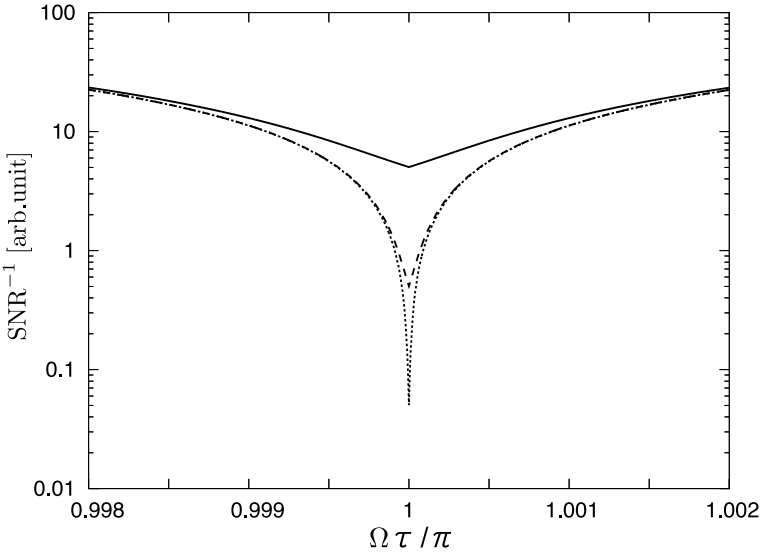

Figure 7.4: Dependence of relative total-noise curve on α. Solid, dashed, and dotted curves are when $\alpha' \approx 200, 2000, 20000$ at $\Omega\tau/\pi = 1$, corresponding to $R_F = 0.99, 0.999, 0.9999$, respectively, and $R_E = 1$.

The subscript of the field E indicates at where the field is defined. D is the amplitude of a carrier field, ω is the angular frequency of carrier light, and $\mathcal{A}$ is the effective cross-section area of a beam. The fields in the RSM are defined in Fig. 7.5. In this section, we set the reflection of the mirrors $R_F = R$ and $R_E = 1$ with no loss.

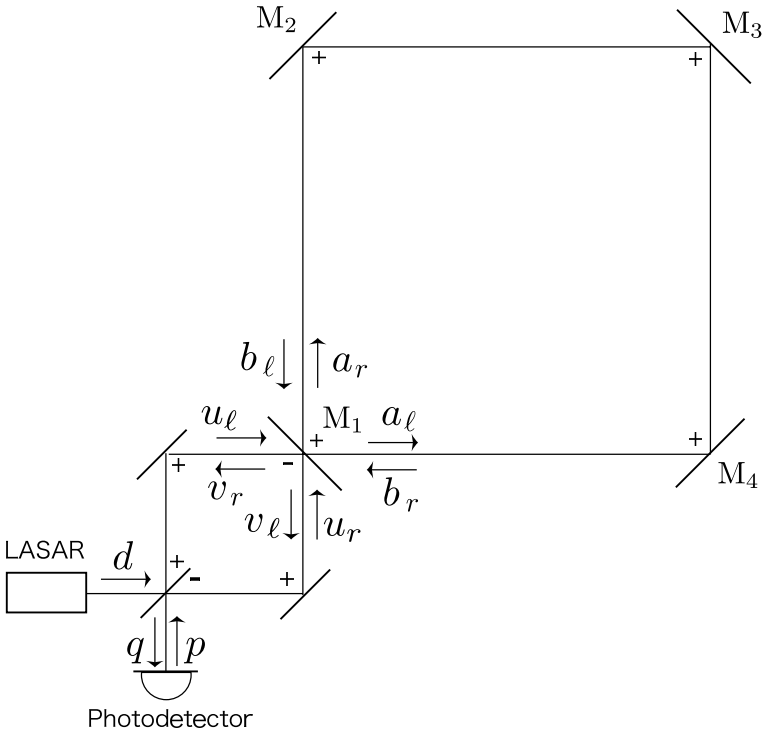

Figure 7.5: Electromagnetic fields in a RSM.

Carrier fields

With the input laser amplitude D, input laser power I_0 is given by

$$I_0 = \frac{\mathcal{A}c}{8\pi} D^2 \ .$$

Since CW and CCW beams are symmetric in the case of carrier fields, we consider only CW beam (fixed the subscript r). From the relations

$$\begin{aligned} U_r &= D/\sqrt{2}, & A_r &= B_r \ , \\ V_r &= -R\,U_r + T\,B_r, & A_r &= R\,B_r + T\,U_r \ , \end{aligned}$$

the carrier-field amplitude A_r in the cavity is

$$A_r = \frac{T}{1-R}\frac{D}{\sqrt{2}} \ .$$

Thus, the laser power inside the cavity is

$$I_c = \left(\frac{T}{1-R}\right)^2 \frac{I_0}{2} \ . \tag{7.17}$$

Sideband fields

Each field is related like

$$\begin{aligned} u_\ell &= \frac{1}{\sqrt{2}}(d+p), \qquad u_r = \frac{1}{\sqrt{2}}(d-p) \ , \\ q &= \frac{1}{\sqrt{2}}(v_r - v_\ell) \ , \end{aligned} \tag{7.18}$$

at the beam splitter, and

$$\begin{aligned} v_r &= -R\,u_r + T\,b_r, \qquad v_\ell = -R\,u_\ell + T\,b_\ell \ , \\ a_r &= R\,b_r + T\,u_r, \qquad a_\ell = R\,b_\ell + T\,u_\ell \ , \end{aligned} \tag{7.19}$$

at the recycling mirror M_1.

In the recycling cavity, we will first consider only CW beam (fixed the subscript r). The equations for the CCW beam is easily obtained from those for the CW beam. The fields before and after one round trip in the cavity are related by

$$E_{br}(t) = E_{ar}(t - 4\tau - \Delta t_r) \ , \tag{7.20}$$

where the perturbation of the retarded time Δt comes from that due to GWs and radiation pressure:

$$\Delta t_r = \Delta t_r^{\rm GW} + \Delta t_r^{\rm RP} \ .$$

Here we assume no classical noise, perturbing mirror positions. Substituting Eq. (7.16) into Eq. (7.20) and using the resonant condition $4\omega\tau = 2\pi n,\ n = 1, 2, \cdots$ and the condition $\Delta t_r \ll \tau$, the fields inside the cavity are approximately related as

$$b_{r1} = e^{4i\Omega\tau} a_{r1} \tag{7.21}$$

$$b_{r2} = e^{4i\Omega\tau} a_{r2} + \omega\sqrt{\frac{2I_c}{\hbar\omega}}\left[\tilde{\Delta t}_r^{\rm RP} + \tilde{\Delta t}_r^{\rm GW}\right] \ , \tag{7.22}$$

where Eq. (7.17) is used. Note that Eqs. (7.21) and (7.22) are valid up to the first order of the sideband amplitude and $\tilde{\Delta} t_r$. As for the CCW beam, $\tilde{b}_{\ell 1}$ and $\tilde{b}_{\ell 2}$ can be obtained by changing the subscripts $r \leftrightarrow \ell$ and $2 \leftrightarrow 4$ in Eqs. (7.21) and (7.22).

Radiation pressure

Radiation pressure is exerted on all mirrors in the cavity, and fluctuates them. However, since CW and CCW beams senses the displacement of the mirrors M_1 and M_3 simultaneously, the radiation pressure noise at M_1 and M_3 cancels when two beams are recombined at the beam splitter. Therefore, we do not take M_1 and M_3 into account, and the radiation-pressure noise comes from M_2 and M_4. For the CW beam, the retarded time due to the mirror displacements is

$$\Delta t_r^{\rm RP} = \frac{\sqrt{2}}{c}[x_2(t-3\tau) + x_4(t-\tau)] \ . \tag{7.23}$$

The classical part of radiation pressure force exerted on M_4 is given by

$$F_{\rm RP}(t) = \frac{\sqrt{2}W}{c} = \frac{\mathcal{A}}{2\sqrt{2}\pi}\left[\bar{E^2_{ar}}(t-3\tau) + \bar{E^2_{a\ell}}(t-\tau)\right] .$$

W is the power of the electromagnetic field, and $\bar{E^2}$ means E^2 is time-averaged over the time scale ω^{-1}. The fluctuating part of the radiation pressure is

$$\begin{aligned}\delta F_{\rm RP}(t) &= \frac{\mathcal{A}}{2\sqrt{2}\pi} A_r \left[E_{ar1}(t-3\tau) + E_{a\ell 1}(t-\tau)\right] \\ &= \frac{2\sqrt{\hbar\omega I_c}}{c}\int_{-\infty}^{\infty}(a_{r1}\, e^{3i\Omega\tau} + a_{\ell 1}\, e^{i\Omega\tau})\, e^{-i\Omega t}\frac{d\Omega}{2\pi} .\end{aligned}$$

We assume that the mirrors are at the balanced position by classical radiation pressure and gravity. Consequently, from the equation of motion, $\ddot{x}_4^{\rm BA}(t) = \delta F_{RP}(t)/m$, the Fourier component of x_4 is obtained,

$$\tilde{x}_4 = -\frac{2\sqrt{\hbar\omega I_c}}{m\Omega^2 c}(a_{r1}\, e^{3i\Omega\tau} + a_{\ell 1}\, e^{i\Omega\tau}) .$$

As for M_2, $\tilde{x}_2$ can be obtained by changing the subscripts $r \leftrightarrow \ell$ and $2 \leftrightarrow 4$,

$$\tilde{x}_2 = -\frac{2\sqrt{\hbar\omega I_c}}{m\Omega^2 c}(a_{\ell 1}\, e^{3i\Omega\tau} + a_{r1}\, e^{i\Omega\tau}) .$$

Therefore, the Fourier component of Eq. (7.23) is

$$\begin{aligned}\tilde{\Delta t}_r^{\rm RP} &= \frac{\sqrt{2}}{c}\left[\tilde{x}_2 e^{3i\Omega\tau} + \tilde{x}_4 e^{i\Omega\tau}\right] , \\ &= -\frac{4\sqrt{2\hbar\omega I_c}}{m\Omega^2 c^2} e^{4i\Omega\tau}\left[a_{r1} + a_{\ell 1}\,\cos 2\Omega\tau\right] . \qquad (7.24)\end{aligned}$$

As for the CCW beam, $\tilde{\Delta t}_\ell^{\rm RP}$ can be obtained by changing the subscripts $r \leftrightarrow \ell$ and $2 \leftrightarrow 4$ in Eq. (7.24).

At ultra-high frequencies, there is an awkward issue that the mirror does not respond to the radiation pressure as a rigid body. In other words, the fractional piece of the mirror can respond the radiation pressure. Consequently, one has to use an effective mirror mass for m in the above equations. For an accurate estimate of the effective mirror mass, one has to perform fully numerical calculations such as finite-element simulations. However, it can be roughly estimated with the beam cross-section area and the sound speed in the material of the mirror as

$$m_{\rm eff}(f) = \rho\,\mathcal{A}\,\frac{c_s}{f} ,$$

where ρ is the density of the mirror material, $\mathcal{A}$ is the beam spot size, c_s is the sound speed in the material of the mirror, and f_0 is an observation frequency. In the case of a fused silica, $\rho = 2.22\,{\rm g/cm^3}$, $c_s = 5.97\times10^{-3}\,{\rm cm}$. For $\mathcal{A} \approx 1\,{\rm mm}$ and $f = 100\,{\rm MHz}$, the effective mass is $m_{\rm eff} \approx 1.4\times10^{-4}\,{\rm g}$. This means that the radiation-pressure noise is ~ 7500 times larger than that in the rigid mirror at the same frequency.

GW signal

From Eq. (7.11), the retarded time due to GWs for the CW beam is

$$\tilde{\Delta}t_r^{\rm GW} = \frac{4\tilde{h}}{i\Omega}\, e^{2i\Omega\tau}\, \sin^2(\Omega\tau/2)\, \cos\Omega\tau\ . \tag{7.25}$$

For the CCW beam, $\tilde{\Delta}t_\ell^{\rm GW}$ can be obtained by changing the overall sign in the right-hand side of Eq. (7.25).

Total input-output relation

Combining Eqs. (7.18), (7.19), (7.21), (7.22), (7.24), and (7.25) and expressing the output field q with the input field p, we can finally obtain the total input-output relation:

$$\begin{aligned} q_1 &= e^{2i\Psi}\, p_1 \\ q_2 &= e^{2i\Psi}\, [p_2 - K_{\rm RSM}\, p_1] + \sqrt{2K_{\rm RSM}}\, e^{i\Psi} \left(\frac{\tilde{h}}{h_{\rm SQL}}\right) \end{aligned}$$

where

$$K_{\rm RSM}(\Omega) \equiv \frac{16\omega I_c}{m\Omega^2 c^2}\frac{T^2}{1+R^2-2R\,\cos 4\Omega\tau}\,\sin^2\Omega\tau\ , \tag{7.26}$$

$$\Psi(\Omega) \equiv \arctan\left[\frac{1+R}{1-R}\tan 2\Omega\tau\right] + \frac{\pi}{2}\ ,$$

$$h_{\rm SQL}(\Omega) \equiv \sqrt{\frac{2\hbar}{mc^2\,\sin^2\Omega\tau}}\left(\frac{\tan\Omega\tau}{\tan(\Omega\tau/2)}\right)\ . \tag{7.27}$$

7.2.2 Spectral density

We define the output field detected by the homodyne measurement with an arbitrary phase ζ:

$$\begin{aligned} q_\zeta &= q_1\,\cos\zeta + q_2\,\sin\zeta \\ &= e^{2i\Psi}\,[p_1\,\cos\zeta + (p_2 - K_{\rm RSM}\,p_1)\,\sin\zeta] + \sqrt{2K_{\rm RSM}}\, e^{i\Psi}\,\sin\zeta\left(\frac{\tilde{h}}{h_{\rm SQL}}\right)\ . \end{aligned} \tag{7.28}$$

We assume that the input state is in a vacuum state. The same procedure from Eq. (F.7) to Eq. (F.8) in Appendix F yields the noise spectral density

$$S_{\rm h}(\Omega) = \frac{h_{\rm SQL}^2}{2}\left[\frac{1+(\cot\zeta - K_{\rm RSM})^2}{K_{\rm RSM}}\right]\ . \tag{7.29}$$

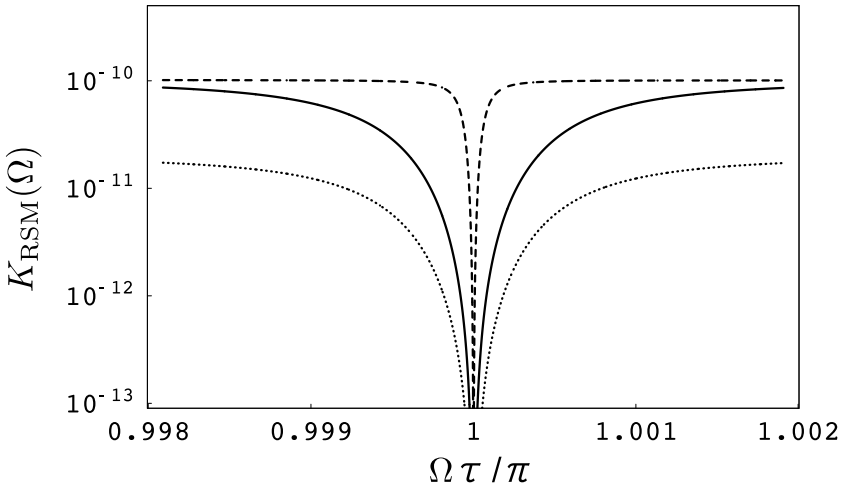

Figure 7.6: $K_{\rm RSM}$ when $R = 0.99$ and $I_0 = 100\,{\rm W}$ (solid curve), $R = 0.999$ and $I_0 = 100\,{\rm W}$ (dashed curve), $R = 0.99$ and $I_0 = 20\,{\rm W}$ (dotted curve), with parameters $\omega = 1.77 \times 10^{15}\,{\rm rad\,sec^{-1}}$, $L = 1.5\,{\rm m}$ and $m = 10^{-4}\,{\rm g}$ (corresponding to the effective mirror mass at 100 MHz.). These parameters are just for an illustrative purpose, and the corresponding radiation-pressure noise is negligibly small.

Since the fields in Eq. (7.28) are linear with respect to the amplitude, the spectral density can be decomposed into three parts: shot noise, radiation-pressure noise, and correlation noise. Devoting our attention to the mirror mass, each noise contribution in the spectral density is given by

$$\begin{aligned} S_{\rm h}^{\rm shot} &= \frac{h_{\rm SQL}^2}{2}\frac{1}{K_{\rm RSM}\sin^2\zeta}\ , \\ S_{\rm h}^{\rm RP} &= \frac{h_{\rm SQL}^2}{2}K_{\rm RSM}\ , \qquad (7.30) \\ S_{\rm h}^{\rm cor} &= -h_{\rm SQL}^2\cot\zeta\ . \qquad (7.31) \end{aligned}$$

Since the coefficient $K_{\rm RSM}$ is proportional to the laser power in the cavity, the shot noise and the radiation-pressure noise are inversely proportional and proportional to the power, respectively. This implies that, if the homodyne angle is selected as $\zeta = \pi/2$ so that the quadrature amplitudes have no quantum correlation between them, there is a minimum noise level at a certain frequency with fixed power. The noise level gives the SQL, which is

$$S_{\rm h} \geq h_{\rm SQL}^2 = \frac{2\hbar}{mc^2\,\sin^2\Omega\tau}\left(\frac{\tan\Omega\tau}{\tan(\Omega\tau/2)}\right)^2\ .$$

The equality is satisfied when $K_{\rm RSM} = 1$, and gives the definition in Eq. (7.27).

Can we overcome the SQL with quantum correlation in Eq. (7.31)? To minimize the noise, it is obvious from Eq. (7.29) that the homodyne phase should be selected so that $\zeta_{\rm FD}(\Omega) = {\rm arccot}[K_{\rm RSM}(\Omega)]$, which is frequency-dependent. However, since the RSM has

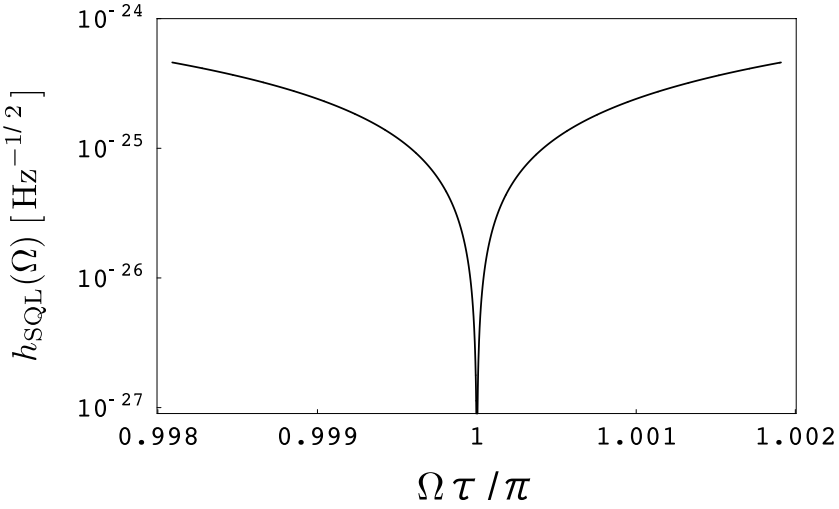

Figure 7.7: $h_{\rm SQL}$ with the mirror mass $m = 10^{-4}\,$g (corresponding to the effective mirror mass at 100 MHz.).

good sensitivity only in a narrow frequency band, the frequency-independent homodyne phase is adequate for us to optimize the noise at a resonant frequency. Therefore, the optimized homodyne phase at the first resonance of the RSM, $\Omega_{\rm res} = \pi/\tau$, is $\zeta_{\rm res} = \pi/2$. In this case, the quantum correlation vanishes, and one cannot circumvent the SQL. This is a natural consequence, because, in the RSM, the radiation-pressure noise is already canceled at the resonant frequency, as one can see from Eqs. (7.26) and (7.30). The plots of $K_{\rm RSM}$ and $h_{\rm SQL}$ around the resonant frequency are shown in Fig. 7.6 and Fig. 7.7.

In conclusion, in the RSM, the displacement noise including the radiation-pressure noise is automatically canceled, in contrast to the L-shaped SRI, in which the displacement noise is amplified. However, the SQL is not circumvented in the RSM, because the cancellation stems from a classical correlation. Thanks to the cancellation, the sensitivity at the resonant frequency is limited by shot noise, and is improved more and more by increasing both the finesse of the cavity and the laser power. Furthermore, it allows us to lower the resonant frequency by enlarging the detector size and to enhance the sensitivity to GWs, not being hindered by the displacement noise.

7.3 Sensitivity to GWB

In this section, let us calculate how much sensitivity to GWB one can achieve with two RSMs. According to the cancellation of the displacement noise of the cavity mirrors, the sensitivity of the RSM to GWB is limited only by shot noise [4]. Since the observational bandwidth of the RSM is narrow, the integrand of the formula for the SNR can be

[4]Residual noise in the Sagnac part cannot be canceled. However, it could be ignored because no amplification of the displacement noise occurs, while the GW signal is amplified.

regarded as frequency-dependent. So, Eq. (5.16) can be approximated to

$$\mathrm{SNR} \approx \frac{3H_0^2}{10\pi^2}\sqrt{T}\left[2\,\Delta f(f_0)\frac{\gamma^2(f_0)\Omega_{\rm gw}^2(f_0)}{f_0^6 P_1(f_0)P_2(f_0)}\right]^{1/2} ,$$

where f_0 is the resonant frequency, Δf is the observational bandwidth. We assume that the overlap reduction function is $\gamma_{\rm opt} = 0.377$ at the resonant frequency, as well as that for L-shaped SRI in Sec. 6.3.3 [5]. For SNR = 1, the minimum reachable $\Omega_{\rm gw}$ is

$$\Omega_{\rm gw}^{\rm min}(f_0) \approx \frac{10\pi^2 f_0^3}{3H_0^2\gamma_{\rm opt}}\sqrt{\frac{P_1(f_0)P_2(f_0)}{2\,T\Delta f(f_0)}} .$$

If we select the observation time $T = 1\,\mathrm{yr}$ and conservative parameters $I_0 = 100\,\mathrm{W}$ and $R = 0.99999$, $P_i|_{100\,\mathrm{MHz}} \approx 1.86\times10^{-47}$ and $\Delta f|_{100\,\mathrm{MHz}} \approx 100\,\mathrm{MHz}/\mathcal{F} \approx 160\,\mathrm{Hz}$. Then, $\Omega_{\rm gw}^{\rm min}|_{100\,\mathrm{MHz}} \approx 1.5\times10^{9}$. For advanced parameters $I_0 = 1000\,\mathrm{W}$ and $R = 0.999999$, $P_i|_{100\,\mathrm{MHz}} \approx 1.86\times10^{-50}$ and $\Delta f|_{100\,\mathrm{MHz}} \approx 16\,\mathrm{Hz}$. Then, $\Omega_{\rm gw}^{\rm min}|_{100\,\mathrm{MHz}} \approx 1.5\times10^{6}$. At 100 MHz, the limit is still weak and is not so interesting for cosmologists. If the detector size is larger, the resonant frequency $f_0 = c/(2L)$ is lower. It is interesting to consider the sensitivity at relatively lower frequencies. The noise power and the bandwidth also scale as $P_i \propto f_0^2$ and $\Delta f \propto f_0$, respectively. Then, $\Omega_{\rm gw}^{\rm min}(f_0)$ scales proportional to $f_0^{9/2}$. Consequently, the limit to $\Omega_{\rm gw}$ is drastically improved by enlarging the detector size, though, of course, the detector size is practically restricted on the Earth. In Fig. 7.8, the sensitivity achievable with two large RSM is plotted.

At $1-100\,\mathrm{MHz}$, the sensitivity to GWB is not good and is less interest in a cosmological context. However, at lower frequencies corresponding to a relatively large-scale detector, the sensitivity can overcome the critical energy density of the universe and even the indirect bound due to the big-bang nucleosynthesis.

[5] Strictly speaking, γ for RSMs and SRIs are slightly different, but it is negligible.

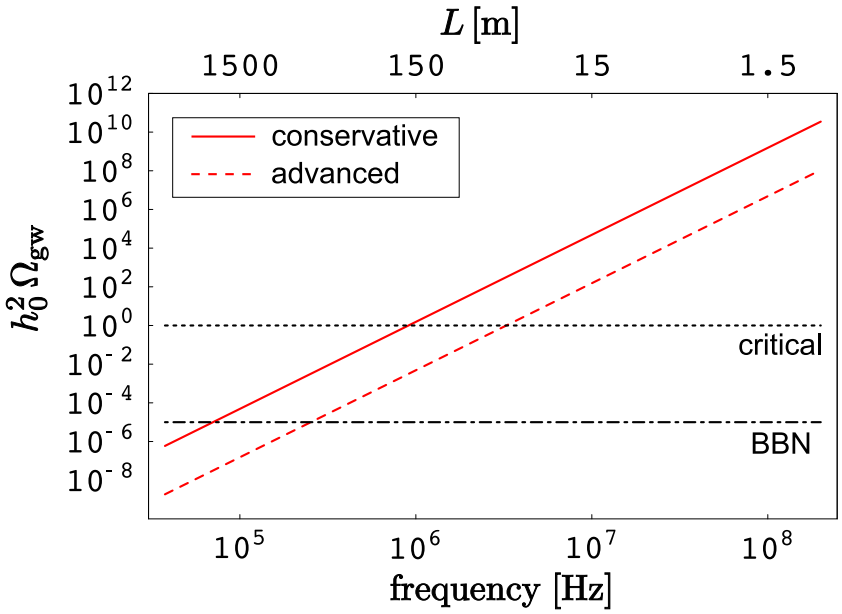

Figure 7.8: Sensitivity of the RSMs to GWB. The plots are the sensitivity to GWB with the conservative parameters (red solid curve) and with the advanced parameters (red dashed curve), critical energy density of the universe (black dotted line), and the limit due to big-bang nucleosynthesis (black dot-dashed line). The detector size L corresponding to the resonant frequency is shown on the upper axis.

Chapter 8

Conclusions

8.1 Summary

In this thesis, we studied the general framework of the search for a cosmological GWB, focused on a laser-interferometric GW detector. Such a search is well motivated by the GWB created in the early universe. Particularly, the quintessential inflation and the pre-big-bang model generate a large GWB at high frequencies. On the other hand, a large-scale laser-interferometric detector on the ground is well developed, and the second-generation detectors, which can reach the theoretically interesting range of the model parameters and could directly detect the GWB, are underway.

First, we investigated the search for the non-tensorial polarization mode of a GWB with large-scale advanced detectors on the Earth such as LIGO and VIRGO. In the theories with extra dimensions and the modified gravity theories, the extra degrees of freedom allows the GWB to have scalar and vector modes besides the tensor mode in the general relativity. To search those extra polarization modes, we extended the conventional formalism of a cross-correlation analysis for the tensor mode to the non-tensorial polarization modes. Then, we calculated the sensitivity to such GWBs. As a result, we found that interferometric GW detectors is capable of detecting the non-tensorial mode with almost the same SNR as the tensor mode. We also discussed the detectability with the real detector pairs and derived the detectable energy density of the GWB.

In the latter of the thesis, we studied the search for a GWB at ultra high frequencies. Since the frequency band corresponds to the epoch of the extremely earth universe, it is important not only for cosmology but also particle physics. In addition, some models such as the quintessential inflation and the pre-big-bang model create the energy peak of the GWB at $\sim 100\,\mathrm{MHz}$. So far only a few experiments have been done and no tight constraint on the GWB with a direct search exists at ultra-high frequencies.

To construct GW detectors and impose a tighter limit, we first investigated the laser-interferometric detector designs that can effectively respond to GW at high frequencies. Comparing the GW response functions of three detector design, we found that the synchronous recycling interferometer (SRI) is the best at these sensitivities, which has better sensitivity than an ordinary Fabry-Perot Michelson interferometer (FPMI) by a factor of 3.3 at 100 MHz. Then, we considered the cross-correlation search

with two SRIs. However, the conventional analytical method of cross correlation is not applicable to our situation around 100 MHz, because the GW wavelength is comparable to the detector size, and the usual assumption of long wavelength limit breaks down. Thus, we generalized the formalism so as to be applied in any frequencies, and investigated the location and orientation dependence of two SRIs. As a result, we found that the sensitivity is nearly optimized and hardly changed if two coaligned detectors are located in a range of $\pm 0.2\,\mathrm{m}$. For such a detector configuration, we derived the optimal location of the two detectors, and showed that two SRIs with conservative parameters can reach the sensitivity of $h_0^2\Omega_{\mathrm{gw}} \approx 1.4 \times 10^{14}$ at 100 MHz. Finally, we described the experiment done by our group with a pair of meter-sized laser-interferometric detectors, and obtained the results of $h_0^2\Omega_{\mathrm{gw}} < 6.0 \times 10^{25}$ as the first step of the experiment. Though this is not stringent limit, we improved the previous constraint on the GWB [45] by eight orders of magnitude.

In the calculation of the sensitivity of the SRI, we assumed the sensitivity is shot-noise limited. But, the SRI has a fatal defect which amplifies not only the GW signal but also the displacement noise of mirrors, and the displacement noise eventually limits the sensitivity. For the solution, we proposed a so-called resonant speed meter (RSM), which is a new detector design based on a ring-shaped cavity. The remarkable feature of this interferometer is that, at certain frequencies, gravitational-wave signals are amplified, while displacement noises are not. Therefore, the RSM has sharp sensitivity to GWs at certain frequency. Next, we studied quantum noise of the RSM and found that the RSM cannot overcome the standard quantum limit, but the sensitivity is shot-noise limited at the resonant frequency since radiation pressure noise is canceled. Thanks to the cancellation of the displacement noise, we showed that a relatively large-scale detector, corresponding to lower resonant frequency, can achieve the sensitivity that overcome the critical energy density of the universe and even the indirect bound due to the big-bang nucleosynthesis.

8.2 Discussions and future prospects

As we mentioned in the summary above, the non-tensorial polarization can be detected with interferometric GW detectors. However, we assumed that only one of the modes is present. In general, the detector output one obtains is a mixture of the tensor, vector, and scalar mode. So, we have to decompose the output signal by using at least three independent signals, and calculate the SNR. It is expected to be possible to decompose because there are several large-scale interferometric detectors on the Earth. It is also interesting to decompose the tensor and scalar modes with a single detector pair, under the assumption of the absence of the vector mode. If we assume only two modes exist, our search method can also be applied to a space-based detector pair. Further investigation on this issue is required. Furthermore, although we chiefly focused on the experiment, it is also important to derive the prediction of a specific theoretical model and to restrict the model parameters.

We investigated the GWB search at ultra-high frequencies $\sim 100\,\mathrm{MHz}$, however, unfortunately, the detector sensitivity with current technologies is not enough to con-

strain the theoretical model and obtain interesting scientific results, since, at 100 MHz, we cannot surpass even the critical energy density of the universe.

Note that the application of our studies in the thesis is not limited at ultra-high frequencies. It can also be applied in the search at low frequencies, if the wavelength of a GW is comparable with the detector size, e.g. LISA. In addition, our results are not specific feature of the SRI, because the detector response functions of a SRI in Eqs. (6.8) and a FPMI (6.9) are identical except for the prefactor $(1 - e^{-2i\Omega\tau})$. Hence, it is possible to perform the same experiment with two FPMIs. One of the ways to reach interesting fields of scientific results is to slightly lower the observation frequency, as seen in Fig. 7.8. As another direction of research, a RSM can be used as a displacement noise-free interferometer [187]. Therefore, in the thesis, we provide the general framework of a cosmological GWB search and the various detector topologies.

Appendix A

Bogolubov transformation and particle creation

Particle creation in a dynamical gravitational field is described by Bogolubov transformation, which is related to smooth connection of mode functions between two phases before and after the phase transition. For the details, see [67].

Suppose that phase I and phase II are the phase before and after a phase transition, respectively. In each phase, a quantum field, for example, a quantized scalar field $\phi(x)$ at a spacetime point can be expanded using complete sets of mode functions, $\{f_{\mathbf{k}}, f^*_{\mathbf{k}}\}$ in phase I and $\{F_{\mathbf{k}}, F^*_{\mathbf{k}}\}$ in phase II,

$$\begin{aligned} \phi(x) &= \sum_{\mathbf{k}} \left[a_{\mathbf{k}} f_{\mathbf{k}} + a^\dagger_{\mathbf{k}} f^*_{\mathbf{k}} \right] , \\ &= \sum_{\mathbf{k}} \left[A_{\mathbf{k}} F_{\mathbf{k}} + A^\dagger_{\mathbf{k}} F^*_{\mathbf{k}} \right] , \end{aligned} \tag{A.1}$$

where $\{a_{\mathbf{k}}, a^\dagger_{\mathbf{k}}\}$ and $\{A_{\mathbf{k}}, A^\dagger_{\mathbf{k}}\}$ are creation and annihilation operators in phase I and phase II, respectively. Since $\{f_{\mathbf{k}}, f^*_{\mathbf{k}}\}$ and $\{F_{\mathbf{k}}, F^*_{\mathbf{k}}\}$ are the complete sets, we can relate one in terns of the others. In general, Bogolubov transformation is defined by

$$\begin{aligned} F_{\mathbf{k}} &= \sum_{\mathbf{k}'} \left(\alpha_{\mathbf{k}\mathbf{k}'} f_{\mathbf{k}'} + \beta_{\mathbf{k}\mathbf{k}'} f^*_{\mathbf{k}'} \right) , \\ f_{\mathbf{k}} &= \sum_{\mathbf{k}'} \left(\alpha^*_{\mathbf{k}'\mathbf{k}} F_{\mathbf{k}'} - \beta_{\mathbf{k}'\mathbf{k}} F^*_{\mathbf{k}'} \right) . \end{aligned} \tag{A.2}$$

From Eqs. (A.1) and (A.2), the creation and annihilation operators between two phases are related as

$$\begin{aligned} a_{\mathbf{k}} &= \sum_{\mathbf{k}'} (\alpha_{\mathbf{k}'\mathbf{k}} A_{\mathbf{k}'} + \beta^*_{\mathbf{k}'\mathbf{k}} A^\dagger_{\mathbf{k}'}) , \\ A_{\mathbf{k}} &= \sum_{\mathbf{k}'} (\alpha^*_{\mathbf{k}\mathbf{k}'} a_{\mathbf{k}'} - \beta^*_{\mathbf{k}\mathbf{k}'} a^\dagger_{\mathbf{k}'}) , \end{aligned}$$

The vacuum states are defined using the annihilation operators by

$$a_{\mathbf{k}} |0\rangle_{\mathrm{I}} = 0 , \qquad A_{\mathbf{k}} |0\rangle_{\mathrm{II}} = 0 .$$

From the commutation relations of $a_{\mathbf{k}}$ and $A_{\mathbf{k}}$, the following relation between Bogolubov coefficients can be found.

$$\begin{aligned} \sum_{\mathbf{k}} \left[\alpha_{\mathbf{k}'\mathbf{k}} \alpha^*_{\mathbf{k}''\mathbf{k}} - \beta_{\mathbf{k}'\mathbf{k}} \beta^*_{\mathbf{k}''\mathbf{k}} \right] &= \delta_{\mathbf{k}'\mathbf{k}''} \ , \\ \sum_{\mathbf{k}} \left[\alpha_{\mathbf{k}'\mathbf{k}} \beta_{\mathbf{k}''\mathbf{k}} - \beta_{\mathbf{k}'\mathbf{k}} \alpha_{\mathbf{k}''\mathbf{k}} \right] &= 0 \ . \end{aligned} \tag{A.3}$$

In the Friedmann-Robertson-Walker universe, according to isotropy and homogeneity, Bogolubov coefficients do not depend on a direction of $\mathbf{k}$ and a spatial coordinate $\mathbf{x}$. Thus, Bogolubov coefficients only depend on a frequency f, and can be written as

$$\begin{aligned} \alpha_{\mathbf{k}\mathbf{k}'} &= \alpha_f \delta_{\mathbf{k}\mathbf{k}'} \ , \\ \beta_{\mathbf{k}\mathbf{k}'} &= \beta_f \delta_{\mathbf{k}\mathbf{k}'} \ . \end{aligned}$$

Consequantly, Eq. (A.3) gives a relation,

$$|\alpha_{\mathbf{k}}|^2 - |\beta_{\mathbf{k}}|^2 = 1 \ . \tag{A.4}$$

Next, particle creation at the phase transition is considered. Particle number operator is defined, $n_f = a_f^\dagger a_f$ in the phase I and $N_f = A_f^\dagger A_f$ in the phase II. A quantum state in the phase I is denoted $|n_f\rangle$. The number of particles created at the phase transition significantly depends on a time scale of the transition. If $\Delta T \ll (2\pi f_*)^{-1}$, where ΔT is the time scale of the transition, and f_* is the frequency of the mode of the particle in which we are interested, the transition is instantaneous and the quantum state does not change. In that case, the expected number of the particle in the phase II is

$$\begin{aligned} N_f &= \langle n_f | A_f^\dagger A_f | n_f \rangle \\ &= n_f + 2|\beta_f|^2 \left(n_f + \frac{1}{2} \right) \ . \end{aligned} \tag{A.5}$$

The second term in the right hand side of Eq. (A.5) show that pre-existing particles before the phase transition are amplified and new particles are created. If the quantum state is in a vacuum state in the phase I, N_f is simply

$$N_f = |\beta_f|^2 \ . \tag{A.6}$$

In a converse situation that the transition occurs very slowly, $\Delta T \gg (2\pi f_*)^{-1}$, the number of the particle is exponentially suppressed because the quantum state can follow a change due to the transition [67]. Therefore, no particle is created.

In a cosmological context, ΔT corresponds to the Hubble time H^{-1}. Hence, for the superhorizon modes $f_* \ll H^{-1}$, particles are created, for the subhorizon modes $f_* \ll H^{-1}$, no particle is created. The boundary frequency, $f \sim H^{-1}$ gives a cutoff frequency of inflationary GWB spectrum.

Appendix B

Formulae of spherical Bessel functions

- Explicit expressions of a spherical Bessel function

$$\begin{aligned} j_0(\alpha) &= \frac{\sin\alpha}{\alpha}\,, \\ j_1(\alpha) &= \frac{\sin\alpha}{\alpha^2} - \frac{\cos\alpha}{\alpha}\,, \\ j_2(\alpha) &= 3\frac{\sin\alpha}{\alpha^3} - 3\frac{\cos\alpha}{\alpha^2} - \frac{\sin\alpha}{\alpha}\,. \end{aligned}$$

- Recurrence formula

$$j_{n+1}(\alpha) = \frac{n+1}{\alpha} j_n(\alpha) - j_{n-1}(\alpha)$$

- Integrated forms

$$\begin{aligned} \int_{-1}^{1} dx\, e^{i\alpha x} &= 2j_0(\alpha) \\ \int_{-1}^{1} dx\, e^{i\alpha x}(1-x^2) &= 4\frac{j_1(\alpha)}{\alpha} \\ \int_{-1}^{1} dx\, e^{i\alpha x}(1-x^2)^2 &= 16\frac{j_2(\alpha)}{\alpha^2} \\ \int_{-1}^{1} dx\, e^{i\alpha x}x^2 &= \frac{2}{3}\Big[j_0(\alpha) - 2j_2(\alpha)\Big] \\ \int_{-1}^{1} dx\, e^{i\alpha x}x^4 &= \frac{2}{35}\Big[7j_0(\alpha) - 20j_2(\alpha) + 8j_4(\alpha)\Big] \end{aligned}$$

- Expressions of $j_n(\alpha)/\alpha^n$ with $j_n(x)$

$$\begin{aligned} \frac{j_1(\alpha)}{\alpha} &= \frac{1}{3}\Big[j_0(\alpha) + j_2(\alpha)\Big] \\ \frac{j_2(\alpha)}{\alpha^2} &= \frac{1}{105}\Big[7j_0(\alpha) + 10j_2(\alpha) + 3j_4(\alpha)\Big] \end{aligned}$$

Appendix C

The calculation of the overlap reduction function for non-tensorial modes

We write down the equation obtained in the course of the calculation of the overlap reduction functions for the vector and scalar modes. As for the procedure of the calculation, see Sec. 5.2.1.

- Vector mode

$$
\begin{aligned}
q_1 &= 0\,, \qquad q_2 = 20 j_0(\alpha)\,, \qquad q_3 = 0\,, \qquad q_4 = \frac{20}{3}\left[2j_0(\alpha) - j_2(\alpha)\right]\,, \\
q_5 &= 20\left[\frac{1}{15}j_0(\alpha) - \frac{1}{21}j_2(\alpha) - \frac{4}{35}j_4(\alpha)\right]\,.
\end{aligned}
$$

$$
\begin{pmatrix} C_1 \\ C_2 \\ C_3 \\ C_4 \\ C_5 \end{pmatrix} = \frac{1}{42}\begin{pmatrix} -28 & -40 & -12 \\ 42 & 30 & -12 \\ 0 & 60 & 60 \\ 0 & -45 & 60 \\ 0 & 0 & -420 \end{pmatrix}\begin{pmatrix} j_0 \\ j_2 \\ j_4 \end{pmatrix}\,.
$$

- Scalar mode

$$
\begin{aligned}
q_1 &= 30\left(\frac{2+\kappa}{1+2\kappa}\right)j_0(\alpha)\,, \qquad q_2 = 60\left(\frac{1+\kappa}{1+2\kappa}\right)j_0(\alpha)\,, \\
q_3 &= \frac{20}{1+2\kappa}\left[(2+\kappa)j_0(\alpha) + 2(1-\kappa)j_2(\alpha)\right]\,, \\
q_4 &= \frac{40}{1+2\kappa}\left[(1+\kappa)j_0(\alpha) + (1-2\kappa)j_2(\alpha)\right]\,, \\
q_5 &= \frac{2}{7}\left[7(4+3\kappa)j_0(\alpha) + 20(2-3\kappa)j_2(\alpha) + 12(1+\kappa)j_4(\alpha)\right]\,.
\end{aligned}
$$

$$\begin{pmatrix} C_1 \\ C_2 \\ C_3 \\ C_4 \\ C_5 \end{pmatrix} = \frac{1}{7(1+2\kappa)} \begin{pmatrix} 14(3+\kappa) & -20(3-\kappa) & 3(1+2\kappa) \\ 7(1+2\kappa) & 10(1+2\kappa) & 3(1+2\kappa) \\ 0 & 30(3-\kappa) & -15(1+2\kappa) \\ 0 & -15(1+2\kappa) & -15(1+2\kappa) \\ 0 & 0 & 105(1+2\kappa) \end{pmatrix} \begin{pmatrix} j_0 \\ j_2 \\ j_4 \end{pmatrix} .$$

Appendix D

GW polarizations in higher-dimensional spacetime

In a 4-dimensional spacetime, there are two polarization modes of a GW: plus and cross mode. In a higher-dimensional spacetime, more polarization modes appear, because of extra degrees of freedom.

The number of the polarization mode in a D-dimensional spacetime can easily be counted in the same way in Sec. 2.1. The perturbed metric tensor $h_{\mu\nu}$ has $D(D+1)/2$ independent components. However, by D harmonic gauge conditions, the components are reduced by D the number of independent components. In addition, another D conditions are imposed to completely fix the gauge, which has residual degrees of freedom under an infinitesimal gauge transformation. Then, $D(D-3)/2$ polarization modes exist in the D-dimensional spacetime. For instance, there are 5 polarizations in a 5-dimensional spacetime, and 9 polarizations in a 6-dimensional spacetime.

In this Appendix below, for the simple examples, the GW polarization mode in a higher-dimensional spacetime are provided.

D.1 Pure 5-dimensional Minkowski spacetime

We consider a 5-dimensional Minkowski spacetime without the compactification of an extra dimension. In other words, four spatial dimensions are equivalent. Such a spacetime is not realistic, but it is instructive to see how the polarization modes of a GW appear.

To investigate the explicit components of the GW metric tensor, the requirement for the coordinate system is to satisfy the harmonic gauge conditions and the gauge conditions for an infinitesimal gauge transformation. Suppose the infinitesimal transformation in Eq. (2.16), as

$$\xi^{\mu} = i\, C^{\mu} e^{ik_{\alpha}x^{\alpha}} \ , \tag{D.1}$$

where C^{μ} is the constant of complex number. Substituting Eqs. (2.14) and (D.1) into Eq. (2.17), on can obtain

$$A'_{\mu\nu} = A_{\mu\nu} + (C_{\mu}k_{\nu} + C_{\nu}k_{\mu}) \ . \tag{D.2}$$

We can choose the wave-number vector of a GW as $k_\alpha = (-\omega, 0, 0, \omega\cos\zeta, \omega\sin\zeta)$, without the loss of generality. The angle ζ is the angle between the z axis and the propagation direction of the GW in 5-dimensional spacetime. For the choice of the wave-number vector, the null condition $k_\alpha k^\alpha = 0$ holds. In addition, we choose the coordinate so that $A'_{0\mu} = 0$. So, from Eq. (D.2), the coefficients of the infinitesimal transformation are given by

$$\begin{aligned} C_0 &= \frac{A_{00}}{2\omega}, \quad C_1 = \frac{A_{01}}{\omega}, \quad C_2 = \frac{A_{02}}{\omega}\ , \\ C_3 &= \frac{A_{03}}{\omega} + C_0\cos\zeta, \qquad C_4 = \frac{A_{04}}{\omega} + C_0\sin\zeta\ . \end{aligned} \tag{D.3}$$

On the other hand, to satisfy the harmonic gauge conditions, the first condition of Eq. (2.15),

$$k^\mu A'_{\mu\nu} = 0\ , \tag{D.4}$$

is needed. Hereafter we do not fix the prime at the metric tensor, for simplicity. From Eq. (D.4), one can obtain the relations

$$\begin{aligned} A_{13} &= -A_{14}\tan\zeta\ , \\ A_{23} &= -A_{24}\tan\zeta\ , \\ A_{33} &= A_{44}\tan^2\zeta = -e_{34}\ .\tan\zeta\ . \end{aligned} \tag{D.5}$$

With the help of the traceless condition and Eq. (D.5), A_{33} is related to A_{11} and A_{22} as

$$A_{33} = -(A_{11} + A_{22})\sin^2\zeta\ . \tag{D.6}$$

Therefore, the spatial coponents of $A_{\mu\nu}$ can be written as

$$A_{ij} = \begin{pmatrix} A_{11} & A_{12} & A_{13} & -A_{13}\cot\zeta \\ A_{12} & A_{22} & A_{23} & -A_{23}\cot\zeta \\ A_{13} & A_{23} & -(A_{11}+A_{22})\sin^2\zeta & (A_{11}+A_{22})\sin\zeta\cos\zeta \\ -A_{13}\cot\zeta & -A_{23}\cot\zeta & (A_{11}+A_{22})\sin\zeta\cos\zeta & -(A_{11}+A_{22})\cos^2\zeta \end{pmatrix}\ . \tag{D.7}$$

The A_{ij} has five independent components, which is consistent with the number of the independent polarization modes, mentioned at the beginning of this chapter. When the GW is propagating in our 3-space ($\zeta = 0$), the extra-dimensional components of the A_{ij} diverges, because we express the tensor components with A_{13} and A_{23}. Note that the A_{ij} satisfies the transverse-traceless (TT) conditions, $h^\mu{}_\mu = 0$ and $k^\nu A_{\mu\nu} = 0$.

It is intuitive to express the A_{ij} in terms of the projected components on our 3-space, which is defined in Eq. (5.30). Redefining

$$\begin{aligned} A_{11} &= A_b + A_+, \qquad A_{22} = A_b - A_+, \\ A_{12} &= A_\times, \quad A_{13} = A_x, \quad A_{23} = A_y\ , \end{aligned}$$

the components of Eq. (D.7) projected on our 3-space are

$$\tilde{A}_{ij} = \begin{pmatrix} A_b + A_+ & A_\times & A_x \\ A_\times & A_b - A_+ & A_y \\ A_x & A_y & -2A_b\sin^2\zeta \end{pmatrix}\ .$$

The spatial part of the metric tensor is given by

$$\begin{aligned} h_{ij}(\omega t - \vec{k}\cdot\vec{x}) &= A_+ e^{ik_\alpha x^\alpha}\tilde{e}^+_{ij} + A_\times e^{ik_\alpha x^\alpha}\tilde{e}^\times_{ij} + A_x e^{ik_\alpha x^\alpha}\tilde{e}^x_{ij} + A_y e^{ik_\alpha x^\alpha}\tilde{e}^y_{ij} \\ &\quad + A_b e^{ik_\alpha x^\alpha}\tilde{e}^b_{ij} - \sqrt{2}\sin^2\zeta A_b e^{ik_\alpha x^\alpha}\tilde{e}^\ell_{ij} \ . \end{aligned}$$

Note that, in 5-dimensional Minkowski spacetime, there is a correlation between b and ℓ modes, and exist five polarization modes (two tensor, two vector, one scalar modes).

D.2 Pure 6-dimensional Minkowski spacetime

The calculation of the GW polarization mode in a 6-dimensional Minkowski spacetime without compactification can be done in the same way as that in the case of 5-dimensional Minkowski spacetime, but it is complicated. Here we only show the results.

The wave-number vector of a GW can be chosen as

$$k_\alpha = (-\omega,\, 0,\, 0,\, \omega\cos\zeta,\, \omega\sin\zeta\cos\eta,\, \omega\sin\zeta\sin\eta) \ ,$$

where η is another angle of the propagation direction of a GW. As a result, one obtain the spatial components of $A_{\mu\nu}$,

- independent components

$$A_{11},\, A_{12},\, A_{13},\, A_{14},\, A_{23},\, A_{24},\, A_{33},\, A_{44},\, A_{55},$$

- dependent components

$$\begin{aligned} A_{22} &= -A_{11} - A_{33} - A_{44} - A_{55} \ , \\ A_{15} &= -A_{13}\cot\zeta\csc\eta - A_{14}\cot\eta \ , \\ A_{25} &= -A_{23}\cot\zeta\csc\eta - A_{24}\cot\eta \ , \\ A_{34} &= -[A_{33}\cot\zeta\sec\eta + \tan\zeta(A_{44}\cos\eta - A_{55}\sin\eta\tan\eta))\,]/2 \ , \\ A_{35} &= -[A_{33}\cot\zeta\csc\eta - \tan\zeta\,(A_{44}\cos\eta\cot\eta - A_{55}\sin\eta))\,]/2 \ , \\ A_{45} &= [A_{33}\cot^2\zeta\csc\eta\sec\eta - A_{44}\cot\eta - A_{55}\tan\eta\,]/2 \ . \end{aligned}$$

Redefining

$$\begin{aligned} A_{11} &= A_b + A_+, \qquad A_{22} = A_b - A_+, \qquad A_{33} = A_\ell \\ A_{12} &= A_\times, \quad A_{13} = A_x, \quad A_{23} = A_y \ , \end{aligned}$$

the projected components on our 3-space are

$$\tilde{A}_{ij} = \begin{pmatrix} A_b + A_+ & A_\times & A_x \\ A_\times & A_b - A_+ & A_y \\ A_x & A_y & A_\ell \end{pmatrix} \ .$$

The six components in our 3-space are all independent. Since there are 9 degrees of freedom in a 6-dimensional Minkowski spacetime, other 3 degrees of freedom are hidden in the extra dimensions.

Appendix E

GW response functions of interferometers: general expressions

E.1 Synchronous-recycling interferometer

The configuration of SRI is shown in Fig. 6.1. We call the mirror A at $\mathbf{X}_1$ the recycling mirror, the mirror B at $\mathbf{X}_1$ the transfer mirror and the mirrors at $\mathbf{X}_2$ and $\mathbf{X}_3$ the end mirrors. The amplitude reflectivities and transmissivities of the transfer mirror and the end mirrors at $\mathbf{X}_2$ and $\mathbf{X}_3$ are (R_B, T_B), (R_2, T_2), (R_3, T_3), respectively. Those of the recycling mirror are $(+R_A, +T_A)$ for the light incident from inside the cavity and $(-R_A, +T_A)$ for the light incident from outside the cavity. The angular frequency of light is ω and the arm length is L. We define $\tau \equiv L/c$. Electric fields at the recycling mirror are defined in Fig. E.1 and are related by the following equations,

$$\begin{aligned} C_\ell &= R_A D_\ell + T_A A_\ell \ , \\ C_r &= R_A D_r + T_A A_r \ , \\ B_\ell &= T_A D_\ell - R_A A_\ell \ , \\ B_r &= T_A D_r - R_A A_r \ . \end{aligned} \tag{E.1}$$

We assume that there is no displacement noise, for example, thermal noise, seismic noise, radiation pressure noise etc., at 100 MHz. Then, D field after circulating the cavity experiences the phase shift $4\omega\tau$ and the GW signal $\delta\phi(t)$,

$$\begin{aligned} D_\ell(t) &= R_c C_\ell(t-4\tau)\ \exp\bigl[i\{4\omega\tau + \delta\phi_\ell(t)\}\bigr] \ , \\ D_r(t) &= R_c C_r(t-4\tau)\ \exp\bigl[i\{4\omega\tau + \delta\phi_r(t)\}\bigr] \ , \end{aligned} \tag{E.2}$$

where we defined the composite reflectivity of mirrors $R_c \equiv R_B R_2 R_3$ and

$$\begin{aligned} \delta\phi_\ell(t) &\equiv \delta\phi_{21}(t) + \delta\phi_{12}(t-\tau) + \delta\phi_{31}(t-2\tau) + \delta\phi_{13}(t-3\tau) \ , \\ \delta\phi_r(t) &\equiv \delta\phi_{31}(t) + \delta\phi_{13}(t-\tau) + \delta\phi_{21}(t-2\tau) + \delta\phi_{12}(t-3\tau) \ . \end{aligned} \tag{E.3}$$

For example, $\delta\tilde{\phi}_{21}$ denotes the phase shift due to GW when light travels from $\mathbf{X}_2$ to $\mathbf{X}_1$ in Fig. 6.1. This can be calculated using Eq. (6.3).

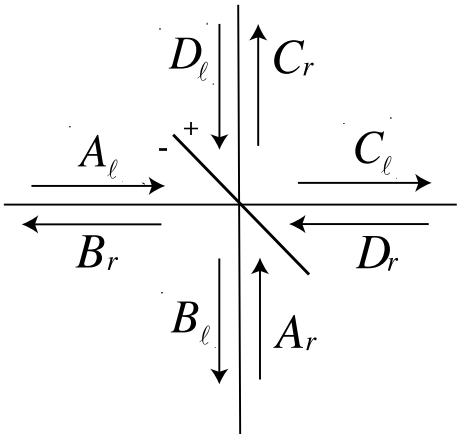

Figure E.1: Electric fields of SRI at the recycling mirror.

Equations (E.2) - (E.2) can be solved separately for right-handed and left-handed fields. The input-output relation of the cavity for the left-handed fields becomes

$$B_\ell(t) = -R_A A_\ell(t) + \sum_{k=1}^{\infty} T_A^2 R_c^k R_A^{k-1} A_\ell(t-4k\tau) e^{4i\omega\tau} \ \exp\left[i \sum_{k'=1}^{k} \delta\phi_\ell\big[t-4(k'-1)\tau\big] \right] .$$

We assume that the cavity is in resonance in the absence of GW, that is $A_\ell(t) = A_\ell(t-4\tau)$. Then,

$$B_\ell(t) = -R_A A_\ell(t) \left\{ 1 - \sum_{k=1}^{\infty} T_A^2 R_c^k R_A^{k-2} \ \exp\left[i \sum_{k'=1}^{k} \delta\phi_\ell\big[t-4(k'-1)\tau\big] \right] \right\} .$$

Using the approximation that the GW signal is small ($|\delta\phi(t)| \ll 1$), we obtain

$$\begin{aligned} B_\ell(t) \ &\approx \ -\frac{R_A - R_c}{1 - R_A R_c} A_\ell(t) \\ &\qquad \exp\left[-i \, \frac{1 - R_A R_c}{R_A - R_c} \sum_{k=1}^{\infty} T_A^2 R_c^k R_A^{k-1} \ \sum_{k'=1}^{k} \delta\phi_\ell\big[t-4(k'-1)\tau\big] \right] . \end{aligned} \tag{E.4}$$

Therefore, the phase shift $\delta\Phi_\ell$ of left-handed light caused by GW is

$$\delta\Phi_\ell(t) = -\frac{1 - R_A R_c}{R_A - R_c} \sum_{k=1}^{\infty} T_A^2 R_c^k R_A^{k-1} \ \sum_{k'=1}^{k} \delta\phi_\ell\big[t-4(k'-1)\tau\big] . \tag{E.5}$$

Fourier transforming Eq. (E.5) and using Eqs. (E.3) and (6.5) give

$$\delta\tilde{\Phi}_\ell = \alpha(\Omega, R_c, R_A)\delta\tilde{\phi}_\ell , \tag{E.6}$$

$$\begin{aligned} \delta\tilde{\phi}_\ell \ &= \ \frac{\omega}{\Omega} \, e^{-i\Omega(\tau + \mathbf{e}_z\cdot\mathbf{X}_1/c)} \sum_A \mathbf{e}^A \tilde{h}_A \\ &\quad : \Big[\ \frac{\mathbf{n}_{12}\otimes\mathbf{n}_{12}}{1-(\mathbf{e}_z\cdot\mathbf{n}_{12})^2} \big\{ \sin\Omega\tau - i(\mathbf{e}_z\cdot\mathbf{n}_{12})(e^{-i\Omega\tau\mathbf{e}_z\cdot\mathbf{n}_{12}} - \cos\Omega\tau) \big\} \\ &\quad + \frac{\mathbf{n}_{13}\otimes\mathbf{n}_{13}}{1-(\mathbf{e}_z\cdot\mathbf{n}_{13})^2} \, e^{-2i\Omega\tau} \big\{ \sin\Omega\tau - i(\mathbf{e}_z\cdot\mathbf{n}_{13})(e^{-i\Omega\tau\mathbf{e}_z\cdot\mathbf{n}_{13}} - \cos\Omega\tau) \big\} \ \Big] , \end{aligned}$$

$$\alpha(\Omega, R_A, R_c) \equiv -\frac{T_A^2 R_c}{(R_A - R_c)(1 - R_A R_c\, e^{-4i\Omega\tau})} \ .$$

The GW signal for the right-handed light can be obtained by simply changing the subscripts $2 \leftrightarrow 3$ because of the symmetry of the system. Therefore, the output of the detector is

$$\begin{aligned}
\delta\tilde{\Phi}_{\rm all} &\equiv \delta\tilde{\Phi}_r - \delta\tilde{\Phi}_\ell \\
&= \alpha(\Omega, R_A, R_c)\delta\tilde{\phi}_{\rm all} \\
\\
\delta\tilde{\phi}_{\rm all} &= (1 - e^{-2i\Omega\tau})\frac{\omega}{\Omega}\, e^{-i\Omega(\tau + \mathbf{e}_z\cdot\mathbf{X}_1/c)} \sum_A \mathbf{e}^A \tilde{h}_A \\
&\quad : [\ (\mathbf{n}_{13}\otimes\mathbf{n}_{13})\, H_{\rm SRI}(\Omega,\, \mathbf{e}_z\cdot\mathbf{n}_{13}) - (\mathbf{n}_{12}\otimes\mathbf{n}_{12})\, H_{\rm SRI}(\Omega,\, \mathbf{e}_z\cdot\mathbf{n}_{12})\}\ ] \ .
\end{aligned} \tag{E.7}$$

with

$$H_{\rm SRI}(\Omega,\, \mathbf{e}_z\cdot\mathbf{n}_{12}) \equiv \frac{1}{1 - (\mathbf{e}_z\cdot\mathbf{n}_{12})^2}\left[\sin\Omega\tau - i(\mathbf{e}_z\cdot\mathbf{n}_{12})(e^{-i\Omega\tau\mathbf{e}_z\cdot\mathbf{n}_{12}} - \cos\Omega\tau)\right] \ .$$

E.2 Fabry-Perot Michelson interferometer

The configuration of FPMI is shown in Fig. 6.2. The amplitude reflectivities and transmissivities of end mirrors at $\mathbf{X}_{E1}$ and $\mathbf{X}_{E2}$ are (R_E, T_E), and of front mirrors at $\mathbf{X}_{F1}$ and $\mathbf{X}_{F2}$ are $(+R_F, +T_F)$ for the light incident from inside the cavities and $(-R_F, +T_F)$ for the light incident from outside the cavities. The arm length is L. Electric fields at the front mirror are defined in Fig. E.2. First, we will consider only one FP cavity and calculate the input-output relation. At the end of our calculation, we will derive the full output of FPMI.

The fields are related by the following equations,

$$E_{\rm out} = -R_F E_{\rm in} + T_F E_B \ , \tag{E.8}$$

$$E_A = R_F E_B + T_F E_{\rm in} \ . \tag{E.9}$$

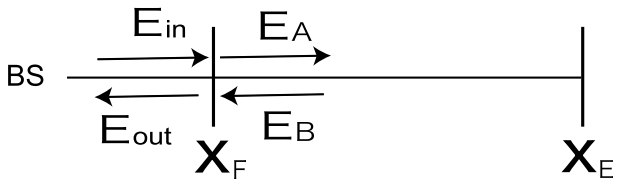

Figure E.2: Electric fields of FPMI.

E_A is reflected at the end mirror and returns to the front mirror after experiencing the phase shift 2τ and the modulation due to GW. The relation between E_A and E_B

is

$$
\begin{aligned}
E_B(t) &= R_E E_A(t-2\tau)\,\exp\bigl[i\{2\omega\tau+\delta\phi_{\rm cav}(t)\}\bigr]\,, &\text{(E.10)}\\
\delta\phi_{\rm cav}(t) &\equiv \delta\phi_{EF}(t)+\delta\phi_{FE}(t-\tau)\,, &\text{(E.11)}
\end{aligned}
$$

where $\delta\phi_{EF}$ denotes the phase shift due to GW when light propagates from the end mirror to the front mirror and the specific form is given by Eq. (6.3). Similarly, $\delta\phi_{FE}$ is the one from the front mirror to the end mirror. From Eqs. (E.8) - (E.10), the input-output relation for the FP cavity becomes

$$
\begin{aligned}
E_{\rm out}(t) &= -R_F E_{\rm in}(t)\\
&\quad +R_E T_F^2\sum_{k=1}^{\infty}(R_F R_E)^{k-1}E_{\rm in}(t)\,\exp\left[i\sum_{k'=1}^{k}\delta\phi_{\rm cav}\bigl[t-2(k'-1)\tau\bigr]\right]\\
&\approx -\frac{R_F-R_E}{1-R_F R_E}E_{\rm in}(t)\\
&\quad \times\exp\left[-i\frac{R_E T_F^2(1-R_F R_E)}{R_F-R_E}\sum_{k=1}^{\infty}(R_F R_E)^{k-1}\sum_{k'=1}^{k}\delta\phi_{\rm cav}\bigl[t-2(k'-1)\tau\bigr]\right]\,,
\end{aligned}
$$

where we used the approximation $|\delta\phi_{\rm cav}(t)|\ll 1$. Therefore, the phase shift $\delta\Phi$ caused by GW is

$$
\delta\Phi(t)=-\frac{R_E T_F^2(1-R_F R_E)}{R_F-R_E}\sum_{k=1}^{\infty}(R_F R_E)^{k-1}\sum_{k'=1}^{k}\delta\phi_{\rm cav}\bigl[t-2(k'-1)\tau\bigr]\,. \qquad \text{(E.12)}
$$

Fourier transforming Eq. (E.12) and using Eqs. (E.11) and (6.5) gives

$$
\begin{aligned}
\tilde{\Phi}(\Omega) &= \alpha(\Omega,R_F,R_E)\delta\tilde{\phi}_{\rm cav}(\Omega)\,,\\
\tilde{\delta\phi}_{\rm cav} &= \frac{\omega}{\Omega}\sum_A \mathbf{e}^A\tilde{h}_A\,e^{-i\Omega(\tau+\mathbf{e}_z\cdot\mathbf{X}_F/c)}\frac{\mathbf{n}\otimes\mathbf{n}}{1-(\mathbf{e}_z\cdot\mathbf{n})^2}\\
&\quad\times\ [\ \sin\Omega\tau-i(\mathbf{e}_z\cdot\mathbf{n})(e^{-i\Omega\tau\mathbf{e}_z\cdot\mathbf{n}}-\cos\Omega\tau)\ ]\,,\\
\alpha(\Omega,R_F,R_E) &\equiv -\frac{R_E T_F^2}{(R_F-R_E)(1-R_F R_E\,e^{-2i\Omega\tau})}\,,
\end{aligned}
$$

where $\mathbf{n}\equiv(\mathbf{X}_E-\mathbf{X}_F)/L$. This formula is consistent with the previous result, Eq.(6) in [188], except for an overall constant factor.

Using the result obtained above, we can easily obtain the full-output signal for the FPMI. We fix the subscripts 1 and 2 to distinguish north and east arms in Fig. 6.2, and define $\mathbf{n}_i\equiv(\mathbf{X}_{Ei}-\mathbf{X}_{Fi})/L,\ i=1,2$. For simplicity, we assume that the two front mirrors on both arms are located at the same place, that is, $\mathbf{X}_F=\mathbf{X}_{F1}=\mathbf{X}_{F2}$. This assumption is valid because it hardly affects the GW signal. Then, total output of

FPMI is

$$\begin{aligned}\delta\tilde{\Phi}_{\rm all} &\equiv \delta\tilde{\Phi}_1 - \delta\tilde{\Phi}_2 \\ &= \alpha(\Omega, R_F, R_E)\delta\tilde{\phi}_{\rm all}\end{aligned}$$

$$\begin{aligned}\delta\tilde{\phi}_{\rm all} &= \frac{\omega}{\Omega}\, e^{-i\Omega(\tau+\mathbf{e}_z\cdot\mathbf{X}_F/c)} \sum_A \mathbf{e}^A \tilde{h}_A \\ &\quad : \left[(\mathbf{n}_1\otimes\mathbf{n}_1)\, H_{\rm FPM}(\Omega,\, \mathbf{e}_z\cdot\mathbf{n}_1) - (\mathbf{n}_2\otimes\mathbf{n}_2)\, H_{\rm FPM}(\Omega,\, \mathbf{e}_z\cdot\mathbf{n}_2)\right] .\end{aligned} \tag{E.13}$$

with

$$\begin{aligned}H_{\rm FPM}(\Omega,\, \mathbf{e}_z\cdot\mathbf{n}_1) &\equiv \frac{1}{1-(\mathbf{e}_z\cdot\mathbf{n}_1)^2}\left[\sin\Omega\tau - i(\mathbf{e}_z\cdot\mathbf{n}_1)(e^{-i\Omega\tau\mathbf{e}_z\cdot\mathbf{n}_1} - \cos\Omega\tau)\right] , \\ &= H_{\rm SRI}(\Omega,\, \mathbf{e}_z\cdot\mathbf{n}_1) .\end{aligned}$$

E.3 L-shaped cavity Michelson interferometer

The configuration of LMI is shown in Fig. 6.3. The amplitude reflectivities and transmissivities of end mirrors at $\mathbf{X}_{E1}$ and $\mathbf{X}_{E2}$ are (R_E, T_E), and of front mirrors at $\mathbf{X}_{F1}$ and $\mathbf{X}_{F2}$ are $(+R_F, +T_F)$ for the light incident from inside the cavities and $(-R_F, +T_F)$ for the light incident from outside the cavities. The two mirrors at $\mathbf{X}_{C1}$ and $\mathbf{X}_{C2}$ are completely reflective. The arm length is L. Electric fields at the front mirror are defined in Fig. E.3. First, we will consider only one L-shaped cavity and calculate the input-output relation. At the end of our calculation, we will derive the full output of LMI.

The relation between the fields is the same as Eqs. (E.8) and (E.9) for FPMI. The relation between E_B and E_A is almost the same as FPMI. However, only differences are that the round-trip time of LMI in the cavity is 4τ and that light is reflected by

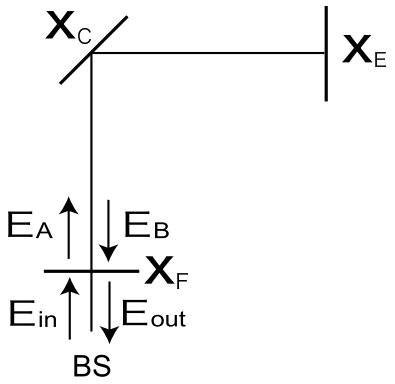

Figure E.3: Electric fields of LMI.

the mirror at $\mathbf{X}_c$ during the trip. Thus, it is given by

$$E_B(t) = R_E E_A(t-4\tau)\ \exp\bigl[i\{4\omega\tau + \delta\phi_{\rm cav}(t)\}\bigr]\ , \tag{E.14}$$
$$\delta\phi_{\rm cav}(t) \equiv \delta\phi_{CF}(t) + \delta\phi_{EC}(t-\tau) + \delta\phi_{CE}(t-2\tau) + \delta\phi_{FC}(t-3\tau)\ , \tag{E.15}$$

where $\delta\phi_{IJ},\ I,J = F,E,C$ denotes the phase shift due to GW when the light propagates from the I-th mirror to the J-th mirror. From Eqs. (E.8), (E.9) and (E.14), the input-output relation for the L-shaped cavity becomes

$$\begin{aligned} E_{\rm out}(t) &= -R_F E_{\rm in}(t) \\ &\quad + R_E T_F^2 \sum_{k=1}^{\infty} (R_F R_E)^{k-1} E_{\rm in}(t)\ \exp\left[i \sum_{k'=1}^{k} \delta\phi_{\rm cav}\bigl[t - 4(k'-1)\tau\bigr] \right] \\ &\approx -\frac{R_F - R_E}{1 - R_F R_E} E_{\rm in}(t) \\ &\quad \times \exp\left[-i \frac{R_E T_F^2 (1 - R_F R_E)}{R_F - R_E} \sum_{k=1}^{\infty} (R_F R_E)^{k-1} \sum_{k'=1}^{k} \delta\phi_{\rm cav}\bigl[t - 4(k'-1)\tau\bigr] \right]\ , \end{aligned}$$

where we used the approximation $|\delta\phi_{\rm cav}(t)| \ll 1$. Therefore, the phase shift $\delta\Phi$ caused by GW is

$$\delta\Phi(t) = -\frac{R_E T_F^2 (1 - R_F R_E)}{R_F - R_E} \sum_{k=1}^{\infty} (R_F R_E)^{k-1} \sum_{k'=1}^{k} \delta\phi_{\rm cav}\bigl[t - 4(k'-1)\tau\bigr]\ , \tag{E.16}$$

Fourier transforming Eq. (E.16) and using Eqs. (E.15) and (6.5) gives

$$\begin{aligned} \tilde{\delta\Phi}(\Omega) &= \alpha(\Omega, R_F, R_E) \tilde{\delta\phi}_{\rm cav}(\Omega)\ , \\ \tilde{\delta\phi}_{\rm cav} &= \frac{\omega}{\Omega} \sum_A \mathbf{e}^A \tilde{h}_A\ e^{-i\Omega(2\tau + \mathbf{e}_z \cdot \mathbf{X}_C/c)} \\ &\quad \times \Bigl[\frac{\mathbf{n}_{CE} \otimes \mathbf{n}_{CE}}{1 - (\mathbf{e}_z \cdot \mathbf{n}_{CE})^2} \bigl\{ \sin\Omega\tau - i(\mathbf{e}_z \cdot \mathbf{n}_{CE})(e^{-i\Omega\tau \mathbf{e}_z \cdot \mathbf{n}_{CE}} - \cos\Omega\tau) \bigr\} \\ &\qquad - \frac{\mathbf{n}_{CF} \otimes \mathbf{n}_{CF}}{1 - (\mathbf{e}_z \cdot \mathbf{n}_{CF})^2} \bigl\{ \sin\Omega\tau (1 - 2e^{-i\Omega\tau \mathbf{e}_z \cdot \mathbf{n}_{CF}} \cos\Omega\tau) \\ &\qquad\qquad + i(\mathbf{e}_z \cdot \mathbf{n}_{CF})(e^{-i\Omega\tau \mathbf{e}_z \cdot \mathbf{n}_{CF}} \cos 2\Omega\tau - \cos\Omega\tau) \bigr\} \Bigr]\ , \end{aligned}$$

$$\alpha(\Omega, R_F, R_E) \equiv -\frac{R_E T_F^2}{(R_F - R_E)(1 - R_F R_E\ e^{-4i\Omega\tau})}\ ,$$

where $\mathbf{n}_{CE} \equiv (\mathbf{X}_E - \mathbf{X}_C)/L$、 $\mathbf{n}_{CF} \equiv (\mathbf{X}_F - \mathbf{X}_C)/L$.

Using the result obtained above, we can easily obtain the full-output signal for the LMI. We fix the subscripts 1 and 2 in order to distinguish the two arms in Fig. 6.3, and define $\mathbf{n}_1 \equiv \mathbf{n}_{C2E} = -\mathbf{n}_{C1F}$ and $\mathbf{n}_2 \equiv -\mathbf{n}_{C2F} = \mathbf{n}_{C1E}$. For simplicity, we assume that the two front mirrors and the two end mirrors on both arms are located at the same place, that is, $\mathbf{X}_F = \mathbf{X}_{F1} = \mathbf{X}_{F2}$ and $\mathbf{X}_E = \mathbf{X}_{E1} = \mathbf{X}_{E2}$, respectively. This assumption

is valid because it hardly affects the GW signal. Then, total output of LMI is

$$\begin{aligned} \delta\tilde{\Phi}_{\rm all} &\equiv \delta\tilde{\Phi}_1 - \delta\tilde{\Phi}_2 \\ &= \alpha(\Omega, R_F, R_E)\delta\tilde{\phi}_{\rm all} \end{aligned} \tag{E.17}$$

$$\begin{aligned} \delta\tilde{\phi}_{\rm all} &= \frac{\omega}{\Omega}\, e^{-i\Omega(2\tau+\mathbf{e}_z\cdot\mathbf{x}_F/c)} \sum_A \mathbf{e}^A \tilde{h}_A \\ &\quad : [\ (\mathbf{n}_2\otimes\mathbf{n}_2)\, H_{\rm LMI}(\Omega,\, \mathbf{e}_z\cdot\mathbf{n}_2) - (\mathbf{n}_1\otimes\mathbf{n}_1)\, H_{\rm LMI}(\Omega,\, \mathbf{e}_z\cdot\mathbf{n}_1)\ ]\ , \end{aligned} \tag{E.18}$$

with

$$\begin{aligned} H_{\rm LMI}(\Omega,\, \mathbf{e}_z\cdot\mathbf{n}_1) \equiv\ & \frac{1}{1-(\mathbf{e}_z\cdot\mathbf{n}_1)^2}\,[\ \sin\Omega\tau\ (e^{-ip_1}+e^{-ip_2}-2\cos\Omega\tau) \\ & -i(\mathbf{e}_z\cdot\mathbf{n}_1)(e^{-i(p_1+p_2)}+\cos 2\Omega\tau-(e^{-ip_1}+e^{-ip_2})\cos\Omega\tau)\ ]\ , \end{aligned}$$

where we defined $p_1 \equiv \Omega\tau(\mathbf{e}_z\cdot\mathbf{n}_1)$ and $p_2 \equiv \Omega\tau(\mathbf{e}_z\cdot\mathbf{n}_2)$.

Appendix F

Quantum theory in a laser interferometer

Full-quantum treatment of quantum noise has been formulated by Kimble et al. (hereafter "KLMTV") [185]. Recent calculations of quantum noise in a laser interferometer for GWs are based on the formalism. In this Appendix, we will review it briefly.

F.1 Quantum formalism

In the Heisenberg picture, a quantized electromagnetic field with positive frequencies can be written as [1]

$$E^{(+)} = \int_0^\infty \sqrt{\frac{2\pi\hbar\omega}{\mathcal{A}\,c}}\; a_\omega e^{-i\omega t}\frac{d\omega}{2\pi}\;. \tag{F.1}$$

Here $\mathcal{A}$ is the effective cross-section area of a beam, and a_ω is the annihilation operator with a frequency ω, which holds the commutation relations:

$$[a_\omega, a_{\omega'}] = 0\;, \qquad [a_\omega, a^\dagger_{\omega'}] = 2\pi\delta(\omega-\omega')\;. \tag{F.2}$$

We split the field into side bands about the carrier frequency ω_0: $\omega = \omega_0 \pm \Omega$, and define

$$a_+ \equiv a_{\omega_0+\Omega}\;, \qquad a_- \equiv a_{\omega_0-\Omega}\;.$$

The commutation relation (F.2) implies

$$[a_+, a^\dagger_{+'}] = 2\pi\delta(\Omega-\Omega')\;, \qquad [a_-, a^\dagger_{-'}] = 2\pi\delta(\Omega-\Omega')\;,$$

and Eq. (F.1) becomes

$$E^{(+)} = \sqrt{\frac{2\pi\hbar\omega_0}{\mathcal{A}\,c}}e^{-i\omega_0 t}\int_0^\infty \left(a_+e^{-i\Omega t} + a_-e^{+i\Omega t}\right)\frac{d\Omega}{2\pi}\;.$$

[1] We use ω for the angular frequency of an electromagnetic field and ω_0 for the angular frequency of laser light, only in this chapter of Appendices.

Here we used the approximation $\omega_0 \pm \Omega \approx \omega_0$ in the square root, since, in general, $\omega_0 \approx 1.8 \times 10^{15}\,\mathrm{rad\,sec^{-1}}$ and $\Omega \leq 10^9\,\mathrm{rad\,sec^{-1}}$. We also formally extend the integrals over Ω to infinity, for ease of notation.

Next, we introduce two-photon mode formalism [189, 190], where the upper and lower sidebands $a_\pm$ are treated together. The two-photon mode formalism is adequate for an interferometric GW detector, because mirror motions due to GWs and external disturbances simultaneously create both sidebands. Defining field-amplitude operators for quadrature mode [2]

$$a_1 \equiv \frac{a_+ + a_-^\dagger}{\sqrt{2}}\,, \qquad a_2 \equiv \frac{a_+ - a_-^\dagger}{\sqrt{2}i}\,, \tag{F.3}$$

and using $E = E^{(+)} + E^{(-)}$ together wtih $E^{(-)} = [E^{(+)}]^\dagger$, one can write the electromagnetic field into the following form,

$$\begin{aligned} E &= \sqrt{\frac{4\pi\hbar\omega_0}{\mathcal{A}\,c}}\left[\cos(\omega_0 t)\int_0^\infty \left(a_1 e^{-i\Omega t} + a_1^\dagger e^{i\Omega t}\right)\frac{d\Omega}{2\pi}\right. \\ &\qquad \left. + \sin(\omega_0 t)\int_0^\infty \left(a_2 e^{-i\Omega t} + a_2^\dagger e^{i\Omega t}\right)\frac{d\Omega}{2\pi}\right]\,. \end{aligned} \tag{F.4}$$

The new operators a_1 and a_2 satisfy the commutation relations:

$$\begin{aligned} &[a_1, a_{2'}^\dagger] = -[a_2, a_{1'}^\dagger] \;= 2\pi i\delta(\Omega - \Omega')\,, \\ &[a_1, a_{1'}] = [a_1, a_{1'}^\dagger] = [a_1^\dagger, a_{1'}^\dagger] = [a_1, a_{2'}] = [a_1^\dagger, a_{2'}^\dagger] = 0\,. \end{aligned}$$

F.2 Conventional Fabry-Perot Michelson interferometer

Hereafter we consider the case of Fabry-Perot Michelson interferometer (FPMI) [185]. However, the qualitative descriptions also hold for any other laser interferometers. In the FPMI, quantum noise is caused by a vacuum field a entering an interferometer from the dark port [3] [182, 183], as shown in Fig. F.1. The a field is shot noise itself and also produces radiation-pressure noise, coupled with the carrier light in the Fabry-Perot (FP) cavity. b is the output field, which includes shot noise, radiation-pressure noise and GW signal.

[2] Strictly speaking, the field amplitudes for quadrature modes are defined by

$$a_1 \equiv \sqrt{\frac{\omega_0+\Omega}{2\omega_0}}a_+ + \sqrt{\frac{\omega_0-\Omega}{2\omega_0}}a_-^\dagger, \qquad a_2 \equiv -i\sqrt{\frac{\omega_0+\Omega}{2\omega_0}}a_+ + i\sqrt{\frac{\omega_0-\Omega}{2\omega_0}}a_-^\dagger$$

However, in our case, since $\omega_0 \gg \Omega$, they are approximated to Eq. (F.3)

[3] In practice, losses of optics allow vacuum fluctuation to come into the interferometer through not only the dark port but also other paths, for example, end mirrors with finite transmissivity and loss, or light scattering at mirrors and a beam splitter.

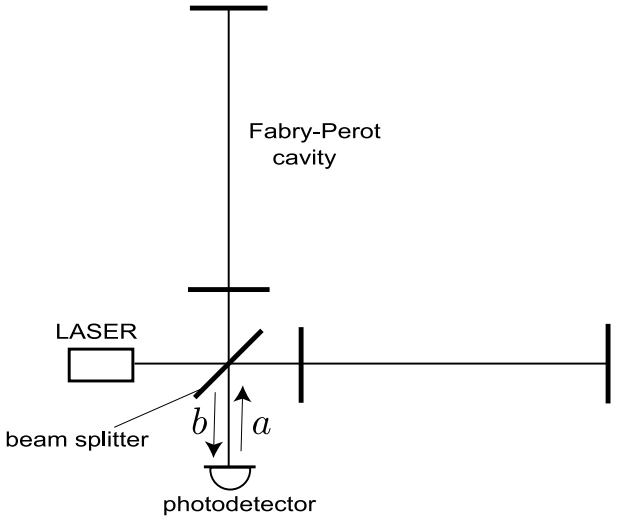

Figure F.1: Input field a and output field b in a Fabry-Perot Michelson interferometer.

What we need to calculate the power spectrum of quantum noise is the relation between the input and output fields. The input field is given by Eq. (F.4) and the output field is written as

$$\begin{aligned} E_{\rm out} &= \sqrt{\frac{4\pi\hbar\omega_0}{\mathcal{A}\,c}}\left[\cos(\omega_0 t)\int_0^\infty \left(b_1 e^{-i\Omega t} + b_1^\dagger e^{i\Omega t}\right)\frac{d\Omega}{2\pi}\right. \\ &\qquad \left. + \sin(\omega_0 t)\int_0^\infty \left(b_2 e^{-i\Omega t} + b_2^\dagger e^{i\Omega t}\right)\frac{d\Omega}{2\pi}\right] . \end{aligned}$$

Then, after long but straightforward calculation, one can obtain the input-output relation [185]:

$$\begin{aligned} b_1 &= a_1 e^{2i\beta} \\ b_2 &= a_2 e^{2i\beta} - K a_1 e^{2i\beta} + \sqrt{2K}\left(\frac{h}{h_{SQL}}\right) e^{i\beta} . \end{aligned} \tag{F.5}$$

where various quantities are defined as below.

$$\begin{aligned} \gamma &= \frac{T^2 c}{4L} , \\ \beta &= \arctan(\Omega/\gamma) , \\ I_{\rm SQL} &= \frac{mL^2\gamma^4}{4\omega_0}, \\ K &= \frac{2(I_0/I_{\rm SQL})}{(\Omega/\gamma)^2[1+(\Omega/\gamma)^2]}, \\ h_{\rm SQL} &= \sqrt{\frac{8\hbar}{m\Omega^2 L^2}} . \end{aligned} \tag{F.6}$$

In the calculation, it is assumed that all optics have no losses and that the end mirrors are completely reflective. T is the amplitude transmissivity of FP cavity's front mirror [4]. γ is FP-cavities' half bandwidth, which determines the characteristic frequency of the FP cavity, and β is the effective phase shift of a sideband field in the FP cavity. K is a coupling constant between a carrier field and a sideband field, which determines the intensity of radiation-pressure. h_{SQL} is the square root of the SQL spectral density and I_{SQL} is the laser power required to reach SQL at $\Omega = \gamma$. In Eq. (F.5), the first term is shot noise, the second term is radiation-pressure noise, and the third term is the GW signal.

Converting the noise signal to GW amplitude, h_n is defined as

$$h_n(\Omega) = \frac{h_{SQL}}{\sqrt{2K}}(a_2 - Ka_1)e^{i\beta} \ . \tag{F.7}$$

Then, spectral density is defined as the variance of the reduced noise amplitude by

$$\frac{1}{2}2\pi\delta(\Omega - \Omega')S_h(\Omega) \equiv \langle \mathrm{in}|h_n(\Omega)h_n^\dagger(\Omega')|\mathrm{in}\rangle_{\mathrm{sym}} \ ,$$

where subscript "sym" means calculating by replacing $h_n(\Omega)h_n^\dagger(\Omega')$ with

$$\frac{1}{2}\left(h_n(\Omega)h_n^\dagger(\Omega') + h_n^\dagger(\Omega')h_n(\Omega)\right) \ ,$$

and $|\mathrm{in}\rangle$ is an input state. In our configuration, input state at the dark port is in its vacuum state, defined using annihilation operators for each sideband by

$$a_+|0_a\rangle = a_-|0_a\rangle = 0 \ .$$

Using the relation

$$\langle 0_a|a_j(\Omega)a_k^\dagger(\Omega')|0_a\rangle_{\mathrm{sym}} = \frac{1}{2}\,2\pi\delta(\Omega - \Omega')\delta_{jk} \ ,$$

we can obtain the spectral density of quantum noise in the FPMI,

$$S_h = \frac{h_{\mathrm{SQL}}^2}{2}\left(\frac{1}{K} + K\right) \ . \tag{F.8}$$

This spectral density reaches the minimum noise level, the so-called standard quantum limit (SQL), at $\Omega = \gamma$ when the laser power I_0 is I_{SQL}. This indicates that there exists optimal laser power in order to minimize the noise at a certain frequency, since the shot noise and radiation pressure noise are proportional and inversely proportional to the laser power, respectively. Therefore, in this configuration of the FPMI, one cannot overcome the SQL, because shot noise and radiation pressure noise have no dynamical correlation.

[4] This is different from the definition in KLMTV's paper.

F.3 Optional quantum configurations

Although one cannot overcome the SQL in the conventional configuration of the FPMI, but, quantum mechanically, the SQL can be circumvented. Several methods to overcome the SQL with quantum correlations have been proposed.

Squeezed input

If a squeezed vacuum field is injected from the dark port, instead of the coherent vacuum field, shot noise level can be reduced. The original idea is proposed by Unruh [191] in the early 1980s. In the case of a coherent vacuum input, the quadrature modes a_1 and a_2 in Eq. (F.5) have the same amplitude. If the vacuum state is squeezed, one of the quadrature amplitude is reduced, while the other amplitude orthogonal to it become worse. In other words, one can perform more accurate phase measurement of a beam with shot noise less than that of the coherent vacuum, if the detection phase is properly selected. This technique is completely based on quantum correlations.

The squeezing of light was first confirmed experimentally by Slusher *et al.* in 1985. Soon after the first detection, it was demonstrated that the shot-noise level is improved below that of zero-point fluctuations by using the squeezed vacuum incident into the interferometer [192]. Then, the experimental demonstrations toward the installation of the squeezing into a large-scale interferometer has been reported by many authors [193, 194, 195, 196, 197, 198].

Variational output

Vyatchanin and Matsko [199, 200, 201] invented this design conceptually in the early 1990s. The detector input is the same as that in a conventional one, but the output is modified. This method takes advantage of the fact that the output field is ponderomotively squeezed due to the mirror motion induced by radiation pressure, which was first recognized by Braginsky and Manukin [202]. Thus, if the phase of the homodyne detection is properly selected, the quantum noise can be reduced and circumvents the SQL without modifying the input of the interferometer.

Signal recycling

This method uses one extra mirror, called a signal recycling (SR) mirror [5]. This additional mirror can reshape the noise curve and make two dips on it [203, 204]. Recently, quantum noise has been calculated in the case of Advanced-LIGO, in which SR mirror is put at the dark port of the interferometer [205, 206]. The SR mirror creates dynamical correlations between shot noise and radiation-pressure noise, and makes it possible to circumvent the SQL. The signal recycling is planned to apply to the next-generation interferometers such as Advanced LIGO [33], Advanced VIRGO [34], LCGT [36], and

[5]The interferometer configuration is called signal recycling, detuned signal recycling or resonant sideband extraction, depending on the microscopic position of the extra mirror at the dark port. Here we call all of them signal recycling.

AIGO [35]. This method has been extended in another detector configuration [207], a so-called differential-type FPMI, which detects signals for each arm independently and combines (differentiates) them after the detection. In the configuration with two SR mirrors, three dips appear on the noise curve.

References

[1] A. Einstein, *Annalen der Physik*, 49 (1916).

[2] C. M. Will, *Theory and experiment in gravitational physics*, (Cambridge University Press (1993).

[3] J. H. Taylor and J. M. Weisberg, *Astrophys. J.* **253**, 908 (1982).

[4] J. H. Taylor and J. M. Weisberg, *Astrophys. J.* **345**, 434 (1989).

[5] M. J. Valtonen *et al.*, *Nature* **452**, 851 (2008).

[6] C. W. Misner, K. S. Thorne, and J. A. Wheeler, *Gravitation* (W. H. FREEMAN AND COMPANY, New York, 1970).

[7] M. Maggiore, *Phys. Rep.* **331**, 283 (2000).

[8] A. A. Penzias and R. W. Wilson, *Astrophys. J.* **142**, 419 (1965).

[9] G. F. Smoot *et al.*, *Astrophys. J.* **396**, L1 (1992).

[10] D. N. Spergel *et al.*, *Astrophys. J. Suppl. Ser.* **148**, 175 (2003).

[11] H. V. Peiris *et al.*, *Astrophys. J. Suppl. Ser.* **148**, 213 (2003).

[12] C. L. Bennett *et al.*, *Astrophys. J. Suppl. Ser.* **148**, 1 (2003).

[13] A. Kogut *et al.*, *Astrophys. J. Suppl. Ser.* **148**, 161 (2003).

[14] G. Hinshaw *et al.*, *Astrophys. J. Suppl. Ser.* **148**, 135 (2003).

[15] E. Komatsu *et al.*, arXiv:0803.0547 (2008).

[16] A. H. Guth, *Phys. Rev.* D **23**, 347 (1981).

[17] K. Sato, *Mon. Not. R. Astron. Soc.* **195**, 467 (1981).

[18] A. D. Linde, *Phys. Lett.* B **108**, 389 (1982).

[19] A. Albrecht and P. J. Steinhardt, *Phys. Rev. Lett.* **48**, 1220 (1982).

[20] M. Tegmark *et al.*, *Phys. Rev.* D **69**, 103501 (2004).

[21] M. Tegmark *et al.*, *Phys. Rev.* D **74**, 123507 (2006).

[22] U. Seljak *et al.*, *Phys. Rev.* D **71**, 103515 (2005).

[23] S. E. Whitcomb, *Class. Quantum Grav.* **25**, 114013 (2008).

[24] J. Weber, *Phys. Rev.* **117**, 306 (1960).

[25] J. Weber, *Phys. Rev. Lett.* **22**, 1320 (1969).

[26] Z. A. Allen *et al.*, *Phys. Rev. Lett.* **85**, 5046 (2000).

[27] P. Astone *et al.*, *Phys. Rev.* D **68**, 022001 (2003).

[28] P. Astone *et al.*, *Phys. Rev.* D **76**, 102001 (2007).

[29] R. Takahashi *et al.*, *Class. Quantum Grav.* **25**, 114036 (2008); TAMA300 webpage, http://tamago.mtk.nao.ac.jp/tama.html.

[30] D. Sigg *et al.*, *Class. Quantum Grav.* **25**, 114041 (2008); LIGO webpage, http://www.ligo.caltech.edu/.

[31] F. Acernese *et al.*, *Class. Quantum Grav.* **25**, 114045 (2008); VIRGO webpage, http://wwwcascina.virgo.infn.it/.

[32] H. Grote *et al.*, *Class. Quantum Grav.* **25**, 114043 (2008); GEO600 webpage, http://geo600.aei.mpg.de/.

[33] Advanced LIGO webpage, http://www.ligo.caltech.edu/advLIGO/scripts/summary.shtml, http://www.ligo.caltech.edu/ ligo2/.

[34] Advanced VIRGO webpage, http://wwwcascina.virgo.infn.it/advirgo/.

[35] D. G. Blair *et al.*, *J. Phys. Conf. Ser.* **122**, 012001 (2008); AIGRC webpage, http://www.gravity.uwa.edu.au/.

[36] K. Kuroda *et al.*, *Prog. Theor. Phys. Suppl.* **163**, 54 (2006); LCGT webpage, http://gw.icrr.u-tokyo.ac.jp:8888/lcgt/.

[37] ET webpage, http://www.et-gw.eu/.

[38] LISA webpage, http://lisa.jpl.nasa.gov/ (NASA), http://lisa.esa.int/science-e/www/area/index.cfm?fareaid=27 (ESA), LISA mission documents are in LISC webpage, http://www.lisa-science.org/resources/talks-articles/mission.

[39] S. Kawamura *et al.*, *J. Phys. Conf. Ser.* **122**, 012006 (2008).

[40] G. M. Harry P. Fritschel, D. A. Shaddock, W. Folkner, and E. S. Phinney, *Class. Quantum Grav.* **23**, 4887 (2006).

[41] F. Pegoraro, L. A. Radicati, Ph. Bernard, and E. Picasso, *Phys. Lett.* A **68**, 165 (1978).

[42] Ph. Bernard, G. Gemme, R. Parodi, and E. Picasso, *Rev. Sci. Instrum.* **72**, 2428 (2001).

[43] A. M. Cruise, *Mon. Not. R. Astr. Soc.* **204**, 485 (1983).

[44] A. M. Cruise, *Class. Quantum Grav.* **17**, 2525 (2000).

[45] A. M. Cruise and R. M. J. Ingley, *Class. Quantum Grav.* **23**, 6185 (2006).

[46] F. Y. Li, M. X. Tang, D. P. Shi, *Phys. Rev.* D **67**, 104008 (2003).

[47] M. L. Tong, Y. Zhang, and F. Y. Li, *Phys. Rev.* D **78**, 024041 (2008).

[48] A. Nishizawa *et al.*, *Phys. Rev.* D **77**, 022002 (2008).

[49] A. Nishizawa *et al.*, *Class. Quantum Grav.* **25**, 225011 (2008).

[50] T. Akutsu *et al.*, *Phys. Rev. Lett.* **101**, 101101 (2008).

[51] B. Allen and J. D. Romano, *Phys. Rev.* D **59**, 102001 (1999).

[52] G. Hinshaw *et al.*, *Astrophys. J. Suppl. Ser.* **170**, 288 (2007).

[53] M. R. Nolta *et al.*, arXiv:0803.0593 (2008).

[54] S. H. S. Alexander, M. E. Peskin, and M. M. Sheikh-Jabbari, *Phys. Rev. Lett.* **96**, 081301 (2006).

[55] D. H. Lyth, C. Quimbay, and Y. Rodriguez, *J. High Energy Phys.* **03** (2005) 016.

[56] R. A. Isaacson, *Phys. Rev.* **166**, 1263 (1968).

[57] R. A. Isaacson, *Phys. Rev.* **166**, 1272 (1968).

[58] E. W. Kolb and M. S. Turner, *The Early Universe* (Westview Press, 1990).

[59] A. R. Liddle and D. H. Lyth, *Cosmological Inflation and Large-Scale Structure* (Cambridge University Press, 2000).

[60] L. P. Grishchuk, *Sov. Phys. JETP* **40**, 409 (1975).

[61] V. A. Rubakov, M. V. Sazhin, and A. V. Veryastin, *Phys. Lett.* B **115**, 189 (1982).

[62] R. Fabbri and M. D. Pollock, *Phys. Lett.* B **125**, 445 (1983).

[63] L. F. Abbott and M. B. Wise, *Nucl. Phys.* B **244**, 541 (1984).

[64] L. F. Abbott and D. D. Harari, *Nucl. Phys.* B **264**, 487 (1986).

[65] B. Allen, *Phys. Rev.* D **37**, 2078 (1988).

[66] S. Nakamura, N Yoshino, and S. Kobayashi, *Prog. Theor. Phys.* **88**, 1107 (1992).

[67] N. D. Birrell and P. C. W. Davies, *Quantum fields in curved space* (Cambridge University Press, 1982).

[68] A. G. Muslimov, *Class. Quantum Grav.* **7**, 231 (1990).

[69] D. S. Salopek and J. R. Bond, *Phys. Rev.* D **42**, 3936 (1990).

[70] A. R. Liddle, P. Parsons, and J. D. Barrow, *Phys. Rev.* D **50**, 7222 (1994).

[71] W. H. Kinney, *Phys. Rev.* D **66**, 083508 (2002).

[72] E. D. Stewart and D. H. Lyth, *Phys. Lett.* B **302**, 171 (1993).

[73] A. Kosowsky and M. S. Turner, *Phys. Rev.* D **52**, 1739 (1995).

[74] T. L. Smith, M. K. Kamionkowski, and A. Cooray, *Phys. Rev.* D **73**, 023504 (2006).

[75] M. S. Turner, M. White, and J. E. Lidsey, *Phys. Rev.* D **48**, 4613 (1993).

[76] S. Chongchitnan and G. Efstathiou, *Phys. Rev.* D **73**, 083511 (2006).

[77] P. J. E. Peebles and A. Vilenkin, *Phys. Rev.* D **59**, 063505 (1999).

[78] R. R. Caldwell, R. Dave, P. J. Steinhardt, *Phys. Rev. Lett.* **80**, 1582 (1998).

[79] I. Zlatev, L. Wang, and P. J. Steinhardt, *Phys. Rev. Lett.* **82**, 896 (1999).

[80] L. H. Ford, *Phys. Rev.* D **35**, 2955 (1987).

[81] T. Damour and A. Vilenkin, *Phys. Rev.* D **53**, 2981 (1996).

[82] M. Giovannini, *Phys. Rev.* D **58**, 083504 (1998).

[83] M. Giovannini, *Phys. Rev.* D **60**, 123511 (1999).

[84] L. Kofman, A. Linde, and A. A. Starobinsky, *Phys. Rev.* D **56**, 3258 (1997).

[85] G. Felder, L. Kofman, and A. Linde, *Phys. Rev.* D **59**, 123523 (1999).

[86] G. Felder, L. Kofman, and A. Linde, *Phys. Rev.* D **60**, 103505 (1999).

[87] H. Tashiro, T. Chiba, and M. Sasaki, *Class. Quantum Grav.* **21**, 1761 (2004).

[88] G. Veneziano, *Phys. Lett.* B **265**, 287 (1991).

[89] M. Gasperini and G. Veneziano, *Astropart. Phys.* **1**, 317 (1993).

[90] A. Buonanno, M. Maggiore, and C. Ungarelli, *Phys. Rev.* D **55**, 3330 (1997).

[91] M. Gasperini and G. Veneziano, *Phys. Rev.* D **50**, 2519 (1994).

[92] M. Gasperini and M. Giovannini, *Phys. Rev.* D **47**, 1519 (1993).

[93] M. Gasperini and M. Giovannini, *Phys. Lett.* B **282**, 36 (1992).

[94] M. Gasperini and M. Giovannini, *Phys. Rev.* D **47**, 1519 (1993).

[95] R. Brustein, M. Gasperini, M. Giovannini, and G. Veneziano, *Phys. Lett.* B **361**, 45 (1995).

[96] V. Mandic and A. Buonanno, *Phys. Rev.* D **73**, 063008 (2006).

[97] S. Khlebnikov and I. Tkachev, *Phys. Rev.* D **56**, 653 (1997).

[98] R. Easther and E. A. Lim, *J. Cosmol. Astropart. Phys.* **04** (2006) 010.

[99] R. Easther, J. T. Giblin, Jr., and E. A. Lim, *Phys. Rev. Lett.* **99**, 221301 (2007).

[100] J. Garcia-Bellido and D. G. Figueroa, *Phys. Rev. Lett.* **98**, 061302 (2007).

[101] J. Garcia-Bellido, D. G. Figueroa, and A. Sastre, *Phys. Rev.* D **77**, 043517 (2008).

[102] A. Kosowsky, M. S. Turner, and R. Watkins, *Phys. Rev. Lett.* **69**, 2026 (1992); A. Kosowsky, M. S. Turner, and R. Watkins, *Phys. Rev.* D **45**, 4514 (1992).

[103] M. Kamionkowski, A. Kosowsky, and M. S. Turner, *Phys. Rev.* D **49**, 2837 (1994).

[104] A. Kosowsky, A. Mack, and T. Kahniashvili, *Phys. Rev.* D **66**, 024030 (2002).

[105] A. D. Dolgov, D. Grasso, and A. Nicolis, *Phys. Rev.* D **66**, 103505 (2002).

[106] A. Nicolis, *Class. Quantum Grav.* **21**, L27 (2004).

[107] C. Grojean and G. Servant, *Phys. Rev.* D **75**, 043507 (2007).

[108] T. W. B. Kibble, *J. Phys.* A **9**, 1387 (1976).

[109] R. R. Caldwell and B. Allen, *Phys. Rev.* D **45**, 3447 (1992).

[110] T. Damour and A. Vilenkin, *Phys. Rev. Lett.* **85**, 3761 (2000).

[111] T. Damour and A. Vilenkin, *Phys. Rev.* D **71**, 063510 (2005).

[112] X. Siemens, V. Mandic, and J. Creighton, *Phys. Rev. Lett.* **98**, 111101 (2007).

[113] C. J. Copi, D. N. Schramm, and M. S. Turner, *Phys. Rev.* D **55**, 3389 (1997).

[114] A. Stewart and R. Brandenberger, *J. Cosmol. Astropart. Phys.* **08** (2008) 012.

[115] T. L. Smith, E. Pierpaoli, and M. Kamionkowski, *Phys. Rev. Lett.* **97**, 021301 (2006).

[116] D. R. Lorimer, *Living. Rev. Relativity* **8**, 7 (2005).

[117] F. B. Estabrook and H. D. Wahlquist, *Gen. Relat. Gravit.* **6**, 439 (1975).

[118] S. Detweiler, *Astrophys. J.* **234**, 1100 (1979).

[119] V. M. Kaspi, J. H. Taylor, and M. F. Ryba, *Astrophys. J.* **428**, 713 (1994).

[120] G. Hobbs, arXiv: astro-ph/0412153 (2004); Parkes Pulsar Timing Array webpage, http://www.atnf.csiro.au/research/pulsar/ppta/.

[121] M. Kramer, arXiv: astro-ph/0409020 (2004); For the update, see, Square Kilometre Array webpage, http://www.skatelescope.org/.

[122] F. A. Jenet, G. B. Hobbs, K. J. Lee, and R. N. Manchester, *Astrophys. J.* **625**, L123 (2005).

[123] F. A. Jenet *eq al.*, *Astrophys. J.* **653**, 1571 (2006).

[124] S. M. Kopeikin, *Phys. Rev.* D **56**, 4455 (1997).

[125] J. W. Armstrong, L. Iess, P. Tortora, and B. Bertotti, *Astrophys. J.* **599**, 806 (2003).

[126] H. Kudoh, A. Taruya, T. Hiramatsu, Y. Himemoto, *Phys. Rev.* D **73**, 064006 (2006).

[127] E. E. Flanagan, *Phys. Rev.*, D **48**, 2389 (1993).

[128] N. Seto and A. Taruya, *Phys. Rev.* D **77**, 103001 (2008).

[129] B. Abbott *et al.*, *Astrophys. J.* **659**, 918 (2007).

[130] B. Abbott *et al.*, *Phys. Rev.* D **69**, 122004 (2004).

[131] E. Gustafson *et al.*, LIGO project document report, No. T990080-00-D (1999).

[132] A. G. Riess *et al.*, *Astron. J.* **116**, 1009 (1998).

[133] S. Perlmutter *et al.*, *Astrophys. J.* **517**, 565 (1999).

[134] K. J. Lee, F. A. Jenet, and R. H. Price, *Astrophys. J.* **685**, 1304 (2008).

[135] D. M. Eardley, D. L. Lee, A. P. Lightman, R. V. Wagoner, and C. M. Will, *Phys. Rev. Lett.* **30**, 884 (1973).

[136] E. Alesci and G. Montani, *Int. J. Mod. Phys.* D **14**, 1 (2005), arXiv: gr-qc/0411028.

[137] A. Frolov and L. Kofman, arXiv: hep-th/0209133 (2002).

[138] C. Charmousis, R. Gregory, N. Kaloper, and A. Padilla, *J. High Energy Phys.* **10**, 066 (2006).

[139] S. Capozziello and C. Corda, *Int. J. Mod. Phys.* D **15**, 1119 (2006).

[140] S. Capozziello, C. Corda, and M. D. Laurentis, *Mod. Phys. Lett.* A **22**, 2647 (2007).

[141] M. Maggiore and A. Nicolis, *Phys. Rev.* D **62**, 024004 (2000).

[142] S. Capozziello, C. Corda, and M. F. De Laurentis, *Phys. Lett.* B **669**, 255 (2008).

[143] C. Corda, *Astropart. Phys.* **30**, 209 (2008).

[144] W. L. S. de Paula, O. D. Miranda, and R. M. Marinho, *Class. Quantum Grav.* **21**, 4595 (2004).

[145] M. E. Tobar, T. Suzuki, and K. Kuroda, *Phys. Rev.* D **59**, 102002 (1999).

[146] A. S. Goldhaber and M. M. Nieto, *Phys. Rev.* D **9**, 1119 (1974).

[147] C. Talmadge, J.-P. Berthias, R. W. Hellings, and E. M. Standish, *Phys. Rev. Lett.* **61**, 1159 (1988).

[148] L. S. Finn and P. J. Sutton, *Phys. Rev.* D **65**, 044022 (2002).

[149] M. Maggiore and A. Nicolis, *Phys. Rev.* D **62**, 024004 (2000).

[150] N. Christensen, *Phys. Rev.* D **46**, 5250 (1992).

[151] B. J. Carr, *Quantum Gravity: From Theory to Experimental Search (Lecture Notes in Physics)*, edited by C. Kiefer, C. Lammerzahl, and D. Giulini (Springer-Verlag, 2003); B. Carr, arXiv: astro-ph/0511743 (2005).

[152] Ya. B. Zeldovich and I. D. Novikov, *Sov. Astron. A. J.* **10**, 602 (1967).

[153] S. Hawking, *Mon. Not. R. Astr. Soc.* **152**, 75 (1971).

[154] T. Nakamura, M. Sasaki, T. Tanaka, and K. S. Thorne, *Astrophys. J.* **487**, L139 (1997).

[155] K. Ioka, T. Chiba, T. Tanaka, and T. Nakamura, *Phys. Rev.* D **58**, 063003 (1998).

[156] K. T. Inoue and T. Tanaka, *Phys. Rev. Lett.* **91**, 021101 (2003).

[157] L. Randall and R. Sundrum, *Phys. Rev. Lett.* **83**, 3370 (1999).

[158] L. Randall and R. Sundrum, *Phys. Rev. Lett.* **83**, 4690 (1999).

[159] S. S. Seahra, C. Clarkson, and R. Maartens, *Phys. Rev. Lett.* **94**, 121302 (2005).

[160] C. Clarkson and S. S. Seahra, *Class. Quantum Grav.* **24**, F33 (2007).

[161] R. W. P. Drever, *Gravitational Radiation*, edited by N. Deruelle and T. Piran (North-Holland, Amsterdam, 1983), pp.321-338.

[162] J. Y. Vinet, B. J. Meers, C. N. Man and A. Brillet, *Phys. Rev.* D **38**, 433 (1988).

[163] B. J. Meers, *Phys. Rev.* D **38**, 2317 (1988).

[164] Y. Chen and S. Kawamura, *Phys. Rev. Lett.* **96**, 231102 (2006).

[165] R. Schilling, *Class. Quantum Grav.* **14**, 1513 (1997).

[166] M. Rakhmanov, *Class. Quantum Grav.* **25**, 184017 (2008).

[167] T. Chiba, Y. Himemoto, M. Yamaguchi, and J. Yokoyama, *Phys. Rev.* D **76**, 043516 (2007).

[168] A. Nishizawa, S. Kawamura, and M. Sakagami, *Phys. Rev. Lett.* **101**, 081101 (2008).

[169] T. Akutsu, *Search for a stochastic background of gravitational waves at 100 MHz with laser interferometers*, Ph.D. thesis, University of Tokyo (2007).

[170] R. W. P. Drever, J. L. Hall, F. V. Kowalski, J. Hough, G. M. Ford, A. J. Munley, and H. Ward, *Appl. Phys.* B **31**, 97 (1983).

[171] S. Kawamura and Y. Chen, *Phys. Rev. Lett.* **93**, 211103 (2004).

[172] Y. Chen and S. Kawamura, *Phys. Rev. Lett.* **96**, 231102 (2006).

[173] Y. Chen *et al.*, *Phys. Rev. Lett.* **97**, 151103 (2006).

[174] S. Sato, K. Kokeyama, R. L. Ward, S. Kawamura, Y. Chen, A. Pai, and K. Somiya, *Phys. Rev. Lett.* **98**, 141101 (2007).

[175] K. Somiya and K. Goda and Y. Chen and E. E. Mikhailov, *J. Phys. Conf. Ser.* **66**, 012053 (2007).

[176] Y. Chen *et al.*, *Phys. Rev. Lett.* **97**, 151103 (2006).

[177] V. B. Braginsky and F. Ya. Khalili, *Phys. Lett.* A **147**, 251 (1990).

[178] V. B. Braginsky, M. L. Gorodetsky, F. Y. Khalili, and K. S. Thorne, *Phys. Rev.* D **61**, 044002 (2000).

[179] P. Purdue, *Phys. Rev.* D **66**, 022001 (2002).

[180] P. Purdue and Y. Chen, *Phys. Rev.* D **66**, 122004 (2002).

[181] Y. Chen, *Phys. Rev.* D **67**, 122004 (2003).

[182] C. M. Caves, *Phys. Rev. Lett.* **45**, 75 (1980).

[183] C. M. Caves, *Phys. Rev.* D **23**, 1693 (1981).

[184] V. B. Braginsky and F. Ya. Khalili, *Quantum Measurement*, edited by K. S. Thorne (Cambridge University Press, 1992).

[185] H. J. Kimble, Y. Levin, A. B. Matsko, K. S. Thorne, and S. P. Vyatchanin, *Phys. Rev.* D **65**, 022002 (2001).

[186] V. B. Braginsky, *Sov. Phys. JETP*, **26**, 831 (1968).

[187] S. P. Vyatchanin, arXiv:0808.3445 (2008).

[188] R. Schilling, *Class. Quantum Grav.* **14**, 1513 (1997).

[189] C. M. Caves and B. L. Schumaker, *Phys. Rev.* A **31**, 3068 (1985).

[190] B. L. Schumaker and C. M. Caves, *Phys. Rev.* A **31**, 3093 (1985).

[191] W. G. Unruh, *Quantum Optics, Experimental Gravitation, and Measurement Theory*, edited by P. Meystre and M. O. Scully, p647, (Plenum, New York, 1982).

[192] M. Xiao, L. A. Wu, and H. J. Kimble, *Phys. Rev. Lett.* **59**, 278 (1987).

[193] K. McKenzie, D. A. Shaddock, D. E. McClelland, B. C. Buchler, and P. K. Lam, *Phys. Rev. Lett.* **88**, 231102 (2002).

[194] K. McKenzie, N. Grosse, W. P. Bowen, S. E. Whitcomb, M. B. Gray, D. E. McClelland, and P. K. Lam, *Phys. Rev. Lett.* **93**, 161105 (2004).

[195] H. Vahlbruch, S. Chelkowski, B. Hage, A. Franzen, K. Danzmann, and R. Schnabel, *Phys. Rev. Lett.* **95**, 211102 (2005).

[196] H. Vahlbruch, S. Chelkowski, B. Hage, A. Franzen, K. Danzmann, and R. Schnabel, *Phys. Rev. Lett.* **97**, 011101 (2006).

[197] H. Vahlbruch, M. Mehmet, S. Chelkowski, B. Hage, A. Franzen, N. Lastzka, S. Goβler, K. Danzmann, and R. Schnabel, *Phys. Rev. Lett.* **100**, 033602 (2008).

[198] K. Goda *et al.*, *Nature Phys.* **4**, 472 (2008).

[199] S. P. Vyatchanin and A. B. Matsko, *Sov. Phys. JETP* **77**, 218 (1993).

[200] S. P. Vyatchanin and A. B. Matsko, *Sov. Phys. JETP* **82**, 1007 (1996).

[201] S. P. Vyatchanin and A. B. Matsko, *Sov. Phys. JETP* **83**, 690 (1996).

[202] V. B. Braginsky and A. B. Manukin, *Sov. Phys. JETP* **25**, 987 (1967).

[203] B. J. Meers, *Phys. Rev.* D **38**, 2317 (1988).

[204] J. Mizuno, K. A. Strain, P. G. Nelson, J. M. Chen, R. Schilling, A. Rudiger, W. Winkler, and K. Danzmann, *Phys. Lett.* A **175**, 273 (1993).

[205] A. Buonanno and Y. Chen, *Phys. Rev.* D **64**, 042006 (2001).

[206] A. Buonanno and Y. Chen, *Phys. Rev.* D **65**, 042001 (2002).

[207] A. Nishizawa, M. Sakagami, and S. Kawamura, *Phys. Rev.* D **76**, 042002 (2007).

Acknowledgement

I would like to thank all who have supported me, in Japanese.

本論文を書き上げるにあたっては、多くの人々にお世話になりました [6]。

京都大学の阪上雅昭 教授には修士課程入学当時から未熟な私にも辛抱強くご指導頂き、物理に限らず研究に対する心構えまで多岐に渡って教えて頂いた事は心から感謝致します。また、国立天文台の川村静児 準教授には博士課程より受託院生として快く受け入れて頂き、ご指導・助言を頂くと共に、自由に研究に専念出来る環境を提供して頂いた事に深く感謝致します。

この学位論文のテーマの 1 つである超高周波数帯における重力波探査に関して、次の方々にお世話になりました。国立天文台の新井宏二 助教、辰巳大輔 助教、山元一広 研究員には実験に関する質問に対応して頂き、また論文の内容に関して助言を頂きました。同研究室・大学院生の阿久津智忠 氏には本実験だけではなく、その他の様々な議論にも付き合って頂きました。名古屋大学の杉山直 教授および高橋龍一 研究員、日本大学の千葉剛 準教授には本研究の理論面において支えて頂きました。学位論文のもう 1 つのテーマである重力波の偏極モードに関する研究では、東京大学の樽家篤史 助教にご多忙にも関わらず時間を割いて議論して頂きました。それ以外にも、カリフォルニア工科大学の Yanbei Chen 助教および宗宮健太郎 研究員、東京大学の安東正樹 助教、国立天文台の瀬戸直樹 研究員、大阪市立大学の神田展行 教授は私の研究に興味を示して下さり、貴重なご意見を頂きました。

以下の方々には国立天文台で行われている実験に共同研究として快く参加させて頂きました。国立天文台の佐藤修一 研究員、同・大学院生の苔山圭以子 氏には変位雑音フリー重力波検出器実験で、国立天文台の阪田紫帆里 研究員および Volker Leonhardt 研究員には量子非破壊測定実験で、同・宮川治 研究員および同・大学院生の川添史子 氏には RSE 実験でお世話になりました。また、同・事務支援員である近藤さん、西村さん、吉住さんには出張手続きを始めとして種々の事務作業に関してお世話になりました。京都大学での同研究室の丹羽佳人 氏および奥住聡 氏、国立天文台での同研究室の和泉究 氏とは研究の合間に研究に関する事やどうでも良い事をよく議論しました。そのような日常会話も研究生活の一助となりました。

最後に、陰ながら暖かく見守り続けてくれた両親に感謝します。

[6] 役職名は主にお世話になった当時のものです。また、海外研究機関の場合の役職名は対応する日本での役職名にしてあります。